A particle-γ coincidence study of ^{26}Na using the transfer reaction $^{25}Na(d,p\gamma)^{26}Na$

Ilker Can Celik

Department of Physics,
University of Surrey,
Guildford,
GU2 7XH

Submitted for the Degree of Doctor of Philosophy

Department of Physics,

Faculty of Engineering and Physical Sciences,

University of Surrey,

Guildford, GU2 7XH.

November 30, 2014

ProQuest LLC.
789 East Eisenhower Parkway
P.O. Box 1346
Ann Arbor, MI 48106 – 1346

Abstract

In this thesis, the radioactive beam (RIB) ^{25}Na at 5 MeV/u with an intensity of up to 3×10^7 pps is exploited to study states in ^{26}Na using a $0.5 mg/cm^2$ deuterated polyethylene (CD_2) target via the highly selective $(d, p\gamma)$ transfer reaction. The reaction products are recorded by using both SHARC (the Silicon Highly-segmented Array for Reactions and Coulex) and TIGRESS (The TRIUMF-ISAC Gamma-Ray Escape-Suppressed Spectrometer). The SHARC array is installed at the ISAC-2 facility in TRIUMF (Canada) to study a variety of reactions, but single-particle transfer with a radioactive ion beam is the reaction mechanism of interest here. This experimental study was the first radioactive beam experiment making use of the TIGRESS/SHARC detector set-up in 2009. This work significantly extends an earlier analysis.

The motivation of this work is to combine the information extracted from the particle and the γ detection in $^{25}Na(d, p\gamma)^{26}Na$ reaction data to compare the experimentally observed results and the shell model predictions. A total of 24 states were studied, of which 10 had not been reported previously, and detailed new information was extracted for most of these. Properties measured and discussed include: (1) the observed γ-ray decay branching ratios, (2) the observed spectroscopic factors (population strength) in the (d,p) reaction, (3) the observed angular momentum transfer in the (d,p) reaction, (4) a comparison between experimental and the predicted excitation energies from shell model calculations, (5) spin assignments based on the predicted reaction strengths and observed γ-ray decay scheme, and (6) analogies with the experimentally observed gamma-decay properties of the isotone ^{28}Al. An extra new feature of this work, for the important

interpretation of similar future experiments, is a detailed study of the γ-ray angular distributions and their dependence upon the scattered proton angles in (d,p).

Contents

Chapter 1

Introduction

1.1 Motivation to Study Single-Neutron Transfer Using Radioactive Beam

One powerful tool to populate certain energy states in a particular nucleus is the highly selective single neutron transfer reaction. It is because the energy of these particular states have a structure given by the core of the original nucleus and the transferred neutron in an orbit around the nucleus as in the current experiment $^{25}Na(d,p\gamma)^{26}Na$. This structure becomes more interesting to study as we go far from stability with radioactive beams like ^{25}Na. With a great endeavour put into this work, the shell model orbitals and their energies are compared to those in the populated states of ^{26}Na. Radioactive beam facilities provide more experiment opportunities to investigate nuclear structure via the (d,p) transfer reaction in neutron rich nuclei.

Even though there are complications to understanding the experimental data in connection to related theories, the interpretation of experimental results usually show selectivity of the transfer reaction on a single particle state. Generally speaking, states

with a large overlap with the simple core-plus-particle structure is strongly favourable in the selectivity. This plays an important factor in the current study. Most of the time, some states will be hidden under the background of other states which have close proximity in energy. It is also because these suppressed states may have rather complex wave functions combining different combinations of couplings from proton and neutron shells with same parities that have an odd number of nucleons. This can be seen between one un-paired proton in the $1d_{5/2}$ shell and the neutron shells in $1d_{5/2}$, $2s_{1/2}$, $1d_{3/2}$, and $1f_{7/2}$ for the transferred neutron as in the ^{26}Na nucleus.

Starting from strongly and easily populated states in the experiment, one can try to refine theoretical results given by the shell model. And, this will eventually help to understand more how the energy level diagram can be constructed differently. Complexity in the interpretation of the data arises once one tries to assess the wave function of a specific state overlaps with the wave function corresponding to both core and particle [2]. In the case of a (d,p) reaction in ^{25}Na, the requirement of a strong spatial overlap of the wave function, $< \psi_1 | \psi_2 >$, of a valence proton with the wave function of a valence neutron tends to require both the same or similar principal quantum number "n" and a similar angular momentum quantum number "l" for a particularly strong interaction. For example, the $d_{5/2}$ interaction with $d_{3/2}$ is expected to be seen dominantly in ^{26}Na. This is indeed what the experimental results are aimed to reflect in comparison with the current shell model predictions.

With suitably served assumptions, transfer reactions provide an extremely effective tool for uncovering the structures of exotic nuclei. And, by studying exotic nuclei, we can understand how and where the heavy elements were formed in the early universe [3]. Although there is no solid answer to this question, we certainly know these heavy

elements were formed in hot explosive environments and involved neutron rich isotopes that are many nucleons away from stability (the so-called r-process). The r-process may never be measured in the laboratory due to species that have short half lives, but the neutron capture reactions stay relevant to study the evolution of the nuclei. On the other hand, there are indirect methods involving nuclear reactions that we can use to extract the information of astrophysical interest as explained in detail in [4].

The neutron induced reaction (such as in the $^{25}Na(d,p\gamma)^{26}Na$ reaction) with rare isotopes plays an important role in astrophysics since it is one way to get heavy elements that exist in the stars. For closed shell targets, as for the neutrons in ^{25}Na, this problem can be addressed within a three-body model n + p + A where the ingredients of the theory are effective interactions among them. Therefore, the adiabatic wave approximation (ADWA) [5] theory is used as the choice of a tool to understand the nuclear force and the origin of the elements in some perspective.

1.1.1 Migration of Shell Gaps and Magic Numbers Far from Stability

Figure 1.1 represents a simplified presentation of the shell model orbital energies and occupancies for the protons and neutrons for ^{22}O, ^{24}Ne, ^{28}Si, and their isotopes populated via one neutron transfer reaction. The Schrödinger equation, which gives an interpretation of the physical meaning of the wave function of a particle or a system, solves the problem of showing the occupancy of a particular energy level for each nucleon for a mean field potential in the nuclear shell model. The binding effect of the rest of the nucleons in the nucleus is presented by this potential field. The Pauli exclusion principle, which forbids the occupation of the same quantum state simultaneously by two identical fermions (particles with half-integer spin), enables us to build the nuclear structure by filling the orbitals

starting from the lowest energy.

In the simplest model, the nuclear structure is obtained by filling orbitals from the lowest energies, obeying the Pauli exclusion principle. In more complicated models, the interactions due to coupling between valence nucleons in different or same orbitals result in different energy levels. One can represent the valence nucleon interaction energies as matrix element in some proper basis. This can be calculated with all of its dependence on spatial variables, spin and orbital angular momentum from the solutions for the mean field and an expression for the nucleon-nucleon interaction. If the calculated matrix elements are alternating by the fit to variety of experimental data, then the shell model calculations will be more representative and reflective to the results of these experiments. This can be done by establishing an effective and valid interaction in a particular model space that was used for the fitting procedure.

If it is supposed that the valence nucleons provide an interaction potential and an energy related to this interaction, then this interaction causes a change in the orbital energy levels to some extent. This interaction potentials can be analysed in terms of a multipole expansion [2] where the monopole term in the expansion may change the effective energies of the orbitals. The energy of the orbital and the sum of the monopole components of its interaction with other active valence nucleons determine the energy of a single valence nucleon in a particular orbital. Thus, interactions with partially filled orbitals should be taken into consideration instead of closed shells. Firstly, the type of the nucleon defines the strength of the interaction, and it is the interaction between proton and neutron which is the strongest. Secondly, the same number of radial nodes for orbitals indicates the strongest interaction as well as the same angular momentum has even stronger effect. This is because the degree of spatial overlap of the wave functions.

For example, the interaction between protons in an open $0d_{5/2}$ orbital and neutrons in an open $0d_{3/2}$ orbital is particularly strong. In that case, 0 is the node number for the first $d_{5/2}$ orbital.

In figure 1.1, the structure of the N = 14 isotones is shown with their isotopes that can be achieved via one neutron transfer. Due to the coupling of "l" and "s" quantum numbers, the shells have different "j" quantum numbers. The energy splitting due to observed spin orbital coupling arises from a sequence of complicated effects due to the nuclear force [[6] p.1]. The examples of ^{22}O, ^{24}Ne, and stable ^{28}Si have respectively 8, 10, and 14 protons. Since the $0d_{5/2}$ neutron shell is closed, an additional neutron is placed in to the $0d_{3/2}$ where spin and orbital quantum numbers are anti-aligned. In the nuclear potential, the spin orbit interaction becomes repulsive in the case of anti-alignment ($l \downarrow$) [[6] p.1]. To go from $^{28}Si_{14}$ to $^{22}O_{14}$, the proton removal is need. As one removes the proton, the possibility of having more interaction with a valence neutron decreases. This procedure makes the nuclei more exotic, that is to say, more neutron rich. The valence neutron shown in green is in the $0d_{3/2}$ shell, which means it has a repulsive interaction with a valence proton in $0d_{5/2}$ shell. Then, the proton-neutron interaction between $l+1/2$ and $l-1/2$ nucleons will show decrease in the energy of the corresponding orbital. It's because of the number of protons are decreased in neutron rich $^{22}O_{14}$ nucleus. That also means the shell gap is now at N=16. On the other hand, $0f_{7/2}$ and $1p_{3/2}$ shells with $l+1/2$ nucleons have repulsive interaction that lowers the energy of the orbital. This also explains why ^{24}O becomes unbound as it gets neutron rich [[2] p.3].

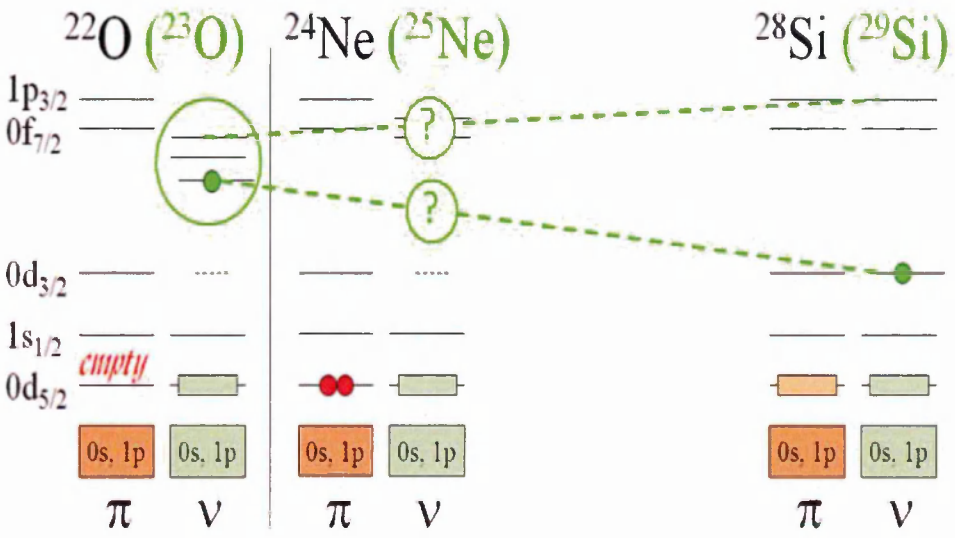

Figure 1.1: The effective energies of valence orbitals are modified by the presence or otherwise of protons in $0d_{5/2}$ orbital. The effect is to replace the N=20 neutron shell gap by a gap at N=16 when the nucleus becomes more exotic [2]. Also, another version of this diagram can be found in [7].

This example shows surprisingly but also realistically that N = 20 shell gap seen for nuclei near stability is replaced by N=16. Furthermore, it also tends to displace the N = 28 gap to a higher number (N = 34). In the present work, ^{25}Na and ^{26}Na are directly of interest because of this particular migration of orbital energies. What we measure experimentally are the energies of actual states in the populated nucleus of interest, and not the energies of the shell model orbitals. One of the aims of this work is to find a strong connection between the energies of the states and the orbitals as seen in the experiment and the shell model predictions.

1.1.2 Possibility of Having Different Structures in the Neutron Configuration

It is not always possible to have a simple structure of states that are populated via the transfer reaction as in the interest of this work. The explanation of a neutron orbiting the original core nucleus in ^{21}O is one of the examples given here. By one neutron transfer into a ^{20}O, even-odd nucleus can be reached where the transferred neutron can be placed into either the $1s_{1/2}$ or $0d_{3/2}$ orbit as in the illustration 1.2. If one wants to measure the energy of a particular state in ^{21}O, the difference between the energy when the transferred neutron is in the $0d_{3/2}$ and the energy of the ground state with the $0d_{5/2}$ shell filled by four neutrons as shown on the left side of the figure 1.2 will give the energy of the populated state. In this situation, the coupling of two holes in the $0d_{5/2}$ shell is oversimplified. On the another side of the figure 1.2, the two holes coupling to 2^+ state in ^{20}O may also couple with the un-paired neutron in the $1s_{1/2}$ neutron shell by resulting in two states one of which is $3/2^+$. Therefore, it is said that the residual interaction between valence nucleons can give the mixture of different configurations by splitting the amplitude of a single particle state into two states [2]. Again, the possibility of having more complex situations to show coexistence of single particle structure and other structures exists by giving more amplitude contribution in the wave function of the final state.

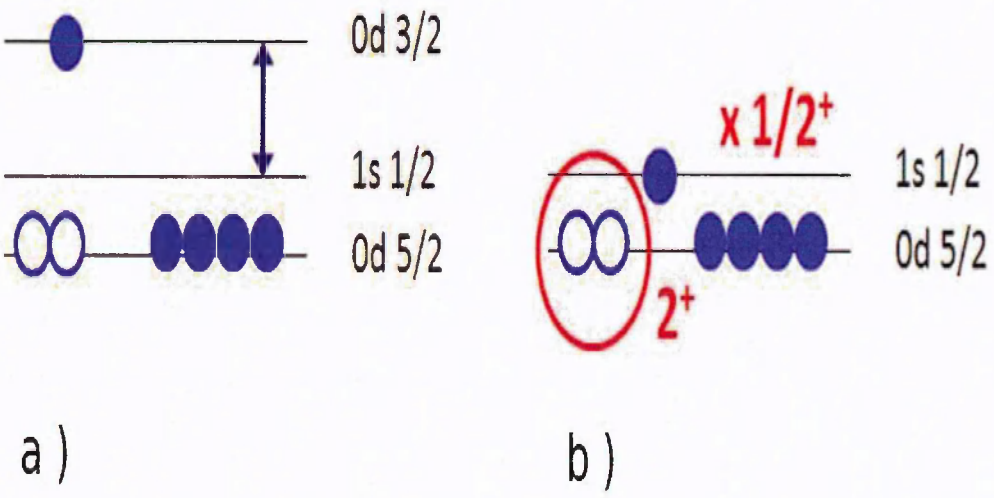

Figure 1.2: Neutron structure for states in ^{21}O to make a low-lying state with spin $3/2^+$ can be organised: a) by transferring a neutron into the vacant $0d_{3/2}$ orbital, or b) by having a neutron in $1s_{1/2}$ coupled to a 2^+ ^{20}O core, where two holes in $0d_{5/2}$ are coupled to spin 2 [2].

1.1.3 Explanation of Spectroscopic Factor to Describe Single Particle Structure

A single particle state, which can be imagined as a system with un-paired nucleon or a vacant orbital orbiting the core of the nucleus, can be found mixed with different structures of the states with same spin and parity. In this simplified version, each single particle state will have its own strength in the overall mixture with a value called "spectroscopic factor". In this work, the spectroscopic factor (SF) will be measured by scaling the theoretical scattered proton differential cross sections in the (d,p) reaction to those extracted in the experimental data. In the end, it is expected to have the same shape in data as in the

theory to assign a particular orbital angular momentum to a particular state. As explained before, the intensity of a single particle state will be spread across a range of states in the final nucleus as the same case may occur for ^{26}Na in the current work. The figure 1.3 displays the strength of a single particle as a function of excitation energy in MeV. In addition, the weighted average of the excitation energies will be regarded as the energy of the orbital where all the states contains partial strength for this specific "l-j" (orbital and total angular momentum quantum numbers) orbital. In the current work, the extraction of this information (SF) from the experimental data will be restricted by the intensity of the radioactive beam. In these circumstances, different approaches can be followed by relying on a theory more for the interpretation of the state energies and the reaction strengths (SF) based on comparisons of strongly populated states, using analogies with isotone nucleus. That is to say that the shell model results will be deployed for comparisons. Then, this can give us enough evidence about how to adapt the theoretical calculations to give an improved set of the shell model predictions. If a range of states are compared consistently by using the same theory, this approach can reasonably be expected to yield good outcomes.

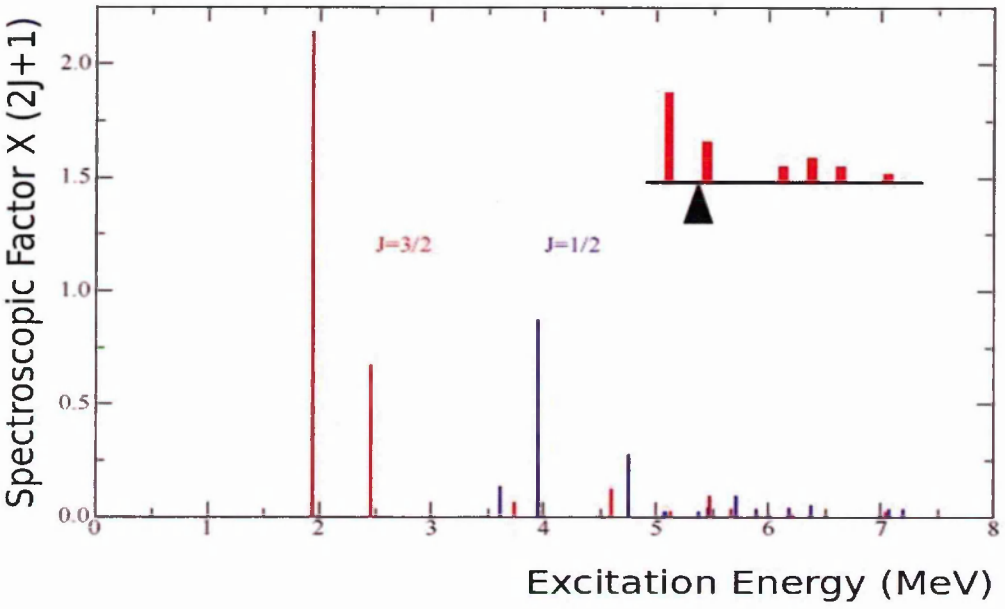

Figure 1.3: Spectroscopic factor versus excitation energy for $3/2^-$ (red) and $1/2^-$ (blue) states in the reaction $^{40}Ca(d,p)^{41}Ca$. Accepted "1" is equal 1. The strength for a given spin is split between states in the final nucleus. The original figure is done by John Schiffer. Here, it's shown how the weighted average of the $3/2^-$ excitation energies can be calculated, which gives a measure of the energy of the $1p_{3/2}$ single particle orbital [2].

1.1.4 Brief Introduction to the Shell Structure, Magic Numbers, Exotic Nuclei, and Nuclear Forces

Exotic nuclei are defined by having different ratio of neutron number to proton number than that of naturally occurring nuclei. The structure of exotic nuclei as compared to stable nuclei can be explained depending on several characteristic effects of nuclear forces. The shell structure of nuclei has been proposed by Mayer and Jensen [8] and [9] to be kept valid basically for all nuclei with well-known magic numbers, 2, 8, 20, 28, 50, ... Recent researches have shown that nuclear forces is about to change this paradigm. The evolution

of shell structure occurs in various ways as more neutrons and/or protons are added as one example is given in the figure 1.1. The monopole interaction of nuclear forces explains basic points of this shell evolution. Mainly, three types of nuclear forces are claimed by Otsuka [10] to have an impact on the nuclear structure. These are respectively tensor force that can alter the spin–orbit splitting depending on the occupation of specific orbits, central force which explains how same proton–neutron interaction drives the shell evolution together with tensor force, and lastly a three–body force that originates in the particle excitation as introduced by Fujita and Miyazawa long time ago. This last force is shown to create a repulsive interaction between valence neutrons after averaging effects from the third nucleon in the core. It is the same three-body force that plays role in neutron stars [10]. Since the experiments with stable nuclei were around, the magic numbers suggested by Mayer and Jensen have remained valid, and the shell structure have been understood well in terms of the harmonic oscillator potential with a spin–orbit splitting. This potential combines nearly constant nucleon density inside the nucleus (density saturation) and short-range attraction from nuclear forces. For more detail, if one looks at a particular nucleon inside a nucleus, there should be an approximately constant number of nucleons within the range of nuclear forces. This means that the effect of the nuclear force does not depend on the location of this particular nucleon as long as it is well inside the nucleus. We thus obtain rather flat mean potential inside the nucleus. In contrast, the location of this nucleon might be near the surface of the nucleus. In that case, the number of nucleons interacting with this nucleon through the nuclear force decreases by leading to shallower potential. On the other hand, the mean potential vanishes if the nucleon is far from the nuclear surface. This perceptive consideration leads us to a Woods–Saxon potential that can be further approximated by a harmonic oscillator potential inside and near the

surface of the nucleus. The wave functions of bound nucleons are not stretched outside the surface with sizeable amplitudes, so the difference outside the surface does not matter [10]. With the addition of the spin–orbit splitting, the harmonic oscillator potential and the spin–orbit model can be reached as Mayer and Jensen postulated in 1949 [8] and [9] (Nobel Prize in Physics for their work on the shell model in 1963). Therefore, all these models continue to compose the base of more complex theories.

1.2 Brief Explanation of the Experiment $^{25}Na(d,p\gamma)^{26}Na$

A particle-γ coincidence study of ^{26}Na using the transfer reaction $^{25}Na(d,p\gamma)^{26}Na$ has been conducted at TRIUMF (TRI-University Meson Facility) using SHARC (the Silicon Highly-segmented Array for Reactions and Coulex) and TIGRESS (The TRIUMF-ISAC Gamma-Ray Escape-Suppressed Spectrometer) in conjunction with BGO scintillator detector in 2009 at Isotope Separator and Accelerator (ISAC-2) facility in TRIUMF, Canada.

During the experiment, only eight of the TIGRESS clovers has been used together with the two DSSSD BOX and one upstream annular CD detector in SHARC. One of these TIGRESS clovers as seen in the figure 1.4 with SHARC has 32 segments and 4 cores in its angle and detection separation. However, each BOX part of the SHARC set-up consist of four DSSSD in the upstream and two DSSSD detectors on both sides of the downstream. Upstream direction here refers to incoming beam direction to the system from the accelerator at 180° θ angle as seen in the figure 1.5. Thus, the beam moves from azimuthal angle 180° to 0°. With regard to the position of the TIGRESS clovers, four of them are placed at 90°, and the rest of the four are installed at 135°. These highly segmented HPGe detectors help us to differentiate the populated states in ^{26}Na via detected gamma rays. These angle positioning will affect the efficiency of the

gamma detectors in the analysis throughout the thesis. Therefore, it's chosen to investigate everything separately for the clovers at 90° and 135°. As to the instrumentation of the SHARC DSSSD parts, only one side of the downstream box is fully instrumented. There were no detectors on lower and upper side of the downstream BOX at the time of the experiment. Thus, this will change both the solid angle of the detector and the number of protons detected in overall SHARC system. To obtain full energy deposition, two PAD detectors, which are basically one sided flat silicon surfaces, are implemented in downstream part only in addition to two DSSSD detectors on sides. This action has been necessary because the outgoing proton from the (d,p) reaction and other particles in compound nucleus reaction may have enough energy to penetrate through the DSSSD as the first layer to interact with the detector system according to the calculations by using LISE++ [11]. In that way, the need for PAD detectors in downstream is approved after considering the thickness of the detector parts in the compact SHARC set-up as briefly seen in the figure 1.5. Comparison to backward angles, the forward angles of SHARC, where the upstream box detector with 4 DSSSD and 1 upstream CD detector are, are less important part due to the reaction of interest. Therefore, the cost of the experiment is also reduced by omitting the PAD detectors from the upstream part as far as the full energy absorption of the particles concerns. It's known from the kinematic lines that all the heavy recoil particles will be forward focused in small cone of angle range when the scattered ejectile proton, for instance, will be distributed from 0° to 180° in θ angle along the beam direction and from 0° to 360° in ϕ angle around the SHARC.

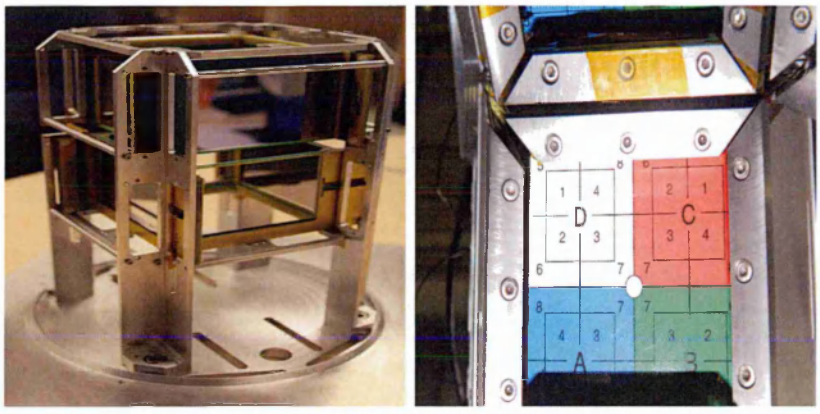

(a) Two box parts (b) 4 cores and 32 segments

Figure 1.4: The SHARC array and front face of TIGRESS clover as an illustration

As in the figure 1.4, the bottom part of picture "a" shows the upstream box part of the SHARC; whereas, the upper part is the downstream box. The bottom part, where the flange connects SHARC to the beam line, is the fixed part to the beam line when the target chamber moves back and forth either to put the radioactive sources into SHARC or to fix anything with detector connections during the experiment.

With the help of the schematics in figure 1.5, it is easier to explain exactly what happened in the experiment. After the radioactive beam, ^{25}Na, has been accelerated at ISAC-2 facility at $5MeV/u$, it follows the beam line as shown on the schematic until it hits the target, CD_2, in the middle of the SHARC detector. As a result of this reaction, we get not only the main reaction product of proton, γ, and recoil ^{26}Na, but also alpha, deuteron, tritium, carbon, and other heavy compounds due to the fusion evaporation on the carbon component of the target, CD_2. Since we know our interest is only focused on proton, excited states of ^{26}Na, and the γ decays coming from excited state of ^{26}Na, we need to eliminate the rest of the undesired particles in the experiment. To do that, some tools have been used; such as 30μm Al foil and 10μm TRIFOIL which is the zero degree

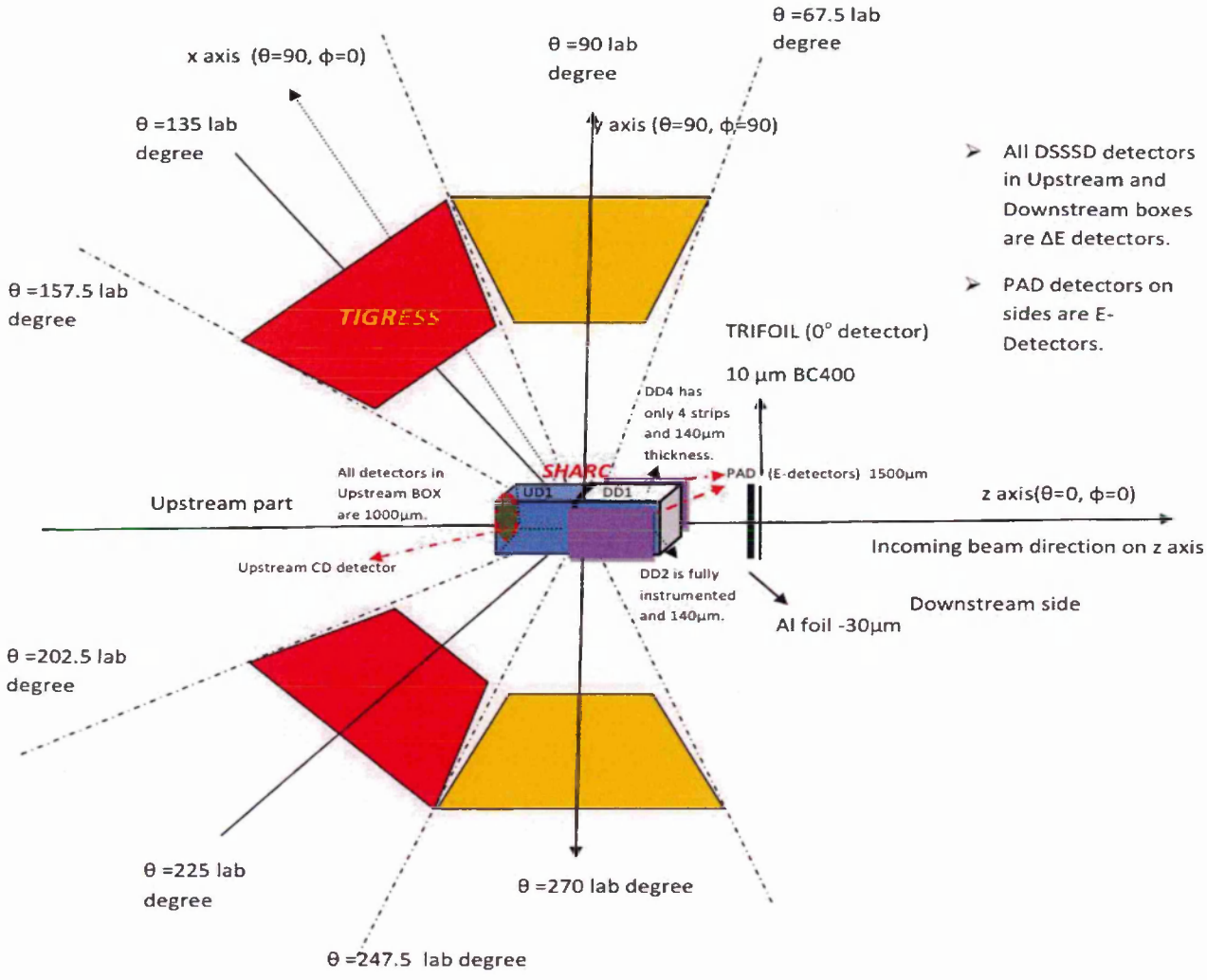

Figure 1.5: Schematic of the SHARC and TIGRESS set-up

detector after SHARC and before beam dump. The purpose of Al foil is to catch the evaporation products from carbon(C) in the target. due to the energy loss depending on the Z of the particle. The fusion reaction with carbon creates a higher Z nucleus which can be stopped more quickly; however, the transfer products and beam, which have atomic number only up to 11, can pass through the Aluminium foil and the TRIFOIL which is deliberately very thin to let them through. And, this is a valuable feature of the TRIFOIL that it transmits the particles that it detects, so that they can be dumped further away from the actual set-up. For that important reason, such a detector is used to distinguish between beam particles and transfer products during the analysis by using it as a gate.

This method is essential for us because the light reaction products and the beam can be stopped and deposited a long way from the target and the gamma ray detectors at "beam dump" which is such a place to stop the beam and to measure the intensity of the transmitted beam.

1.3 TRIFOIL Detector

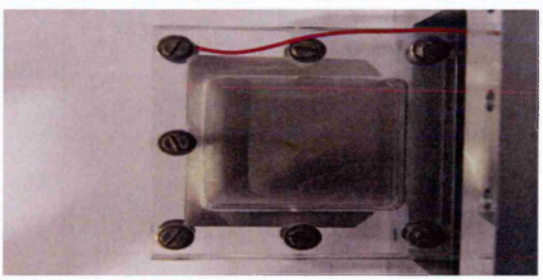

Figure 1.6: 10 μm TRIFOIL with 30μm aluminum foil with the beam spot for a demonstration.

TRIFOIL is the zero degree detector to detect a signal from the beam while passing through it if not stopped in the aluminium foil placed in its upstream side to stop compound nucleus before reaching to the TRIFOIL. The TRIFOIL itself consists of 3 photomultiplier tubes

attached to 10μm plastic scintillator to collect the light as the beam passes through. The fabrication name of the plastic scintillator is BC400 which has 1.032 g/cc density, 1.58 refractive index, and whose base is Polyvinyltoluene. It's also recommended to be used in vacuum. With regard to light output, at 60°C it is 95 percent of that at 20°C; however, it is independent of temperature from -60°C to 20°C. The scintillator frame is made by plexiglass whose outer area is 70×70 mm^2, but the active area of the TRIFOIL plastic scintillator is 40×40 mm^2.

The cathode voltage of the photomultiplier tubes was set to 950 V as a negative bias to amplify the yield of the scintillator. In the experiment, there were mainly three types of reactions to be observed; however, most of the time the beam passes through without any reaction at all. These reactions are elastic scattering of (d,d) or (p,p), inelastic scattering of (d,t'), $(d,^3He)$, *or* (d,p') transfer reactions, fusion evaporation with C in the 0.5 mg/cm^3 CD_2 target. The possible compound nucleus can be found with their most likely percentage by using PACE4 [12] program in LISE++ [11]. Then, one can estimate possible thickness of the aluminium foil to be used to stop the compound nucleus by using physical calculator in LISE++ [11]. For our experiment, 30μm aluminium foil has been used.

The way the number of events recorded in each part of the detector system works for our set-up is explained as follows. We have three types of detectors for different purposes in our entire system. The way how they trigger different detectors depends on their purposes. For SHARC array, it is a particle detector combined with DSSSD and PAD detectors which gives us unique opportunity to detect particles; such as proton, deuteron, tritium, and alpha particles. For instance, if we have a (d,p) reaction seen in the SHARC spectrum, we should see only 1 proton coming out and hitting on one of the DSSSD detectors. Then, we will have signal for this event. Conversely, if we have fusion

evaporation, we will more likely detect more than one particle. What happens in this situation is that we detect those particles in a slightly different time period for an event in some certain time window. Thus, they do not have to hit the detectors at the same time in this case.

On the other hand, we have also TIGRESS detector with the addition of BGO around it and CsI detectors in the back for the aim of γ ray suppress to avoid any escape from the clover. As long as we populate any excited particle in the reaction or inelastic scattering, it will enable us to detect its γ-ray energy to locate the excited state in the γ-ray level scheme.

The last part of our set-up is the TRIFOIL detector. As we briefly mentioned before, TRIFOIL works only when there is a beam passing through it. Otherwise, it'll have no signal on the TRIFOIL since compound nucleus and fusion evaporation products will be blocked on SHARC or aluminium foil before the TRIFOIL. In the present experiment, the trigger that initiated the readout of all detectors was for a signal to be recorded by any silicon detector.

1.4 Findings in the Previous Work [1]

The most recent work on $^{25}Na(d,p\gamma)^{26}Na$ reaction is done by Gemma Wilson [1]. This Ph.D thesis is build on the top of the current knowledge from her work, and the current work represents independent analysis of the same raw data from the same experiment. Especially for elastic scattering data analysis, information about ADWA, the USD and s-p-sd-pf interaction calculations in the shell model for the theory, one should refer to her thesis since this part will not be heavily discussed in this thesis. As it will be mentioned also later in the current thesis, the so-called normalization factor is calculated from the

best fit of the elastic scattering cross section theories to the data. In the experiment, it's possible to observe different type of elastic scattering reactions as well as the other inelastic scatterings. Thus, (p,p) and (d,d) elastic scattering parts in the data from the kinetic energy of the proton versus θ_p plots are used to check various optical potential parameters for different elastic scattering theoretical parameters used by other theoreticians. Rutherford scattering cross section is also compared with other theories on the (p,p) and (d,d) data. To get the elastic scattering cross sections in theory, DWUCK4 [13] is used in the previous work [1], but one can also use FRESCO code [14], instead.

In conclusion, the normalization factor for the calculation of the differential cross section of the proton in (d,p) reaction is found as the multiplication of $(\varepsilon_{Si} * I * n_d)$ values. Where the efficiency of the silicon detectors (ε_{Si}), the number of particles in the beam current (I), and the number of particles in the deuteron target (n_d) are represented in this multiplication, respectively. However, there is no point to have those individual values since we only need the multiplication for the purpose of our calculation in the later section where the proton differential cross sections for different states in ^{26}Na are extracted from the data. It turned out the optical model parameters presented by Meurders [15] are found giving the best fit. Thus, only this corresponding potential with its parameters is used to get the final result of 38000±1000 mb^{-1} [1] for the $(\varepsilon_{Si} * I * n_d)$ value as a "normalization factor" of the proton angular distributions. In that way, the unit can be changed from counts to mb/sr. Thus, this result above for elastic scattering normalization was adapted from the previous work [1]. All the other key results from that reference are summarized below, but were also analysed independently in the present work with other extra analysis, as described in the subsequent chapters.

The second crucial finding in the previous work [1] is the gamma efficiency curves,

which one can refer to the previous work [1], for TIGRESS detectors in clovers at 90° and 135° as shown in the figure 1.5. To get the gamma efficiencies separately for these two clovers is inevitable part of the analysis since everything in the thesis is studied as two individual experiments for these TIGRESS angles. Then, the final results either are summed up as in the gamma-ray angular distribution part or averaged using weighted averaged method.

The third important result is the solid angle of the SHARC detector in the laboratory frame. It is necessary to know this as a histogram ,so we can extract proton differential cross sections from the data in the end of the analysis to scale our theory results on to the data.

The fourth result indicates final level scheme as in the figure 1.7 which was built up level by level from the bottom to the higher energies using detected gamma rays, gamma coincidences, excitation energies for a specific gamma transition, and so on. The detail explanation will be presented in analysis part of this thesis.

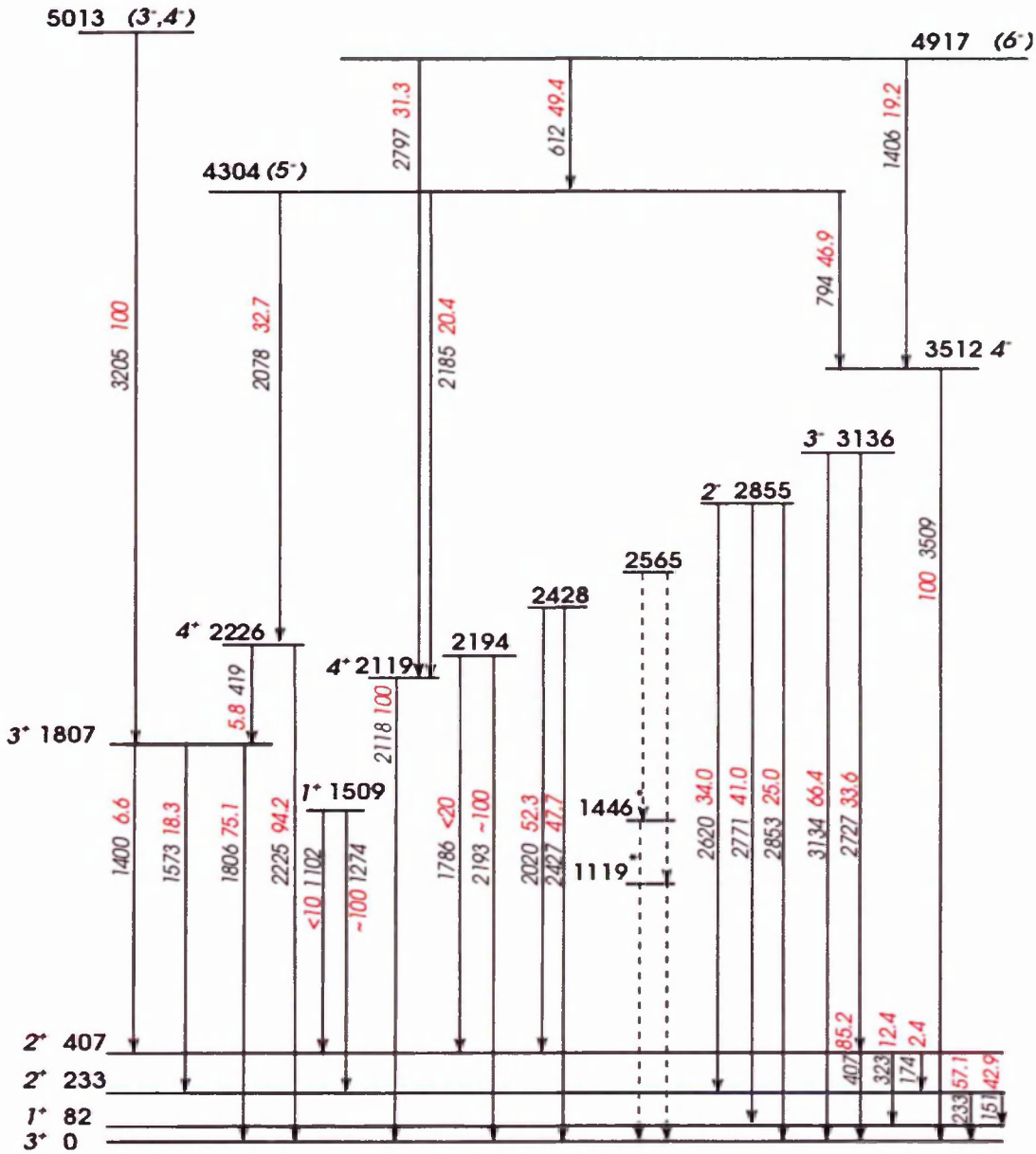

Figure 1.7: Final level scheme showing spins and parities for ^{26}Na. Branching ratios are shown in red, and dotted lines are for tentative decays and states.

The final conclusion is listed in the table 1.1 in terms of the extracted spectroscopic factors of the states decaying only to the ground state of ^{26}Na from the state levels shown

in the table. The Johnson-Soper (JS) adiabatic approximation [5] to the neutron, proton, and target three-body system using the phenomenological nucleon nucleus optical model potentials [16] was used to find the transfer cross-sections in TWOFNR code [17] as the details aer also explained in paper [18]. As in the table 1.1, the differential cross sections of only 7 excited sates in ^{26}Na were extracted in the previous work [1] from the data to retrieve their corresponding spectroscopic factors.

State (keV)	J^π	S.F.	Coupling	State (keV)	J^π	S.F.	Coupling
233	2^+.	0.144 .	$s_{1/2}$	3134	3^-	0.0983	$p_{3/2}$
407	2^+	0.337	$s_{1/2}$	3509	4^-	0.540	$p_{3/2}$
1806	3^+	0.216	$d_{3/2}$	4303	(5^-)	-	-
2118	4^+	0.216	$d_{3/2}$	4915	(6^-)	-	-
2225	4^+	0.432	$d_{3/2}$	5011	$(3^-,4^-)$	-	-
2853	2^-	-	-	-	-	-	-

Table 1.1: Previously assigned states with their spins, parities, and spectroscopic factors for ^{26}Na in $^{25}Na(d,p\gamma)^{26}Na$ [1].

Chapter 2

Theory

2.1 The Proton and Neutron Coupling in the Extreme Independent Particle Model and Complete Shell Model

The main two application of the shell model to consider are "the extreme independent particle model" and "the complete shell model" as they are called by Krane [19] (see page 131). In the first model, any closed shell does not contribute to the nuclear properties of a nucleus; whereas, the motion of the single unpaired nucleon plays a crucial role. Alternatively, all valence nucleons in a nucleus can change the structure of the nucleus in the complete shell model. Experimental results as shown in figure 2.1 for ${}^{41}_{20}Ca_{21}$ and ${}^{43}_{20}Ca_{23}$ prove this fact by showing different excitation energy levels due to the additional 2 neutrons as valence nucleons. The type of nucleon in the last shell of the nucleus can also affect the energy levels of the excited state in nuclei. The excitation energy diagram in the figure 2.1 for ${}^{41}_{20}Ca_{21}$ and ${}^{41}_{21}Sc_{20}$ provides a good example of this effect. Another example to show the consequence of the different number of nucleons to be paired and the outcome of one paired valence proton on one unpaired valence neutron is between the

excitation energy levels of $^{41}_{20}Ca_{21}$ and $^{43}_{22}Ti_{21}$ in the figure 2.1.

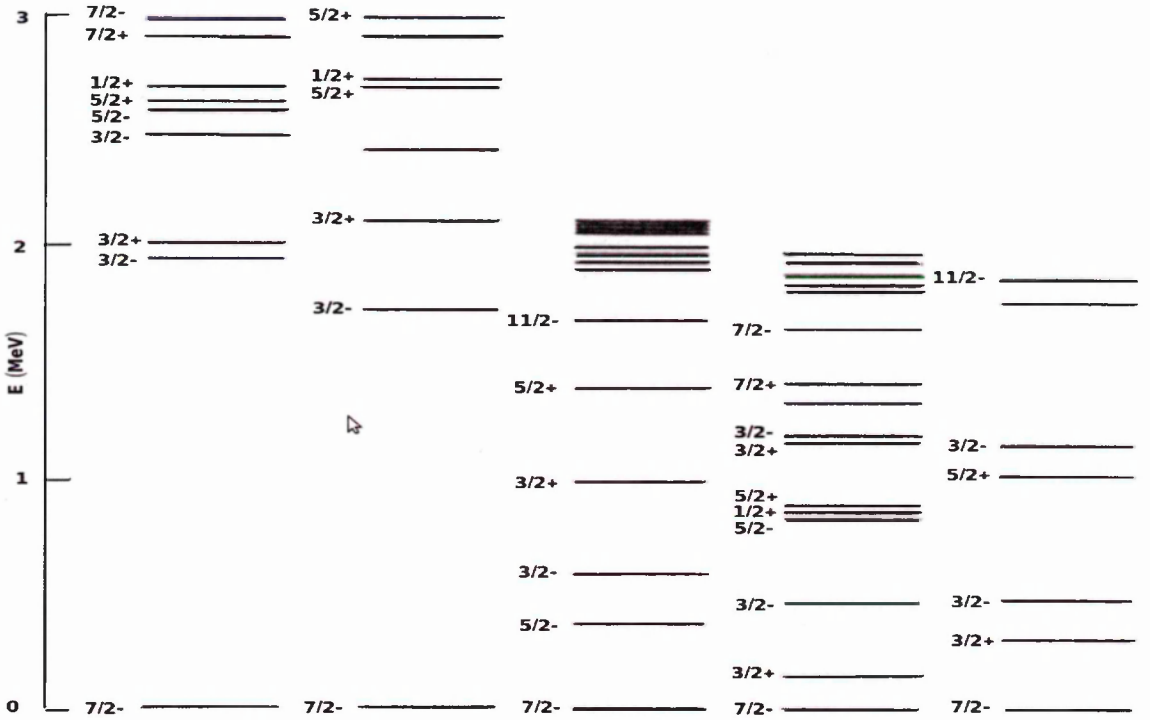

Figure 2.1: Energy levels of nuclei, $^{40}_{20}Ca_{21}$, $^{41}_{21}Sc_{20}$, $^{43}_{20}Ca_{23}$, $^{43}_{21}Sc_{22}$, and $^{43}_{22}Ti_{21}$, with odd particles in the $1f_{7/2}$ shell [19].

All nucleons stay in the nuclear potential, and the simplified form of the nuclear potential has preferentially smooth edges as in the simplified intermediate form of $V(r) = \frac{-V_o}{1+\exp[(r-R)/a]}$ that is used in figure 2.2. The R and a represent respectively the mean radius and skin thickness of the shell model potential. To select the right potential is important. The purpose of all these features of the desired nuclear potential is to explain well the charge distribution and matter distribution in the nucleus [19].

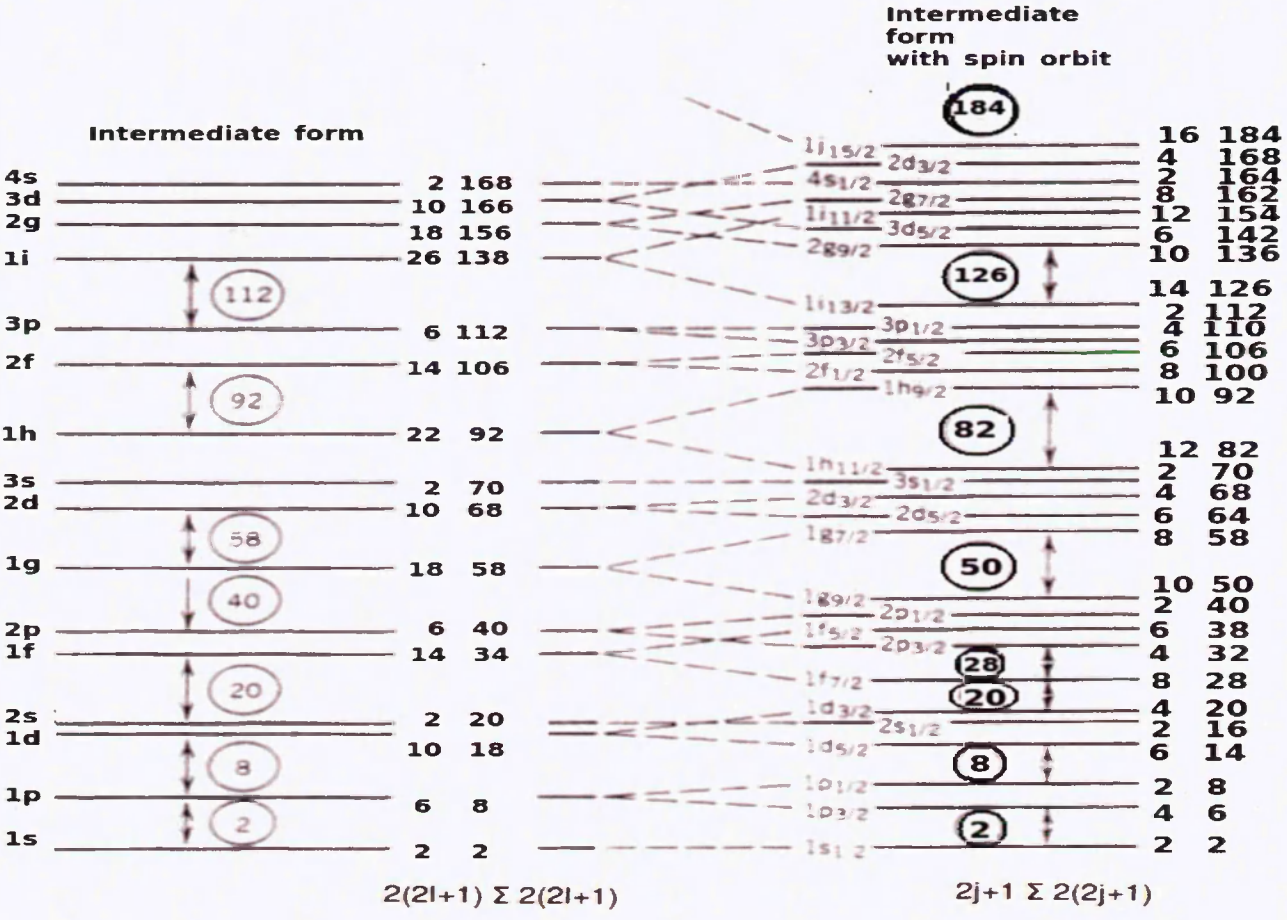

Figure 2.2: At the left are the energy levels calculated with the nuclear potential in its intermediate form as shown in the text. To the right top of each level are shown its capacity and the cumulative number of nucleons up to that level. The right side of the figure shows the effect of the spin-orbit interaction, which splits the levels with $l > 0$ into two new levels. The shell effect is quite apparent, and the magic numbers are exactly reproduced [19].

To understand how the extreme independent particle model works, let's start with an example of ${}^{17}_{8}O_9$ and ${}^{17}_{9}F_8$. In the figure 2.2, it's clear the single valence neutron is in the $1d_{5/2}$ shell. Since the orbital quantum number is 2 for the d orbital, the parity of the state is $5/2^+$ from $\pi=(-1)^l$. With regard to excited states, the first two that we can think of easily are $1/2^+$ state and $3/2^+$ state corresponding to the higher $2s_{1/2}$ and

$1d_{3/2}$ shells. To get to $1/2^-$, $3/2^-$, and $5/2^-$ excited states, one should see the difficulty of reaching $2p_{1/2}$, $2p_{3/2}$, and $1f_{5/2}$ upper shells due to higher excitation energy. Instead, it is easier to break the pair in sub-shells. The simplest break down which can be done is to take the one nucleon from lower $1p_{1/2}$ shell to $1d_{5/2}$ upper shell. Thus, the paired shell in $1d_{5/2}$ shell won't affect our state. On the contrary, the unpaired nucleon in the $1p_{1/2}$ shell defines the state's property. The new excited state will be $1/2^-$ state ,instead. A similar reasoning can be applied to get the $3/2^-$ state.

Another example for a comparison between "the complete shell model" and "the extreme independent particle model" can be given in more detail with the nuclei ${}^{41}_{20}Ca$, ${}^{41}_{21}Sc$, and ${}^{43}_{20}$Ca as their excitation energy levels are shown in their figure 2.1. Whereas ${}^{41}_{20}Ca$ has one unpaired neutron in the $1f_{7/2}$ in the ground state, ${}^{41}_{21}Sc$ has one proton in the same shell in its ground state. This unpaired proton and neutron give different excited states for these two nuclei; however, ${}^{43}_{20}Ca$ has 3 neutrons in its $1f_{7/2}$ shell by giving more combination in terms of coupling among these valence nucleons. As a result, it's seen that ${}^{43}_{20}Ca$ does possess more energy levels with different spins and parities. This proves all three valence nucleons play an important role to have a great effect on the nuclear structure as opposed to the extreme independent particle model (see page 132 in reference [19]).

2.2 Spin-Orbit Coupling Effect on Active Potentials in a Nucleus

With so many other nucleons to collide with and with such a strong force acting between them, how can a nucleon go around a complete orbit without a collision?

The explanation relies heavily on the Pauli exclusion principle. In reality, the nucleus

is a quantum system in which nucleons are restricted to a very limited number of allowed orbits. The Pauli exclusion principle applies a further restriction which says that only one nucleon (either neutron or proton) can occupy a given energy state. This severely limits the possibilities for collisions, and nucleons start to fill the orbitals from the lowest energy to the highest energy orbital. [20]

A nucleon moves while the nucleus is full of all the other nucleons as well, and the force that other nucleons apply to one particular nucleon is governed by the nuclear potentials of the neutron and proton as shown in figure 2.3(a). These potentials have a different width for different particles in the nucleus. The shape of the proton potential can be constructed from the addition of a Coulomb potential to the neutron potential in figure 2.3.

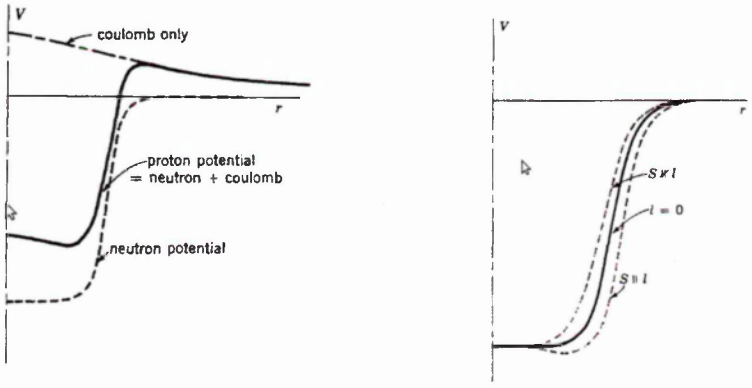

(a) Neutron, proton, and Coulomb potentials

(b) Spin and orbital coupling

Figure 2.3: The changes in the nuclear potentials

Another important phenomenon in physics with regard to the coupling of the "l" and "s" quantum numbers can be easily explained in figure 2.3(b). This figure indicates the change in the width of the shell theory potential in terms of coupling. When these two

quantum numbers "l" and "s" are opposite to each other in vector diagram, they result in a narrower potential. However, the potential expands while they align parallel to each other. Namely, the wider the potential, the lower the energy of the orbital for a particular particle will be. These effect can be easily seen in the figures 2.4 and 2.2.

The equations 2.1 and 2.2 are used to calculate the centrifugal potential in the nucleus constituted by the nucleons and the shell model energy levels. Then, these equations help to understand how the energy levels behave in the figure 2.4.

$$2\pi r = l\lambda_\theta = \frac{lh}{MV_\theta} = \frac{lh}{M\omega r}, \qquad L = Mr^2\omega = \frac{lh}{2\pi} = l\hbar, \qquad L = \sqrt{l(l+1)}\hbar, \quad (2.1)$$

$$F_{cf} = M\omega^2 r = \frac{L}{Mr^3} = \frac{l(l+11)\hbar}{Mr^3}, \qquad V_{cf} = \int_\infty^r F_{cf}dr = \frac{l(l+1)\hbar^2}{2Mr^2} \quad (2.2)$$

The complete potential to be used in calculating the wavelength is the sum of the potential V(r) arising from forces plus the centrifugal potential V_{cf}. Thus, the differential equation for u(r), which is defined as $\vec{r}\psi(r)$, can be given as below [20].

$$-\frac{\hbar^2}{2M}\frac{d^2u}{dr^2} + [V(r) + \frac{l(l+1)\hbar^2}{2Mr^2}]u = Eu \quad (2.3)$$

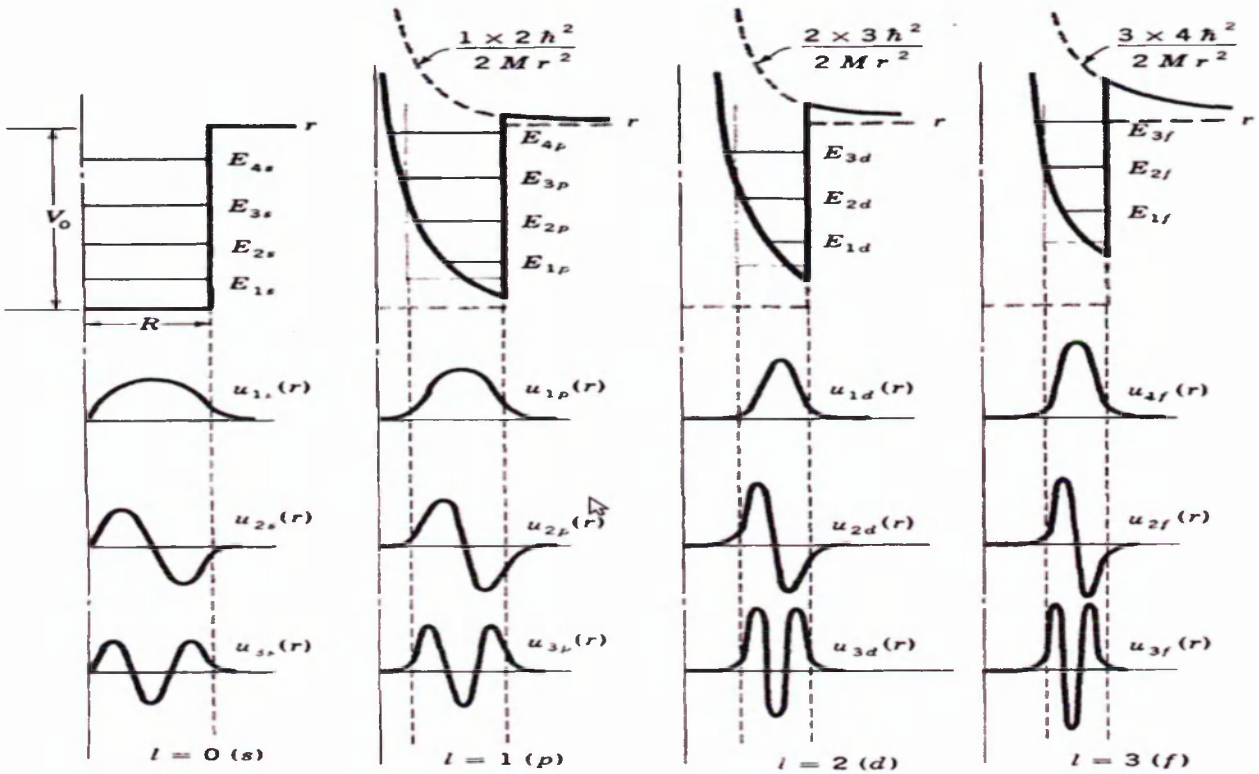

Figure 2.4: Energies and wave functions u(r) obtained from the solution of 2.3 square well. The four columns are the solutions for l=0, 1,2 , and 3, respectively. The top row shows the two contributors to the effective potential, V(r) and V_{cf} as dashed lines, and their sum, the effective potential, as solid lines. Note that the wave functions have n half wavelengths in the range of r covered by the potential well with exponentail tails going rapidly to zero in the region outside the potential well. [20]

It's immediately evident that as l increases, the potential well becomes both narrower and shallower in the figure 2.4. The narrowing arises from the fact that a particle with high orbital momentum is strongly repelled from small radii by the centrifugal force. As the well becomes narrower, the wavelength of the well becomes smaller. Therefore, in accordance with $\lambda = \frac{h}{\sqrt{2M(E-V)}}$, the shorter wavelength leads to higher value of (E-V) [20]. Thus, the distance from the bottom of the equivalent square well to any given energy

level, say E_{1l}, increases with l. In addition, the bottom of the well rises with increasing l, thereby pushing the energy levels up even higher. For both these reasons, E_{1l}, E_{2l}, E_{3l}, etc., increase monotonically with increasing l. The wave functions are simultaneously squeezed toward larger radii. [20]

For the wells other than a square well, everything happens in a quantitatively similar way. For the $1/r$ well encountered in the hydrogen atom, E_{1p} is pushed up so far that it coincides in energy with E_{2s}. Similarly , E_{1d}, E_{2p}, E_{3s} coincide in energy; etc. This maybe expressed as

$$E_{nl} = E_{(n+l)(l-1)} = ... = E_{(n+l)(0)}$$

The n quantum number commonly used in atomic physics is n+l in our notation. This coincidence in energies is valid only for the $1/r$ potential; the potentials applicable in nuclear physics do not deviate from a square well nearly as dramatically as the $1/r$ potential does, so the shifting of E_{nl} with increasing l is much less rapid in nuclear physics.

2.3 Nuclear Reactions

If it is allowed for a beam to hit the target after accelerating to particular energies, a nuclear reaction will most likely occur depending on the cross section. In 1919, Rutherford made a nuclear reaction experiment using alpha particles on ^{14}N target, which then results in proton and ^{17}O products. Also, Cockcroft and Walton constructed the first particle accelerator in 1930 observing the reaction of p+^{7}Li $\rightarrow$ ^{4}He $+\alpha$.

In most cases, the energy is considered to be low if it is in the order of 10MeV per nucleon or less, or it is regarded as medium if it is in the range of 100MeV to 1GeV which enables meson generation and alteration of protons and neutrons. And lastly, it reaches the high energy scale after 1GeV offering a close look to the arrangement of quarks and

fundamental particles of nucleons. [19]

A symbolic nuclear reaction can be written as

$a + X \rightarrow Y + b$,

where a is the projectile, X is the target, Y and b are the reaction products respectively. Generally, the convenient way of showing the reaction is X(a,b)Y. In the case of γ for a , it is called "nuclear photo-effect", but rarely b will be the γ giving the name of the "radioactive capture" to the reaction.

We also differentiate reactions in various ways. If the projectile and ejectile particles are the same, it is a "scattering process" , "elastic" if Y and b are in their ground state and "inelastic" in the case of their excited states. Sometimes, the incoming particle alters the target by replacing itself into one of the constituents of the target; such as a neutron or proton in the target. In this case, it is called "knockout reaction". When one or more nucleons are exchanged between the incident particle and target, it is named "transfer reaction". Specifically, (d,n) or (d,p) type of reactions are called "deuteron stripping reaction". Conversely, it is called "pickup reaction" when the projectile takes a nucleon from the target; such as (p,d) reaction.

Another way of naming the reactions is to consider the process that rules the action. If only very few particles become a part of the reaction, most likely the single nucleon can be taken out or put into the shell giving the option of probing the structure of nuclei. This kind of reactions are named as "direct reactions". At lower beam energies, the projectile can be absorbed into the target, forming a compound nucleus. The spacing among the states can be negligible compared to any width of individual states. This results in a sharing of the energy before any outgoing particle is ejecting. In this case, the reaction is called "compound reaction". Instead of a continuum in the compound nucleus, if we

have discrete excited energy levels for low incident energy, the "quasibound" state (virtual quantum level) may either re-eject the incident particle or decay by γ emission. Therefore, it is called "resonance reaction" [19].

2.3.1 Observables in the Nuclear Reactions

By using different methods, we can measure main details about nuclei; such as energy, cross section, mass, angular distribution, lifetime, modes of decays, spin, parity, magnetic dipole moment, and electric dipole moment of the outgoing particles. For instance, "the differential cross section" is the probability of detecting particle b at a specific angle (θ,ϕ) with a definite energy according to the beam axis. Thus, one can find the probability of the desired particle. In addition to that, the spin distribution of the product Y can be deduced mainly by using polarized incoming beam and target with spectrometer to analyse the product particle b with "polarization experiment". If the Y product is in an excited state, it will emit γ radiation or conversion electrons to reach the stable ground state. In this case, we make use of particle b and the angular distribution of γ radiations to know the populated excited state or its spin-parity assignment [19].

2.3.2 Derivation of Proton Cross Sections in Theory

To understand why we need the proton angular distribution and the gamma ray angular distribution, we first need to dig into the meaning of cross section in terms of a nuclear physics perspective. Statistically speaking, cross section shows the probability of having a reaction. As we know, most of the time the beam we fire passes through the target without any interaction. By increasing the incident beam current, we basically trying to have more chance for a reaction.

If the reaction is $X(a,b)Y$ where X is the beam, a is the target , b is the light ejectile,

and Y is the heavy recoil, then the cross section is

$$\sigma = \frac{R_b}{I_X.n_a} \tag{2.4}$$

where R_b is the rate which particle b appears in the reaction, I_X is the beam intensity, and n_a is the number of the target particles. Therefore, the cross section is the ratio of outgoing particles to input particles in the system. Considering the solid angle of our detectors, we never detect all the outgoing particles out of the reaction. For that reason, what we really get in terms of cross section is $d\sigma$ which is a fraction of the total cross section deduced from the fraction of R_b we detect.

$$d\sigma = \frac{dR_b}{I_X.n_a} \tag{2.5}$$

If we let the angular distribution of outgoing particles be represented by $N_b(\theta, \phi)$, then $dR_B = N_b(\theta)$. Since the SHARC detector has essentially a full ϕ coverage, we'll assume this distribution will only depend on θ angle of scattered ejectile particles. The distribution of the ejectile, $N_b(\theta)$, found in the experimental data includes already the contribution of the solid angle of SHARC detector ($d\Omega$), efficiency of Silicon detectors ϵ_{Si}, and gamma efficiency of HPGe detectors (ϵ_γ). For simplicity, we'll assume all these contributions are omitted from $N_b(\theta, \phi)$ term. This will then reperesent the pure distribution of detected ejectiles as counts per θ angle. A simplified version of the differential cross section can be written as

$$\frac{d\sigma}{d\Omega} = \frac{N_b(\theta)}{I_X.n_a} \tag{2.6}$$

A more complicated form will be mentioned in section 3.7 when finding the angular distribution of protons in $^{25}Na(d, p\gamma)^{26}Na$.

2.3.3 Direct Reaction with Deuteron Stripping Process

Inelastic scattering is when the incoming particle's kinetic energy is not conserved during the process. And, both the direct process and the compound nucleus process can contribute to this scattering. As direct reaction is a type of reaction where the incoming particles interact with the surface nucleons of the target; however, the compound nucleus reaction has a definite intermediate state where target and beam particles share their energies by merging into a compound nucleus. One of the obvious differences between the two is the time that the process lasts. Typically, direct process takes 10^{-22}s, and compound nucleus process lasts 10^4 or 10^6 times longer. The second clear characteristic for direct reaction is to have more sharply peaked angular distributions for outgoing particles; such as, proton in (d,p) reaction.

As far as our interest is concerned, the (d,p) single neutron transfer reactions are the study of investigating low-lying shell model excited states. For a given scattered proton energy, we can calculate a particular shell model state with the help of angular distribution of outgoing particles. This angular distribution of the emitted particles gives the spin and the parity of this excited state.

While the first and possibly the second maximum in angular distribution in figure 2.6 can be estimated by the plane wave Born approximation (PWBA), distorted-wave Born approximation (DWBA) can predict better results for fitting since it includes any scattering and absorption of the incoming particles to the target. This effect is oversimplified in the PWBA by considering only the reaction that makes the interaction [20]. A DWBA calculation treats incoming and outgoing particles as moving particles in the "optical-model potential". This potential can be thought as a complex form of $U(r) = V(r) + iW(r)$ [19]. While the first real function (V(r)) is responsible for elastic scattering, the second part de-

scribes absorption. In that way, the first part of this potential resembles somehow the shell model potential by explaining the interaction between projectile and target. In addition to these two theories, adiabatic distorted wave approximation (ADWA) [5] describes the break-up of the deuteron more precisely than other two theories. Thus, it can give better fits for deuteron induced reactions, such as (d,p), (p,d), (d,n), and (n,d). Descriptions can be found, for example, in the articles and books by Glendenning [21], Satchler [22], and similar theory books.

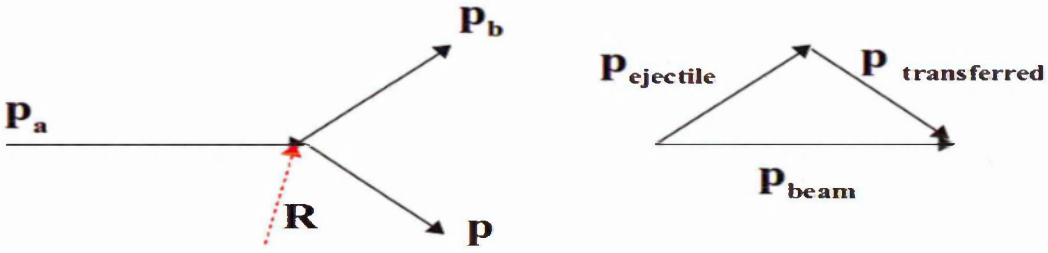

Figure 2.5: Momentum vector diagram showing the transferred momentum ($p_{transferred}$) as the vector of difference between the momenta of the incident and emitted particles in Direct Reactions while the collision occurs on the surface of the nucleus with R radius.

Let's take a close look at the angular momentum transfer in a deuteron stripping reaction. We can solve this problem in two ways by using the law of cosines: $p_t^2 = p_i^2 + p_e^2 - 2p_i p_e \cos\theta$.

In the first way, we use the notations, p for a residual nucleus which is target plus transferred nucleon, p_a for a beam, and p_b for an outgoing particle as shown on the figure 2.5. The trigonometric expresssion of $\cos\theta = 1 - 2\sin^2\frac{\theta}{2}$ is also used.

$$p^2 = p_a^2 + p_b^2 - 2p_a p_b \cos\theta = (p_a - p_b)^2 + 2p_a p_b(1 - \cos\theta) = (p_a - p_b)^2 + 2p_a p_b(2\sin^2\frac{\theta}{2}) \quad (2.7)$$

The angular momentum rule , $\overrightarrow{L} = \overrightarrow{R} \times \overrightarrow{p}$, becomes $l = R.p$ when $\overrightarrow{R}$ and $\overrightarrow{p}$ are

perpendicular to each other. By using $\overrightarrow{L} = \overrightarrow{l}.\hbar$, we can deduce "l" value as below:

$$l = \frac{R.p}{\hbar} = \frac{R}{\hbar}\sqrt{(p_a - p_b)^2 + 2p_a p_b(2\sin^2\frac{\theta}{2})} \tag{2.8}$$

And, if $p_a \simeq p_b$, 2.8 reduces to :

$$l = \frac{R.2.\sin\frac{\theta}{2}}{\hbar}\sqrt{p_a p_b} \tag{2.9}$$

Then, we expect to see the scattered proton from (d,p) reaction at the angle calculated below for corresponding "l" transfer for a given energy.

$$\theta = 2\arcsin\frac{l\hbar}{2R\sqrt{p_a p_b}} \tag{2.10}$$

In the second method, we let $p_{beam} = p$, $p_{emitted} = p - \delta$, and $p_{transfer} = p_t$. From the triangle rule in the figure 2.5 ,

$$p^2_{transfer} = p^2_{beam} + p^2_{emitted} - 2p_{beam}p_{emitted}\cos\theta \tag{2.11}$$

Then, it turns to

$$p_t^2 = p^2 + (p-\delta)^2 - 2p(p-\delta)\cos\theta = 2p^2 - 2p^2\cos\theta - 2p\delta + 2p\delta\cos\theta + \delta^2 \tag{2.12}$$

By using $\cos\theta = 1 - \frac{\theta^2}{2}$ from small angle approximation here,

$$p_t^2 = 2p^2 - 2p^2(1 - \frac{\theta^2}{2}) - 2p\delta + 2p\delta(1 - \frac{\theta^2}{2}) + \delta^2 \tag{2.13}$$

We reduce the formula into:

$$p_t^2 = p^2\theta^2(1 - \frac{\delta}{p}) + \delta^2 \tag{2.14}$$

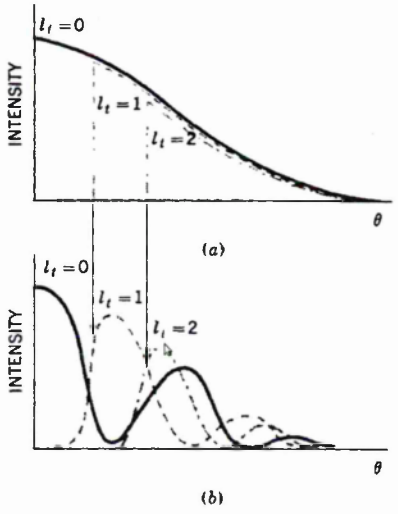

Figure 2.6: Elementary derivation of angular distributions in direct reactions. The basic angular distribution is forward–peaked the one labelled $l_t = 0$ in the upper drawing. For $l_t = 1, 2, 3, ...,$ increasing portions of the low angle part are eliminated to satisfy angular momentum conservation. Due to the wave effects, the angular distributions in the upper drawing become like those in the lower drawing [20].

This time, the angle where we see the maximum in angular distributions is calculated as

$$\theta^2 = \frac{(\frac{p_t}{p})^2 - (\frac{\delta}{p})}{1 - \frac{\delta}{p}} \tag{2.15}$$

The orbital angular momentum value in quantum physics is $|\vec{L}| = \hbar\sqrt{l_t(l_t+1)}$, and the maximum value it can get is classically $|\vec{L}| = |\vec{r}|.|\vec{p_t}|$. Thus,

$$p_t \geq \frac{\hbar\sqrt{l_t(l_t+1)}}{R} \tag{2.16}$$

If we put 2.16 into 2.15, with the help of $\lambda\!\!\!^{-} = \frac{\hbar}{p}$, it gives

$$\theta^2 \geq \frac{\frac{\lambda^2}{R^2} l_t(l_t+1) - (\frac{\delta}{p})^2}{1 - \frac{\delta}{p}} \tag{2.17}$$

The result of θ and the effect of different "l" values can be seen in figure 2.6. As noticed, angular distributions for scattered ejectile particles are forward focused for direct reactions. For more information about the derivation of cross sections from spherical Bessel functions, which is proportional to the angular distribution of outgoing particles, one can refer to books in references [19] and [20].

In the end, the relationship between experimental and theoretical cross sections can be found as below.

$$\frac{d\sigma}{d\Omega}(experimental) = S\frac{d\sigma}{d\Omega}(ADWA) \tag{2.18}$$

The way to find this spectroscopic factor from data is to compare the theoretical cross section calculated in TWOFNR with proton angular distributions coming from the (d,p) reaction. The scaling factor gives our "spectroscopic factor".

2.4 Description of the Shell Model Calculations

The nuclear shell model for nuclei in the mass region considered in the present work, i.e. ^{26}Na and nearby nuclei, involves the following orbitals, beginning with the lowest energy orbital: $0s_{1/2}$ (the lowest shell), $0p_{3/2}$ and $0p_{1/2}$ (the p-shell), $0d_{5/2}$ and $1s_{1/2}$ and $0d_{3/2}$ (the sd-shell) and $0f_{7/2}$, $1p_{3/2}$, $0f_{5/2}$, and $1p_{1/2}$ (the fp-shell). For ^{26}Na the eleven protons and the 15 neutrons separately occupy these same orbitals, in accordance with the Pauli principle. In general, many different configurations of the nucleons in these orbitals can produce states in ^{26}Na of the same spin and parity. Also, the nucleons (and especially the valence nucleons, in the shells that are not full) can interact with each other

and affect the precise energy of each configuration. This can be treated in perturbation theory, and the final wavefunctions of the nucleus are linear combinations of the simple configurations that can be written down using the shell model orbitals. The method to find these linear combinations, which are the solutions that take proper account of the interactions between valence nucleons, is to solve a matrix diagonalization problem. An initial, non-diagonal matrix is built within a model space comprising selected shell model orbitals and calculating the interactions between the valence nucleons. The matrix is then diagonalized using appropriate algebraic procedures and in the process the basis states are calculated wherein the matrix is diagonal. The diagonality of the matrix means that all of the basis vectors are orthogonal to each other, just as a complete set of true wavefunctions must be. These new basis vectors, which are linear combinations of the initial shell model configurations, are then the final wavefunctions for the nucleus. The input to such a calculation includes: the shell model orbitals that are considered to be involved, the energies of these orbitals, the quantum numbers of these orbitals and the two-body matrix elements that represent the interaction between two separate nucleons as they scatter from one pair of orbitals to another pair. The set of matrix elements is generally called the *interaction* and will apply to a specific choice of orbitals to include, which is called the *space* for the calculation.

If we put the protons and neutrons into orbitals, from the lowest energy upwards and in accordance with the Pauli principle, then we end up with three protons in the $0d_{5/2}$ orbital and a single neutron in the $1s_{1/2}$ orbital. This suggests that the ground state of ^{26}Na should be a state in which these two nucleons couple together to form a state with a spin of either 2 or 3 depending on the coupling. To determine which of these spins will be the lowest in energy, and hence the ground state, involves adding up the valence

nucleon residual interaction energies for all relevant valence particles. Also, as mentioned above, these residual interactions will cause a mixing of other configurations so that the final wavefunction is a linear combination of configurations. In the case of ^{26}Na, a good choice of nucleons to consider as the valence nucleons would be those that are found in the *sd*-shell since the *p*-shell is completely filled in the most simple picture. This would then be a problem of solving the matrix diagonalization for configurations involving the three protons and the seven neutrons. In order to be as realistic as possible in the calculation (by avoiding the exclusion of things that might reasonably happen) the calculation could be done so as to allow the protons and neutrons to occupy any of the three orbitals within the *sd*-shell. Such a calculation is indeed possible, and the appropriate interaction to use, i.e. the one found in the literature that gives the best agreement with experiment over a wide range of nuclei, is called the Universal SD, or USD interaction [23]. In regions of neutron rich exotic nuclei such as ^{25}Ne [24] and ^{27}Ne [25] (close to ^{26}Na) a modified version of this interaction called USD-A [26] has been found to give better agreement, particularly for states involving occupancy of the $0d_{3/2}$ orbital for neutrons. Therefore we will include calculations using the USD-A interaction, to compare with our data. These calculations are only able to predict the properties of positive parity states in ^{26}Na because all of the orbitals in the *sd*-shell space are of positive parity.

In order to calculate the properties of negative parity states in ^{26}Na, it is necessary to include configurations from beyond the *sd*-shell. If a single nucleon is excited from the *sd*-shell to the *fp*-shell then this can make a negative parity state. It would also be true if three neutrons were promoted, but such a calculation is very demanding computationally and there is no properly developed model (or interaction) available in the literature to take such excitations into account. Therefore, in this thesis we will consider only those

calculations that have a maximum of one nucleon promoted across a major shell closure. In addition to the fp-shell promotion, an alternative possibility would be the promotion of a single nucleon (proton or neutron) from the p-shell to the sd-shell. A calculation has been developed in the literature, taking into account all such promotions of a single nucleon, using all of the orbitals from the lowest $0s_{1/2}$ orbital to the $0f_{5/2}$ orbital. This is called the WBP interaction [27]. For exotic neutron rich nuclei, a modification of this has been developed called the WBP-M [25] which agrees better with experiment. We have therefore included calculations using the WBP-M interaction and we refer to these as *full* $1\hbar\omega$ calculations to indicate that they allow any promotion of one nucleon between the major shells. The WBP-M calculations are also able to include configurations with no promotion of nucleons across major shells and hence make predictions for positive parity states. For these calculations for positive parity states, the WBP-M calculations use the USD interaction for nucleons within the sd-shell, which are included in this thesis for completeness, but are expected to be inherently less good for the positive parity states than the USD-A calculations.

The final set of shell model calculations that will be presented in this work, and which were previously presented by Wilson [1], are a simplification of the full $1\hbar\omega$ calculations in which the promoted nucleon is only allowed to move from the sd-shell to the fp-shell. The interaction is again the WBP-M interaction. We refer to these as sd-pf $1p$-$1h$ calculations because they have a single particle-hole excitation between the sd and fp shells. These calculations have only one advantage, which is simplicity and speed of calculation, and are expected to be inherently less good as a representation of the actual level scheme of ^{26}Na. This is because they omit the other possible excitations, such as the excitation of a proton from the p-shell to the sd-shell, which is very often going to be a small component

of any wavefunction in the full calculation but which can have some important effects on the energies of the states in the final level scheme. Because the wavefunction components that are omitted are generally very small in amplitude, this restricted calculation might be expected to give reasonable estimates for spectroscopic factors for the states. This is basically correct, but it is not the complete story because of the indirect effects arising from the changes in the energies of the states. This can result in the relative spacings of levels being different in the restricted and full calculations, which in turn can result in significant differences in the mixing between configurations in the calculations. Thus, the main reason for retaining the *sd-pf* $1p$-$1h$ calculations in the present work is for comparisons with the previous work of Wilson [1].

In the following tables (2.1 and 2.2), we compare the calculated energies for the low-lying levels in ^{26}Na according to the three different shell model calculations described above. It should be emphasised that the calculations are not all considered to be equally reliable as predictions of the ^{26}Na structure. For the positive parity states, as indicated above, the USD-A calculations should be the most reliable. For the negative parity states, similarly, the WBP-M calculations should be the most reliable. The other calculations are shown simply for a comparison, to indicate the model sensitivity of the results. All of these calculations were performed using the shell model code OXBASH [28].

In order to predict which of the shell model states should correspond to strongly excited states in the (d,p) transfer reaction, spectroscopic factors have been calculated using the shell model. In each case, the wavefunction for ^{25}Na was calculated in the same basis as the ^{26}Na states. The best predictions, only, are shown: positive parity states are for USD-A and negative parity states are for WBP-M. Table 2.3 shows the spectroscopic factors S for positive parity states for all states up to 6 MeV that have

a significant spectroscopic factor according to the calculation. Any state not shown has smaller spectroscopic factors. The values of S correspond to neutron transfer into the indicated shell model orbital in ^{25}Na and making the relevant final state in ^{26}Na. Table 2.4 shows the same information but for negative parity states.

All of these predictions will be discussed in relation to the information about the ^{26}Na states that is determined in the analysis of the data in this thesis.

Spin	Count	Excitation energy (MeV)		
		USD-A	$1p$-$1h$	WBP-M
		sd	*sd-pf*	*spsdpf*
3+	1	0.000	0.182	
1+	1	0.077	0.000	
2+	1	0.148	0.187	
2+	2	0.416	0.413	
1+	2	1.409	1.531	
0+	1	1.522	1.601	
3+	2	1.676	1.430	
4+	1	1.758	1.652	
4+	2	2.048	1.830	
2+	3	2.142	1.845	
5+	1	2.240	2.459	
1+	3	2.412	2.272	
2+	4	2.452	2.166	
1+	4	2.600	2.721	
3+	3	2.930	2.797	
2-	1		3.499	2.936
2+	5	3.115	2.954	
5+	2	3.118	3.006	
4+	3	3.191	2.934	
3-	1		3.741	3.228
2+	6	3.392	3.548	
1-	1		4.267	3.439
0+	2	3.488	2.884	
4-	1		3.977	3.513
4+	4	3.530	3.365	
1-	2		5.390	3.550
3+	4	3.635	3.577	
2-	2		4.530	3.690
1+	5	3.768	3.530	
3+	5	3.904	3.710	
1+	6	3.950	4.053	
4+	5	3.975	3.905	

Table 2.1: Excitation energies for 0-4 MeV in ^{26}Na according to various shell model interactions. Ordering is by USD-A (positive parity) and WBP-M (negative parity). The positive parity energies for WBP-M are the same as for $1p$-$1h$.

Spin	Count	Excitation energy (MeV)		
		USD-A	$1p$-$1h$	WBP-M
		sd	*sd-pf*	*spsdpf*
2+	7	4.180	4.020	
3+	6	4.360	4.067	
1-	3		6.231	4.381
5-	1		4.807	4.401
2+	8	4.429	4.109	
3-	2		5.249	4.462
4+	6	4.529	4.205	
2+	9	4.555	4.319	
3+	7	4.575	4.428	
1-	4		6.376	4.595
6+	1	4.622	4.578	
1+	7	4.715	4.356	
4-	2		5.391	4.731
4+	7	4.737	4.544	
0+	3	4.760	4.415	
3-	4		5.997	4.774
3+	8	4.845	4.698	
5+	3	4.865	4.767	
6-	1		5.207	4.881
3+	9	4.934	4.853	
5+	4	5.057	4.962	
1+	8	5.086	4.749	
4+	8	5.127	5.129	
2+	10	5.204	5.089	
3-	3		5.629	5.260
6+	2	5.264	4.924	
5+	5	5.285	5.111	
3-	7		6.775	5.286
3+	10	5.308	5.076	
4-	4		5.940	5.389
1+	9	5.411	5.327	
1-	6		6.949	5.501
2-	9		7.174	5.593
6+	3	5.707	5.744	
1+	10	5.761	5.444	
2-	10		7.471	5.722
3-	8		7.167	5.824
4+	9	5.873	5.469	
4+	10	6.003	5.824	

Table 2.2: Excitation energies 4-6 MeV for ^{26}Na according to various shell model interactions. Ordering is by USD-A (positive parity) and WBP-M (negative parity). The positive parity energies for WBP-M are the same as for $1p$-$1h$.

Spin	Count	Excitation energy (MeV)	SF $0d_{5/2}$	SF $1s_{1/2}$	SF $0d_{3/2}$
3	1	0.000	0.01	0.06	0.01
1	1	0.077	0.11		0.29
2	1	0.148	0.09	0.15	0.10
2	2	0.416	0.03	0.27	0.03
1	2	1.409	0.10		0.09
0	1	1.522	0.21		
3	2	1.676	0.02	0.00	0.33
4	1	1.758	0.04		0.03
4	2	2.048	0.01		0.51
2	3	2.142			
5	1	2.240	0.08		
1	3	2.412			
2	4	2.452	0.00	0.13	0.23
1	4	2.600	0.01		0.07
3	3	2.930	0.02	0.00	0.01
2	5	3.115			
5	2	3.118			
4	3	3.191			
2	6	3.392	0.01	0.03	0.29
0	2	3.488			
4	4	3.530			
3	4	3.635			
1	5	3.768	0.00		0.08
3	5	3.904			
1	6	3.950			
4	5	3.975	0.00		0.12
2	7	4.180			
3	6	4.360	0.00	0.02	0.11
2	8	4.429	0.01	0.03	0.08
4	6	4.529			
2	9	4.555			
3	7	4.575			
6	1	4.622			
1	7	4.715	0.02		0.23
4	7	4.737			
0	3	4.760			
3	8	4.845			
5	3	4.865			
3	9	4.934	0.02	0.02	0.10

Table 2.3: Spectroscopic factors for states in ^{26}Na as predicted by USD-A calculations for positive parity states. Here, the shells are represented with node numbers starting from 0 for the first level of a kind.

Spin	Count	Excitation energy (MeV)	SF $0f_{7/2}$	SF $1p_{3/2}$	SF $1p_{1/2}$
2	1	2.936	0.201	0.045	0.044
3	1	3.228	0.127	0.15	0.016
1	1	3.439	0.109	0.145	
4	1	3.513	0.003	0.439	
1	2	3.550	0.011	0.103	
2	2	3.690	0.027	0.312	
1	3	4.381	0.023	0.098	
5	1	4.401	0.46		
3	2	4.462	0.095	0.095	
1	4	4.595	0.042		
4	2	4.731	0.372	0.05	
3	4	4.774	0.047	0.279	
6	1	4.881	0.61		
3	6	5.260	0.033		0.185
3	7	5.286			0.162
4	4	5.389	0.101	0.049	
1	6	5.501			
2	9	5.593	0.026		0.117
2	10	5.722	0.164	0.003	0.049
3	8	5.824	0.083		0.048
1	9	6.076	0.001	0.025	
5	5	6.287	0.04		
6	5	7.390	0.17		

Table 2.4: Spectroscopic factors (SF) for states in ^{26}Na as predicted by WBP-M calculations for negative parity states. Here, the shells are represented with node numbers starting from 0 for the first level of a kind.

2.5 Explanation of Finding the γ-Ray Strengths

To compute the actual strength of a transition (from the experimental half-life) in Weisskopf units, the equations below can be deployed.

$$\lambda_{experimental} = \frac{ln2}{t_{1/2}} \qquad strength = \frac{\lambda_{experimental}}{\lambda_{Weisskopf\ in\ w.u}} \tag{2.19}$$

A Weisskopf unit is the theoretical estimate for a transition rate, derived in an idealized single particle model, assuming that the transition derives from a single nucleon making the transition. A transition whose strength is much larger than 1 W.u. is labelled as collective; otherwise it is regarded as non-collective. The collective transition refers to a "rotational band" or "vibrational state" for the nucleus. On the other hand, non-collective means the transition is coming from a "shell model state", instead. [29] In real nuclei, the Weisskopf estimates are not perfect, and there has been a compilation of typical observed transition strengths, for example by Endt [30].

For ^{26}Na, all the states that we see have T_z (isospin) =2, so all transitions take place without changing T values. T_z is equal to $\frac{N-Z}{2}$ where N and Z refer to neutron and proton numbers. These are called isoscalar. For that reason, only the values of the isoscalar (IS) part will be taken into consideration. The shaded areas in figure 2.7 are used to get corresponding typical values of the transition strengths. These typical values are based on where the Y axis values show the highest value. The range on the X axis corresponding to where the highest value that is read on the Y axis was noted as the number of Weisskopf units to use in the calculations of theoretical branching ratios.

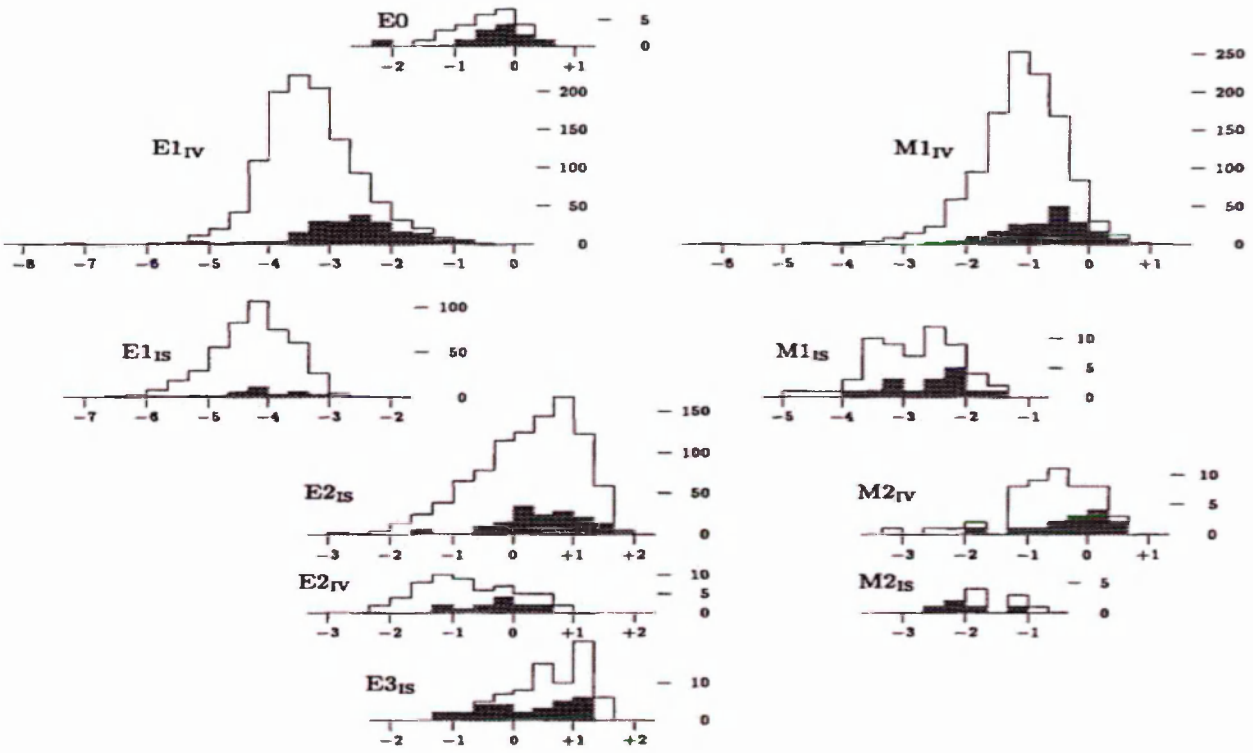

Figure 2.7: Strength histograms of A =5-44 γ-ray transitions classified according to character (E or M, multipolarity, isospin retardation; IS= isoscalar, IV= isovector.) The "abscissa scale" indicates the logarithm of the strength (in Weisskopf units, for E0 in Wilkinson units). The full lines relate to transitions in A=5- 44 and the black areas to the subset of transitions in the A=5-20 region (see page 174 in reference [30]). Y axis in the figure shows frequency (counts).

The results of the interpretation of the figure 2.7 are presented as seen in the table 2.5. While Recommended upper limits are noted from a table in the paper by Endt [30], typical values are decided reading the ranges in the figure 2.7 as briefly explained.

Recommended Upper Limits (RUL) for $\gamma-$Ray Strengths in Weisskopf Units (W.u) [30]	
$E1_{isoscalar} = 0.002$	$M1_{isoscalar} = 0.05$
$E2_{isoscalar} = 100$	$M2_{isoscalar} = 0.2$
$E3_{isoscalar} = 50$	$M3_{isoscalar} = 0$ (for unknown)
$E4_{isoscalar} = 50$	$M4_{isoscalar} = 0$ (for unknown)
$E5_{isoscalar} = 0$ (for unknown)	$M5_{isoscalar} = 0$ (for unknown)
Typical Values (TV) for $\gamma-$Ray Strengths in Weisskopf Units (W.u)	
$E1_{isoscalar} = 0.0001$	$M1_{isoscalar} = 0.01$
$E2_{isoscalar} = 1$	$M2_{isoscalar} = 0.01$
$E3_{isoscalar} = 1$	$M3_{isoscalar} = 1$ (for unknown)
$E4_{isoscalar} = 1$ (for unknown)	$M4_{isoscalar} = 1$ (for unknown)

Table 2.5: The Weisskopf unit(W.u) table for gamma strengths (see page 174 and 197 in reference [30]). Instead of unknown values, the values in the table are used.

The Weisskopf estimates are compiled in table 2.5 for convenience to calculate branching ratios. For example, if there is a transition from 4^- to 3^+ state via 3511 keV γ-ray, then we can say the first three strongest transition types will be E1, M2, and E3. The $\lambda \times RUL$ and $\lambda \times TV$ values can be determined by using the tables 2.5 and 2.6 for a corresponding transition type. The branching ratios for E1, M2, and E3 can be calculated as in equation 2.20 where the $\lambda_{E1}, \lambda_{M2}$, and λ_{E3} represent the usual Weisskopf values as shown in the table 2.6, RUL and TV indicate the recommended upper limit and typical value that were used as listed in the table 2.5. The equation 2.20 will give the weight of the individual branching ratios for a different transition type.

$$EstimatedBranchingRatio(E1) = \frac{\lambda_{E1} \times TV_{E1}}{(\lambda_{E1} \times TV_{E1}) + (\lambda_{M2} \times RUL_{M2}) + (\lambda_{E3} \times RUL_{E3})}$$

$$EstimatedBranchingRatio(M2) = \frac{\lambda_{M2} \times RUL_{M2}}{(\lambda_{E1} \times TV_{E1}) + (\lambda_{M2} \times RUL_{M2}) + (\lambda_{E3} \times RUL_{E3})}$$

$$EstimatedBranchingRatio(E3) = \frac{\lambda_{E3} \times RUL_{E3}}{(\lambda_{E1} \times TV_{E1}) + (\lambda_{M2} \times RUL_{M2}) + (\lambda_{E3} \times RUL_{E3})} \quad (2.20)$$

The Weisskopf estimates for the transition ptrobablities [31].	
$\lambda_{E1} = 1.0 \times 10^{14} A^{2/3} E^3$	$\lambda_{M1} = 5.6 \times 10^{13} E^3$
$\lambda_{E2} = 7.3 \times 10^{7} A^{4/3} E^5$	$\lambda_{M2} = 3.5 \times 10^{7} A^{2/3} E^5$
$\lambda_{E3} = 34 A^2 E^7$	$\lambda_{M3} = 16 A^{4/3} E^7$
$\lambda_{E4} = 1.1 \times 10^{-5} A^{8/3} E^9$	$\lambda_{M4} = 4.5 \times 10^{-6} A^2 E^9$
$\lambda_{E5} = 1.(unknown)$	$\lambda_{M5} = 1.(forunknown)$

Table 2.6: The decay probablities (λ) are shown in s^{-1} where E_γ is in MeV and A is the nucleon number.

Equation 3.47 in the article by Rose and Brink [32] will be presented as equation 2.21 briefly before giving details about γ-ray angular distribution ($W(\theta_{cm})$) calculations in following section 2.5.3. All we need to know at this stage is $B_K(J_1)$, $P_K(\cos\theta_{cm})$, and $R_K(\bar{L}\bar{L}J_1J_2)$ are coefficients that define the γ-ray angular distribution ($W(\theta_{cm})$) by the help of initial spin J_1, final spin J_2, the lowest multipole $\bar{L}$, and L (as equals to $\bar{L}+1$). This main equation 2.21 is given purely to explain why we really need to find out the strongest transition type for a particular γ-ray transition in this section in advance. Since formula 2.21 will be introduced in detail later, we'll focus on only two multipolarities that contribute to the transition in a particular decay. These multipolarities are presented as "$\bar{L}$" as the lowest and "L" as the next one in ascending order, respectively. That's to say L equals to $\bar{L}+1$. The γ-ray angular distribution formula in the equation 2.21 includes

effect of both transition types in the mixture. As the first transition type is regarded as mostly the strongest, this is not always the case. To prove that, we need to use the equation 2.20 one by one for E1, M2, and E3 transitions as in the previous example for 3511 keV γ-ray. Then, whichever has the highest value will define the mixing ratio (δ) that needs to be used in the equation 2.21. For simplicity, zero will be used to show the dominant transition type is the one which has the lowest multipolarity as $\bar{L}$, otherwise the value of 10^6 will put as the value of mixing ratio to dominate the second multipole (shown as L) in the mixture.

$$W(\theta_{cm}) = \sum_K B_K(J_1) P_K(\cos\theta_{cm}) \frac{R_K(\bar{L}\bar{L}J_1J_2) + 2\delta R_K(\bar{L}LJ_1J_2) + \delta^2 R_K(LLJ_1J_2)}{1+\delta^2} \tag{2.21}$$

2.5.1 The Angle Transformation due to the Headlight Effect

Consider a light source moving with velocity v in frame S. In frame S', which is moving with velocity v" away from S, then light source is at rest. Consider a photon travelling at angle θ' as measured in S'. Clearly the x-component of the velocity of the photon is $u'_x = c.\cos\theta'$. In S frame, the x-component is $u_x = c.\cos\theta$. From the velocity transformations:

$$u_x = \frac{u'_x + v}{1 + \frac{v.u'_x}{c^2}} \;,\quad c.\cos\theta = \frac{c.\cos\theta' + v}{1 + \frac{v.c.\cos\theta'}{c^2}} \;,\quad \cos\theta = \frac{\cos\theta' + \frac{v}{c}}{1 + \frac{v.\cos\theta'}{c}} \;,\quad \cos\theta = \frac{\cos\theta' + \beta}{1 + \beta.\cos\theta'} \tag{2.22}$$

where θ is the lab frame angle and θ' is the centre of mass angle. Suppose $\beta = \frac{v}{c}$ is 0.1 and θ' is 90°, the angle in laboratory frame (θ) will be calculated as $\approx 84°$. This angle transformations will be deployed especially in the γ-ray angular distribution calculations.

2.5.2 Classic and Relativistic Doppler Correction

a) Classic Doppler Correction:

$E_o = \frac{E_\gamma}{(1+\beta.\cos\theta)}$ (E_o is the gamma energy we need to find; however, "E_γ" is the gamma energy we measure during the experiment. The β is given as the ratio of "$\frac{v}{c}$").

b) Relativistic Doppler Correction :

$E_o = \gamma.E_\gamma.(1 - \beta.\cos\theta) \longrightarrow$ (γ is the coefficient of $\frac{1}{(\sqrt{1-\beta})}$).

We can give an example of this case in our gamma spectra. For 511 keV annihilation radiation, we see corresponding peaks depending on which clover of TIGRESS detectors they were detected at. We placed our HPGe detectors at 90° and 135°. If one does the calculation to see where exactly we expect to see these 511 keV gamma ray by using $\beta = 0.09145$ for (d,p) reaction for 90° and 135°, the values 513.1462 keV and 546.323 keV can be calculated. Of course, the Doppler correction shown here for 511 keV γ-rays is just as an illustration since it is not appropriate to apply it for stationary sources. However, all the γ-ray peaks will be seen at the calculated energies in the data analysis.

2.5.3 Brief Explanation of How Angular Correlation Experiments can be Done in General

The experimental aim is to gain information about the multipolarity of a gamma ray to help to infer the spins and parities of the initial and final states involved in the particular γ-ray transition. This can be achieved by means of angular correlation measurements.

An angular correlation measurement is simply the measurement of variation of gamma-ray intensity as a function of angle between the direction of gamma-ray emission and another fixed direction in space. This direction may be fixed in a particular experiment to be the direction of an incident beam which excites the gamma-decaying

state, or the direction of the emission of a particle , or a gamma ray which results in the alignment of the gamma-decaying state. [33]

The γ-ray intensity as a function of angle in terms of Legendre polynomials may be represented as stated below:

$$W(\theta) = \sum_{K=0}^{n} a_K P_K(\cos(\theta)) \tag{2.23}$$

where the coefficients a_K can be found experimentally and compared to the predictions of reaction models. The way to find this a_K coefficient experimentally is to detect the gamma ray counts in a certain period in the laboratory, and then using the known Legendre polynomials in the equation provided above, we can calculate the desired a_K coefficients.

The experimental values of a_0 for various gamma rays from a single initial state determine the branching ratios, or relative strengths of the various transitions. The γ angular distribution normalized to an average value of one is stated below:

$$W(\theta) = 1 + \sum_{K=1}^{n} B_K(J_1) P_K \cos(\theta) \tag{2.24}$$

Consider a gamma-ray transition between an initial state with spin and parity $J_1^{\pi_1}$ and the final state with spin and parity $J_2^{\pi_2}$. If there is no polarization, then the angular distribution will be isotropic, i.e., $B_K(J_1) = 0$ for all K. The same isotropic case occurs also if all magnetic sub-states of the initial state have equal populations.

Note that the total number of γ-rays emitted isotropically is given by

$$N = \int_{\theta,\phi} A_0 W(\theta_\gamma) d\Omega \;=\; A_0 \int_{\theta,\phi} \sin\theta d\theta d\phi \;=\; 4\pi A_0. \tag{2.25}$$

where A_0 is the average number observed γ-rays at any particular θ angle, by a detector of fixed solid angle.

Let us define a population parameter $w(M_1)$ such that $\sum_{M_1} w(M_1) = 1$. Then the case of equal sub-state populations would be expressed by $w(M_1) = 1/(2J_1 + 1)$ for all M_1. . There are departures from this case which can produce anisotropic angular distributions,

a) If there is a polarization, for which $w(M_1) \neq w(-M_1)$ for some values of M_1.

b) If there is an alignment condition, for which $w(M_1) = w(-M_1)$, but $w(M_1) \neq 1/(2J_1 + 1)$ for some value of M_1.

1) From these conditions, it is apparent that a spin 0 state can not be polarized or aligned.

2) Spins with 1/2 can be polarized, but not aligned to get the anisotropic situation.

3) States with spin 1 or larger can be polarized or aligned.

Thus, gamma rays from a spin 0 state must be isotropic, and gamma rays from a spin 1/2 state can be anisotropic only if the state is polarized.

The angular distribution when the gamma-ray polarization is not observed is given by

$$W(\theta_{cm}) = \sum_K B_K(J_1) P_K(\cos\theta_{cm}) \frac{R_K(\bar{L}\bar{L}J_1J_2) + 2\delta R_K(\bar{L}LJ_1J_2) + \delta^2 R_K(LLJ_1J_2)}{1+\delta^2} \tag{2.26}$$

where $\frac{R_K(\bar{L}\bar{L}J_1J_2)+2\delta R_K(\bar{L}LJ_1J_2)+\delta^2 R_K(LLJ_1J_2)}{1+\delta^2}$ term can also be labelled as $R_K(J_1J_2)$ while only two multipole contribution exists. The part related only with R coefficient above depends only on quantities which characterize the nuclear transition. And, the formula simplifies when the mixing ratio δ is zero as below.

$$W(\theta_{cm}) = \sum_{K} B_K(J_1) P_K(\cos\theta_{cm}) R_K(\bar{L}\bar{L}J_1J_2) \tag{2.27}$$

$$B_K(J_1) = \sum_{M_1=0}^{M_1=J_1} w(M_1)\rho_K(J_1M_1) \tag{2.28}$$

Here, $\bar{L}$ is the lowest allowed multipolarity. The coefficient $B_K(J_1)$ depends only on the nuclear alignment due to the weight of the sub-states, $w(M_1)$, in the populated state. The weight of these sub-states will be produced by program called TWOFNR [17]. Individual values for the $\rho_K(J_1M_1)$ and $R^q_K(LL'J_1J_2)$ in the main formula 2.26 can be found as written below when L' is equal to L+1.

$$\rho_K(J_1M_1) = (2 - \delta_{M_1,0})(-)^{J_1-M_1}(2J_1+1)^{1/2}(J_1J_1M_1 - M_1 \mid K0) \tag{2.29}$$

$$R^q_K(LL'J_1J_2) = (-)^{q+J_1-J_2+L'-L-K}(2J_1{+}1)^{1/2}(2L{+}1)^{1/2}(2L'{+}1)^{1/2}(LL'q{-}q \mid K0)W(J_1J_1LL';KJ_2) \tag{2.30}$$

$B_0(1) = 1$

There is a maximum value of K allowed by the properties of the Racah and Clebsch-Gordan coefficients, represented by W and (...|..) respectively. This maximum value K_{max} is the lesser of $2J_1$ or $2L_{max}$.

In practice, the experimenter usually chooses experimental conditions which restrict the possible values of $w(M_1)$, and then uses the experimental correlation coefficients (a_K coefficient) to determine possible values of J_1, J_2, and δ for a particular gamma-ray transition as mentioned before.

To get these results correct, the experimenter must integrate the theoretical predictions over the finite solid angle subtended by the gamma-ray detector as the equation below when comparing the predictions to this experimental results.

If the nucleus is moving in the laboratory frame by emitting γ-rays, then the number of γ-rays detected can be written as

$$Integral = \int_{\theta_{lab1}}^{\theta_{lab2}} W(\theta_{lab}) d\Omega_{lab} = \int_{\theta_{cm1}}^{\theta_{cm2}} W(\theta_{cm}) d\Omega_{cm} \tag{2.31}$$

$$W(\theta_{cm}) = \sum_{K=0}^{n} a_K P_K(\cos\theta_{cm}) \tag{2.32}$$

where the integral $d\Omega$ includes the range of azimuthal angle ϕ and polar angle θ spanned by the detector. For simplicity, the efficiency $\epsilon_\gamma = 1$ is assumed. From the conscrvation of the detected gamma rays in both lab and centre of mass frame:

$$Integral = 2\pi \sum_{K=0}^{K_{max}} a_K \int_{\theta_{cm1}}^{\theta_{cm2}} P_K(\cos\theta_{cm}) \sin\theta_{cm} d\theta_{cm} \tag{2.33}$$

If we name the part $\int_{\theta_{cm1}}^{\theta_{cm2}} P_K(\cos\theta_{cm}) \sin\theta_{cm} d\theta_{cm}$ as I_K coefficient, then the integral term 2.33 will only depend on the substate weights which are already considered in the a_K coefficient. It is because the I_K term gives just a value corresponding to the limits of the θ_{cm} angle range. Thus, the equation 2.33 can be rewritten as below.

$$Integral = 2\pi \sum_{K=0}^{K_{max}} a_K I_K \tag{2.34}$$

All in all, this integral value should be taken as a percentage of the gamma rays which the detectors can count as defined by the angle range spanned by the gamma ray detector set-up in three dimensions.

To find the gamma ray angular distribution in the laboratory frame, note that the total gamma ray count is the same in both the laboratory and the centre of mass frames according to conservation rule. This can be written as:

$$W(\theta_{lab})d\Omega_{lab} = W(\theta_{cm})d\Omega_{cm} \tag{2.35}$$

That is ,

$$W(\theta_{lab})\sin(\theta_{lab})d\theta_{lab} = W(\theta_{cm})\sin(\theta_{cm})d\theta_{cm} \tag{2.36}$$

The headlight effect gives us the relativistic relation between the angles in the centre of mass (CM) and laboratory frames. The formula for that relation is :

$$\cos\theta_{cm} = \frac{\cos\theta_{lab} - \beta}{1 - \beta\cos\theta_{lab}} \quad and \quad \cos\theta_{lab} = \frac{\cos\theta_{cm} + \beta}{1 + \beta\cos\theta_{cm}} \tag{2.37}$$

where $\beta = \frac{v}{c}$ is the speed of the source in laboratory frame.

The formula of $\frac{d}{d\theta_{cm}}(\cos\theta_{lab})$ can be written with the help of the formula 2.37 and the product rule in derivation as below.

$$\frac{d(\cos\theta_{lab})}{d\theta_{cm}} = \frac{d(\cos\theta_{lab})}{d(\cos\theta_{cm})} \times \frac{d(\cos\theta_{cm})}{d\theta_{cm}} = \frac{d}{d(\cos\theta_{cm})}\left(\frac{\cos\theta_{cm} + \beta}{1 + \beta\cos\theta_{cm}}\right) \times \frac{d(\cos\theta_{cm})}{d\theta_{cm}} \tag{2.38}$$

$$\frac{d(\cos\theta_{lab})}{d\theta_{cm}} = \frac{(1 - \beta^2)}{(1 + \beta\cos\theta_{cm})^2} \times (-\sin\theta_{cm}) \tag{2.39}$$

The same formula as 2.38 can also be written as below.

$$\frac{d(\cos\theta_{lab})}{d\theta_{cm}} = \frac{d(\cos\theta_{lab})}{d(\theta_{lab})} \times \frac{d(\theta_{lab})}{d\theta_{cm}} = (-\sin\theta_{lab}) \times \frac{d\theta_{lab}}{d\theta_{cm}} \tag{2.40}$$

Since the formula 2.39 and 2.40 are equal, we can easily say that

$$\frac{d\theta_{lab}}{d\theta_{cm}} = \frac{\sin\theta_{cm}}{\sin\theta_{lab}} \times \frac{(1-\beta^2)}{(1+\beta\cos\theta_{cm})^2} \tag{2.41}$$

Now, if we use the formula 2.36 again with the equation 2.41, we can reach $W(\theta_{lab})$ without any complexity.

$$W(\theta_{lab}) = W(\theta_{cm}) \times \frac{(1+\beta\cos\theta_{cm})^2}{(1-\beta^2)} \tag{2.42}$$

In my code, I have used the coefficient above 2.42 to convert CM frame γ ray distribution to lab frame γ ray distribution since we always calculate values in the CM frame.

In the case of any unobserved γ-rays preceding the observed gamma ray in the cascade, one should use $U_K(J_1J_2)$ coefficients for each unobserved gamma ray as below. For example, 5 unobserved γ-rays before the observed γ-ray,

$$W(\theta) = \sum_K B_K(J_1)P_K(\cos\theta)U_K(J_1J_2)U_K(J_2J_3)U_K(J_3J_4)U_K(J_4J_5)U_K(J_5J_6)R_K(J_6J_7) \tag{2.43}$$

I need to emphasise that there is a slightly irregularity in the labels used for γ-ray multipolarity in the Rose and Brink article (see [32]). Thus, I'll make all these symbols and their referrals as clear as possible here. The $\bar{L}$ value in R coefficient as discussed earlier refers to the lowest multipolarity, and L equals $\bar{L}+1$.

The γ-ray multipolarity for unobserved transitions is dealt with $U_K(J_1J_2)$ coefficients as defined in equation 2.44. As for the R coefficients, there is a simplified form when two lowest allowed multipolarities are the only contributions. In much the same way as L and L' were used in the term $R^q_K(LL'J_1J_2)$ before, the $\bar{L}$ value in U coefficient refers to the lowest multipolarity, and L equals $\bar{L}+1$.

$$U_K(J_1J_2) = \frac{U_K(\bar{L}_{12}J_1J_2) + \delta^2_{L_{12}} U_K(L_{12}J_1J_2)}{1+\delta^2_{L_{12}}} \tag{2.44}$$

To find the $U_K(J_1J_2)$ above, one first needs to find individual U coefficients to substitute into the formula above as in evaluation of the $R_K(J_1J_2)$ coefficient. The coefficient $U_K(L_{12}J_1J_2)$ can be calculated with the help of Racah coefficients as follows:

$$U_K(L_{12}J_1J_2) = (-)^K \frac{W(J_1J_2J_1J_2;L_{12}K)}{W(J_1J_2J_1J_2;L_{12}0)} = (-)^K \frac{W(J_1J_1J_2J_2;KL_{12})}{W(J_1J_1J_2J_2;0L_{12})} \tag{2.45}$$

Then, to find the Racah coefficients above, we need to use the 6J Wigner formula stated as a matrix below.

$$W(abcd;ef) = \frac{\begin{Bmatrix} a & b & e \\ d & c & f \end{Bmatrix}}{(-1)^{a+b+c+d}} \tag{2.46}$$

To do cross check of our results, the tables in the back of the Rose & Brink article [32] were used. Note that, notation in these tables sometimes can be confusing. As a reminder, L refers to lowest multipolarity, and L' equals to $L+1$ in $R_K(LL'J_1J_2)$ coefficients on these tables. Similarly, L_{12} is the lowest multipolarity, so $L_{12}+1$ is the next one which explicitly stated in $U_K(L_{12}+1\ J_1J_2)$ coefficient on the tables given in the article.

2.5.4 Legendre Polynomials

For convenience, the general Legendre polynomial formula [34] and the specific ones used in the codes to calculate γ-ray angular distributions are presented below.

$$P_l(x) = \frac{1}{2^l \times l!} \times \frac{d^l}{dx^l}[(x^2-1)^l] \qquad , x = cos\theta_\gamma \tag{2.47}$$

Legendre Polynomial Equations	
$P_0(x) =$	1
$P_2(x) =$	$\frac{1}{2} \times (3x^2 - 1)$
$P_4(x) =$	$\frac{1}{8} \times (35x^4 - 30x^2 + 3)$
$P_6(x) =$	$\frac{1}{16} \times (231x^6 - 315x^4 + 105x^2 - 5)$
$P_8(x) =$	$\frac{1}{128} \times (6435x^8 - 12012x^6 + 6930x^4 - 1260x^2 + 35)$

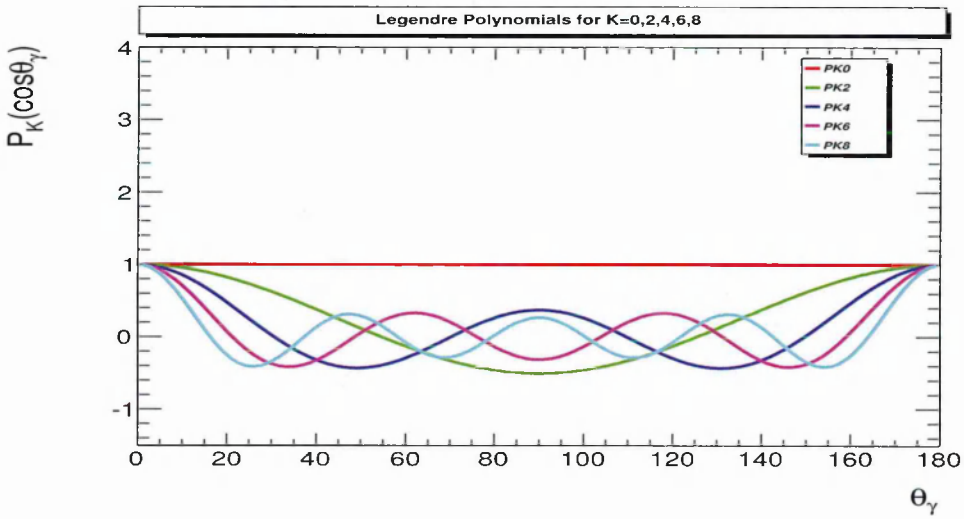

Figure 2.8: Legendre Polynomials

If we refer to I_K term as defined in the equation 2.33 and consider stationary γ sources only, then to find the detection proportion between 90° and 135° clovers of TIGRESS, we should use isotropic γ-ray distribution case. Then, this idea leads us to the formula in 2.48 where we consider only the zeroth order Legendre polynomial as $P_0(x) = 1$ regardless of what x value is.

$$\int_{\theta_{cm1}}^{\theta_{cm2}} P_0(\cos\theta_{cm}) \sin\theta_{cm} d\theta_{cm} = \cos\theta_{cm1} - \cos\theta_{cm2} \tag{2.48}$$

Considering the angles, given below, subtended by TIGRESS clovers in the rest frame of ^{26}Na and laboratory frame, we can calculate the parts constituting the overall I_K coefficient for both clovers at 90° and 135°. Since γ-ray angular distributions are made in the rest frame of ^{26}Na to be converted into laboratory frame afterwards, angles in the rest frame of ^{26}Na should be used in the calculations to find the detection ratio between 90° and 135° clover angles with regard to the beam direction in θ.

For the present experiment specifically, it is useful to consider the fraction of solid angle subtended by the γ-ray detector mounted in 90° and those mounted in 135° to the beam direction. The limits of the detectors in the θ direction are given in table 2.7.

Subtended laboratory frame angles by TIGRESS clovers	
For 90° clovers,	from 74° to 106°
For 135° clovers,	from 119° to 151°
Subtended angles in the rest frame of ^{26}Na by TIGRESS clovers	
For 90° clovers,	from 79.6° to 111.4°
For 135° clovers,	from 123.9° to 153.7°

Table 2.7: Angle conversion for γ-rays are done by headlight effect formula 2.37.

For the polar angle, we can estimate the range easily for the 135° detectors because of the geometry of the array. The four squares of the TIGRESS detector faces are separated by triangular gaps with an area equals to half of the square. Therefore, approximately 2/3 of the whole range of ϕ is covered by these detectors. Eventually, our formula 2.48 turns into :

$$\frac{2}{3} * (\cos(123.9) - \cos(153.7)) = X * (\cos(79.6) - \cos(111.4)) \tag{2.49}$$

where we take into account that we have the same number of detectors(4) at each θ angle. The variable X presents the fractional ϕ coverage at 90°. The X value we seek is now 0.4132 to be used in the angular distribution code when we sum the two contributions from both clover angles to calculate I_K coefficients and hence calculate the fraction of γ-rays detected. This can be calculated for any γ-ray distribution, not just for the isotropic distribution.

In the case of one unobserved gamma ray that follows with one observed γ-ray, the gamma ray angular distribution can be even simplified more as shown below.

$$W(\theta_{cm}) = \sum_{K=0}^{n} a_K * U_K(J_1 J_2) * P_K(\cos\theta_{cm}) \tag{2.50}$$

One should note that a_K and $U_K(J_1 J_2)$ coefficients in this formula are just numbers, so we can regard them as the amplitude of the angular distribution. The Legendre Polynomial part, on the other hand, defines how our distribution distorts depending on the θ_γ due to the shape of the distributions as a functuon of θ_γ defined by the Legendre polynomials in the figure 2.8.

2.5.5 The Efficiency Correction due to Headlight Effect

The efficiency calculations have been done so far with the stationary sources of ^{152}Eu, ^{133}Ba, ^{56}Co, and ^{57}Co as the details given in the tables 2.8. However, in the real experiment, gamma rays that are emitted from recoil will be radiated from a moving source.

Thus, the emission of the γ-rays from a recoil nucleus will occur in the laboratory frame rather than from a stationary source in the centre of mass frame. One should take this into account in the γ-ray efficiencies in use to extract the angular distribution of the γ-ray and differential cross section of a proton from a particular excited state in ^{26}Na

from the data. Thus, previously derived formulas in equations 2.35, 2.41 and 2.42 will be deployed here to find the ratio of the gamma efficiencies in both frames as shown in the equation 2.51 by using the ratio of the total counts of the detected γ-rays in the laboratory and centre of mass frames.

$$\frac{\varepsilon^{lab}_{90^\circ}}{\varepsilon^{cm}_{90^\circ}} = \frac{\int_0^{2\pi}\int_{\theta_1\ lab}^{\theta_2\ lab} W(\theta_{lab})\sin(\theta_{lab})d\theta_{lab}d\phi_{lab}}{\int_0^{2\pi}\int_{\theta_1\ cm}^{\theta_2\ cm} W(\theta_{cm})\sin(\theta_{cm})d\theta_{cm}d\phi_{cm}} \tag{2.51}$$

Then, with the help of equations 2.41 and 2.42, one can reach the formula in the equation 2.52 in terms of the angles in the centre of mass frame.

$$\frac{\varepsilon^{lab}_{90^\circ}}{\varepsilon^{cm}_{90^\circ}} = \frac{2\pi \int_{\theta'_1\ cm}^{\theta'_2\ cm} W(\theta_{cm})\frac{(1+\beta\cos\theta_{cm})^2}{(1-\beta^2)}\frac{(1-\beta^2)}{(1+\beta\cos\theta_{cm})^2}\sin(\theta_{cm})d\theta_{cm}}{2\pi \int_{\theta_1\ cm}^{\theta_2\ cm} W(\theta_{cm})\sin(\theta_{cm})d\theta_{cm}} \tag{2.52}$$

The same formula should be calculated for the TIGRESS gamma coverage angles of the 135 degree clover as in the equation 2.53.

$$\frac{\varepsilon^{lab}_{135^\circ}}{\varepsilon^{cm}_{135^\circ}} = \frac{2\pi \int_{\theta'_1\ cm}^{\theta'_2\ cm} W(\theta_{cm})\frac{(1+\beta\cos\theta_{cm})^2}{(1-\beta^2)}\frac{(1-\beta^2)}{(1+\beta\cos\theta_{cm})^2}\sin(\theta_{cm})d\theta_{cm}}{2\pi \int_{\theta_1\ cm}^{\theta_2\ cm} W(\theta_{cm})\sin(\theta_{cm})d\theta_{cm}} \tag{2.53}$$

To make the angle conversion between the frames, one should use equation 2.54 as given in the section 2.5.1.

$$\theta_{cm} = \arccos\left(\frac{\cos\theta_{lab} - \beta}{1 - \beta\cos\theta_{lab}}\right) \tag{2.54}$$

The angle coverage of TIGRESS was presented for the 90° and 135° clovers in the table 2.7 in both the rest frame of ^{26}Na and laboratory frame. Gamma-ray angular distribution, $W(\theta_{cm})$, can be set up as equal to one to simplify the formulas in the 2.52

and 2.53 to the equations in the 2.55 in the case of isotropic γ-ray distribution. By using these given angles in the table 2.7, the ratio of γ-ray efficiencies in different frames can be found as in equation 2.55.

$$\varepsilon^{lab}_{90^\circ} = \varepsilon^{cm}_{90^\circ}\frac{\cos\theta'_{1\ cm} - \cos\theta'_{2\ cm}}{\cos\theta_{1\ cm} - \cos\theta_{2\ cm}} = \varepsilon^{cm}_{90^\circ}\frac{\cos 79.6^\circ - \cos 111.4^\circ}{\cos 74^\circ - \cos 106^\circ} = \varepsilon^{cm}_{90^\circ} \times 1.077$$
$$\varepsilon^{lab}_{135^\circ} = \varepsilon^{cm}_{135^\circ}\frac{\cos\theta'_{1\ cm} - \cos\theta'_{2\ cm}}{\cos\theta_{1\ cm} - \cos\theta_{2\ cm}} = \varepsilon^{cm}_{135^\circ}\frac{\cos 123.9^\circ - \cos 153.7^\circ}{\cos 119^\circ - \cos 151^\circ} = \varepsilon^{cm}_{135^\circ} \times 0.869 \tag{2.55}$$

In conclusion, the proton differential cross sections during their calculation process simply need to have this efficiency correction due to the headlight effect on γ-rays emitted by the recoil nucleus in motion.

2.6 Energy Calibration and Efficiency Curves in TIGRESS

Energy calibration of the TIGRESS has been done with the well known gamma ray sources of ^{133}Ba, ^{152}Eu, and ^{56}Co . All the detailed information about the gamma sources can be seen in the following tables. To get the efficiency curves for the TIGRESS, 5 data points for ^{133}Ba, 11 data points for ^{152}Eu, and 8 data points for ^{56}Co are used. Gamma-ray efficiency curves will be retrieved separately for 90 and 135 degree clovers. These values will be deployed in the calculation when finding the branching ratios of the gamma rays from excited states of ^{26}Na. Also, these efficiencies will be used effectively to extract the gamma and proton angular distributions in the data. The more data points we use on the efficiency curves corresponding to a wide range of energies covering both low and high energies, the more precise will be the efficiency fit that is achieved in the end.

γ Source	Initial Activity (kBq)	γ Source	Initial Activity (kBq)	γ Source	Initial Activity (kBq)
^{152}Eu	38.11 $\pm$ 1.18kBq	^{133}Ba	34.25 $\pm$ 1.03kBq	^{56}Co	Unkown
Total run time	Activation Date	Total run time	Activation Date	Total run time	Activity found in the experiment at 90°
3479 s	15/09/2006	12522 s	15/09/2008	94500 s	12821.5 $\pm$ 5.99704kBq
	Date of Usage		Date of Usage		Activity found in the experiment at 135°
	18/08/2009		24/08/2009		13477.6 $\pm$ 6.31661kBq
	Activity during experiment		Activity during experiment		
	36.35 $\pm$ 1.13kBq		32.19 $\pm$ 1.06kBq		

Table 2.8: ^{152}Eu R-00856, ^{133}Ba R-0085, and ^{56}Co calibration sources for the efficiency of TIGRESS provided in TRIUMF, Canada.

For the γ source spectra, one can refer to the figures 2.9, 2.10, and 2.11.

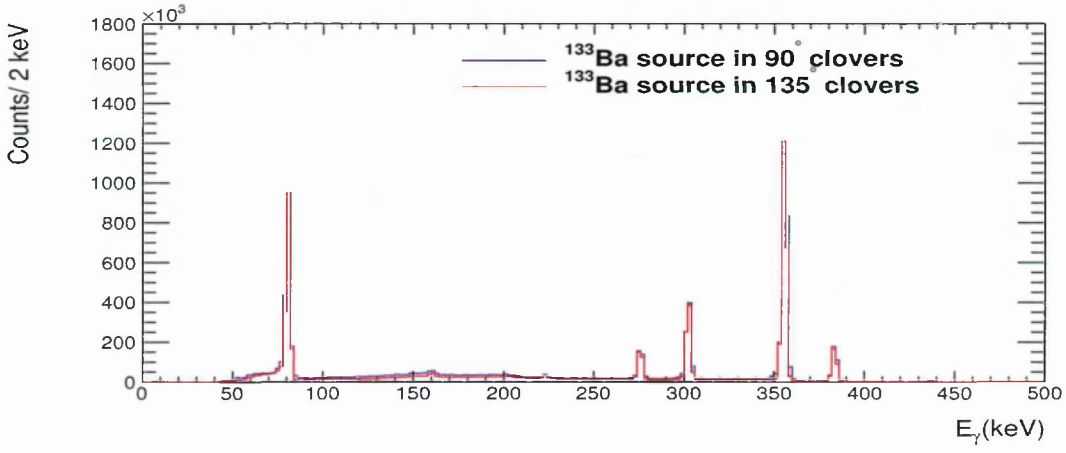

Figure 2.9: γ calibration source spectra for ^{133} Ba.

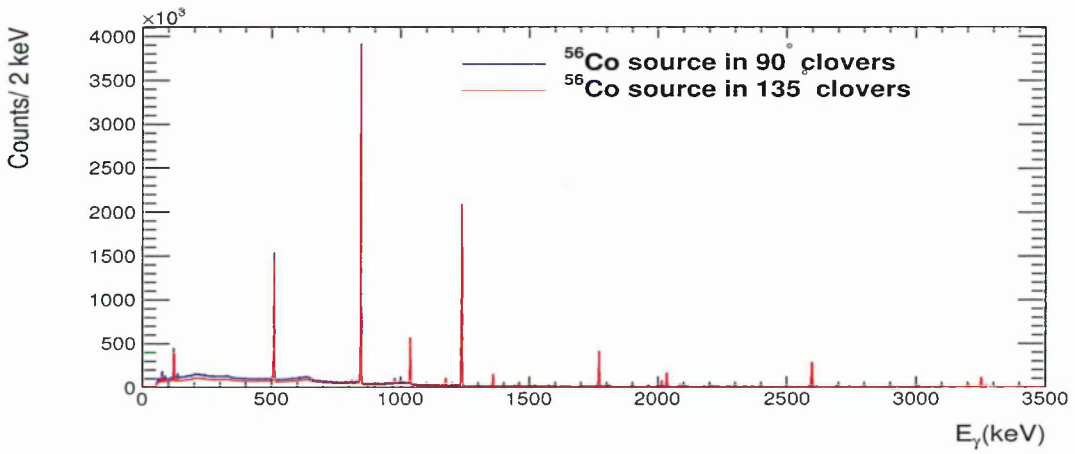

Figure 2.10: γ calibration source spectra for ^{56} Co.

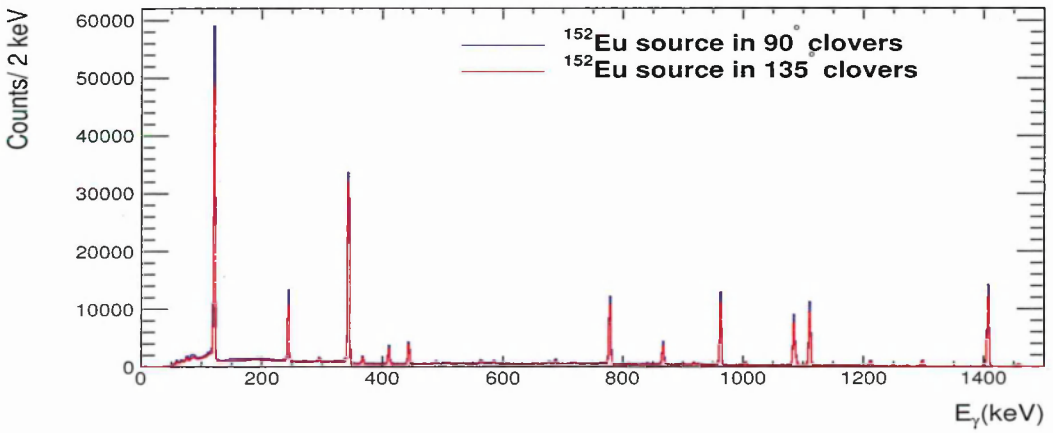

Figure 2.11: γ calibration source spectra for ^{152} Eu.

In order to determine the total counts from each full energy γ-ray peak, Gaussian and first order polynomial functions are fitted together in ROOT [35] to make a suitable background subtraction. Then, all the counts from these detected gamma rays are noted in the tables 2.9, 2.10, 2.11, 2.12, and 2.13.

From the spectra above for the gamma calibration sources, one can easily notice

that the total counts from each peak for different clovers are expected to be similar.

It's useful at this stage to explain how the gamma-ray interacts with the matter because the γ-ray efficiency formula in this part will be based on this information. The signal recorded by the detector will be proportional to the energy deposited by the electron, that are produced, and which then slow down and stop. As they slow down, they produce electron-hole pair in the germanium of the detector via collisions. It is the collection of these liberated electrons and holes that gives the electrical signal from the detector. The most commonly used plots in the figure 2.12 and 2.13 help us to summarize all the interactions in matter for a γ-ray. The first interaction type is called "Compton Scattering". This happens only when the scattered photon does not deposit all of its energy in the matter, so the total energy of the gamma ray will be shared between a scattered gamma ray with bigger wavelength and the electron of the last orbital of the interacted matter. The diagram 2.12 shows the scattered electrons with red arrow for clarity. All energy sharing situation in this diagram 2.12 indicates Compton scattering. The second type of interaction is "photoelectric absorption" in which case the incoming photon transfers its entire energy to the electron. If there is both an electron and a positron exist in the medium, then the combination of these two 511 keV particles result in outcome of the two gamma rays going opposite to each other due to the conservation of energy and linear momentum which also forbid the creation of only one photon. This is called "annihilation". The result of two gamma rays occur only when the energy of the emerging particles have low energy. Otherwise, it's possible to have other additional particles together with two annihilation photons, too. The total energy absorption of these two gamma rays gives a gamma energy at 1022 keV. On the other hand, incoming photon can sometimes creates both electron and positron after the interaction in matter if it has

the energy required to create two particles. Note that, the minimum energy required for this reaction is 1022 keV or more since the rest mass energy of the electron is 511 keV. And, this event is called "pair production".

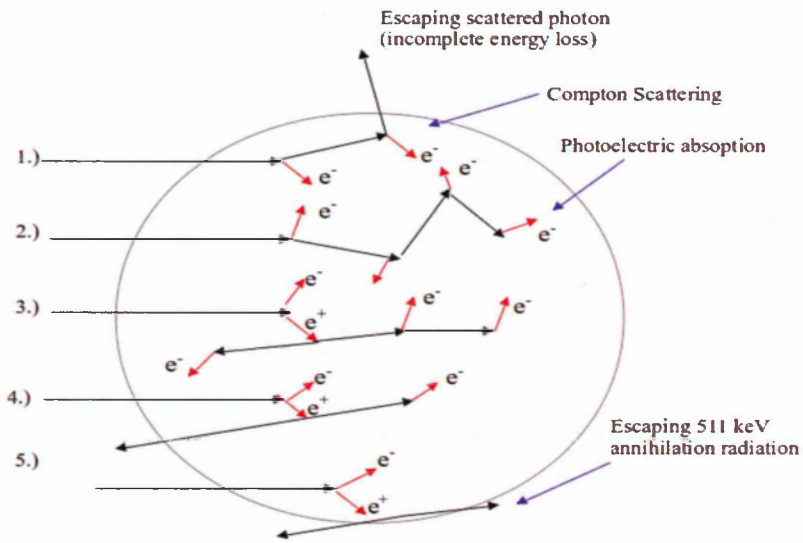

Figure 2.12: Gamma ray interaction types in matter as presented in the reference [19]

In the five different labels of the figure 2.12, we firstly see "a multiple Compton scattered" gamma ray leaving the detector without depositing all its energy. In the second label, "photoelectric absorption" after multiple Compton scattering can be observed. Thus, at this stage, complete energy deposition occurs. Thirdly, the pair production followed by positron annihilation, Compton scattering, and photoelectric absorption are taken place. Thus, complete energy deposition is met. In the fourth case, the scattered gamma ray from the detector medium results in energy loss in comparison to initial photon energy. And finally, both annihilation photons leave the detector giving the 1022 keV energy loss. [19]

By knowing these interaction procedures explained above, the region of effectiveness can be explained with another plot in 2.13 in terms of incoming photon energy and the

atomic number of the absorber material. The most worrying part in our experiment with ^{26}Na is the Compton scattering reaction since we don't want scattering gamma rays from our HPGe detectors. Since the highest energy gamma ray is observed at 3584 keV, as shown later from excited state ^{26}Na in the analysis, it's safe to say the pair production will be out of our interest.

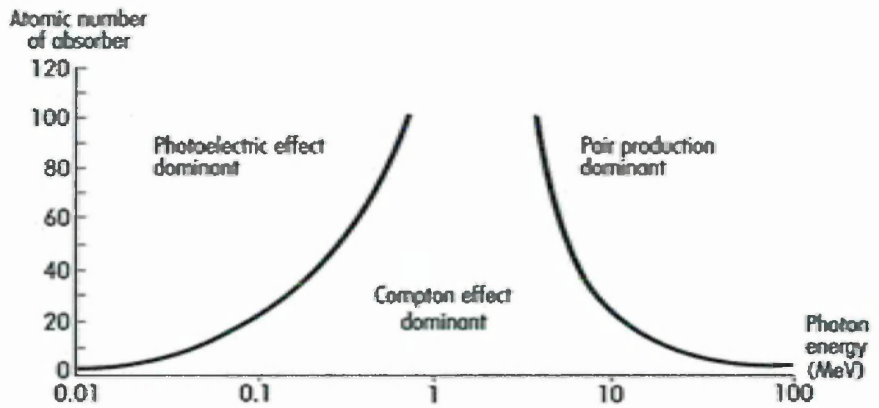

Figure 2.13: Three main gamma interaction processes with corresponding dominant regions [19].

After the detailed explanations above, now we know that most of the time γ-rays may not be detected at all because of the way they behave in the detector material. Namely, there is a possibility for a gamma ray to pass through the material without any interaction. Therefore, the absolute efficiency of the TIGRESS detectors need to be investigated.

The ratio of the detected gamma rays to initially emitted gamma rays from the source will give the efficiency of the detection as in 2.56 with its calculated error in 2.57

$$\epsilon_{absolute}(E_{\gamma_1}) = \frac{N(E_{\gamma_1})}{I_{\gamma_1}(E_{\gamma_1}) \times A \times t} = \epsilon_{\gamma_1} \tag{2.56}$$

$$\epsilon_{absolute}\ error = \epsilon_{\gamma 1} \times \sqrt{(\frac{Error_N}{N})^2 + (\frac{Error_A}{A})^2 + (\frac{Error_t}{t})^2 + (\frac{Error_{I_{\gamma_1}}}{I_{\gamma_1}})^2} \tag{2.57}$$

, where "N" is the total counts, "A" is the activity of the γ source, "t" is the time elapsed, and I_γ is the intensity of the gamma ray. This assumes that any dead time of the

acquisition system is either zero or has been taken into account in the stated acquisition time, t.

E_γ (keV) [36]	Error [36]	Counts	I_γ(%) [36]	Error (%) [36]	ε_γ	ε_γ error
80.9971	0.0014	1468570	34.1	0.3	0.0107	0.0004
276.3997	0.002	274934	7.164	0.022	0.0095	0.0003
302.851	0.001	694453	18.33	0.06	0.0094	0.0003
356.0134	0.0002	2210240	62.05	0.19	0.0088	0.0003
383.348	0.003	303295	8.94	0.03	0.0084	0.0003

Table 2.9: Relative efficiencies for ^{133}Ba source for 90 degree

The results in terms of efficiencies and errors for ^{133}Ba in the table 2.9 are found by using the equation 2.56 and 2.57 to set as a reference for all the other data points. Thus, the efficiency curve with the results in the table 2.9 is plotted for the initial step. Thus, these efficiencies will not be the final data point on the absolute efficiency curve which will be presented in the end of the section.

E_γ (keV) [36]	Error [36]	Counts	I_γ(%) [36]	Error (%) [36]	ε_γ	ε_γ error
121.7817	0.0003	94933.20	28.67	0.15	0.00262	0.000083
244.6975	0.0008	21023.70	7.61	0.04	0.00218	0.000071
344.2785	0.0012	67552.80	26.5	0.5	0.00202	0.000074
411.1163	0.0011	5057.38	2.237	0.025	0.00178	0.000064
443.965	0.003	6892.03	3.148	0.023	0.00173	0.000059
778.904	0.018	23011.30	12.96	0.14	0.00140	0.000047
867.373	0.004	7203.12	4.26	0.03	0.00134	0.000045
964.079	0.018	24075.30	14.65	0.07	0.00129	0.000042
1085.869	0.024	19707.70	10.24	0.05	0.00152	0.000049
1112.069	0.004	20941.00	13.69	0.07	0.00121	0.000039
1408.006	0.003	28861.40	21.07	0.1	0.00108	0.000035

Table 2.10: Relative efficiencies for ^{152}Eu for 90 degree

As a second step, the efficiency values in the table 2.10 are found by using the equation 2.56 and 2.57 to get the shape of the efficiency curve since ^{152}Eu has the highest number of data points in the efficiency curve. And, this is done by using its fit parameters from its efficiency curve as fix parameters. Then, we add one more flexible parameter, which we called it scaling factor, into a fit function. Therefore, every time we fit the function onto data points of particular γ-ray source, we've had another scaling factor with the 6 main parameters fixed in the main fitting function as written in the equation 2.58. The detail of the code written for these complicated steps for each γ source to scale them to the ^{133}Ba curve will not be presented here, but one should know that every data points are eventually scaled to those ^{133}Ba data points by using the efficiencies from the tables of ^{133}Ba, ^{152}Eu, and ^{56}Co sources as presented in this section.

The fit function for efficiency is taken from the RADWARE [37] code which has been found to give a good fit to the efficiency curve for both low and higher energetic γ-rays.

This fit function f(x) can be written with 6 parameters as indicated in closed brackets in the equation 2.58.

$$f(x) = \frac{([0] + [1]\log(x) + [2]\log(x)^2 + [3]\log(x)^3 + [4]\log(x)^4 + [5]\log(x)^5)}{x} \quad (2.58)$$

Another reason why ^{152}Eu curve is scaled to match the ^{133}Ba data points is due to uncertainties in the precise activities and dead times for the two measurements.

E_γ (keV) [36]	Error [36]	Counts	I_γ(%) [36]	Error (%) [36]	ε_γ	ε_γ error
846.771	0.008	7611510	99.94	0.03	80.593	0.037
1037.841	0.006	933560	14.17	0.13	69.717	0.644
1238.252	0.007	4138660	66.9	0.6	65.464	0.588
1360.215	0.012	260037	4.29	0.04	64.143	0.611
1771.351	0.016	781213	15.47	0.14	53.438	0.487
2034.755	0.015	356749	7.89	0.13	47.847	0.792
2598.459	0.013	686676	17.3	0.3	42.002	0.730
3253.416	0.015	266493	8.12	0.17	34.729	0.730

Table 2.11: Relative efficiencies for ^{56}Co for 90 degree

The efficiencies and errors in the table 2.11 are found without taking activity of the source into account by using the equation 2.56 and 2.57. The activity of the source has been found later as 13132.53±4.35 Bq by using scaling of the data points to the ^{133}Ba curve.

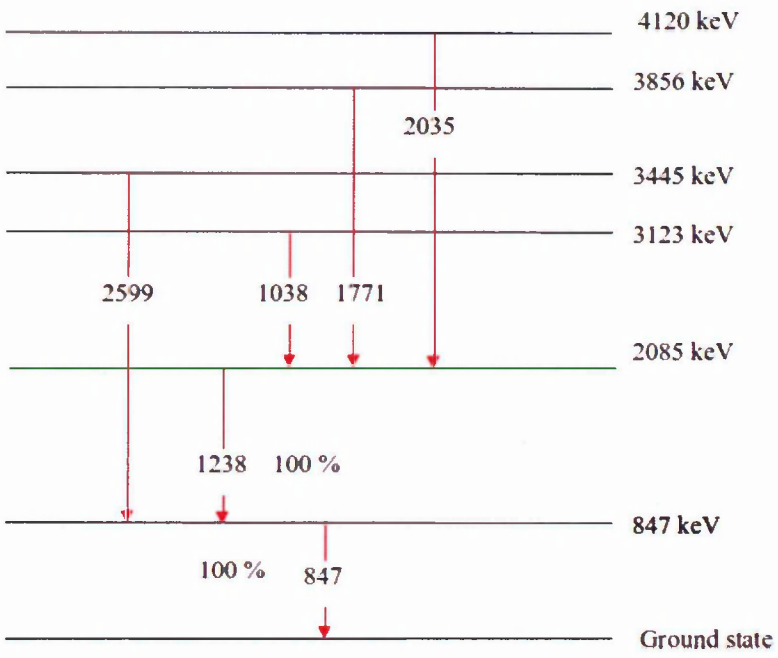

Figure 2.14: The partial level scheme for the coincidences in ^{56}Co γ-ray calibration source [36]

It's possible to have random and true coincidences from ^{56}Co data, so a correction is required to account for random coincidences. The efficiency of the γ_2 which is in coincidence with γ_1 is given in the equation 2.59, where BR_{γ_2} is the branching ratio of the γ_2, together with its error in 2.60. The γ-ray decays in the ^{56}Co level scheme is shown partly in the figure 2.14 as a reference because it helps to interpret the calculations done for the false coincidence corrections in the following part.

$$\epsilon_{\gamma_2} = \frac{N(\gamma_2|\gamma_1)}{N(\gamma_1) \times BR_{\gamma_2}} \tag{2.59}$$

$$Error_{\epsilon_{\gamma 2}} = \frac{\sqrt{N(\gamma_2|\gamma_1)}}{N(\gamma_1)} \tag{2.60}$$

Two γ-ray energies at 847 keV and 1238 keV were selected to look for random coincidences, so they can then be subtracted from the efficiencies using equation in 2.59.

Therefore, the ratio of the total counts of the γ-ray at 847 keV, which is in false coincidence with another 847 keV γ-ray from a different decay, to the number of 847 keV per decay (I_{γ_1}) is shown in equation 2.61. On the other hand, to find the random coincidence probability of the 1238 keV gamma ray, equation 2.62 is used. This makes adjustments for the different emission probabilities and detection efficiencies of the two γ-rays. The ratio of the detection efficiencies is obtain from the combined data of the ^{133}Ba, ^{152}Eu, and ^{56}Co sources. For this purpose, the whole TIGRESS array in both 90° and 135° was used. To get the final efficiencies for ^{56}Co, $p_{random}(847\ keV)$ and $p_{random}(1238\ keV)$ should be subtracted from the previously found efficiencies in 2.59. And, this is given in formula 2.63 with its error in 2.64.

$$p_{random}(847keV) = \frac{N(\gamma_1|\gamma_1)}{N(\gamma_1)} \times \frac{1}{I_{\gamma_1}} \tag{2.61}$$

$$p_{random}(1238keV) = p_{random}(847keV) \times I_{\gamma_{1238keV}} \times \frac{\epsilon_{1238keV}}{\epsilon_{847keV}} \tag{2.62}$$

$$\epsilon_{\gamma_2} = (\epsilon_{\gamma_2} - p_{random}(847)) \times (8/7) \times ratio847keV \tag{2.63}$$

$$\epsilon_{\gamma_2}\ error = \epsilon_{\gamma_2}\ error \times (8/7) \times ratio847keV \tag{2.64}$$

$$\epsilon_{\gamma_2} = (\epsilon_{\gamma_2} - p_{random}(1238)) \times (8./7.) \times ratio1238keV \tag{2.65}$$

$$\epsilon_{\gamma_2}\ error = \epsilon_{\gamma_2}\ error \times (8/7) \times ratio1238keV \tag{2.66}$$

E_{γ_2} (keV) [36]	$E_{\gamma_1}(keV)$ [36]	$N(\gamma_2\|\gamma_1)$	$N(\gamma_1)$	Absolute ε_{γ_2}	Error
846.771	846.771	11996.7	15181200		
846.771	1038.841	64491.5	1887930	0.01902	0.00008
846.771	1238.252	231132.0	8335390	0.01535	0.00003
846.771	1771.351	48303.6	1582140	0.01694	0.00008
846.771	2034.755	22498.3	725950	0.01721	0.00012
846.771	2598.459	42869.1	1387590	0.01712	0.00008
1238.252	1038.841	46111.4	1887930	0.01379	0.00007
1238.252	1238.252	2340.86	8335390		
1238.252	1771.351	40149	1582140	0.01434	0.00007
1238.252	2034.755	18305.1	725950	0.01425	0.00011

Table 2.12: Relative efficiencies for ^{56}Co coincidences without any clover angle gate.

The gamma cascade in the figure 2.14 also explains why we don't need to find the absolute efficiencies of those γ-rays at 847 keV and 1238 keV when they are in false coincidences as shown empty for the related absolute efficiency parts in the table 2.12 here. The figure 2.14 also shows that the emission of a γ-ray of 1238 keV always follows the emission of each of the four γ-rays shown in the last four lines of the table 2.12 as γ_1 except 1238 keV γ-ray. This gives four independent measurements of γ_2 where γ_2 is 1238 keV. In turn, 1238 keV γ-ray is always followed by a γ-ray of 847 keV. Therefore, the initial four γ-rays, plus the 1238 keV γ-ray, together give five independent measurements of ε_{γ_2} where γ_2 is 847 keV.

E_γ(keV) [36]	N_{90°	N_{135°	Ratio of the counts at 90°	Ratio of the counts at 135°
847	7611510	7569030	0.5014	0.4986
1238	4138660	4193860	0.4967	0.5033

Table 2.13: Finding the ratios to separate the efficiencies for clovers at 90 and 135 degree

The absolute efficiencies in the table 2.13 are found step by step by following the equations in 2.59, 2.60, 2.61, 2.62, 2.63 , 2.64, 2.65, and 2.66. Firstly, the formula 2.59 and 2.60 are applied using columns $N(\gamma_2|\gamma_1)$ and $N(\gamma_1)$ in the table 2.12. After getting those individual results for each coincidence situation, one should deduce the random coincidence, shown as $p_{random}(847\text{ keV})$ and $p_{random}(1238\text{ keV})$, from each value found. These reductions are due to random coincidence of 847 keV γ-ray with 847 keV γ-ray and 1238 keV γ-ray with 1238 keV γ-ray. That's to say that γ-rays with same energy, coming from different nuclei in the same γ-ray source, may arrive close enough in time in to the detectors to look for one event.

Then, each value except those at 847 keV and 1238 keV, stated as E_{γ_1}, will be processed for the gamma coincidences with 847 keV γ-ray by the equation in 2.63 and 2.64 and for the gamma coincidences with 1238 keV γ-ray by the equation 2.65 and 2.66. The ratio of $\frac{8}{7}$ results from the fact that every time one clover has hit in TIGRESS, it leaves 7 clovers active for the detection of the coincidence gamma ray among the all 8 clovers.

In conclusion, the absolute efficiencies and their errors for ^{56}Co which are shown in the last two columns of the table 2.12 are the values calculated by the equation 2.63 and 2.65 with the following error equations. The final coincidence data points presented in the table 2.14 are the averaged values of these two columns in the table 2.12 for absolute efficiencies at the data points of 847 keV and 1238 keV. To reach this final table in 2.14, the partitioning for different clover angles of the ^{56}Co data has been done by using the counts on both angles from the single γ-ray spectrum; namely not the coincidence spectrum as the numbers are given in the table 2.13. This method helped to get the separate efficiency values for the ^{56}Co coincidence data information taken without any clover angle gate in

the table 2.12. These two final absolute efficiency data points are then used to scale the relative efficiency curves produced from the source data, resulting in the absolute efficiency curves shown in Figure 2.15. In the end, all the steps have been done separately for the 135° clovers as well, but only the final efficiency curve will be presented here.

E_γ (keV) [36]	Error [36]	Absolute ε_γ	Error
846.771	0.008	0.0172314	0.000078
1238.25	0.007	0.0139519	0.000080

Table 2.14: Relative efficiencies from coincidence data for clovers at 90 and 135 degree

If one follows the same procedures for clover angle 135 degree, two absolute efficiency curves depending on the Doppler corrected gamma energies will be reached as shown in the figure 2.15. These curves represent the absolute efficiencies for detection in the full energy peak. The data were analysed in the same way as for γ-rays from the reaction data. That is to say, they were analysed with full add-back between all detectors in a given clover, and with full Compton suppression applied in the software according to whether any signal was detected in any of the BGO/NaI shields.

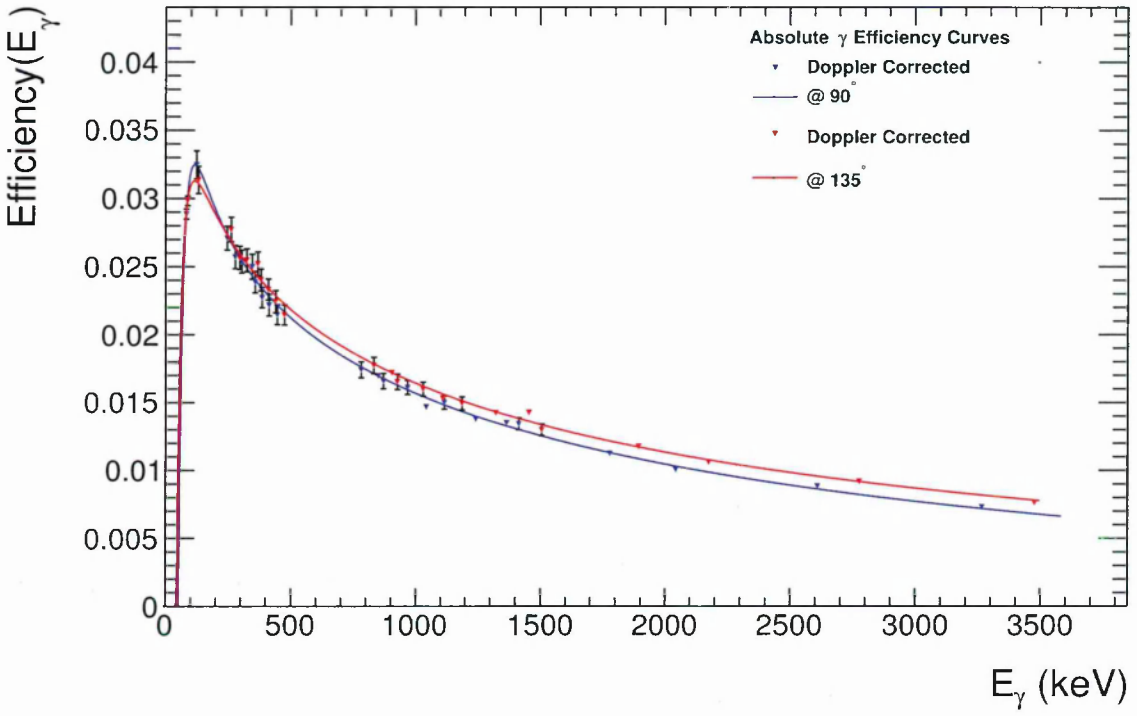

Figure 2.15: The final absolute efficiency curves for 90° and 135° TIGRESS clovers scaled to ^{56}Co gamma coincidence data points at 847 keV and 1238 keV.

2.7 Solid Angle Calculations of the SHARC Detector

The projection of an object's surface onto the unit sphere is called the solid angle Ω subtended by a surface A in units of steradian. This can be written as

$$\Omega = \int\int_A \frac{\vec{r}}{r^3}\hat{n}d\vec{A} = \int\int_{\vec{A}} sin\theta d\theta d\phi \tag{2.67}$$

,where $\vec{r}$ is the vector position of an infinitesimal surface $d\vec{A}$ with respect to the origin of unit sphere which covers the object, and $\hat{n}$ represents the unit vector normal to the $d\vec{A}$ area. Thus, the perfect coverage of the spherical system will give the full coverage

of 4π representing the entire sphere surface.

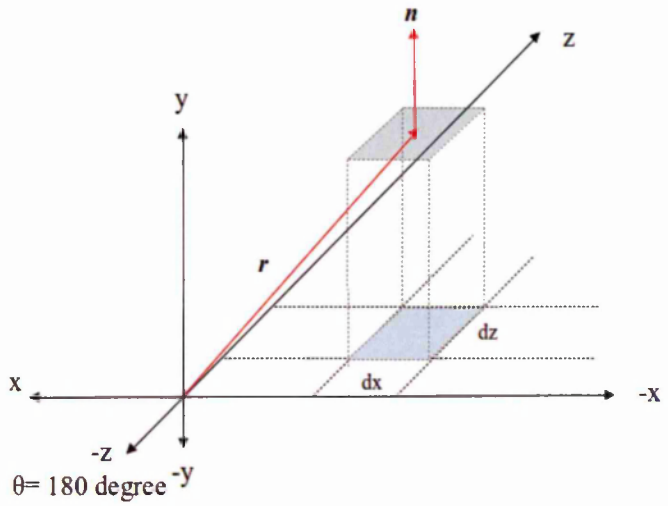

Figure 2.16: A schematic of the solid angle calculation of SHARC detector showing an individual virtual pixel using SHARC set up coordinates.

Using the schematic 2.16, the conversion of Cartesian and spherical coordinates can be written to calculate the solid angle of different parts of the SHARC detector facing different coordinates in terms of x, y, and z as below,

$$x = r\sin\theta\sin\phi \qquad y = r\sin\theta\sin\phi \qquad z = r\cos\theta$$

$$r = \sqrt{x^2+y^2+z^2} \qquad \theta = \arccos(\frac{z}{r}) \qquad \phi = \arccos(\frac{y}{x}) \quad (2.68)$$

Using this information with the equations 2.67 and 2.68, the infinitesimal area for a particular pixel as depicted in the figure 2.16 can be formulated as below.

$$d\vec{A} = dydz\hat{n} \quad if\ the\ detector\ facing\ toward\ x\ axis$$

$$d\vec{A} = dxdz\hat{n} \quad if\ the\ detector\ facing\ toward\ y\ axis$$

$$d\vec{A} = dxdy\hat{n} \quad if\ the\ detector\ facing\ toward\ z\ axis \tag{2.69}$$

And, the vector $\vec{r}$ will be $\vec{r} = x\vec{i} + y\vec{j} + z\vec{k}$ in terms of the unit vectors for the corresponding axis.

From the detail information taken from SHARC measurements as listed in the table 2.15, it's possible to write a $C++$ [38] code to visualize the results in ROOT [35].

Active Area Front Side	$71.9mm$	UDxoff	$42.4mm$
Active Area Back Side	$47.9mm$	UDyoffset	$42.4mm$
DD Exposed length	$79mm$	UDzoffset	$-4.675mm$
DD Wafer length	$76.2mm$	DDxoffset	$40.5mm$
UD Exposed length	$81mm$	DDyoffset	$40.5mm$
UD Wafer length	$76.3mm$	DDzoffset	$8.2mm$
Centre Difference on DD	$(79 - 76.2)/2\ mm$	CD inner radius	$9mm$
Centre Difference on UD	$(81 - 76.3)/2\ mm$	CD Ring pitch	$2mm$
Front Strip pitch	$3\mu m$	CD Ring space	$0.1mm$
Back Strip pitch	$1\mu m$	CD Ring width	$(2.0 - 0.1)\ mm$
CD Sector angle	$3.4°$	Radius of target	$5000\mu m$
CD offset	$-66mm$	Depth of target	$5.4/22.7\mu m$
Tolerance	$100\ keV$		
$mass_1$ (beam)	$24.989953968 * 931.494013\ MeV$		
$mass_2$ (target)	$2.01410177785 * 931.494013\ MeV$		
$mass_3$ (ejectile)	$1.00782503207 * 931.494013\ MeV$		
$mass_4$ (recoil)	$25.992633000 * 931.494013\ MeV$		
Kinetic Energy of the beam	$122.723\ MeV$		

Table 2.15: Detailed information about the SHARC detector in terms of fixed parameters used in the $C++$ code to compute the solid angle. See also the figures in the reference [39].

The depicted pictures of the upstream and downstream parts of the SHARC DSSSD array, and the CD annular detector in the figures 2.17, 2.18, and 2.19 may help to understand how the code can be written in $C++$. Some of the names used in the table 2.15 refer to the distances shown in figures 2.17 and 2.18.

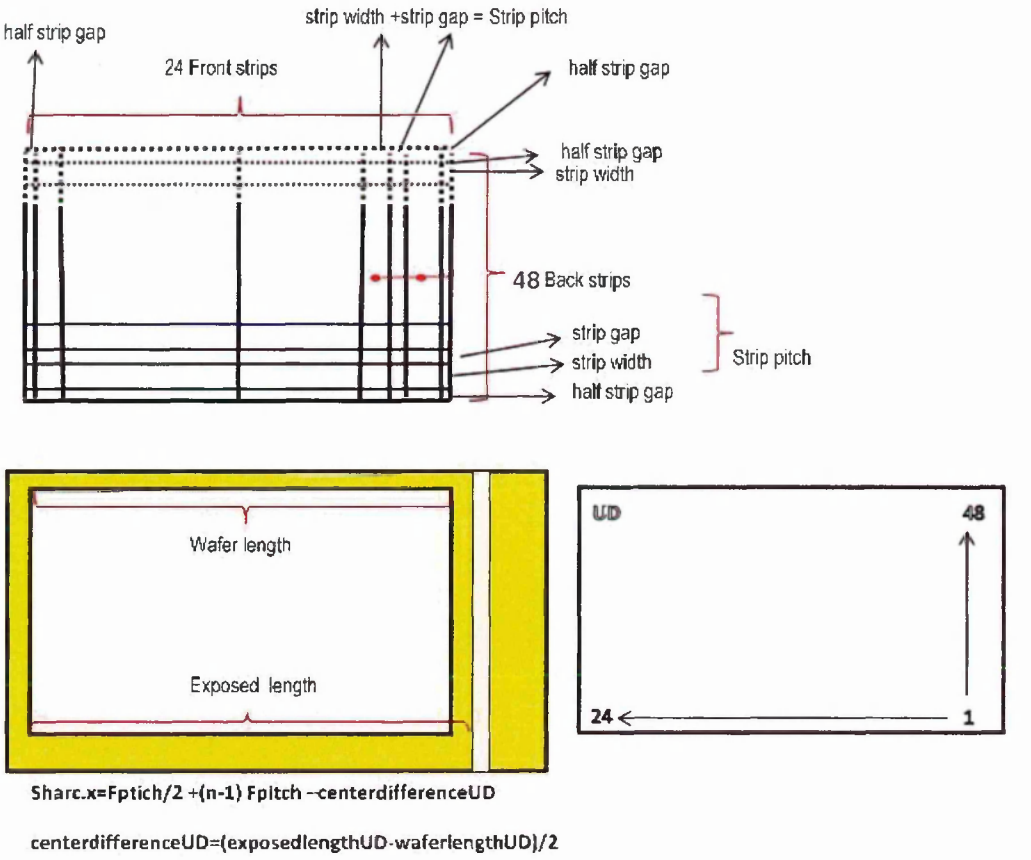

Figure 2.17: Upstream side of the DSSSD of the SHARC. (type BB11 [39])

In the figure 2.17, all the upstream DSSSD detectors have 24 front and 48 back strips with exactly the same strip order. The only thing changing in the compact SHARC configuration is the position of these individual DSSSD detectors, otherwise all the rest of the information stays the same. It can be noticed that everything should be always coded using the strip pitch instead of its constituents, strip gap and strip width. And, another important thing to keep in mind that there is always a half strip gap on both ends of the DSSSD detectors as marked on the picture below. The centre of the two adjacent strips

give the same length as for one strip pitch. As an example, it's also shown for those who may code the SHARC set up in the future that the x distance where any particle hits on the detector can be calculated using "Sharc.x" term in the figure 2.17 as the exposed length and wafer length of the DSSSD detectors can be easily found.

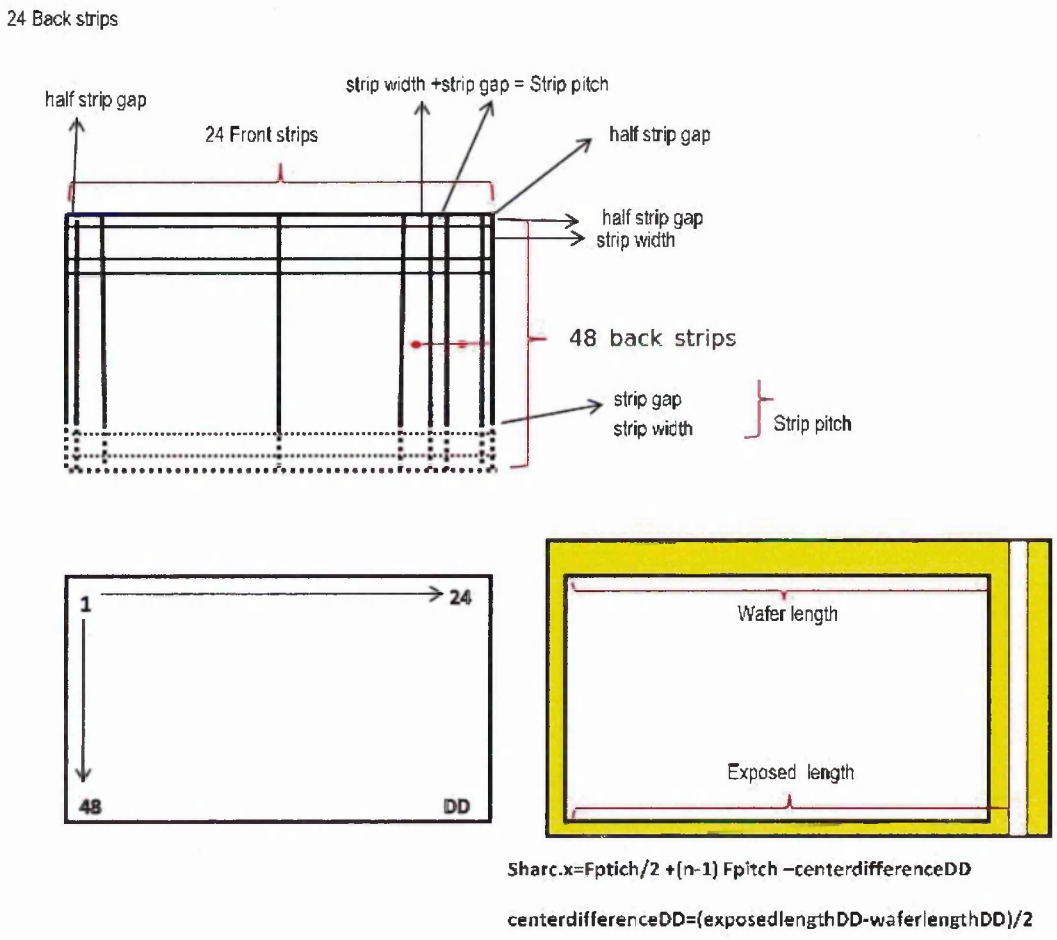

Figure 2.18: Downstream side of the DSSSD of the SHARC (type BB11 [39])

The only difference for the downstream detectors is the direction of the order for strip numbering, otherwise the same procedure can be followed as described for the upstream detectors.

In contrast to upstream and downstream DSSSD detectors, the annular upstream

CD detector has 24 sectors to slice each quartet of the circle and 16 rings to give the different θ positions on the detector for any detected particles. Each sector angle on CD has 3.4° coverage. Due to the 2° offset before any strip starts in each quartet on CD, there is always 6.4° gap on the another end of the each quartet since the entire coverage of each quartet is 81.6° as shown on the figure 2.19.

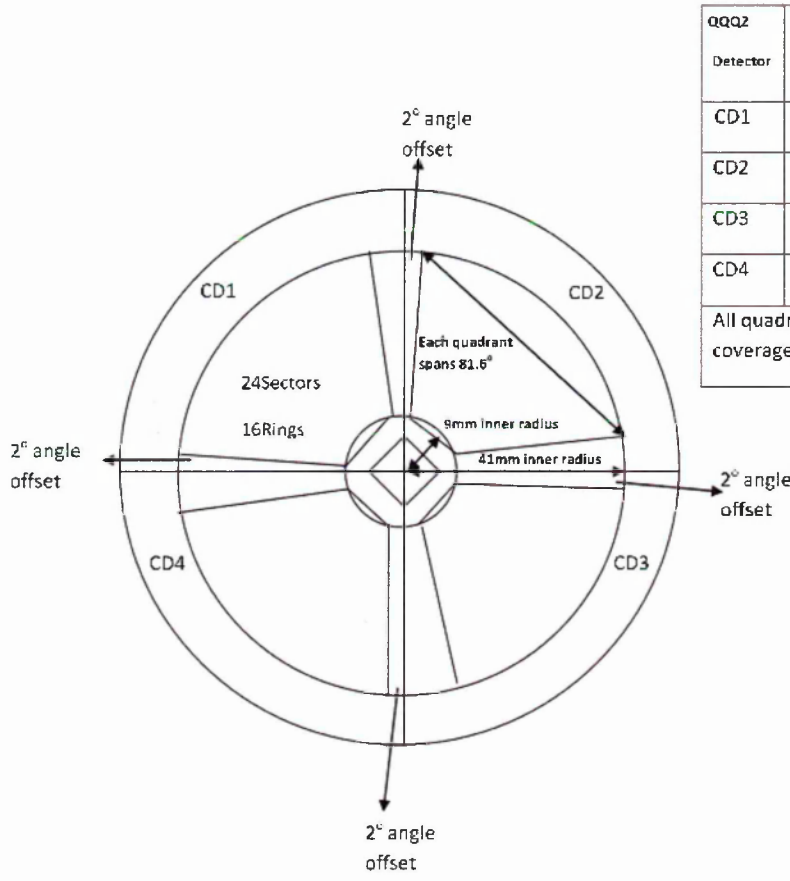

QQQ2 Detector	Lowest angle for strip border	Highest angle for strip border
CD1	90*0+2	90*1-6.4
CD2	90*0+2	90*2-6.4
CD3	90*0+2	90*3-6.4
CD4	90*0+2	90*4-6.4
All quadrants have 81.6° coverage		

Figure 2.19: The front face of the annular CD detector of the SHARC (type QQQ2 [39])

The code which is written to get the solid angle of SHARC array used Lorentz transformations to calculate the recoil and ejectile energies as an extra information. However, the only part that is used in the data analysis extracted from this code is where the Jaco-

bian converts the laboratory frame solid angle to centre of mass frame angle. Therefore, it will be presented here.

$$\begin{gathered} d\Omega_{LAB}=Fpitch\times Bpitch\times\frac{y}{r^3} \\ Jacobian=\frac{d\Omega_{LAB}}{d\Omega_{CM}} \\ Jacobian=\gamma\times p4_{CM}\times(p4_{LAB}-(\beta\times E_{ejectile}\times cos(\theta_{lab})))/(p4_{LAB}\times p4_{LAB}) \\ d\Omega_{CM}=\frac{d\Omega_{LAB}}{Jacobian} \end{gathered} \tag{2.70}$$

where the terms of Fpitch and Bpitch refer to the strip pitch, which is the sum of the strip gap and the strip width, in the front and back side of the DSSSD detectors as shown in the figures 2.17 and 2.18. The distances of y and r are used to indicate the coordinate of a chosen pixel as one of the examples can be seen in the figure 2.16. while the term $p4_{LAB}$ indicates the momentum of the ejectile proton, the term $E_{ejectile}$ refers to the energy of the ejectile proton as in the experiment. The key point here is the Jacobian can be adapted depending on whichever outgoing particle is chosen. For instance, $p4_{LAB}$ is used for ejectile momentum here, but the equation can also be written in terms of recoil mass and energy. And, the equations in 2.70 is indeed for a pixel on UD_1 so-called upstream detector 1 in SHARC array as the figure 2.16 refers an example of a virtual pixel. Lastly, the β is equal $\frac{v}{c}$.

In conclusion, the solid angles in centre of mass and laboratory frame are retrieved by adjusting the strip lengths using division factor of 100, which is flexible to change if needed, to get the histograms as smooth as possible as shown in 2.20. The solid line function shows the full solid angle coverage $d\Omega = \sin\theta d\theta d\phi = (2\times\pi)\times\sin(\theta)\times(binning\times\pi/180)$. Note, that we had roughly 1 downstream, 4 upstream DSSSD detectors, and 1 upstream CD detector. Some of those had few broken strips on them, so those has to be removed. The missing strip numbers found for different parts of the SHARC array are noted as the front strip 13 and the back strips 12, 13, 14, and 15 in the only one fully strip downstream

DSSSD detector, front strip 17 and the back strip 25 in the upstream UD1 on the top part of the SHARC with regard to the beam direction, the back strips 1, 2, 3, and 4 in the UD2 upstream detector on the right side of the SHARC with regard to the beam direction, only the back strip 32 of the UD3 which is the bottom side of the upstream box in SHARC array, and finally the front strip 6, 7, 11, and 12 of the UD4 detector of the SHARC array. The solid angle of these strips are set to zero while filling the histograms as shown in the figure 2.20. Therefore, they already include the effect of those missing strips in the histograms.

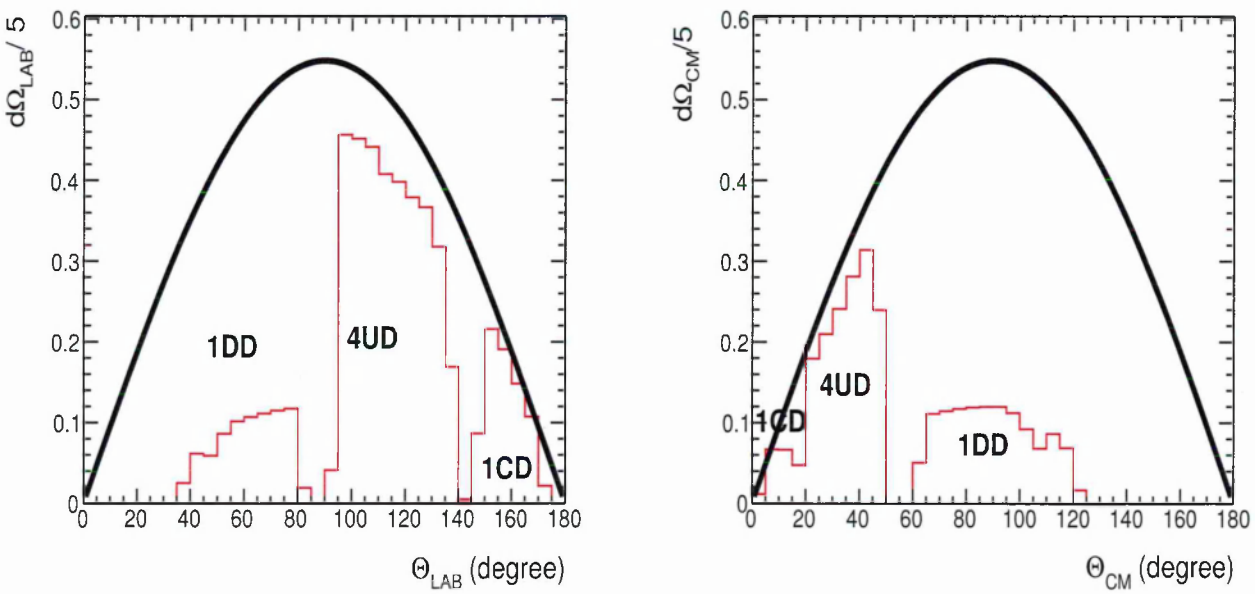

Figure 2.20: Solid angle of the SHARC detector in both frames calculated by $^{25}Na(d,p)^{26}Na$ transfer reaction for the state at 232 keV.

2.8 Populated State Energy Correction due to the Recoil Nucleus of ^{26}Na in the $^{25}Na(d,p)^{26}Na^{\star}$ Reaction

Let's consider the heavy recoil nucleus of $^{26}Na^{\star}$ which is moving with the velocity typically 10 percent the speed of light in laboratory frame in the case of $^{25}Na(d,p)^{26}Na^{\star}$ reaction. Our recoil is on the move throughout the reaction, and it radiates gamma rays as we populate its excited states. The momentum which the emitted photon gives to a nucleus can change the direction of the nucleus for higher energies. However, it has negligible effect with low energy gamma rays. If we consider non-relativistic approach for a start, the effect can be formulated as below :

$$E_{initial} = E_{final} + E_{\gamma} + T_{recoil} \qquad 0 = \mathbf{p_{recoil}} + \mathbf{p}_{\gamma} \tag{2.71}$$

With the help of relativistic energy formula for a gamma ray, $E_{\gamma} = c.\mathbf{p}_{\gamma}$, the energy difference between the initial and final state can be written in terms of decaying gamma ray and the rest mass energy of the recoil. The values for $M_R.c^2$ of the recoil ^{26}Na is $25.992633 * 931.494013$ MeV which results in $2.42e+07$ keV.

$$E_{initial} = E_{final} + E_{\gamma} + T_{recoil} \qquad \Delta E = E_{\gamma} + \frac{E_{\gamma}^2}{2.M_R.c^2} \tag{2.72}$$

By using the formula 2.72 and the fixed value stated above for $M.c^2$ in keV, we can recalculate the real excitation energy shown as $E_{initial}$ by using detected γ-ray energies. However, as shown in 2.73, the effect on the moving recoil nucleus is too small to make any appreciable difference for γ-rays.

$$E_\gamma = M_R.c^2[-1 \pm \sqrt{1 + 2.\frac{\Delta E}{M_R.c^2}}] \qquad E_\gamma \cong \Delta E - \frac{\Delta E^2}{2.M_R.c^2} \qquad \Delta E \cong E_\gamma \quad (2.73)$$

2.8.1 The Recoil Energy Calculation

With regard to the excitation energy calculations, they are calculated from the detected proton energies in the SHARC array. The centre of the CD_2 target is regarded as the point where the reaction occurred. Then, the energy loss of the proton in the target, in the DSSSD detectors of the upstream, in the DSSSD detectors and PAD detectors of the downstream $\Delta E - E$ telescope, upstream annular CD detector, and the dead layers of all downstream, upstream, and CD detector were taken into consideration. The dead layers of the detectors are noted as 0.1 μm and 0.1 μm for the upstream and downstream DSSSD detectors, and 0.7 μm for the upstream CD detector. While the upstream and downstream DSSSD detectors have the Silicon thickness of 1000 μm and 140 μm, respectively, the CD detector and PAD detector have the Silicon thickness of 1000 μm and 1500 μm. The program called SRIM [40] is deployed to read the energy loss per unit distance μm for proton and deuteron separately depending on the reaction type (d,p) or (d,d) on the deuterated polyethylene (CD_2) target and Silicon detectors. In that way, those values were able to retrieve from the file to be used in the sort code for the calculation of the recoil energy. The input file was carrying the information as shown in the figure 2.21 in terms of the energy loss depending on the distance in both Silicon detectors and the target. The specific distance and the corresponding energy values were read from the graph in the code.

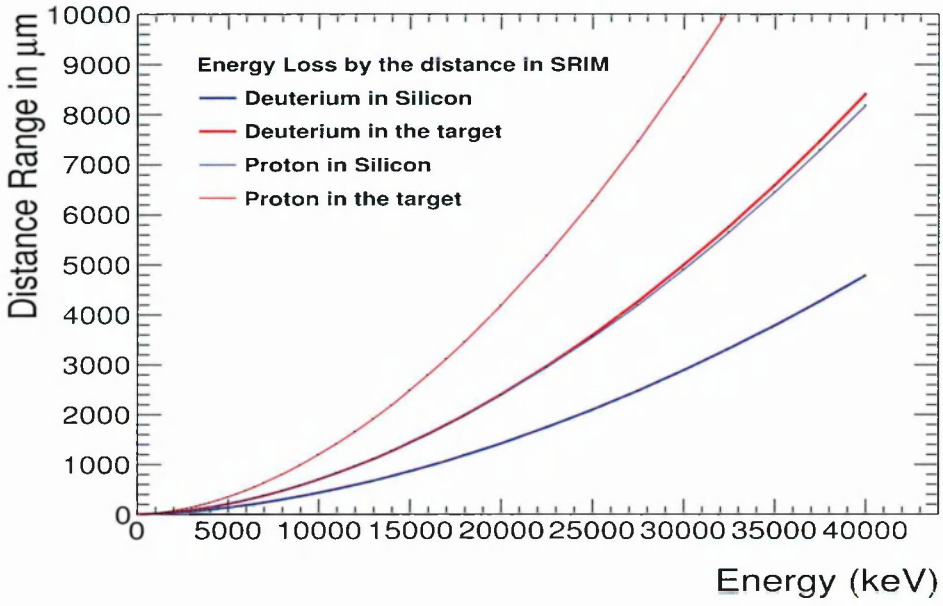

Figure 2.21: The distance and the energy loss relation in Silicon and the CD_2 target in the SHARC array is presented for the proton and deuteron as calculated in SRIM [40] to be able to calculate the recoil energy.

Let's say if the scattered proton hits the downstream detector and the PAD by losing all its energy in the detectors without punching through, then the total energy loss that the proton left in the target, downstream DSSSD, and the PAD detector gives the final energy of the proton that comes out of the (d,p) reaction. This energy will be indeed the kinetic energy of the proton which left the reaction when the interaction between the beam and the target happens. After adding the rest mass energy of the proton, the total energy of the proton will enable to calculate the recoil nucleus energy easily. This is indeed the excitation energies seen in all the figures.

Chapter 3

Analysis

3.1 Analysis for $^{25}Na^{*}$ and $^{26}Na^{*}$ above Neutron Separation Energy via Kinematic Lines

As mentioned before, the neutron separation energy, (S_n), for ^{26}Na is 5.574 MeV. Above this excitation energy, it is possible to populate states via (d,p) that then decay via neutron emission to states in ^{25}Na. At sufficiently high energies, these may be excited states in $^{25}Na^{*}$ and γ-rays corresponding to decays in $^{25}Na^{*}$ will be seen. However, if the reaction was not (d,p), then the assumptions used to calculate the excitation energy from the angle and energy of the detected particle will not be valid. For example, it turns out that inelastic scattering (d, d') will appear as though it is populating high excitation energies via (d,p) reaction. Thus, one needs to investigate whether $^{25}Na^{\star}$ is populated via the reaction of $^{25}Na(d,p)^{26}Na^{\star}(^{1}n)^{25}Na^{\star}$ or $^{25}Na(d,d')^{25}Na^{\star}$. For that reason, the sort code was run for the (d,d) reaction to check if there is any (d,d) elastic scattering and (d, d') inelastic scattering. The energy loss calculations are done in the program called SRIM [40] to extract the input file for our sort code. While the deuterated polyethylene

(CD_2) is used as a target, the Silicon is used as the detector material. The output data from SRIM [40] was in the steps of 100 keV from 100 keV up to 40 MeV in terms of energy loss per thickness in μm.

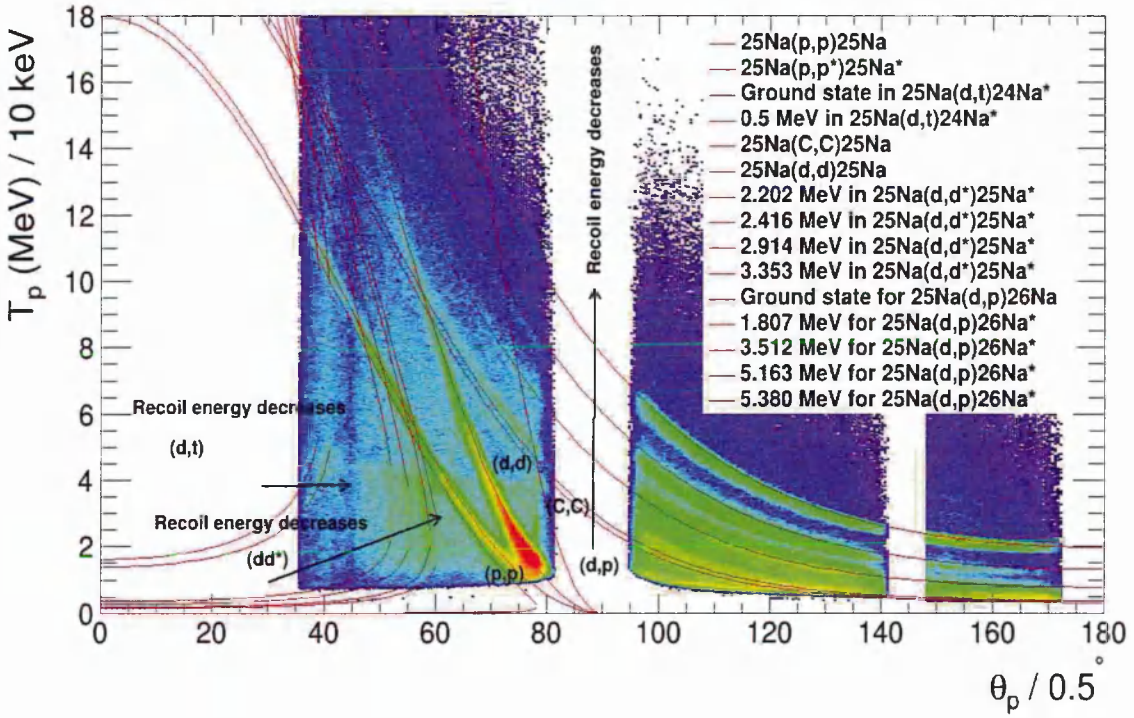

Figure 3.1: Kinematic lines for the identification of the possible reaction types which might be encountered in the experiment with ^{25}Na radioactive beam on a CD_2 target. The behaviour of the different kinematic lines are shown with texts on the figure where the arrows are pointing the direction where recoil energies decrease for a specific type of the reaction. This plot is produced from the (d,p) data. The angle θ_p is in the laboratory frame.

The figure 3.1 shows that other reaction types can also happen in the experiment. The gaps in SHARC coverage between the downstream box and the upstream box and between upstream box and the upstream CD detector are apparent in the figure 3.1. This gives a clear idea about priority of the SHARC parts in the set-up in terms of the reaction

of interest. The angle θ is defined by the direct of the beam and by the back strip number of each DSSD detectors in SHARC. It's now clear why the θ angle is important for proton detection and why the back strips have 48 strips on them in comparison to half strip number on the front side which defines the ϕ angle.

One of the characteristic features of these kinematic lines above 90 degree in the figure 3.1 where we have only upstream detectors and (d,p) reactions is the lowest level energy of detected proton is around 400 keV which defines the cut off in excitation energy of ^{26}Na nucleus around 6470 keV due to the spread in the resolution in figure 3.2. Also, note that it is found that the counts above 4.5 MeV in ^{26}Na becomes so low that this may affect the differential cross section of the protons which will be extracted from the proton angular distribution due to the cut off in the excitation energy in the figure 3.1.

In the figure 3.2, we can see clearly the cut off level for the highest excitation energy which can be reached on the Y axis. And, it is worth emphasizing again that this figure has the excitation energy as calculated, always assuming a (d,p) reaction. It will be shown later that the coincident γ-rays in ^{25}Na do not actually arise from (d,p) reaction, but this possibility first be investigated in more detail. Due to the resolution of the particle detector, these higher energies almost above 6 MeV will be spread on quite a wider range along the Y axis. Thus, one should better refer to the level scheme drawn in the figure 3.3 for the states in ^{25}Na. The 6 magenta data points in the figure 3.2 are for all the strongly seen gamma decays in the table 3.1 and 1 slightly weaker gamma decay via 2825 keV.

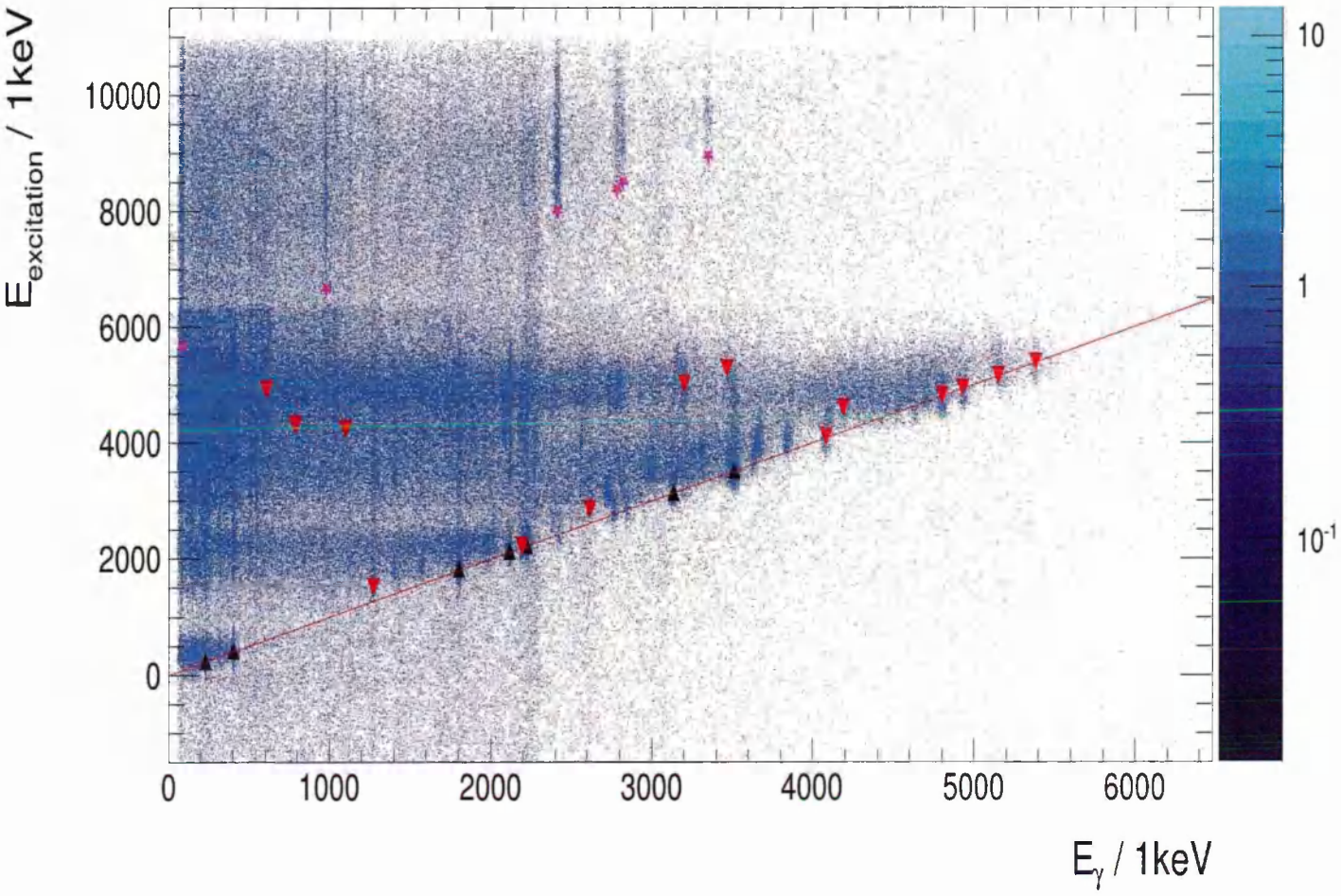

Figure 3.2: Only the black points here show the previously analysed data points for proton angular distributions in the work [1]. However, all the data points including black data points seen in this figure are either revised to update or analysed only in current work. The magenta data points are analysed for the investigation of the possible states in $^{25}Na(d,d)^{25}Na$ where they appear above neutron separation energy from the states of ^{26}Na in $^{25}Na(d,p)^{26}Na$. These magenta data points are shown in level scheme 3.3 on the right side near the energy levels as well. The excitation energies here are calculated assuming that this was (d,p) reaction.

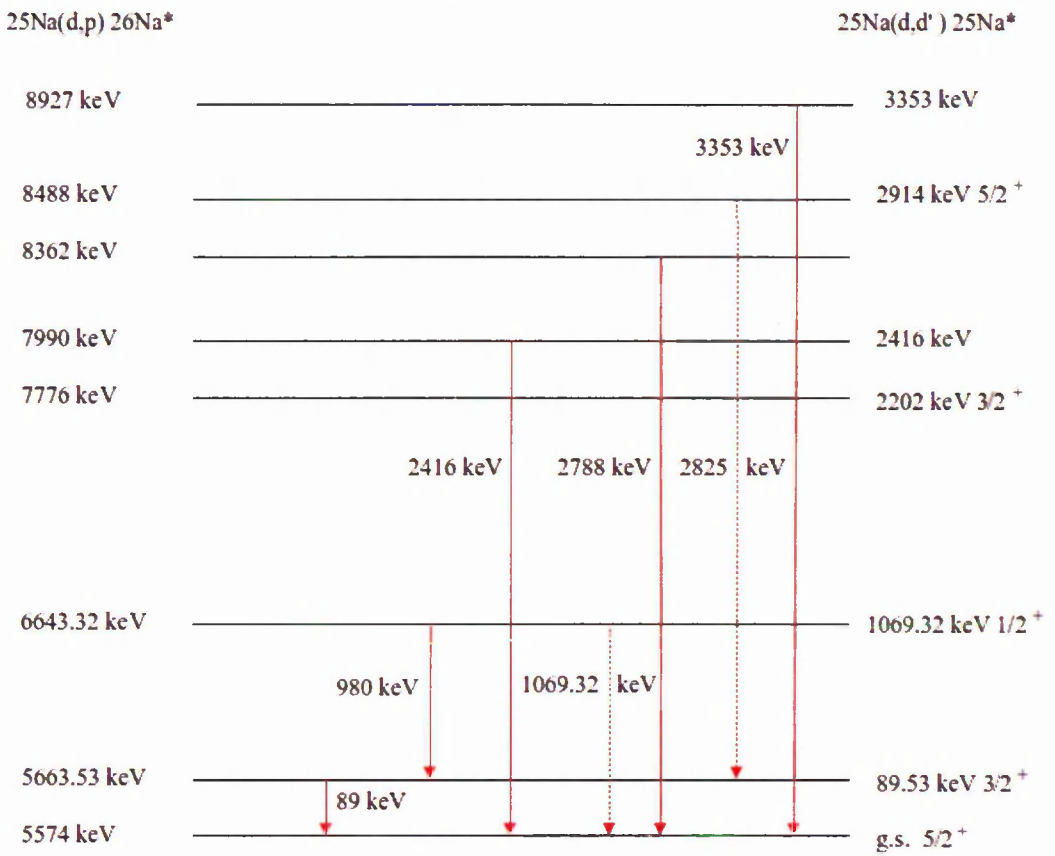

Figure 3.3: Gamma Ray Level Scheme of ^{25}Na with the information provided in [41] in comparison to the state energies for ^{26}Na above the neutron emission threshold at 5.574 MeV at which the indicated transitions would become energetically possible.

In the figure 3.3, the γ-ray and excited state energy levels according to previous findings in $^{25}Na(\beta^-\ decay)$, $^{23}Na(t,\gamma p)26Mg(t,\alpha\gamma)$, $^{26}Mg(d,^3He)$, $(polarized\ \ d,^3He$ reactions [41] are written on the right side of the figure shown under the reaction of $^{25}Na(d,d')^{25}Na^*$. However, the energy levels corresponding to ^{26}Na on the left side is written for a comparison after adding these original levels in ^{25}Na on the top of the neutron separation energy of ^{26}Na. As explained before, there are several possibilities to populate ^{25}Na in our experiment. Firstly, it can be populated through the inelastic scattering of (d,p) via neutron emission. Secondly, elastic scattering of (d,d) may populate the nucleus.

Otherwise, inelastic scattering of (d, d') serves another option.

If one scans the gamma spectrum for all the possible γ-rays that might appear above the neutron emission threshold, the γ-rays listed in table 3.1 in terms of their strength can be seen in the gamma spectrum. Only the strongest example will be shown in the following part which is analysed by the help of kinetic energy plots gated on one of these strongly observed gamma energies, γ-ray energy spectra, and the excitation energy spectra gated on the γ-ray of interest.

Gamma Rays seen from transitions in $^{25}Na^*$ in our data	
Strongly seen γ-ray energies (keV)	Weakly seen γ-ray energies (keV)
89	1036
980	1069
2416	1126
2788	1205
3353	2202
	2825

Table 3.1: Gamma energies seen in the decays of states in ^{25}Na as shown in the figure 3.3.

One of the strongest γ-rays at 2416 keV will be presented as an illustration in the figure 3.4. This is a part of initial analysis before γ-rays in ^{26}Na are looked at.

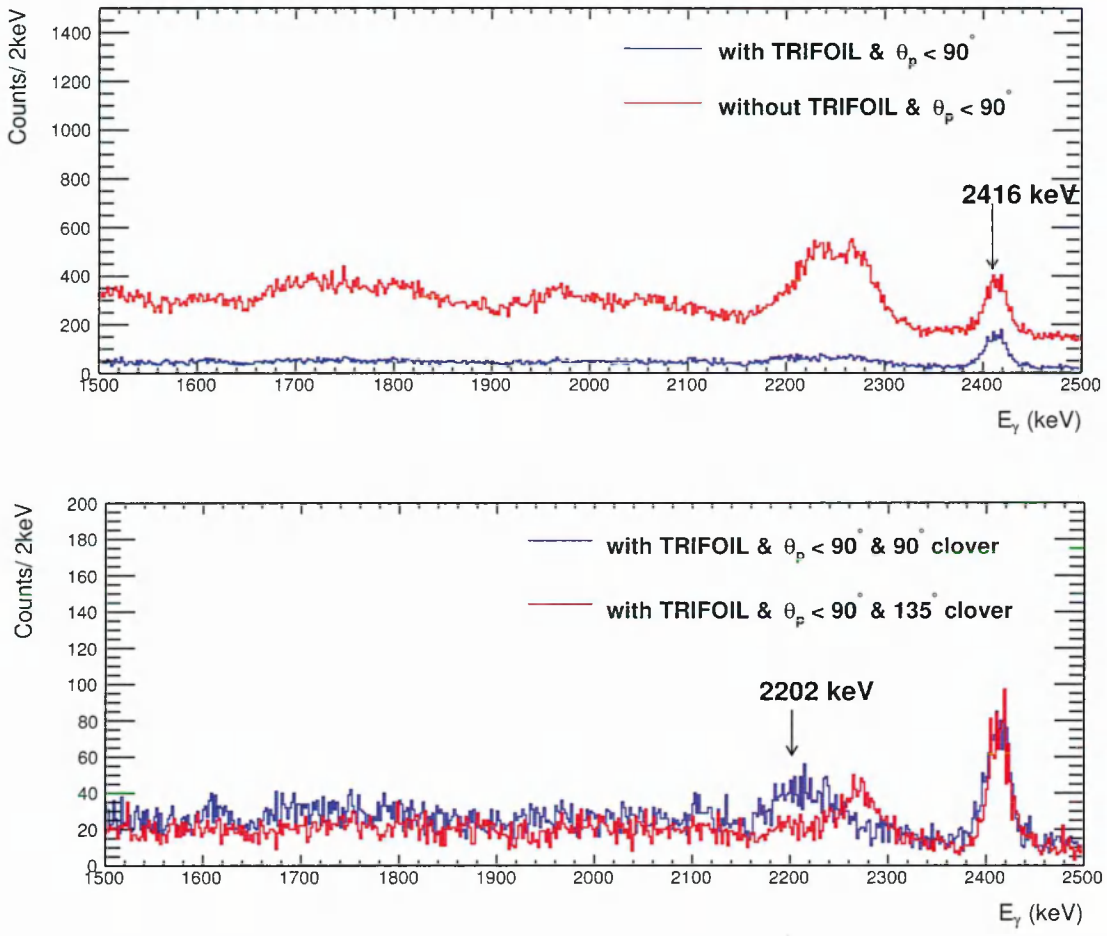

Figure 3.4: Gamma ray energy spectra above neutron separation energy (5.574 MeV) of ^{26}Na gated for 11 MeV $> E_{ex} >$ 5.574 MeV. The upper panel has only proton angle gate and TRIFOIL gate in addition to this excitation energy gate as shown, but the lower panel has TRIFOIL, proton angle, and a clover gate in addition to the same excitation energies.

In this figure 3.4, the count rise around 2202 keV appears probably due to a compound nuclear reaction since the shift in the lower spectra shows that the Doppler correction, done by using $\beta = 0.1\ c$, is not appropriate. However, the gamma peak at 2416 keV in the upper panel indicates a strong transition in ^{25}Na.

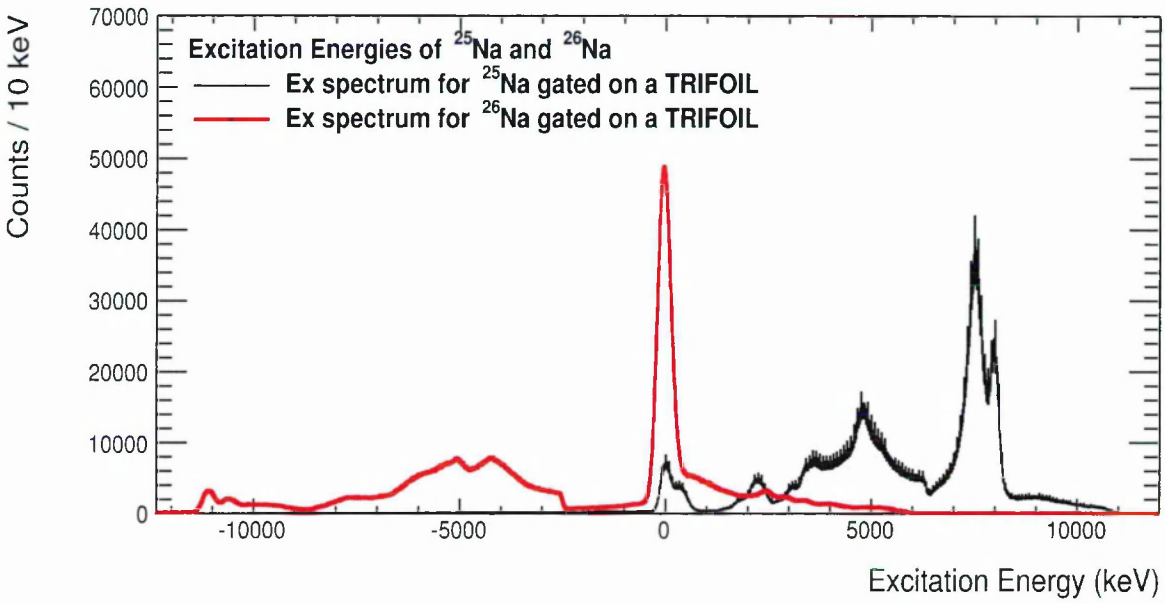

Figure 3.5: Excitation energy spectra of ^{26}Na and ^{25}Na with only TRIFOIL gate are presented here. The two spectra result from calculating the excitation energy for the same data but with two different assumptions for the reaction mechanism, which are (d,p) and (d,d) reactions.

When excitation energy spectra for ^{26}Na and ^{25}Na with the TRIFOIL gate are plotted as in figure 3.5, we clearly see that we populated ^{25}Na in (d,d) elastic scattering and inelastic scattering. The strong peak at 0 keV corresponds to the (d,d) elastic scattering in the figure 3.1. The focus will be on the right side of the 0 keV for the comparison of the γ-ray and excitation energies in (d,p) and (d,d) reactions.

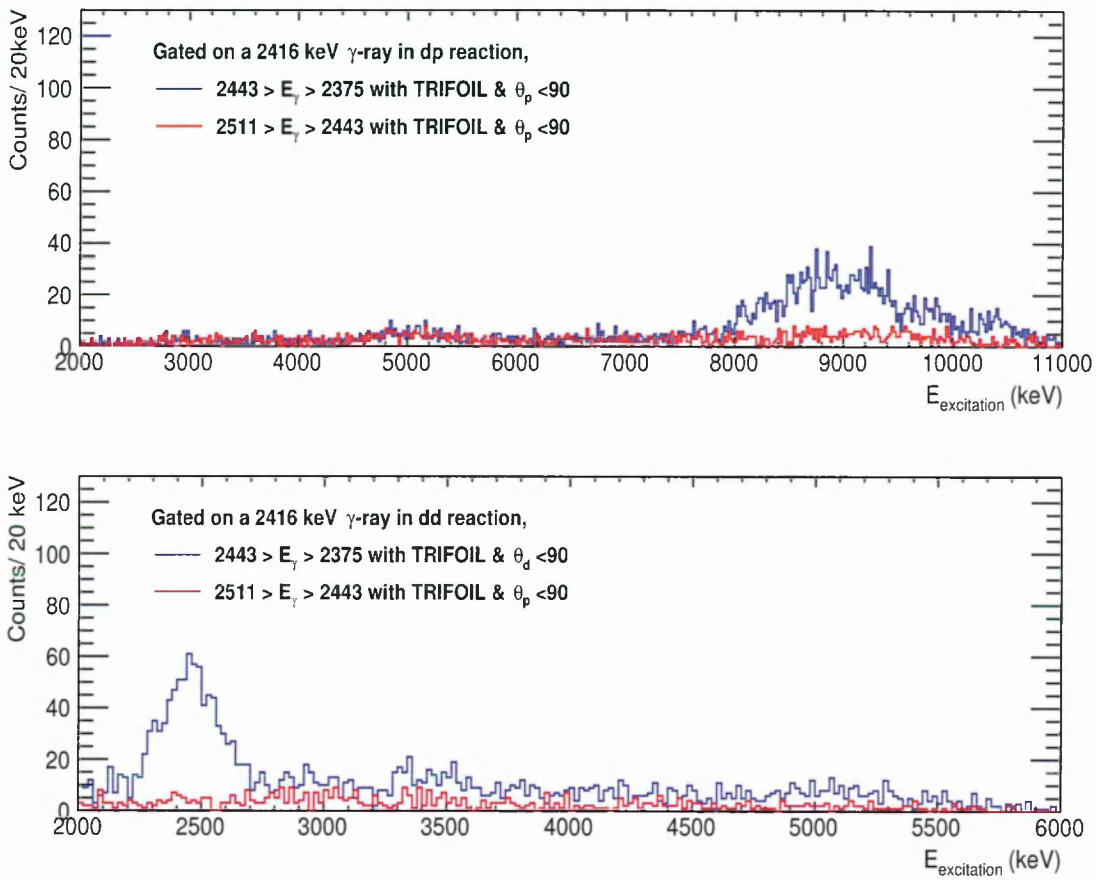

Figure 3.6: Excitation energy spectra of $^{25}Na^{\star}$ and $^{26}Na^{\star}$ gated on E_{γ} at 2416 keV with the energy limits of 2443 keV $> E_{\gamma} >$ 2375 keV.

The level scheme shown in the diagram 3.3 tells that the γ-ray energy at 2416 keV corresponds to both excitation energy at 2416 keV in ^{25}Na and excitation energy at 7990 keV in ^{26}Na above neutron separation energy. While the upper spectra do not reflect the energy as expected in ^{26}Na, the peak appears right where the related state is for ^{25}Na in the lower spectra, supporting the (d,d) origin.

During the analysis in ^{25}Na, the TIGRESS data is kept the same for both (d,p) and (d,d) since regardless of the reaction mechanism we always have the same gamma rays emitted. For that reason, we can say that TIGRESS doesn't know which reaction

happened in the experiment without any support from the particle energies and angles in the SHARC data.

All in all, the conclusion heavily stays on the side of (d, d') reaction instead of the (d,p) reaction. This can be further investigated by plotting kinematic lines of data and theory on top of each other, so we can have more satisfactory and supportive evidence for our claim. The following analysis part will focus on this perspective for ^{25}Na.

The figure 3.7 has 10 keV binning for the kinetic energy part and 0.5° binning for the θ angle. The kinematic lines of interest where the data is expected to match for (d,d) reactions are highlighted in bold black colour.

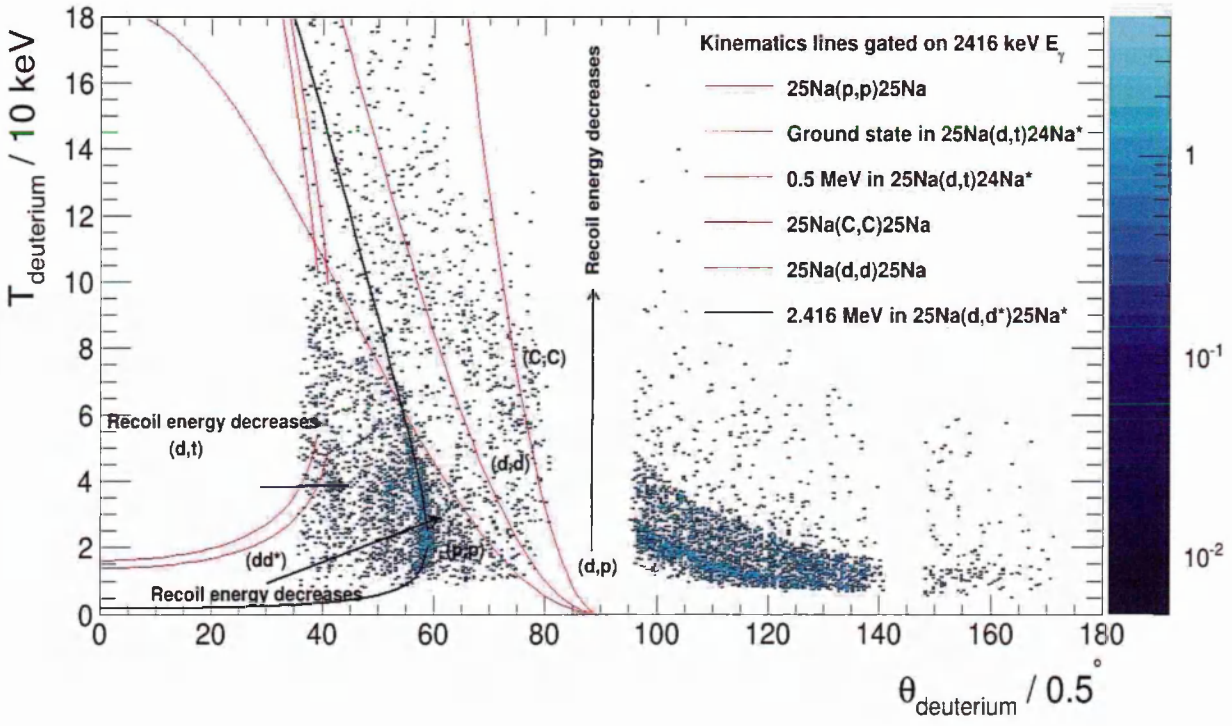

Figure 3.7: Kinematic energy data gated on E_γ at 2416 keV for 2416 keV populated state in $^{25}Na(d, d')^{25}Na^*$.

The figure 3.7 investigates the origin of the 2416 keV γ-ray associated with ^{25}Na.

There is a clear indication of the kinematic line corresponding to the population of the 2.416 MeV state in (d, d') reaction. Together with the γ-ray energy and excitation energy spectra discussed earlier, the origin of these γ-rays in (d, d') is convincing.

In summary, all of the γ-rays are checked for ^{25}Na. It's found that all can be accounted for the (d, d') inelastic scattering reaction, and there is no convincing evidence for the population via (d,p) of excited states in ^{26}Na that subsequently decay by neutron emission. For extra analysis, please refer to online appendix of this thesis [42].

3.2 Analysis of the Data Based on Excitation Energy versus γ-Ray Energy Plot

Before starting the analysis of the $^{25}Na(d, p\gamma)^{26}Na$ transfer reaction via one neutron transfer, two concepts with regard to state population should be known. These are direct and indirect population of the state by the reaction itself. Two example states to use for an explanation here, which have been found in the previous work [1] as seen in the level scheme 1.7, are presented in the figure 3.8 for clarity. For the first example, the populated state at 4304 keV is marked in the figure 3.8. Let's imagine that this state is populated by the (d,p) reaction itself. Then, it decays to ground state in two steps via γ_1 and γ_2. Through these steps, a new state at 2226 keV is populated, but this time the state is said to be indirectly populated in the (d,p) reaction. The initial state at 4304 keV instead will be named as directly populated state via the transfer reaction of interest. The definition becomes relative in the second case where it's marked again in the figure 3.8. Now, the lower lying state at 2226 keV might also be populated directly by the reaction itself not through the cascade from a higher lying state via γ_1. For a particular event, we may not even see the γ-ray in the previous 4304 keV state. Consider another state at 2194 keV

as in case 3, which has no link to the first two states whatsoever. If there is no feeding from a higher lying state as in this example, there is only one possibilty, and the state is populated directly by the reaction.

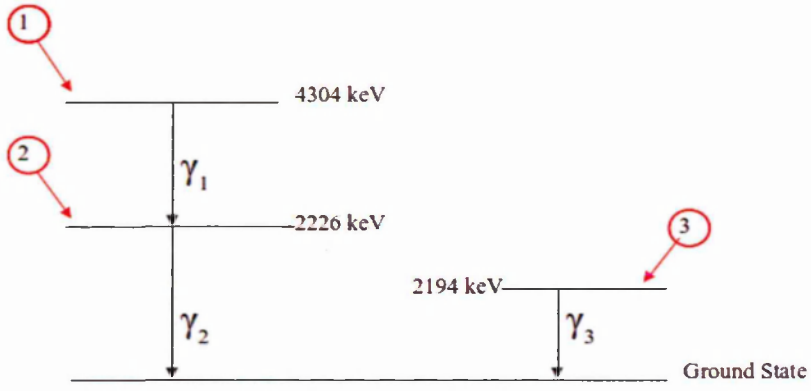

Figure 3.8: One part of the level scheme in the figure 1.7, which has been previously analysed in the reference [1], is used here to explain how one can populate the states either indirectly or directly via one neutron transfer in the highly selective $^{25}Na(d,p\gamma)^{26}Na^*$ transfer reaction. The precise energies of γ-rays and populated states in ^{26}Na are slightly revised in the current work. New values in terms of energies are thought to be more precise at this time.

Now, we can explain the concept direct and indirect population in detail with the help of the main analysis plot used throughout the thesis. In the figure 3.9, we see a plot of excitation energy versus γ-ray energy, where the excitation energies are calculated from the proton energy and an angle that eventually refers to the detector that was hit and the γ-ray energies are Doppler corrected. The states like 2.194 MeV and 2.226 MeV that decay to the ground state by emitting the γ-ray at the same energy as the state energy, appear right along the diagonal of the plot shown as the red line for clarity. As noticed, there are other states on this diagonal where excitation energy is equal to γ-ray energy. This means that one of the possible decays of those states is ground state decay. On the

other hand, our example state at 4.304 MeV does not show up on this diagonal for the reason just explained using the small level scheme in figure 3.8.

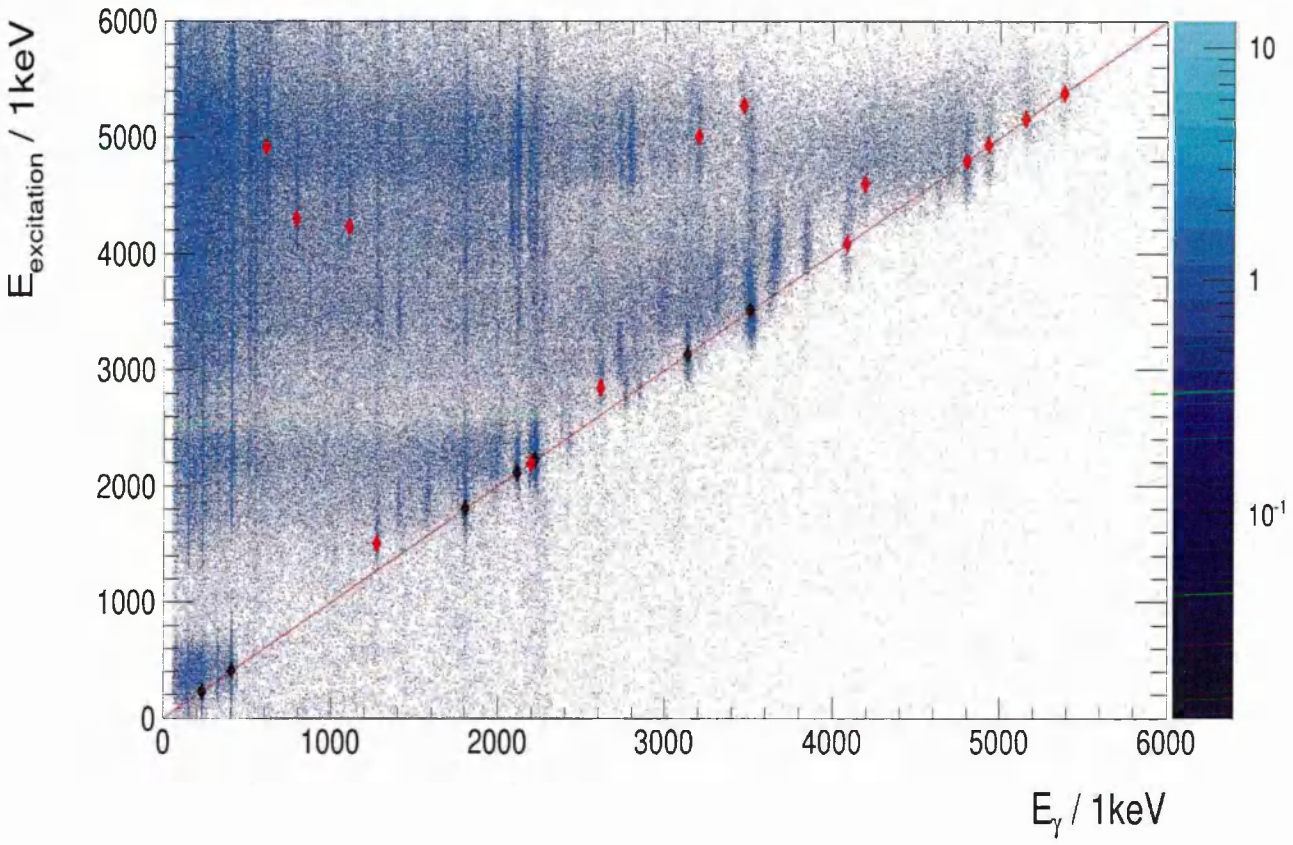

Figure 3.9: This two dimensional plot will be the basis of the thesis in the current work because it gives a broad perspective about where the excitation energies and γ-ray energies are and where the backgrounds for these states should be set as they will be discussed in section 3.6. The black points show states previously analysed by Wilson [1] for their proton differential cross sections; however, the red points are new states that are analysed only in the current work for the same purpose. These points show the states with their excitation energy and a particular γ-ray gate that is chosen to depopulate each state.

The way in which the 4.304 MeV state emerges is via its γ-ray cascade through

γ_1 and γ_2 in the figure 3.8. To decide about excitation energy, the Y axis of the two dimensional histogram should be checked. Because of the resolution of the SHARC array, the range of values recorded for a particular excitation energy will be spread over more than 100 keV in width. This is also a proof that why it is advantageous to use TIGRESS, an array of γ-ray detectors of a HPGe kind. The resolution on the X axis is quite sharp, thus enabling us to differentiate one state from another quite easily. The resolution varies from a few keV up to 65 keV for the highest energy gamma ray in the level scheme. The resolution of the detectors will be presented in more detail in later sections. After finding roughly the excitation energy location of the particular state, the other darker blobs along the same Y axis limits of the state should be searched for a possible decay γ-ray in a cascade in the style of γ_1 and γ_2 for 4.305 MeV state. Therefore, one can say that the state is somehow hidden in that fashion. Let's imagine the state at 2.194 MeV in case 3 above has just one γ_3-ray, namely the branch decaying to ground state. That means we shall not see any related γ rays along the X axis for the corresponding excitation energy limits of the state. One check that somebody can simply try is to add up γ energies of the blobs along the same path of excitation energy limits. If the total energy of the blobs summed up does not reach the state of interest, then it means they don't belong to this particular state. This arises because of the poorer resolution of the calculated excitation energy, which means that states can overlap. Otherwise, the blobs will reflect the gamma rays in the cascade. As in the previous discussion, a state can be reached either in a direct or indirect way. Then, this implies that it's possible to see γ-ray such as that marked as case 2 in figure 3.8 which may appear on the diagonal or above the diagonal in the cascade of a higher lying state.

As a result, all these explanation will be put into a practice in the following parts

by using the X and Y projections of figure 3.9. The X projection of the excitation energy versus γ-ray energy histogram will give the γ-ray energy spectrum for an energy gate that can be placed to select a particular state. In that way, one can scan through all the gamma peaks corresponding to this excitation energy gate. Keep in mind that not all the γ-rays seen will come from just the selected excitation energy due to the resolution of the detectors. Thus, there will be overlapping among adjacent states most of the time. On the hand, the Y projection of the same histogram will provide the excitation energy spectrum for a specific γ-ray gate, since the gamma detector resolution is enough to differentiate the states from each other as far as the resolution in γ-ray energy allows. Thus, it's safe to say most of the time that the excitation energy spectrum taken in that way will correspond to only one state populated via the transfer reaction.

The analysis has been carried out separately at 90° and 135° TIGRESS clovers in terms of their angles with regard to the beam direction. The reason why this analysis method is applied is for consistency in terms of efficiency of the γ-ray detectors since they behave differently in terms of Doppler correction and efficiency. Also, the background underneath the peaks can be different at the two angles. Thus, the data from the two sets of clovers are investigated side by side. The final results are averaged for proton angular distribution analysis, and the results for gamma-ray angular distributions are just plotted on the top of each other since they are in any case defined by the clover angle.

All the steps followed in the analysis of this two dimensional plot mentioned before can be summarized as listed below:

1-) The first step is to gate on either very specific or wider excitation energy range to see all the γ-rays emitted from this excitation energy range. This is done by plotting four different histograms as described below to discriminate if γ-rays come from either

radiated surrounding materials or the beam stopped at the detector, both of which act like the stationary source at the time. In addition to that, most likely the compound nucleus reaction can gives us γ-rays due to the decay of excited fusion evaporation product. The first two gamma spectra are plotted with and without a TRIFOIL gate for reaction mechanism comparison mainly between (d,p) transfer and compound nucleus reactions. As explained in the first chapter, the TRIFOIL detector is designed to give us the ability to eliminate the γ-rays from a compound nucleus reaction and retain those from a transfer reaction. In addition, another two spectra are created for 90° and 135° clovers in TIGRESS separately to see the Doppler shift effect on the γ-rays mostly not emitted by the transfer reaction. The stationary source case can be explained by the possible effect of the radioactive beam if a small fraction of the radioactive outgoing recoil is stopped near TIGRESS. This stationary radioactive source may give us β particle and then some γ-rays originally at one particular energy. However, they appear at different energies due to the different Doppler shift applied for these two clover angles. It's also important to note that the trigger requirement is SHARC detector in the experiment. Thus, we can only see these kind of Doppler shifted γ-rays in the data either when they are in random coincidence with a trigger from SHARC, or while the β particle deposited enough energy in SHARC to give the trigger. The 511 keV gamma ray is a typical example as discussed in the Doppler correction section when the γ-rays emerge at different energies in the histograms for 90° and 135° clovers. And also, sometimes the four sharp peaks in the gamma spectra, which are produced artificially by the Doppler correction, show up due to 4 different segment angles of each clovers.

2-) In the second step, one can gate on a specific γ-ray to see the origin of the state from which it arises. These excitation energy spectra where the specific γ-ray gate is

applied will aim to get the corresponding excitation energy limits. It's very elaborate job to choose the range of the γ-ray peak where one can see only the state of the origin, but not another state which belongs to the contribution from an adjacent overlapping γ peak. This is almost the case at all times. One should also be careful about the background subtraction to get both gamma and proton angular distributions since it's fairly difficult sometimes to choose which side is the best representative of background. In the later parts, a new method to encounter this problem wisely will be introduced.

3-) For the state which do not appear on the diagonal of the figure 3.9, the γ-γ matrix can be deployed to check if these γ-rays are correlated in a way that their sum can give the corresponding excitation energy. In that way, this might be an additional proof to declare the γ cascade in the discussions of declaring a new state.

4-) There is somehow a clever way of looking at the γ-ray spectrum and the $\gamma - \gamma$ coincidence spectrum to identify a particular state. If the state had an excitation energy of 4 MeV, the γ-ray spectrum for that particular state could have only be looked for the γ-rays below 4 MeV. This is indeed only the case where we do not expect any feeding from a higher lying state. However, it might turn into the case where we do see a higher γ-rays than 4 MeV. That means there should be another higher lying states to be searched above 4 MeV. Let's imagine that we did not see any higher γ-rays in the γ-ray spectrum. Then, we can check the $\gamma - \gamma$ coincidence spectrum to confirm this case because we should not see any γ-rays below 4 MeV when the γ-ray gate is higher than 4 MeV.

5-) Above the neutron separation energy of 5.574 MeV in $^{25}Na(d,p)^{26}Na^{*}(n)^{25}Na^{*}$ reaction, there is a possibility of getting excited $^{25}Na^{*}$ state from (d,p) in addition to (d,d') inelastic scattering case when treated as though they were (d,p) events. The (d,d') events are calculated to correspond to higher excitation energies. Thus, one should differentiate

these two reactions and their gamma rays from each other. One way is to put a proton angle gate smaller than 90 degree where we have mostly (d, d') reaction comparison to other inelastic scattering events; such as (d, t) and (d, p) in downstream detectors only. This can be seen later in the kinematic plots where ^{25}Na cases are explained.

Then, if we gate on wide excitation energy range that lies above the neutron separation energy, we can see all gamma rays coming from $^{25}Na^*$. However, we still don't know at this stage whether, or not they are coming from the (d, p) reaction following one neutron emission. Therefore, we use our angle gate and specific gamma ray gate to check the excitation energy spectrum to see the origin of the state where they come from. The γ-rays from $^{25}Na^*$ can be checked in the figure 3.3 for a comparison with the state energies in ^{26}Na. Another method to check if we have $^{25}Na^*$ is to plot T_d versus θ_d where kinetic energy and the angle of the scattered deuteron are calculated in the data by running the sort code for the specific reaction of (d,d) case. Therefore, it's mostly the (d,d) or (d, d') that are seen below 90° in the kinematic plots as in the figure 3.1. The result of both runs from entire data in terms of excitation energy for (d,p) and (d,d) can be clearly see in the figure 3.5.

6-) And lastly, we should keep in mind that there is always possibility of getting the same γ-ray in the level scheme coming from different states. This has low likelihood, but nothing in nature stops this from happening. The best way to notice them is to take all of the spectra produced by placing the excitation energy gates in 500 keV or 1 MeV steps and to assemble them on the top of each other to check the way in which the γ-ray spectrum changes. This is our best way throughout the analysis.

Typical observation from cascades gives us an idea to understand what type of characteristic features we expect to see in our data. In the following part of the discussion,

I'd like to focus on only the histogram in the figure 3.9, its X projection as in the figure 3.10, and its Y projection as shown in the figure 3.11.

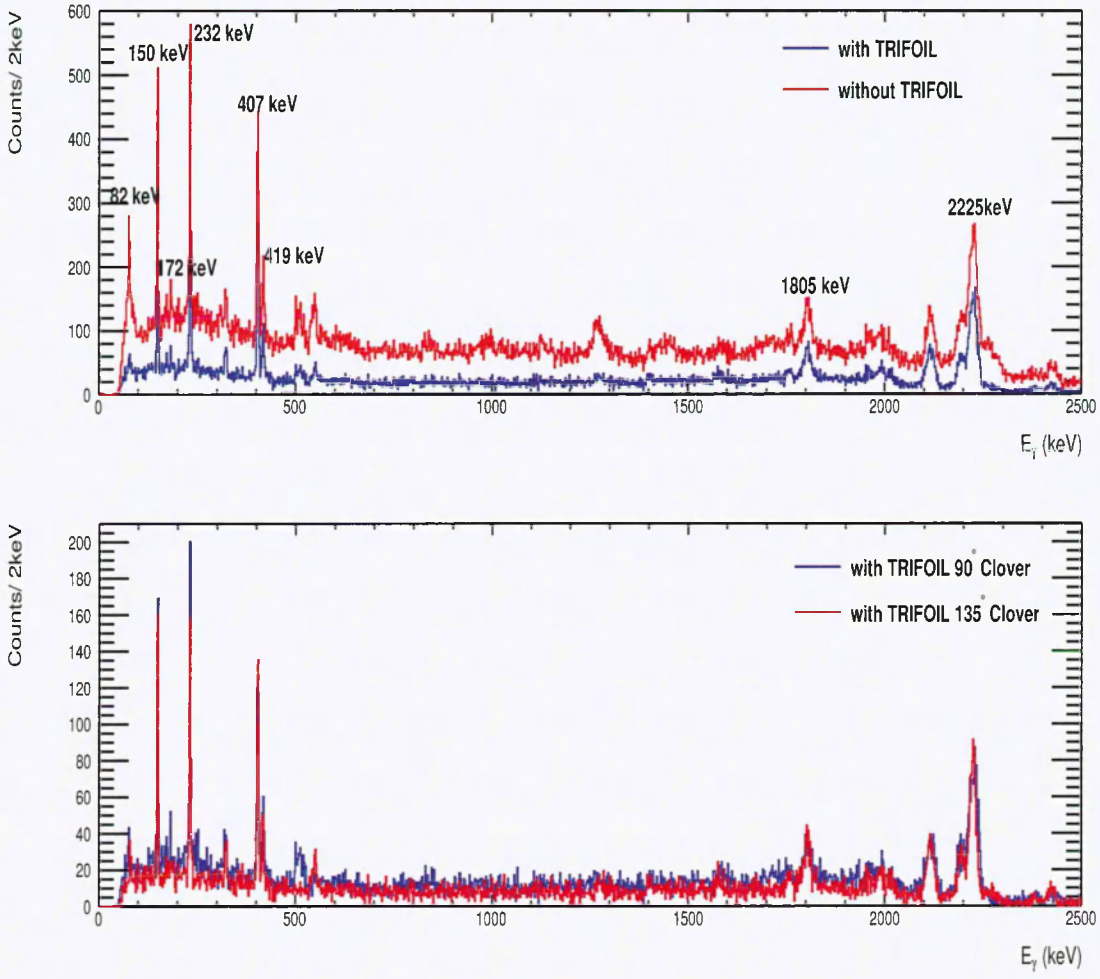

Figure 3.10: The upper panel shows the effect of the TRIFOIL gate for the state at 2225 keV with 2665 keV > Ex > 1952 keV. The lower panel is all with the TRIFOIL requirement that shows the effect of the clover angle change in TIGRESS as an illustration.

The upper spectra in the figure 3.10 are shown with and without TRIFOIL gate to emphasize the elimination of the γ-rays in the compound nucleus reaction from the reaction of interest as explained before. The working principle of the TRIFOIL, scintillator

detector, is explained in previous chapter 1.3. What it basically does is to play a selective role for the reaction products of transfer reaction to let them through to the beam dump. Thus, if the gamma peak only appears in the red spectrum without TRIFOIL, then it means it's most likely not the γ-ray peak of our interest. By the comparison of the two histograms in the upper part of this figure, one can immediately determine the gamma rays of interest as they appear in the blue TRIFOIL gated histogram.

In the lower part of the figure 3.10, the Doppler effect for the γ-rays due to radiated stationary sources can be observed at different energies due to the shift in energy. Note that these gamma rays are emitted originally with same energies before they arrive to different clover detectors in TIGRESS set-up. This sort of quick analysis helps us to identify which gamma rays genuinely arise from the reaction of interest.

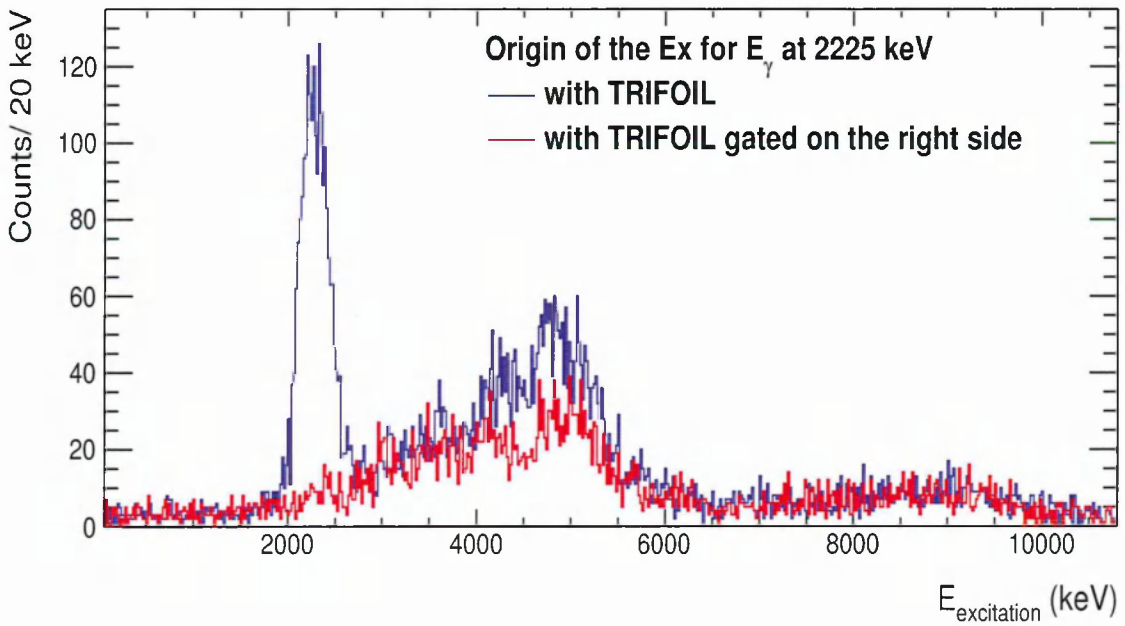

Figure 3.11: The excitation energy spectrum for the state at 2225 keV for the limits of 2250 keV $> E_\gamma >$ 2197 keV. The width of the adjacent gate is the same limits used for the γ-ray peak.

As said earlier, the Y projection of the figure in 3.9 will provide excitation energy spectrum for a particular gamma ray gate. By gating on a specific peak in γ-ray energy, the excitation energy at which this γ-ray originates can be determined. An example of excitation energy spectra is shown in the figure 3.11. Because the γ-ray peak is typically on the top of a background, it is necessary also to compare with the excitation energy spectrum deduced from the background. The first E_γ gate is for the original gamma peak; whereas, a second gamma gate is chosen for the background subtraction. When choosing either to the right or the left side of the γ peak as a background gate, the side is chosen where there is no adjacent peak nearby. This may not be possible all the time, but the aim is to avoid nearby peaks. What is seen differently in the two excitation energy histograms is the excitation energy peak disappears for the background gate. Thus, this makes it so obvious that this is the origin of the 2225 keV γ-ray in terms of excitation energy. The better method will be introduced as the analysis gets more complicated for the background subtraction. Thus, this is just the early stage of the analysis. The spectra of excitation energy shown here indicate that the 2225 keV γ-ray originate primarily from the direct population of the state at 2.225 MeV, but also can follow the population of the states close to 4.3 MeV and 4.9 MeV.

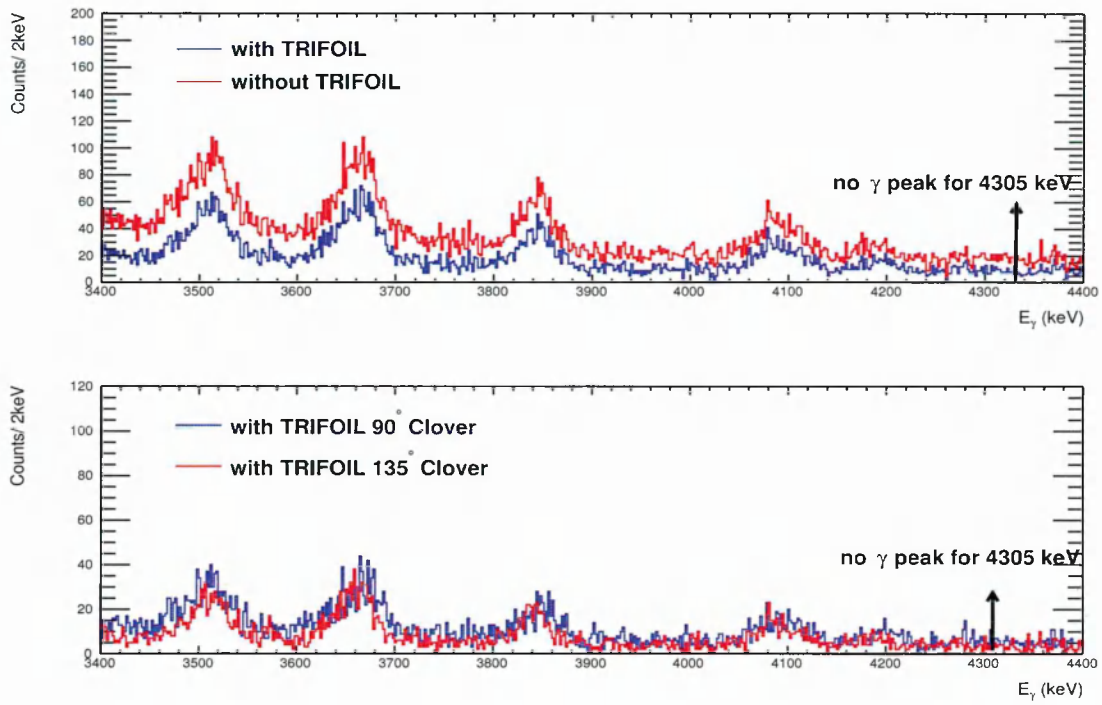

Figure 3.12: To illustrate how one can spot indirectly populated state as for the 4305 keV state for the gate 4761 keV $> Ex >$ 3800 keV.

In the example shown in figure 3.12, the main focus is to figure out if the state at 4305 keV has a ground state decaying branch, or not. If there is no γ-ray seen at 4305 keV to the ground state of ^{26}Na, one can then say this state decays via a gamma cascade. That is, at least two gamma rays are necessary to add up to give the energy of the state.

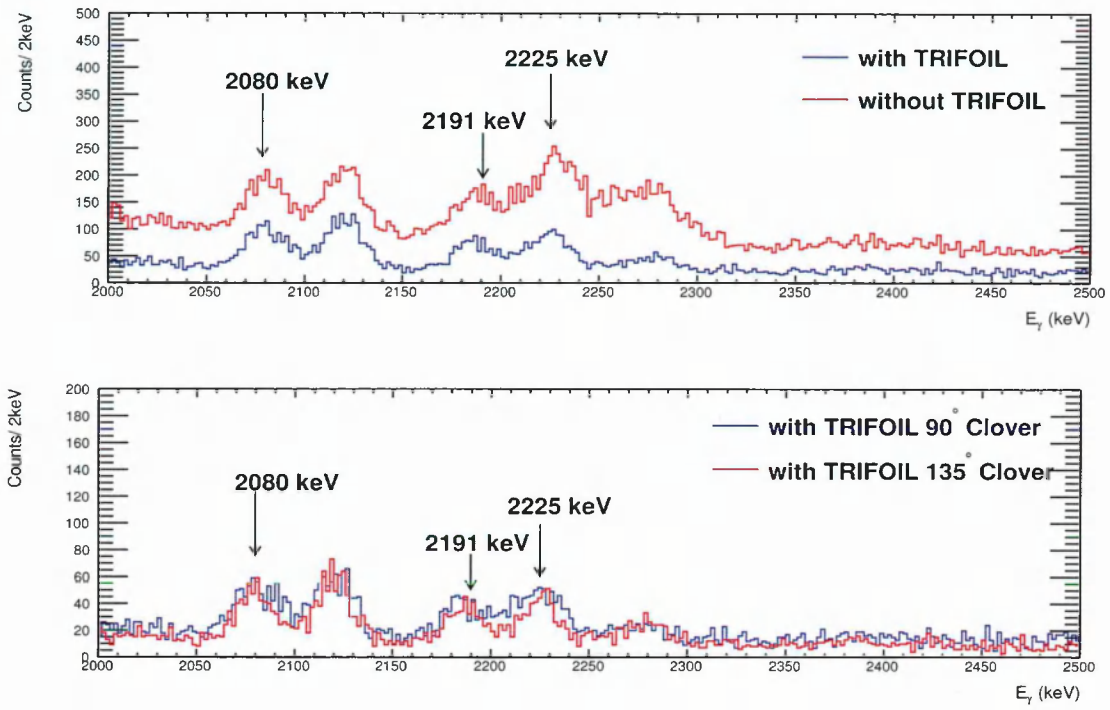

Figure 3.13: Two γ-ray branches in the 2 MeV range for the state at 4305 keV for the gate 4761 keV $> Ex >$ 3800 keV .

From the previous work [1], it's known that the 4.305 MeV state decays via a 2080 keV γ-ray to the 2.225 MeV state, and also it decays via a 2191 keV γ-ray to the 2.116 MeV state as the corresponding γ-rays are shown in the figure 3.13. These gamma energies are corrected in the current work since the analysis is done in more detail. The change of the energies in this particular case can be compared with the previous level scheme shown in the figure 1.7. However, the main focus here is to show how a decay through a γ-ray cascade can be deduced be adding lower gamma energies to the energies of lower lying states. The energy deduced for the state may slightly vary because of the path taken in the γ cascade due to small errors that may exist in the energy determination for individual γ-rays.

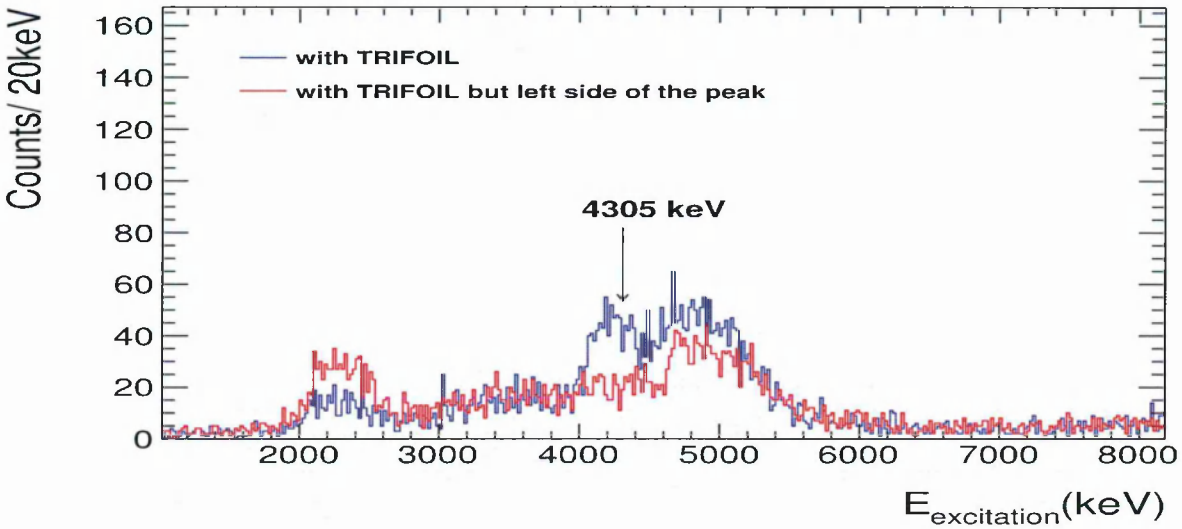

Figure 3.14: Excitation energy spectrum gated on 2080 keV γ-ray for the state at 4305 keV using the limits of 2096 keV $> E_\gamma >$ 2042 keV. The background gate clearly contains counts from a γ-ray associated with excitation energies near 2.2 MeV, but provides better background estimate in the higher excitation energy region.

By using the gamma branch information said earlier, the excitation energy spectrum of the state at 4305 keV via the γ-ray gate at 2080 keV is plotted in the figure 3.14. This stage of the analysis is very preliminary, so one should not expect solid statements about the energy of either the states or the γ-rays. Rather, this part of the analysis is used to quickly check the relationship between specific γ-rays and excitation energies.

Starting with the lines seen in the figure 3.15 as a representation of the earlier figure 3.9, the features associated with ground state and cascade decays can been seen as dashed and continuous lines. Continuous lines represent states decaying to the ground state; whereas, dashed lines are just their spread to indicate the resolution of the state at this energy. The extension as shown with dashed lines indicates that the γ-ray energy at that

level on the X axis may appear in the γ spectrum of the higher lying states as well. That means those higher lying states which appear higher up on the Y axis decay through these lower lying states in their γ cascades. As an example, I'll give one of the strongest states at 2226 keV in ^{26}Na as in the figure 3.15. The details of the possible decays from this state to other lower lying states are listed in the table 3.2.

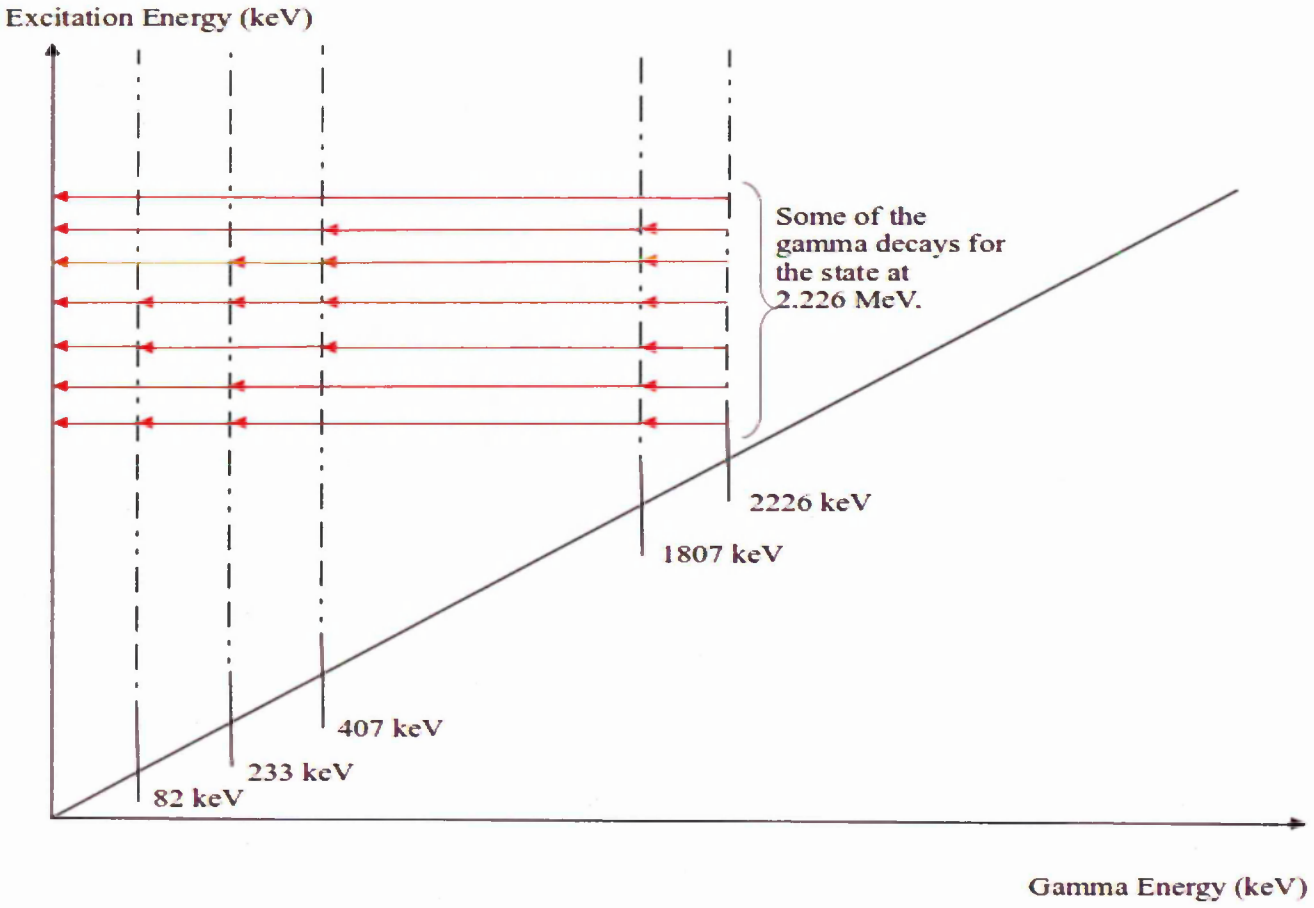

Figure 3.15: Some of the γ-ray decays of the 2.226 MeV state in $E_{excitation}$ vs E_γ plot based on the level scheme in the previous work [1].

Some of the different decay possibilities in the cascade of the state at 2226 keV										
Ex_1 (keV)	E_{γ_1} (keV)	Ex_2	E_{γ_2}	Ex_3	E_{γ_3}	Ex_4	E_{γ_4}	Ex_5	E_{γ_5}	Ground state
2226	2226	g.s								
2226	419	1807	1573	233	233	g.s				
2226	419	1807	1573	233	151	82	g.s			
2226	419	1807	1400	407	g.s					
2226	419	1807	1400	407	174	233	g.s			
2226	419	1807	1400	407	174	233	151	82	82	g.s

Table 3.2: These energy values in keV are shown as displayed in the level scheme 1.7 from the previous work [1].

This state, as shown in the table 3.2, has a ground state decay via 2226 keV gamma ray. Therefore, the data tells that this state should be on the diagonal of the figure 3.9, and then we use this information for the analysis. On the other hand, another example given previously for the state at 4304 keV is depicted as in the figure 3.16. The blue dashed line in the schematic shows the hidden location of the state at 4304 keV. Since the state has no decay directly to the ground state as in the table 3.3, it will not appear on the diagonal of the figure 3.9. This may be difficult to determine from the actual data because it may be that another close-lying state, which overlaps in terms of the excitation energy measurement, has a branch to the ground state.

Some of the different decay possibilities in the cascade of 4304 keV state				
Ex_1 (keV)	E_{γ_1} (keV)	Ex_2	E_{γ_2}	Ex_3
4304	794	3512	3512	g.s
4304	2078	2226	2225	g.s.
4304	2185	2119	2119	g.s.

Table 3.3: Part of the decays in the gamma cascade of the state at 4304 keV as declared in the work [1].

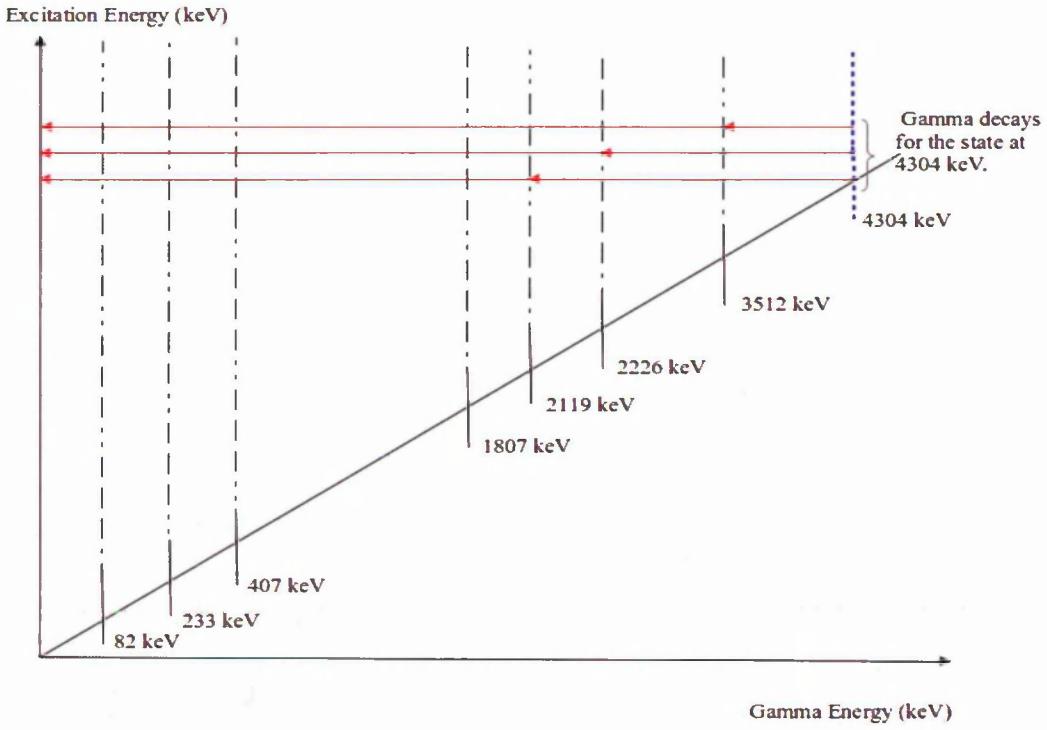

Figure 3.16: Some of the γ-ray decays of the 4.304 MeV state in $E_{excitation}$ vs E_{γ} plot based on the level scheme in the previous work [1]

In conclusion, the description above states how states populated indirectly via the (d,p) reaction appears above the diagonal on the main figure 3.9.

3.2.1 Analysis of the Populated States of $^{26}Na^{*}$ in the Transfer Reaction $^{25}Na(d,p\gamma)^{26}Na^{\star}$

With regard to the analysis in $^{26}Na^{*}$, the first thing is to check individual γ-peak limits and their adjacent regions for the best background subtraction. This is done by gating on a large excitation energy as seen on the Y axis of the figure 3.9. At this preliminary stage, there is no need to worry about different clover angles, so the clover angle gate doesn't need to be applied. A gate set about each individual peak will then help us to plot the

corresponding excitation energy spectrum for this γ-ray, telling us about the possible state energy. By knowing the excitation energy limits now, one can turn back and see what the gamma spectrum shows for this particular range instead of the initially used wider excitation energy range. These steps enable us to narrow the limits of the populated state energy and the number of γ-ray energies which may populate this individual state to search for. With the help of these two information, it is possible to find where the associated area for particular state is in the figure 3.9 as a third step in the analysis. Then, we can make sure that the position of a state in the figure 3.9 in terms of the limits of the γ-ray and excitation energy for a chosen state is correctly checked.

As a variant of this approach, we start with a series of 500 keV windows in excitation energy over the range 0 to 5.5 MeV. For clarity, we plot various slices from 1 MeV to 3 MeV range, and those from 3 MeV to 5.5 MeV separately. The highest excited state found in ^{26}Na in the current work is at 5.376 MeV, so the γ-ray spectrum range is chosen only up to 5.5 MeV. Each 500 keV section is zoomed in to see the γ-ray spectrum change and its characteristic behaviour for different excitation energy ranges. With the help of these comparisons, one can notice drastic appearance and disappearance of certain peaks in a certain excitation energy range.

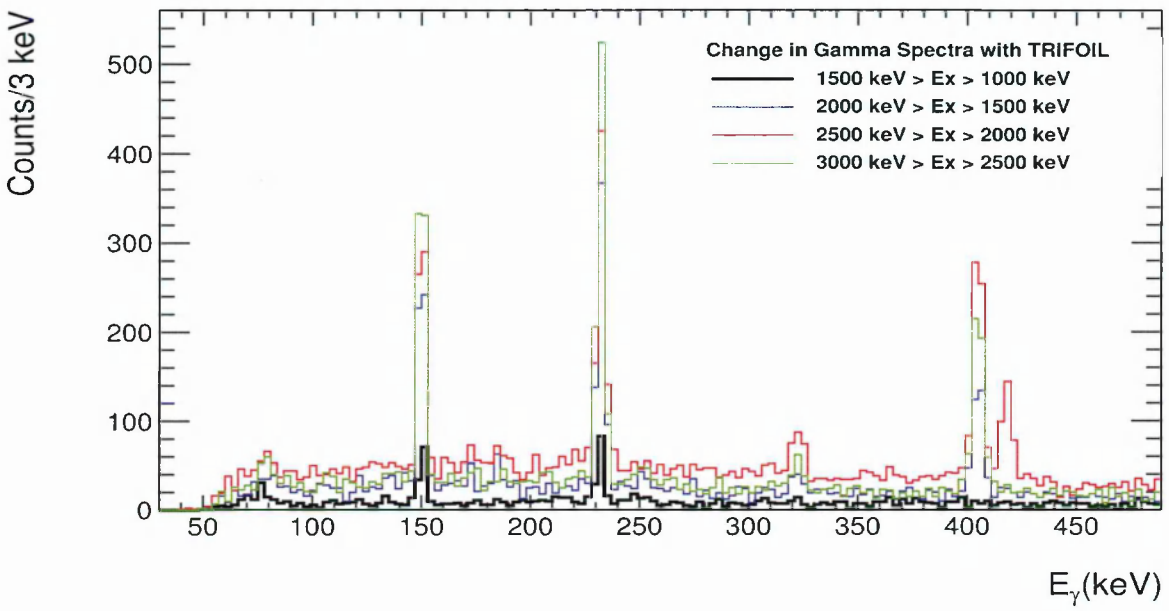

Figure 3.17: HPGe γ-ray spectra are shown when gated on different excitation energy ranges calculated by the highest energetic proton detected in the SHARC detector using 500 keV steps in excitation energy up to 3 MeV. The TRIFOIL gate is also applied as $E_{Trifoil} > 15000$ keV for all of them.

In the figure 3.17, the highlighted black line for excitation energy range between 1 MeV and 1.5 MeV shows clearly the disappearance of the 323 keV, 405 keV, and 418 keV gamma peaks. The gamma peak at 82 keV is almost negligible for all histograms. The drastic increase of the 150 keV, 232 keV, and 405 keV gamma peaks in the blue, red, and green spectra can also be distinguished. Despite this high increase in counts at 150, 232, and 405 keV, the slow increase in the counts of 323 keV γ peak is obvious. These count increases do not necessarily follow the energy order in increasing order. For instance, green, red, blue, black colour is the ordering from the highest counts to lowest counts at 151 and 233 keV. However, this order turns to red, green, blue, black colour for the 323 keV peak. This kind of characteristic behaviour can be seen in the analysis of

the following states as well. In spite of the disappearance of the gamma rays in the black histogram, another important thing to pinpoint here is the appearance of 418 keV γ peak only in the red histogram where the excitation energy limits are from 2 MeV to 2.5 MeV.

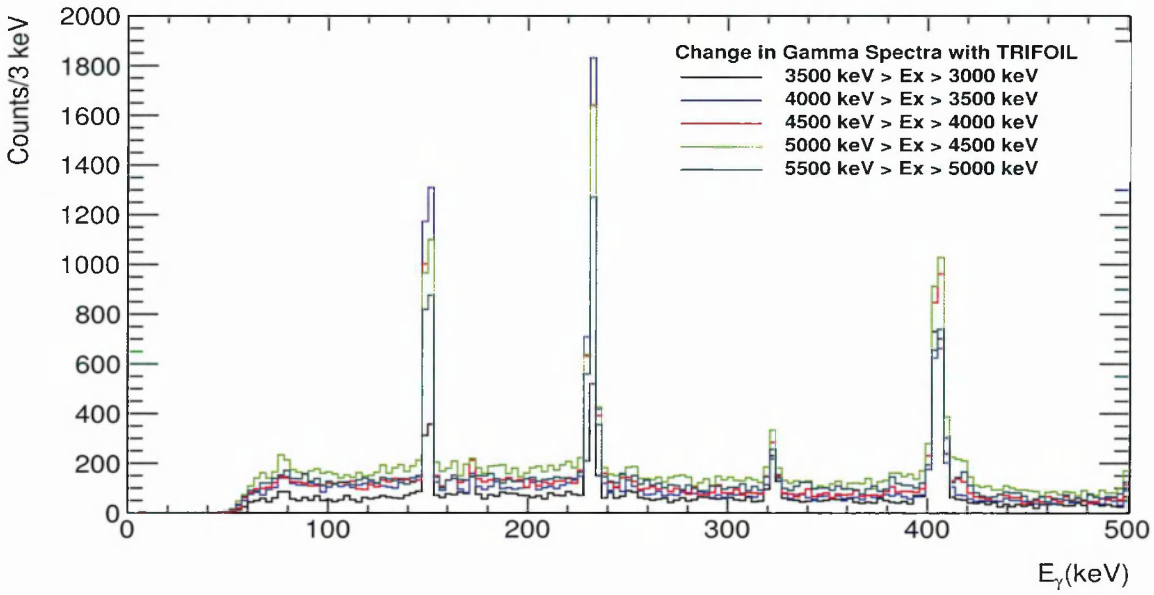

Figure 3.18: HPGe γ-ray spectra are shown when gated on different excitation energy ranges calculated by the highest energetic proton detected in the SHARC detector using 500 keV steps in excitation energy up between 3 MeV and 5.5 MeV. The TRIFOIL gate is also applied as $E_{Trifoil} >$ 15000 keV for all of them.

As we go higher in excitation energy range in the figure 3.18, the total counts under the peaks are almost increasing three times more in comparison to the counts in the figure 3.17. The peak at 323 keV becomes noticeable, but the 82 keV peak is still negligible. We can also say that the 418 keV peak disappears in higher excitation energies after almost 2.5 MeV. One can also interpret the reason of increase in γ counts as being due to the feeding from higher lying states to those lower lying states at 82, 232, and 405 keV.

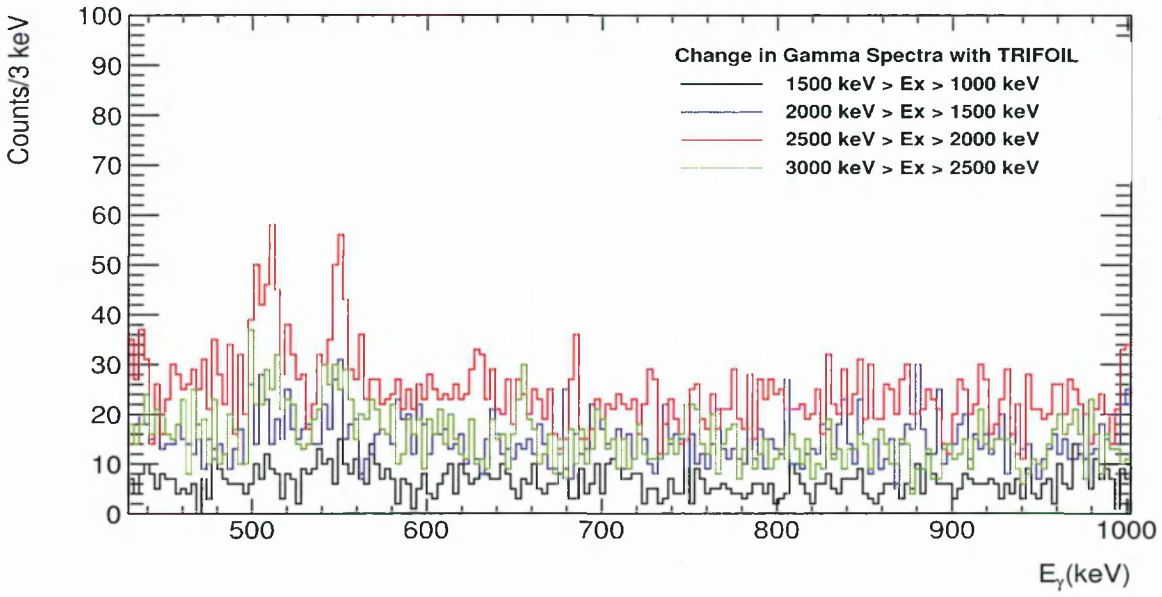

Figure 3.19: HPGe γ-ray spectra are shown when gated on different excitation energy ranges calculated by the highest energetic proton detected in the SHARC detector using 500 keV steps in excitation energy up between 1 MeV and 3 MeV. The TRIFOIL gate is also applied as $E_{Trifoil} >$ 15000 keV for all of them.

In the gamma spectrum range from 430 keV to 1000 keV, there is only the 511 keV annihilation radiation strongly evident for the excitation energy slices up to 3 MeV as seen in the figure 3.19. However, in next figure 3.20 for higher excitation energies, 612 keV γ-ray peak appears for the first time only from 4.5 to 5.5 MeV excitation energy range. Another very crucial γ-ray is at 790 keV which is only identifiable between 4 MeV and 5.5 MeV excitation energies. There is an unidentified 866 keV γ-ray as well in the excitation energy range from 3.5 MeV to 4 MeV.

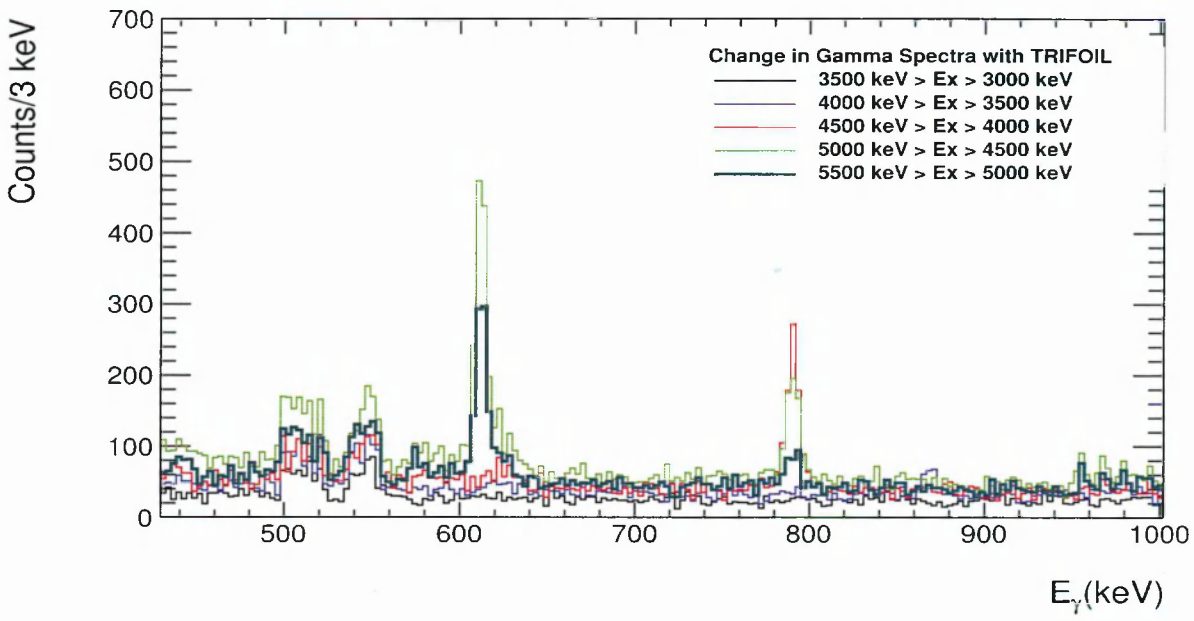

Figure 3.20: HPGe γ-ray spectra are shown when gated on different excitation energy ranges calculated by the highest energetic proton detected in the SHARC detector using 500 keV steps in excitation energy between 3 MeV and 5.5 MeV. The TRIFOIL gate is also applied as $E_{Trifoil} >$ 15000 keV for all of them.

For the excitation energy range between 1.5 MeV and 2 MeV, 1275 keV and 1402 keV γ-rays start to appear dominantly in the figure 3.21. The red spectrum is also a bit promising but not conclusive here in terms of the peaks at the same energies. The other excitation energy range up to 3 MeV do not give any evidence of the 1402 keV γ-ray.

The 1275 and 1402 keV γ-ray peaks are also seen at the higher excitation energies above 3.5 MeV and 4 MeV respectively in the figure 3.22. However, the count raise does not exceed 25 percent of the previous ones for these two gamma rays. This suggests that feeding from higher lying states to these gamma rays is not so strong . The gamma ray of interest here is mostly the 1102 keV gamma ray which shows up only in the excitation energy range between 4 MeV and 5 MeV.

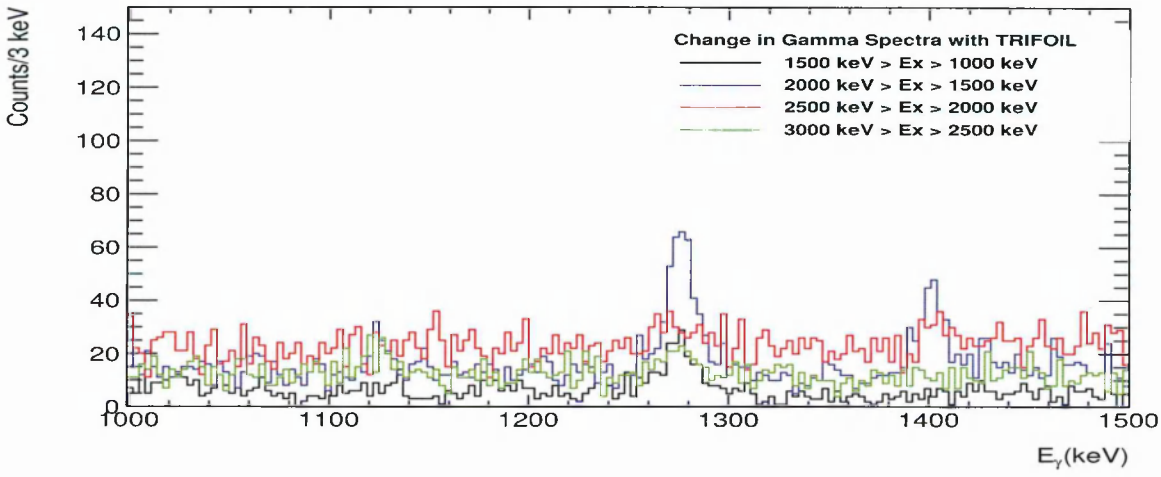

Figure 3.21: HPGe γ-ray spectra are shown when gated on different excitation energy ranges calculated by the highest energetic proton detected in the SHARC detector using 500 keV steps in excitation energy between 1 MeV and 3 MeV. The TRIFOIL gate is also applied as $E_{Trifoil} >$ 15000 keV for all of them.

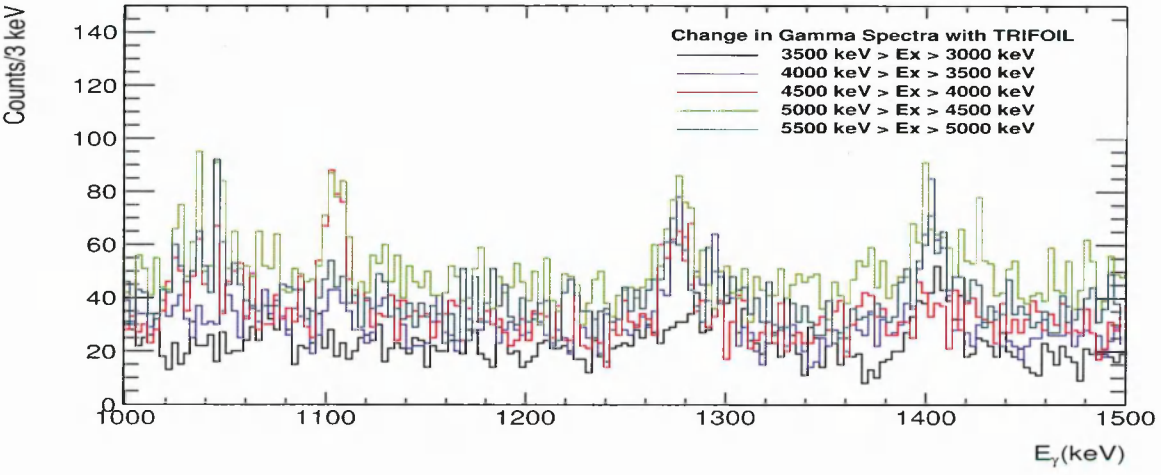

Figure 3.22: HPGe γ-ray spectra are shown when gated on different excitation energy ranges calculated by the highest energetic proton detected in the SHARC detector using 500 keV steps in excitation energy between 3 MeV and 5.5 MeV. The TRIFOIL gate is also applied as $E_{Trifoil} >$ 15000 keV for all of them.

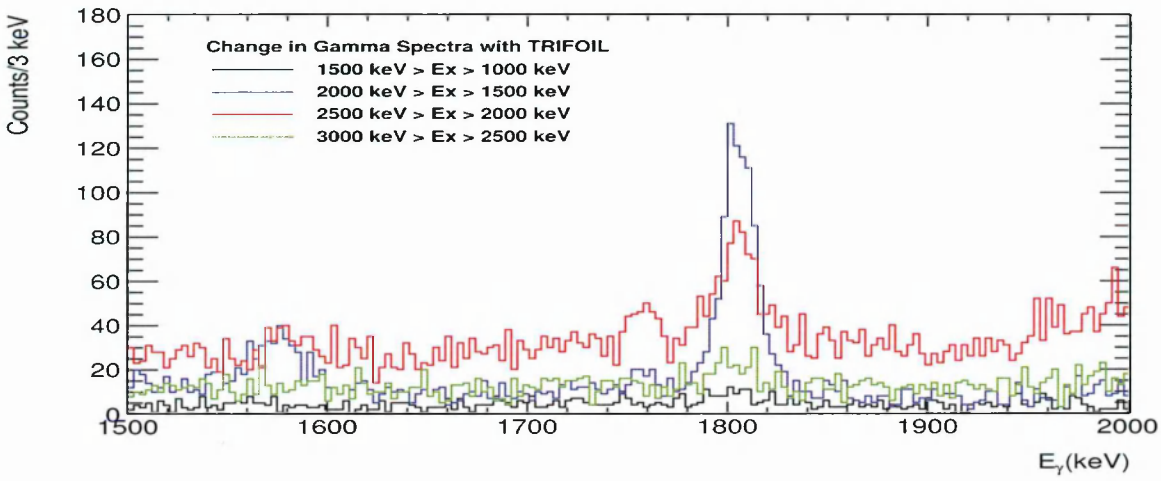

Figure 3.23: HPGe γ-ray spectra are shown when gated on different excitation energy ranges calculated by the highest energetic proton detected in the SHARC detector using 500 keV steps in excitation energy between 1 MeV and 3 MeV. The TRIFOIL gate is also applied as $E_{Trifoil} >$ 15000 keV for all of them.

In figure 3.23, the excitaton energy range from 1.5 MeV to 2 MeV shows strong γ-ray peak at 1805 keV together with the weaker peaks at 1577, 1758 keV, and a tentative peak at 1962 keV. The 1805 keV γ-ray peak predominantly corresponds to excitation energy between 1.5 MeV and 2.5 MeV, and the other three peaks also fall within this range.

The 1805 keV peak is also strongly seen in the gates spanning 4.5 to 5.5 MeV excitation as in figure 3.24. This suggests that this γ-ray energy has a feeding from highler lying states.

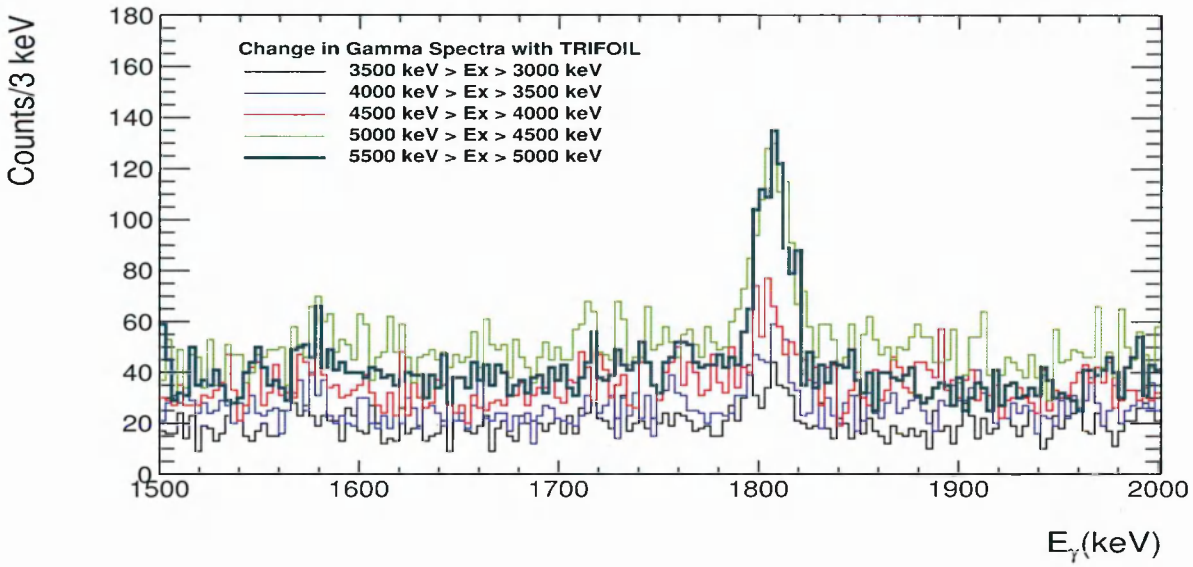

Figure 3.24: HPGe γ-ray spectra are shown when gated on different excitation energy ranges calculated by the highest energetic proton detected in the SHARC detector using 500 keV steps in excitation energy between 3 MeV and 5.5 MeV. The TRIFOIL gate is also applied as $E_{Trifoil} >$ 15000 keV for all of them.

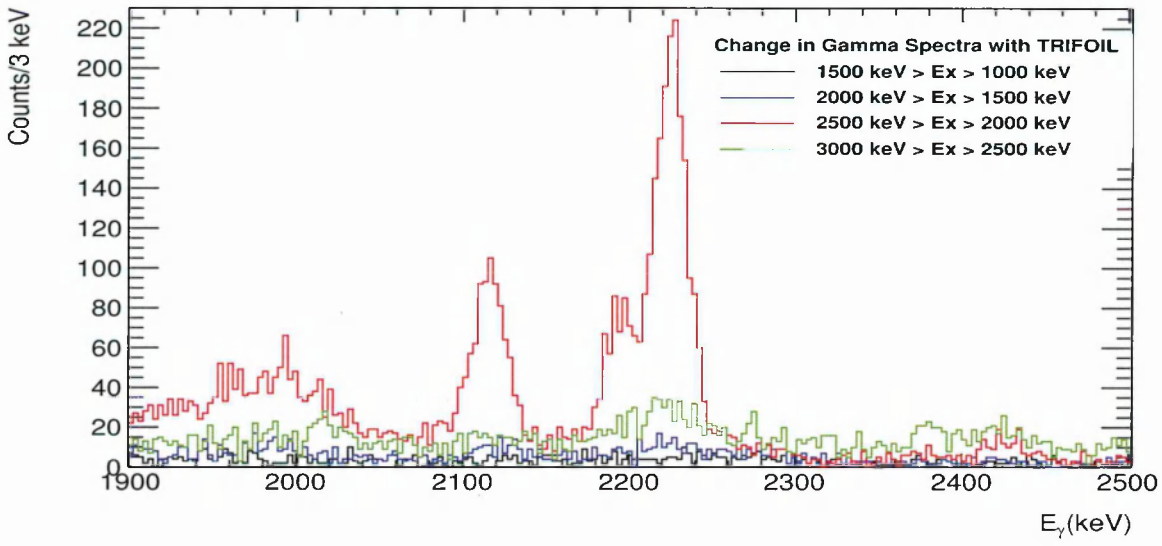

Figure 3.25: HPGe γ-ray spectra are shown when gated on different excitation energy ranges calculated by the highest energetic proton detected in the SHARC detector using 500 keV steps in excitation energy between 1 MeV and 3 MeV. The TRIFOIL gate is also applied as $E_{Trifoil} >$ 15000 keV for all of them.

Depending on the figures 3.25 and 3.26, peaks at 2116 and 2225 keV dominate the spectrum between 1900 and 2500 keV. The 2225 keV peak is seen strongly in the 2-2.5 MeV gate, but not in any other gate below 4 MeV. It is then populated in all gates between 4 to 5.5 MeV at the level of about 40% of the yield in the lower gate. The 2116 keV peak is produced between 2-2.5 MeV and in the gates between 4 and 5.5 MeV. The 2-2.5 MeV gate also selects the 2191 keV peak very clearly and it is again evident between 4 and 5 MeV. Another peak at 2080 keV is only evident for gates between 4 and 5 MeV.

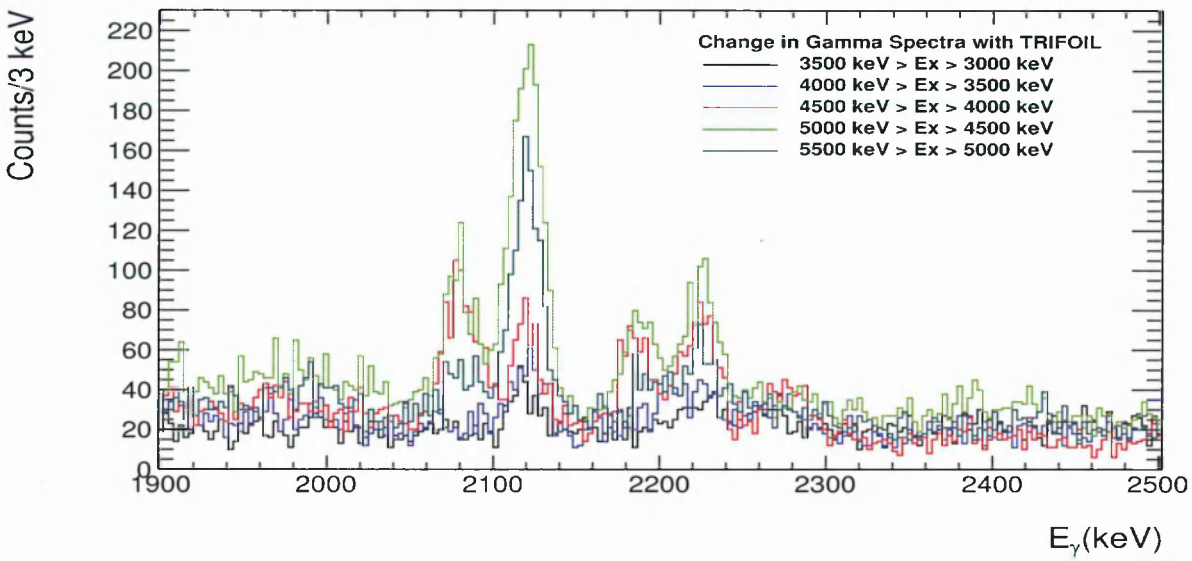

Figure 3.26: HPGe γ-ray spectra are shown when gated on different excitation energy ranges calculated by the highest energetic proton detected in the SHARC detector using 500 keV steps in excitation energy between 3 MeV and 5.5 MeV. The TRIFOIL gate is also applied as $E_{Trifoil} >$ 15000 keV for all of them.

In the figure 3.27, as would be expected, the region of the γ-ray spectrum between 2500 and 3000 keV is correlated with the 2.5-3 MeV gate, and not for any lower-lying states. The strong γ-rays here are respectively at 2616, 2766, and 2843 keV.

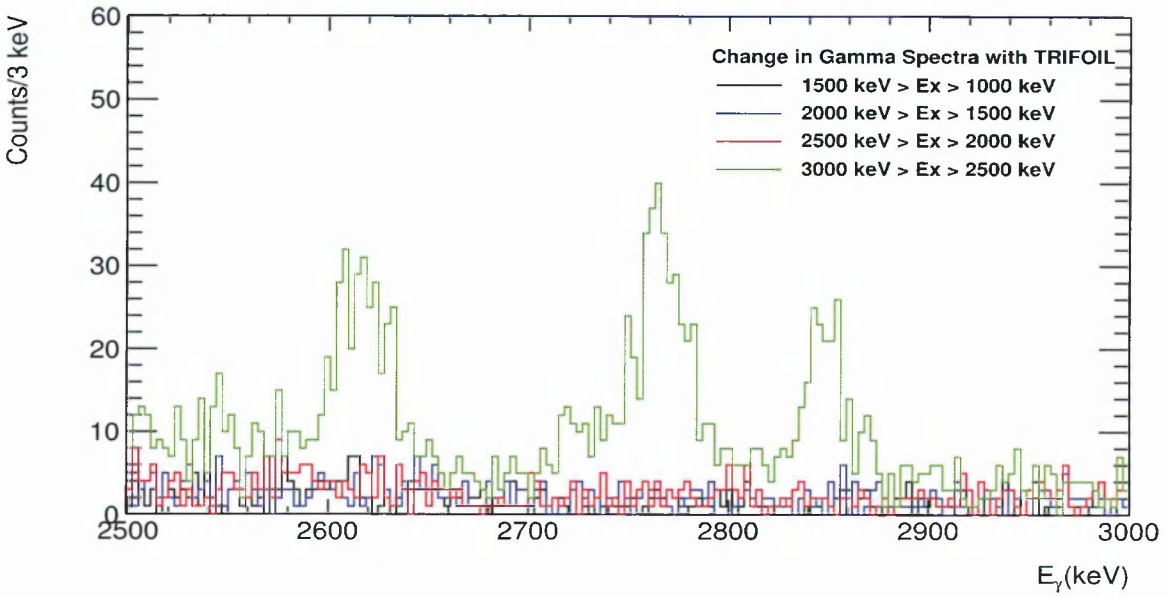

Figure 3.27: HPGe γ-ray spectra are shown when gated on different excitation energy ranges calculated by the highest energetic proton detected in the SHARC detector using 500 keV steps in excitation energy between 1 MeV and 3 MeV. The TRIFOIL gate is also applied as $E_{Trifoil} >$ 15000 keV for all of them.

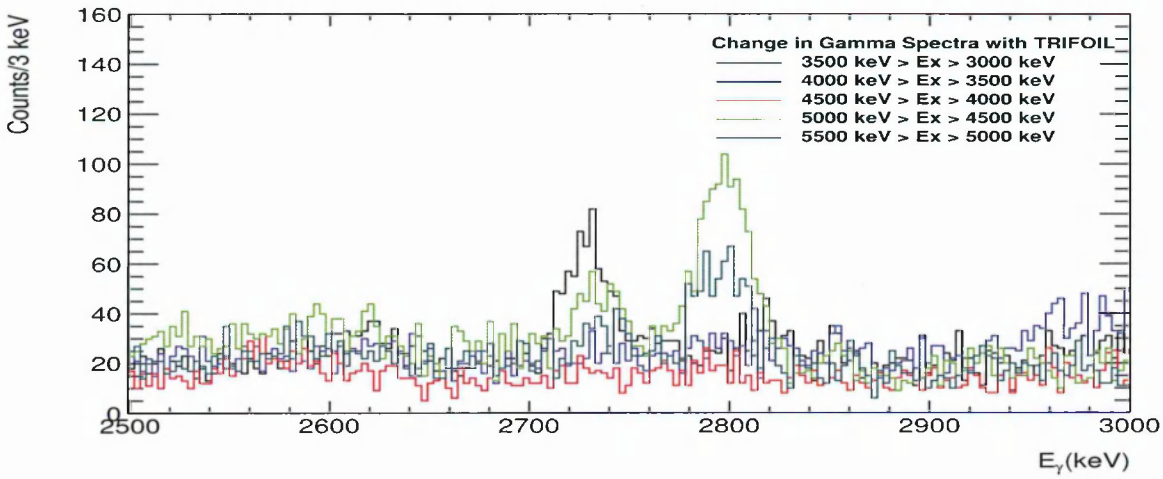

Figure 3.28: HPGe γ-ray spectra are shown when gated on different excitation energy ranges calculated by the highest energetic proton detected in the SHARC detector using 500 keV steps in excitation energy between 3 MeV and 5.5 MeV. The TRIFOIL gate is also applied as $E_{Trifoil} >$ 15000 keV for all of them.

In the figure 3.28, 2728 and 2796 keV γ-ray peaks come up for excitation energy ranges above 3 MeV. The 2728 keV peak is strongest between 3 MeV and 3.5 MeV; however, the 2796 keV peak is strongest between 4.5 MeV and 5 MeV.

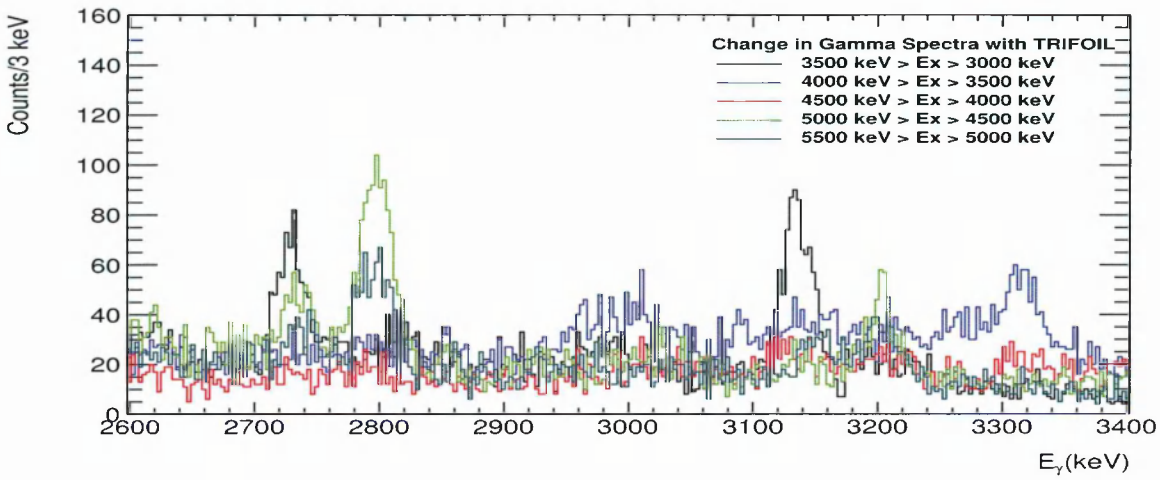

Figure 3.29: HPGe γ-ray spectra are shown when gated on different excitation energy ranges calculated by the highest energetic proton detected in the SHARC detector using 500 keV steps in excitation energy between 3 MeV and 5.5 MeV. The TRIFOIL gate is also applied as $E_{Trifoil} >$ 15000 keV for all of them.

The figure 3.29 shows that there are actually two different γ-rays included in the peak at 2728 keV. A state at 3135 keV turns out to have a ground state decay branch and a decay via 2728 keV γ-ray to the 405 keV lower lying state. This branching ratio must be independent of the gating, but only the peak near 2728 keV is seen for the excitation energy range between 4.5 and 5 MeV. This indicates that the higher lying region also emits the same γ-ray energy by chance but in a different cascade.

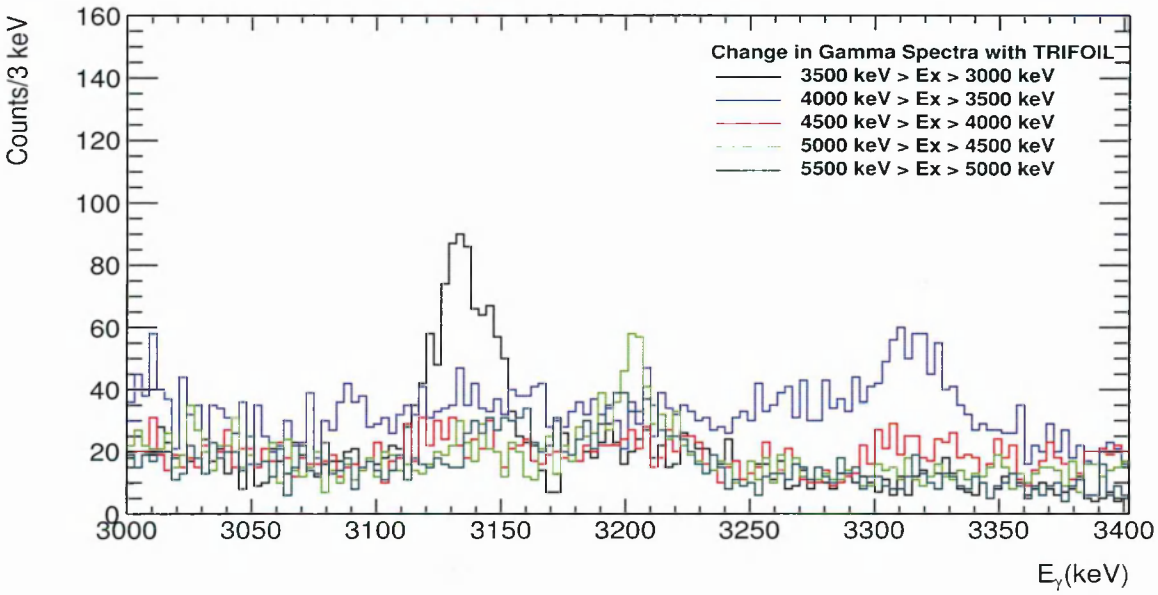

Figure 3.30: HPGe γ-ray spectra are shown when gated on different excitation energy ranges calculated by the highest energetic proton detected in the SHARC detector using 500 keV steps in excitation energy between 3 MeV and 5.5 MeV. The TRIFOIL gate is also applied as $E_{Trifoil} >$ 15000 keV for all of them.

In the figure 3.30, the 3135 keV γ-ray peak emerges only for the 3-3.5 MeV gate. The 3310 keV peak is clearly enhanced for the excitation energy range between 3.5 and 4 MeV. In addition, 3203 keV γ-ray peak only shows up for the higher excitation energy range from 4.5 to 5 MeV.

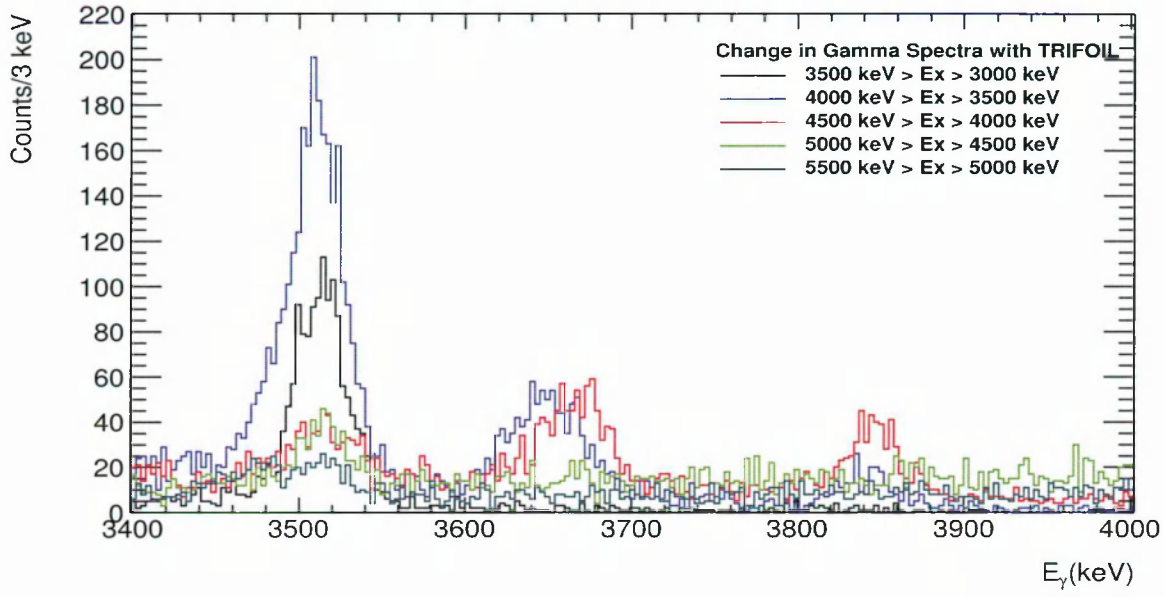

Figure 3.31: HPGe γ-ray spectra are shown when gated on different excitation energy ranges calculated by the highest energetic proton detected in the SHARC detector using 500 keV steps in excitation energy between 3 MeV and 5.5 MeV. The TRIFOIL gate is also applied as $E_{Trifoil} >$ 15000 keV for all of them.

At the γ-ray energies between 3400 and 4000 keV (see fig. 3.31), the drop in counts for the 3511 keV γ peak from the 3.5-4 MeV range to the 4-5.5 MeV range suggests that there is not much feeding to this gamma ray from higher lying states. It's almost certain that the origin of the gamma ray is mostly between 3 MeV and 4 MeV and close to 3,5 MeV. At least two unresolved γ-rays occur between 3600 and 3700 keV. These higher energy gamma rays at 3664 and 3845 keV arise mostly from the 4 to 4.5 MeV.

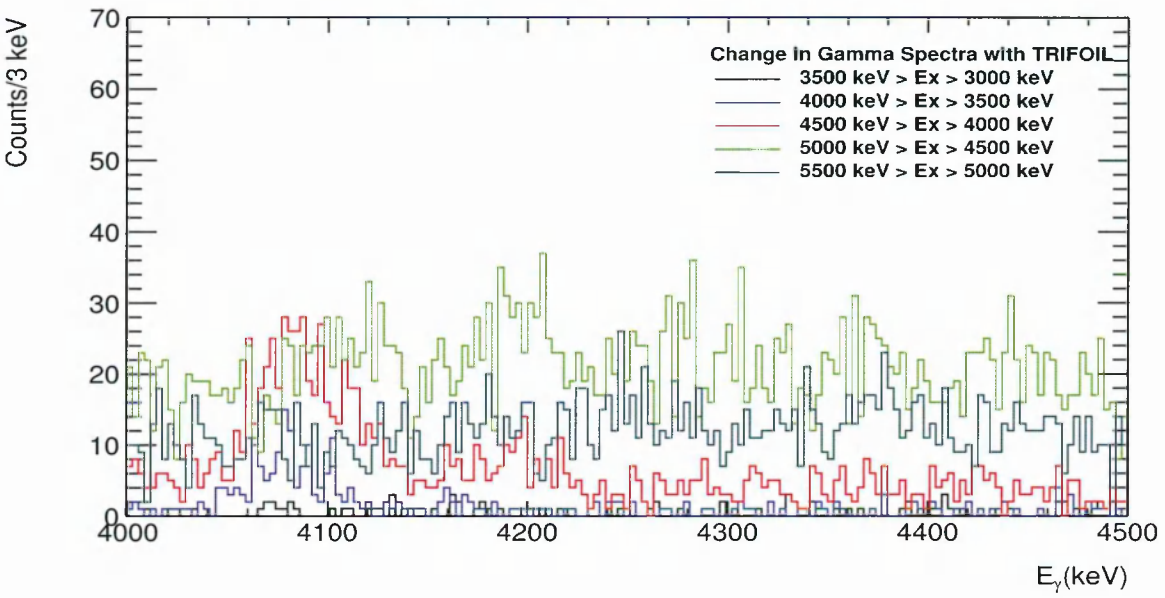

Figure 3.32: HPGe γ-ray spectra are shown when gated on different excitation energy ranges calculated by the highest energetic proton detected in the SHARC detector using 500 keV steps in excitation energy between 3 MeV and 5.5 MeV. The TRIFOIL gate is also applied as $E_{Trifoil} >$ 15000 keV for all of them.

Above 4000 keV (see fig.3.32), a γ peak emerges around 4087 keV between 4 and 5 MeV. This peak almost dies out above 5 MeV excitation energy. This strongly suggests that our excitation energy for this specific gamma ray is restricted in this region. This region of γ-ray energy spectrum shows also a background level that makes it increasingly difficult to distinguish any γ peaks as the γ-ray energy increases.

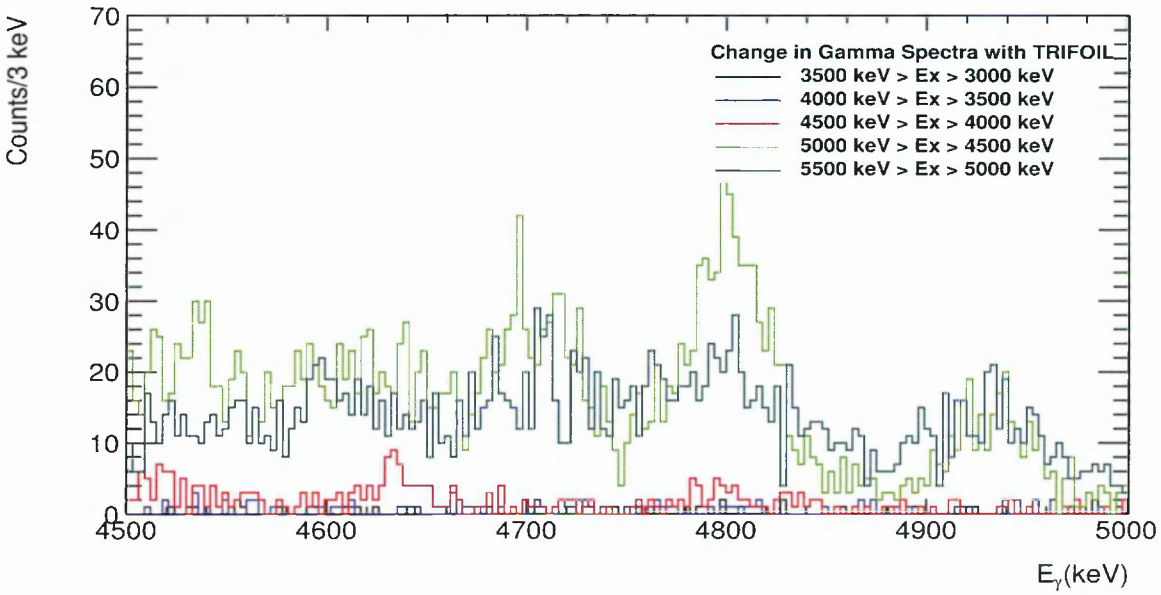

Figure 3.33: HPGe γ-ray spectra are shown when gated on different excitation energy ranges calculated by the highest energetic proton detected in the SHARC detector using 500 keV steps in excitation energy between 3 MeV and 5.5 MeV. The TRIFOIL gate is also applied as $E_{Trifoil} >$ 15000 keV for all of them.

In the figure 3.33, gamma ray energies above 4500 keV are associated with the 4.5 to 5.5 MeV region. For the higher energy peak at 4931 keV, it seems both the 4.5-5 MeV 5-5.5 MeV ranges are matching. However, we have fluctuations in all other areas in terms of counts. The dominant gamma rays here are respectively around 4526, 4705, 4799, and 4931 keV in comparison to tentative γ-ray around 4640 keV.

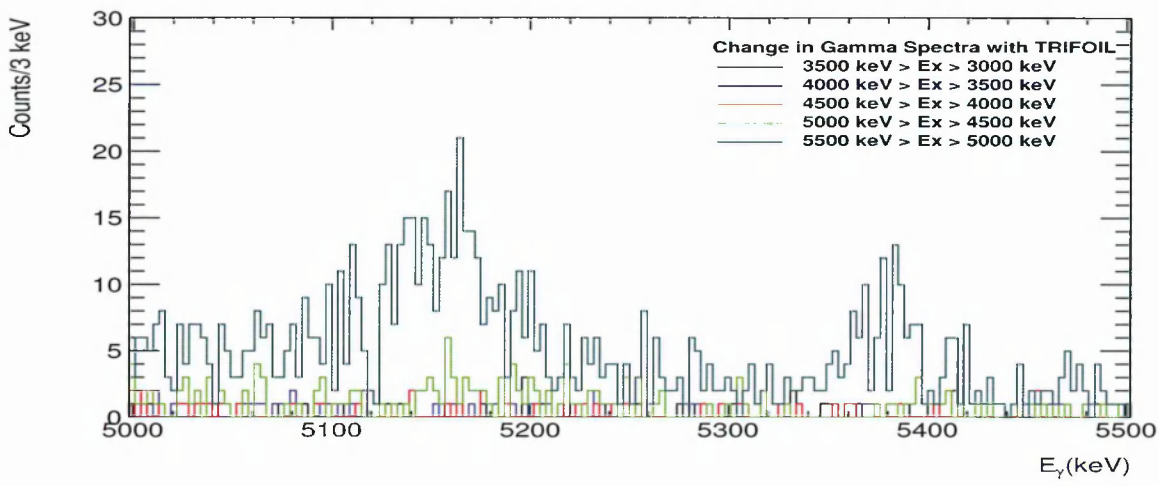

Figure 3.34: HPGe γ-ray spectra are shown when gated on different excitation energy ranges calculated by the highest energetic proton detected in the SHARC detector using 500 keV steps in excitation energy between 3 MeV and 5.5 MeV. The TRIFOIL gate is also applied as $E_{Trifoil} >$ 15000 keV for all of them.

Finally, we reach our last figure (fig.3.34) of this series of gamma spectra which shows γ-ray energies above 5000 keV. This is the last region where we see γ rays, so it proves that we do not populate higher lying states than this energies in the current experiment. These two gamma peaks will turn out to be our highest energy states which decay directly to the ground state of ^{26}Na. The difference between the two γ-ray energies is 213 keV which also proves there is no decay between them because 213 keV gamma ray has not been observed in any excitation energy range. The simple conclusion here is the γ-rays possibly refer to new states at 5.154 MeV and 5.384 MeV.

3.3 Explanation of New States and γ Branches in ^{26}Na

The present work is re-examination of the data already partly analysed by Wilson [1] with the aim of examining γ-ray decays in more detail. In addition, this was a confirmation of the earlier results, which were all re-examined independently, and then an extension of the earlier work by means of improved and newly developed analysis techniques. In this section, the focus is mainly on states at 2.195, 1.992, 4.087, 3.720, 4.800, 4.932, 5.155, 5.387 MeV and γ-rays at 2727, 1102, 1402, and 3470 keV.

3.3.1 Explanation of a New γ Branch for 2195 keV State

Figure 3.35 is designed to illustrate properties of the 2.195 MeV and a new state at 1.992 MeV. As seen in the same figure, the γ peak at 1962 keV only appears in the excitation energy range between 2 MeV and 2.5 MeV. Then, to postulate a decay from the 2195 keV state to the 232 keV lower lying state is natural. To investigate this in more detail, the excitation energy spectrum gated on both 1962 keV γ-ray and its neighbouring region to make background subtraction are shown in the figure 3.36 separately for different TIGRESS clovers. The excitation energy spectrum gated on 1962 keV γ-ray, after background subtraction, shows a dominant peak which can be fitted with a Gaussian function. The resultant excitation energy is 2226±18 keV in 90° clovers and 2266±14 keV in 135° clovers, which supports the idea. The excitation energies can be fluctuated due to the fitting.

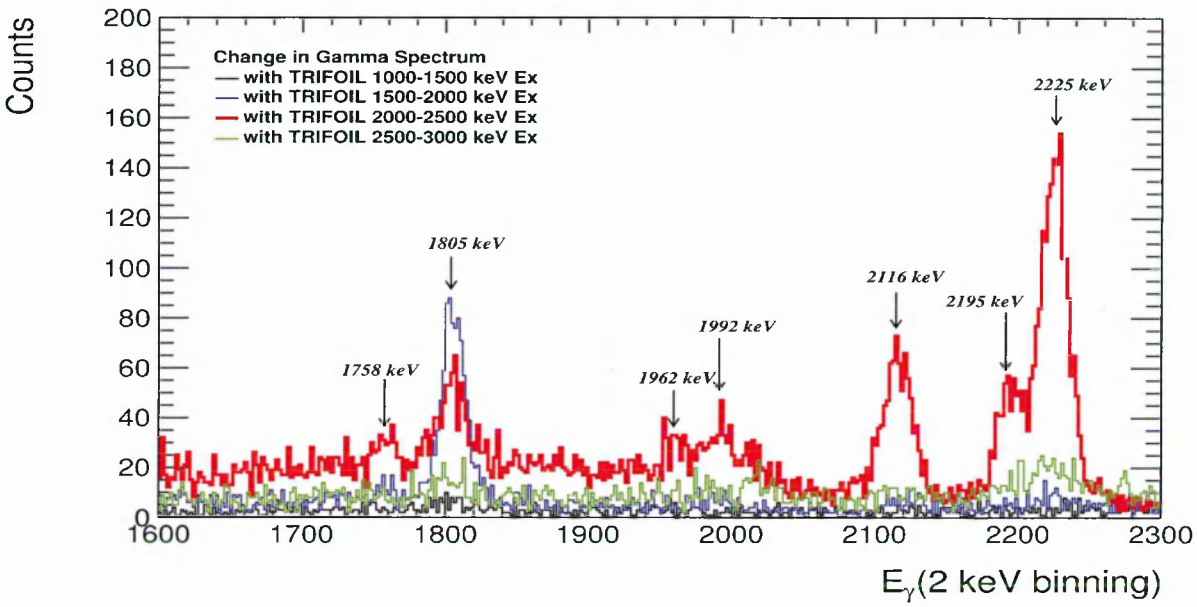

Figure 3.35: Gamma Spectrum in the range from 1600 to 2300 keV for 1 to 3 MeV state in ^{26}Na with TRIFOIL gate.

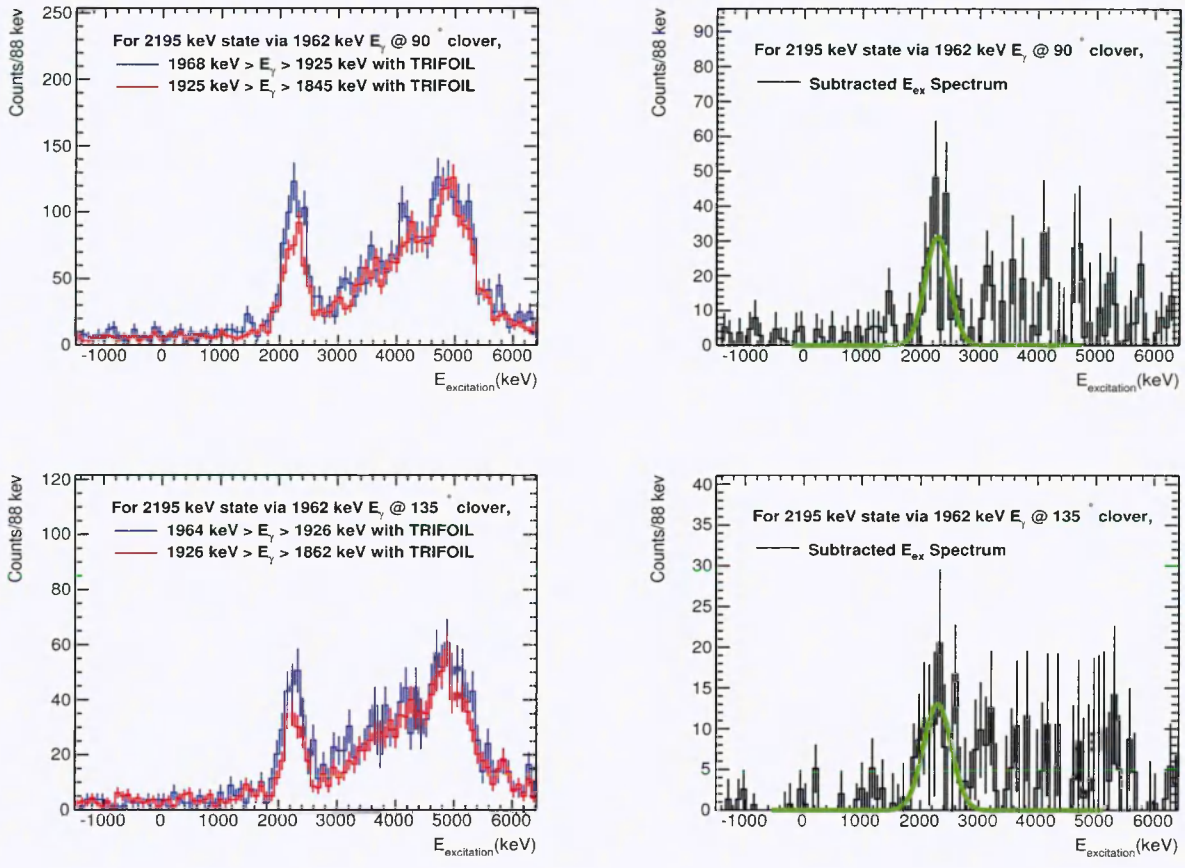

Figure 3.36: Excitation energy spectra gated on 1962 keV γ-ray and its adjacent background with TRIFOIL and 90° and 135° clover angle gate for the reaction $^{25}Na(d,p\gamma)^{26}Na^{*}$.

3.3.2 Explanation of a New State at 1.992 MeV

The figure 3.35 together with figures 3.37 and 3.38 are to explain a newly observed state at 1.992 MeV. Our main focus will be the excitation energy range around 1992 keV and higher range above 4 MeV where possible decays can occur to 2225 keV state. This is because it is initially postulated that the state 1.992 MeV might also be in the cascade from the state 2.225 MeV. However, it'll be shown that it is a new state where there is no feeding from higher lying states, but there is also a new γ-ray branch via 1758 keV to 232

keV state from 1.992 MeV. The reason to look at above 4 MeV excitation energy range is it was known those higher lying states decay to the 2225 keV state. Then, it indicates a possibility of a new decay to a new 1992 keV state via 232 keV γ-ray. However, we'll refute this idea by checking the gamma spectrum from higher lying states in the figure 3.37 and the excitation energy spectrum of 1.992 MeV state in the figure 3.38. The figure 3.37 gives promising evident that 2.225 MeV and 1.992 MeV states are not correlated with the γ-rays corresponding to their state energies. Also, the excitation energy around 1.992 MeV is very strong candidate for the origin of this state as shown in the figure 3.35; whereas, the gamma rays of 1992 keV and 1758 keV gamma rays, which we think decay from 1992 keV state to the ground state and the 233 keV state, die out in the higher excitation region even above 2.5 MeV as in the figure 3.35. Then, the excitation energy spectra gated on a specific γ-ray at 1758 keV , which is thought to be a branch for 1992 keV state in this work, are shown in the figure 3.38. This excitation energy spectra are gated on both the 1758 keV γ-peak and its adjacent region for background subtraction as the subtracted version of excitation energy spectrum is seen in black in the figure 3.38. This excitation energy peak in black spectrum shows prominent peak near 2 MeV, supporting the direct population of the state at 1.992 MeV.

While having a promising excitation energy peak around 1992 keV in the figure 3.38, nothing around higher lying states seems to be convincing. Also, all the γ-rays have been tried to see if any of them makes sense to refer as a γ ray coming from the higher energetic states which might be in coincidence with the γ-ray at 1758 keV. In that case, we could have also claimed that this γ-ray may not be the branch of the new state at 1.992 MeV. All the proofs we have show that there seem to be weak gamma rays at 1758 and 1992 keV both of which belong to the newly identified state at 1.992 MeV.

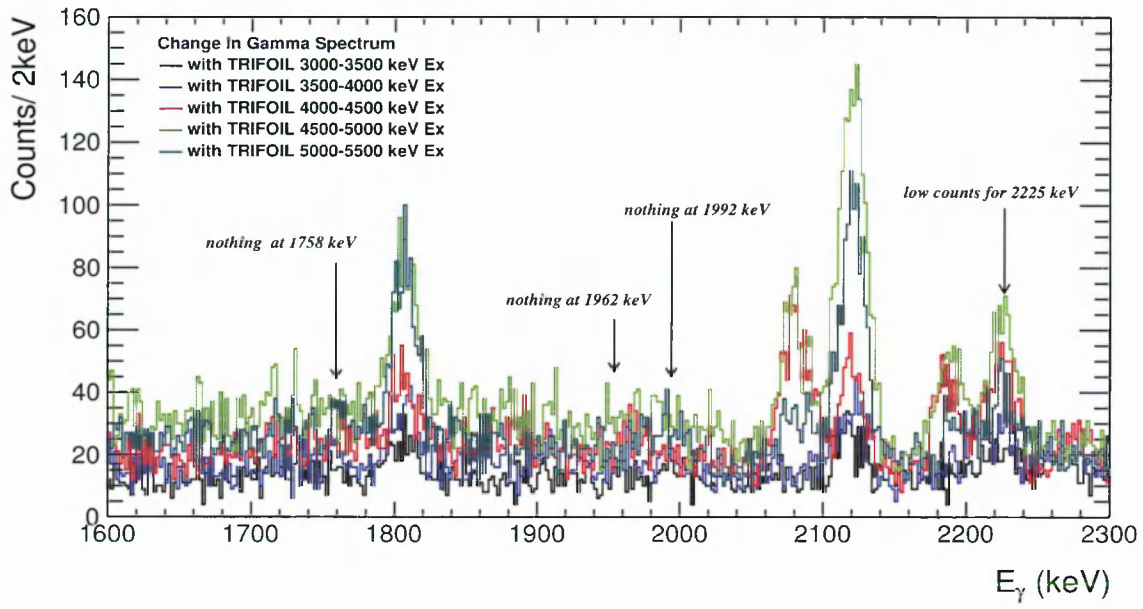

Figure 3.37: Gamma Spectrum Change in the range from 1600 to 2300 keV for 3 to 5.5 MeV state in ^{26}Na with TRIFOIL gate.

In the figure 3.37, even if it may seem like there is a bit count increase at 1962 keV and 1992 keV energies, they don't appear at the same time for a particular excitation energy limits as a gate. Thus, the convincing γ spectrum gated on between 2 MeV and 2.5 MeV excitation energy in the previous figure 3.35 show better proof.

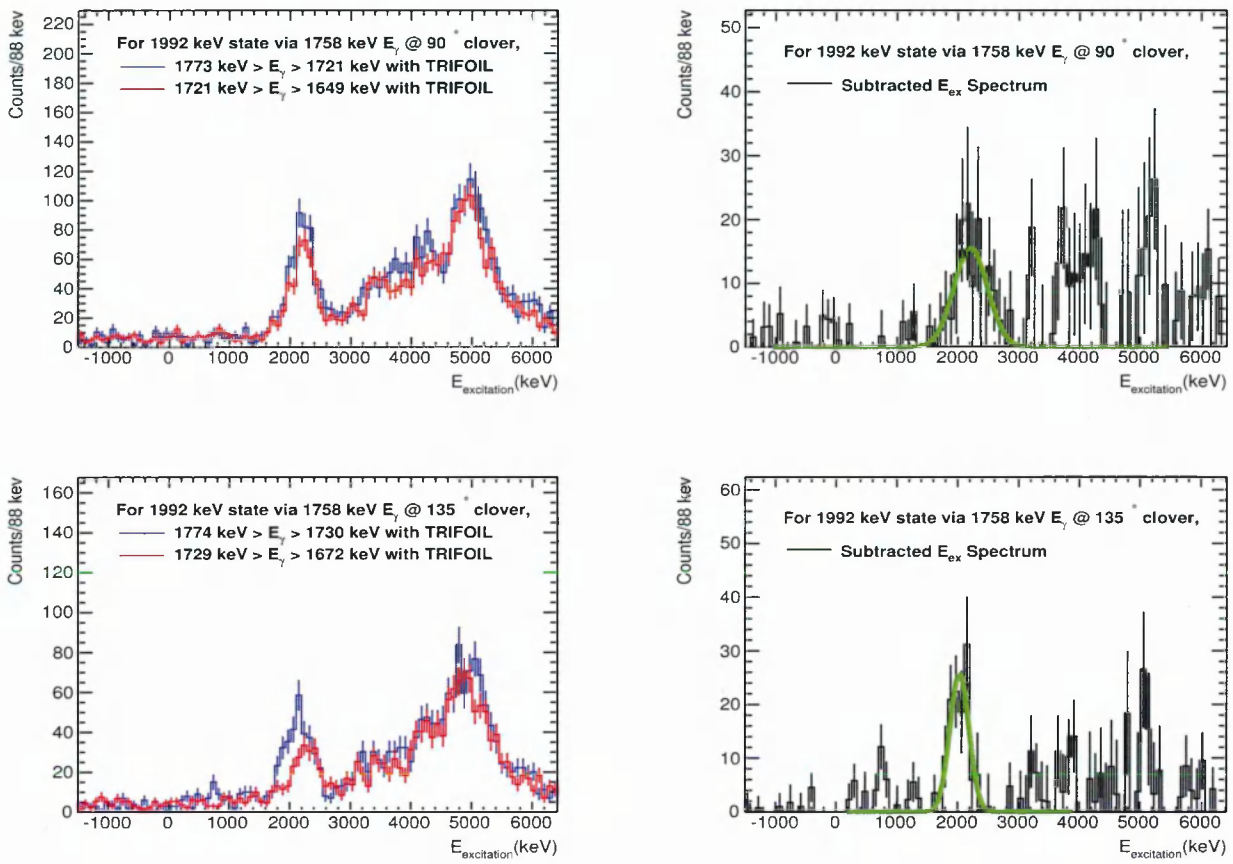

Figure 3.38: Excitation energy spectrum gated on a gamma ray at 1758 keV in ^{26}Na with TRIFOIL gate.

In the figure 3.38, the blue spectrum indicates strong candidate for the excitation energy peak when it's gated on a gamma ray at 1758 keV; whereas, the red spectrum shows the excitation energy spectrum for background subtraction from the γ peak's adjacent. Thus, the right side of the figure indicates the subtraction of these two histograms where we get the final excitation energy spectrum to interpret.

3.3.3 Newly Discovered 2728 keV γ-Ray Arising from the Excitation Energy Range 4-5 MeV

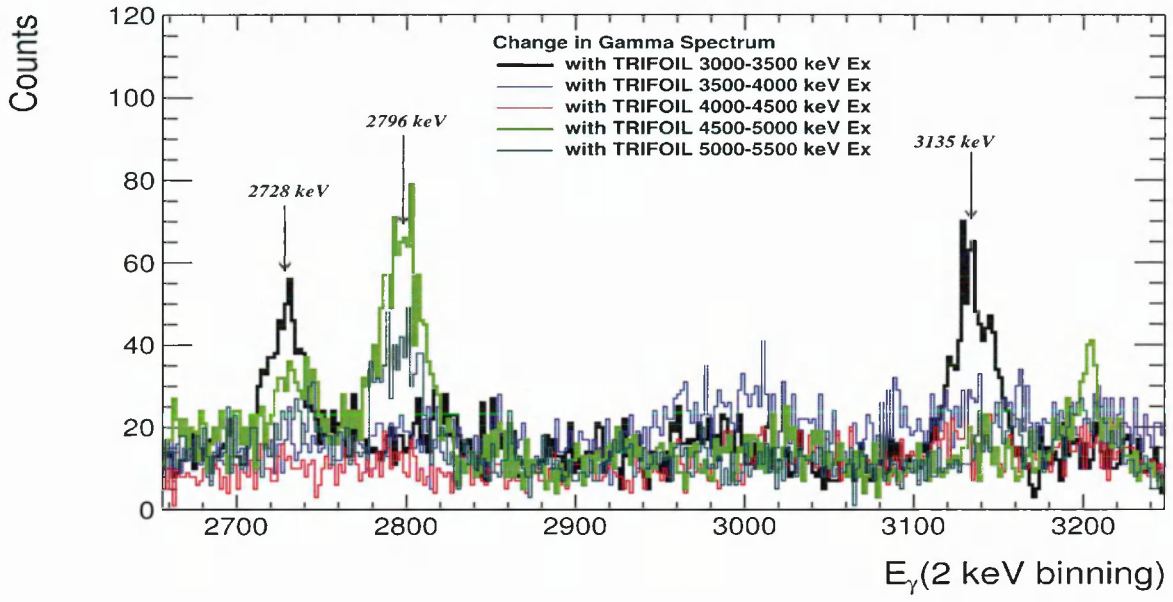

Figure 3.39: Gamma Spectrum focused between 2650 keV and 3250 keV range for 2728 keV gamma ray between 4 MeV to 5.5 MeV excitation energy range in ^{26}Na with TRIFOIL gate.

The figure 3.39 reveals, after careful analysis, that there are two separate γ-rays at the same energy of 2728 keV. From the previous work [1] and verified in the current work, there is a the state at 3.405 MeV that decays to the ground state and to the 405 keV state via a 2728 keV γ-ray. Thus, both γ-rays are highlighted by the 3-3.5 MeV gate. However, the excitation energy range 4.5-5 MeV also shows the 2728 keV γ-ray with lower counts but without the 3135 keV γ-ray. That supports to have a new state above 4 MeV, constructed by placing this new 2728 keV γ-ray on the top of the previously known four states with updated energies at 1.805, 2.116, 2.195, and 2.225 MeV. This results in corresponding state energies at 4.534, 4.845, 4.920, and 4.952 MeV. Gating on the 2728 keV peak shows

an excess of counts, over background, in the region centred on 4.9 MeV in addition to the population of the 3.135 MeV state. Unfortunately, whilst the γ-ray certainly exists and feeds near 2 MeV, it is not possible to make any further deduction about it.

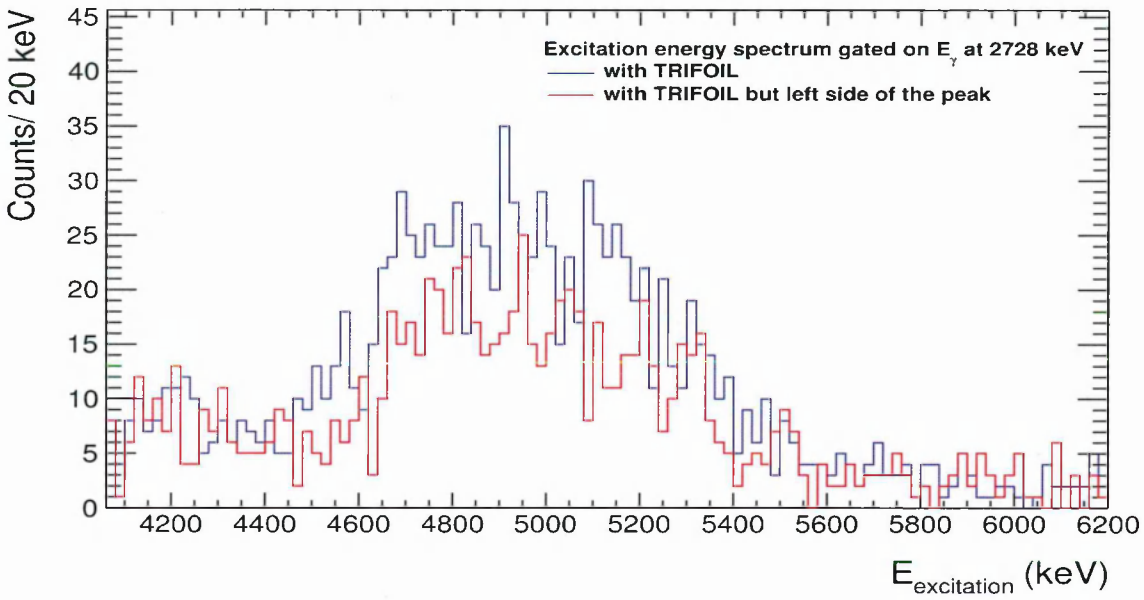

Figure 3.40: Excitation energy spectrum gated on a gamma ray at 2728 keV in ^{26}Na with TRIFOIL gate.

3.3.4 The Explanation of a New State at 3.720 MeV

The investigation of the γ-ray at 3315 keV started with the figure 3.41 since this is the easiest way to spot the excitation energy range that a specific gamma ray can be originated. As the figure shows, the γ-ray peak only appears between 3.5 and 4 MeV excitation energy range.

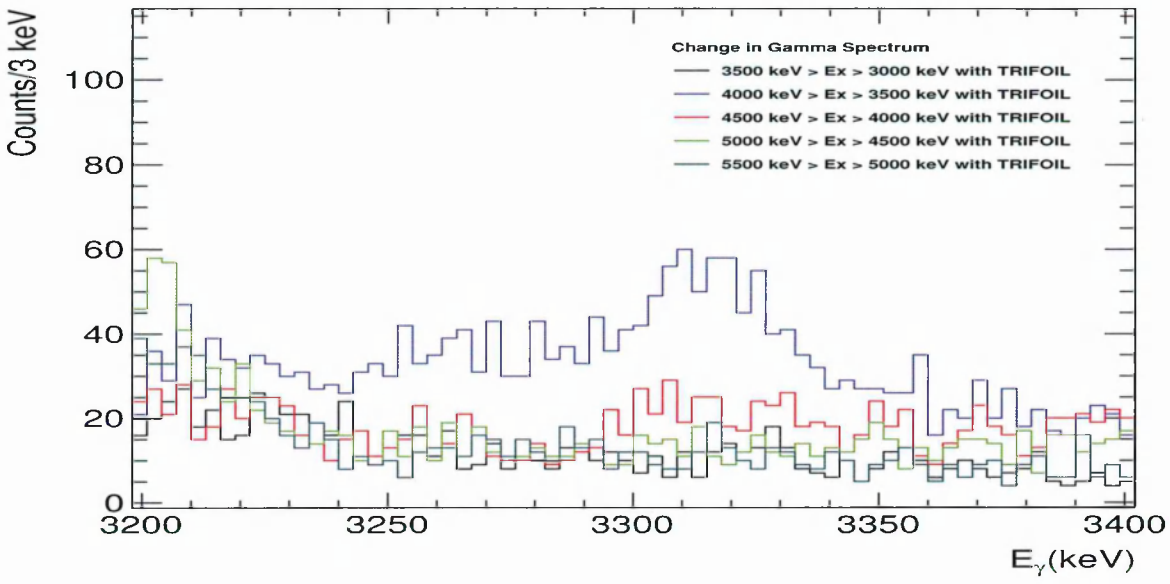

Figure 3.41: Gamma Spectrum for gamma ray at 3315 keV in ^{26}Na with TRIFOIL gate.

After having the gamma limits from the figure 3.41, the excitation energy spectrum can be plotted as shown in the figure 3.42. In this figure, the gamma ray limits shown in the figure are applied to extract two excitation spectra for the 3135 keV γ-ray and its adjacent area. The second limits refers to a gate for background spectrum in red. After the subtraction, the excitation energy limits are given as 3751±11 keV in the fit which agrees with what we see in the black spectrum of the figure 3.42.

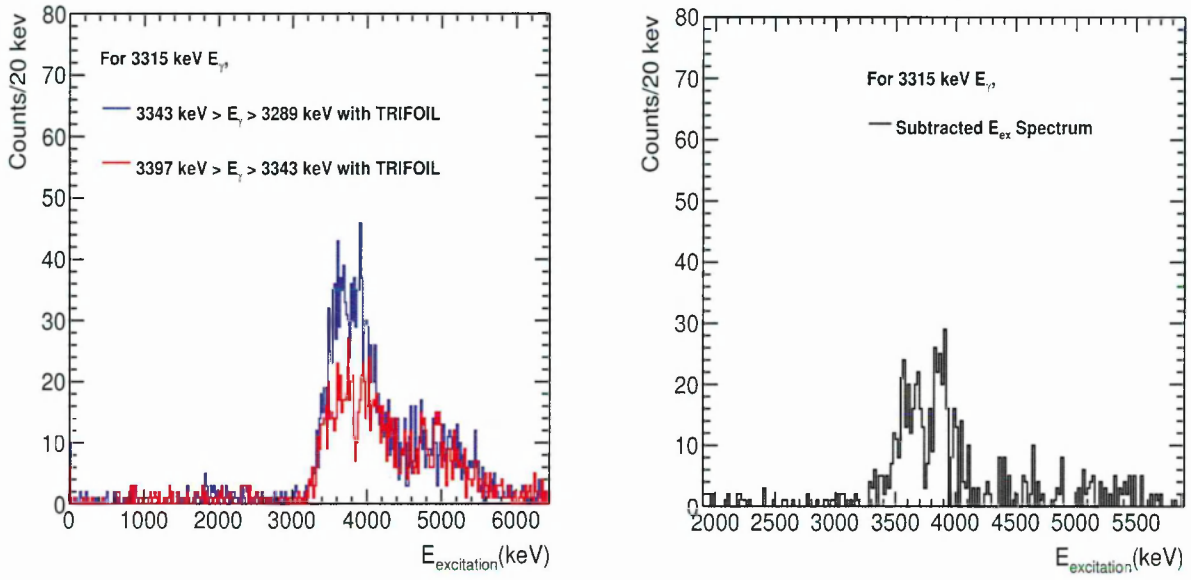

Figure 3.42: Excitation energy spectrum gated on a gamma ray at 3315 keV in ^{26}Na with TRIFOIL gate.

By using the same excitation energy limits as seen in the figure 3.42, gamma spectra can be plotted to check for a γ-ray peak around 3315 keV in the figure 3.43. The fit result of 3316 $\pm$2 keV for a γ-ray peak around 3315 keV agrees with both the γ-ray energy and the excitation energy where it is originated. The lower panel of the figure 3.43 shows no indication of another type of reaction which may emit the 3315 keV γ-ray since the peak is consistent with upper panel as well. This information is based on what TRIFOIL and different clover angles are used for as a gate in the figure.

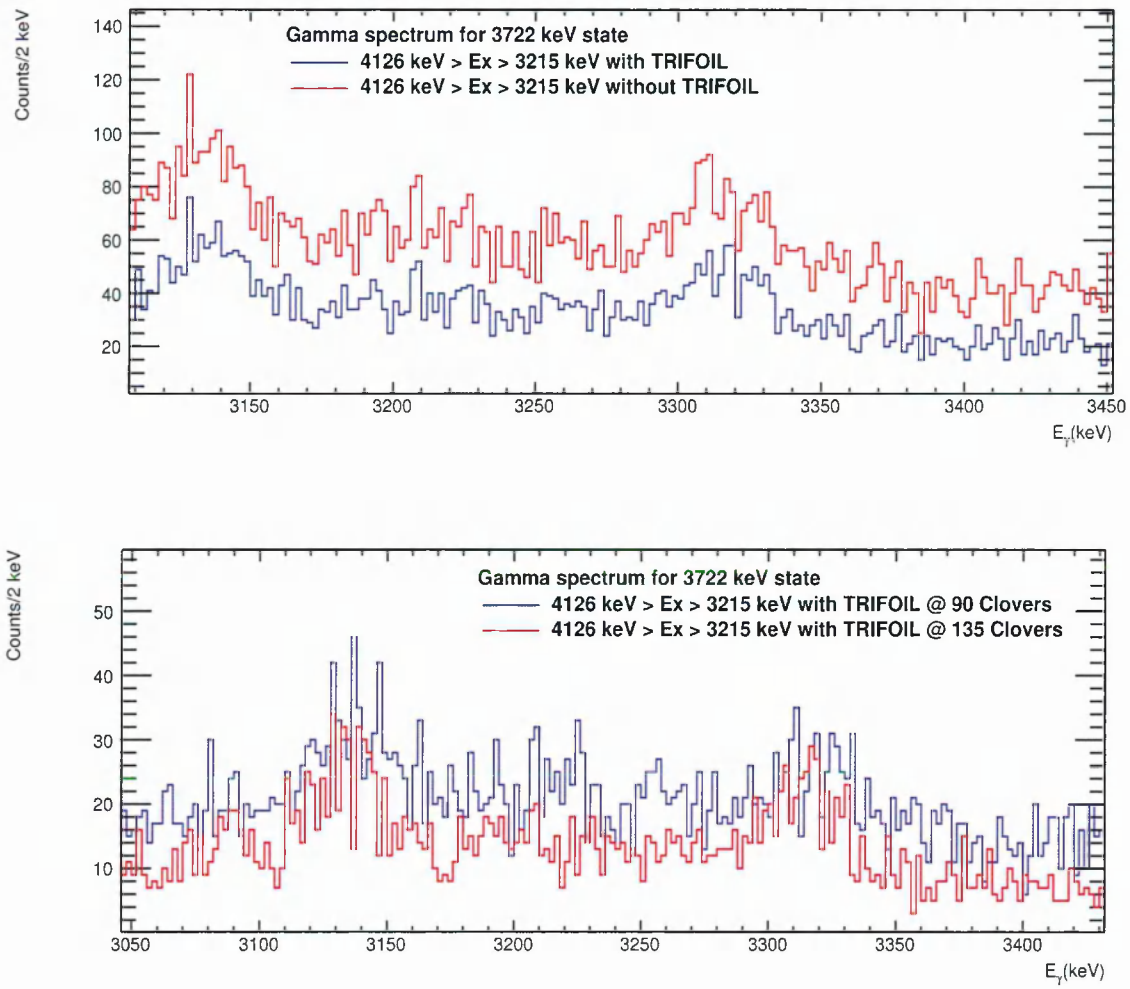

Figure 3.43: Gamma energy spectrum for 3315 keV peak in ^{26}Na with TRIFOIL gate.

Lastly, the $\gamma-\gamma$ coincidence data serves another evidence for a specific cascade which may belong to a state around 3.722 MeV. In the figure 3.44, all the γ-rays in coincidence with 405 keV can be seen, and one of them is the evident γ-ray at 3135 keV. That refers to a new cascade through the 405 keV state. To sum up, 405 keV and 3315 keV will result in a new state at 3.720 MeV.

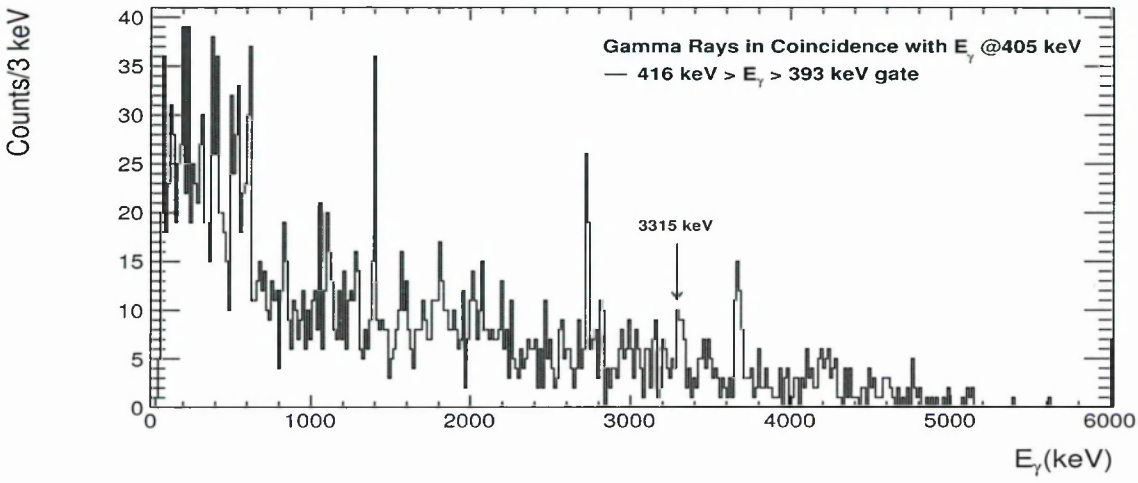

Figure 3.44: Gamma coincidence energy spectrum for 3315 keV peak in ^{26}Na with TRIFOIL gate.

3.3.5 The Explanation of a New State at 4.087 MeV

By using a comparison among the gamma spectra for different excitation energy ranges as in the figure 3.45, it's easy to see how the three γ-rays marked in the same figure change their counts. The excitation energy range between 4 MeV and 4.5 MeV shows predominantly three γ-rays at 3664, 3845, and 4087 keV. Almost all the other excitation energy gates except 3.5-4 MeV region display no γ peak in the γ-ray spectrum.

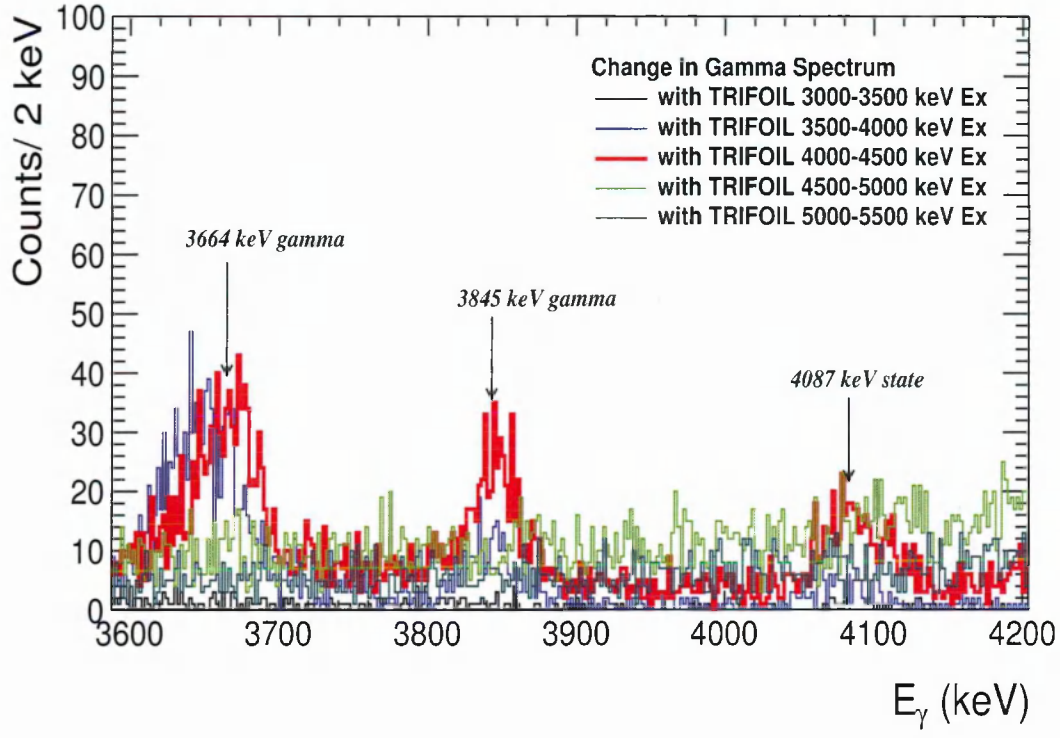

Figure 3.45: Gamma spectrum change between 3 MeV and 5.5 MeV excitation energy to investigate a state at 4087 keV in ^{26}Na.

By using the excitation energy range 3.5-4.5 MeV from the figure 3.45, one should try to find a combination of states and γ-rays that can add up to this excitation energy range. If one supposes that 4.087 MeV is the state which decays to lower lying states via high γ-rays energies at 3664, 3845, and 4087 keV, then it will be easy to add them up on to the lower lying states which already exist at the ground state, 232 keV, and 405 keV states as shown in the level scheme 1.7. Of course, the order of the γ-rays in the γ cascade can not be known in advance. However, excitation energy plots gated on specific γ-rays in the discussion will provide information about a new state or states.

In addition to the information above, the excitation energy spectra shown in the figure 3.46 and 3.47 are gated on γ-rays at 3664 keV and 3845 keV, respectively. The γ peak limits can be retrieved from the previous γ-ray spectra. Thus, the right side of the γ-ray peaks at 3664 keV and 3845 keV with same width are found to be a good representative as a background gate for the excitation energy spectra shown in red in the figures 3.46 and 3.47. These two figures prove that these γ-rays belong to the state at 4.087 MeV.

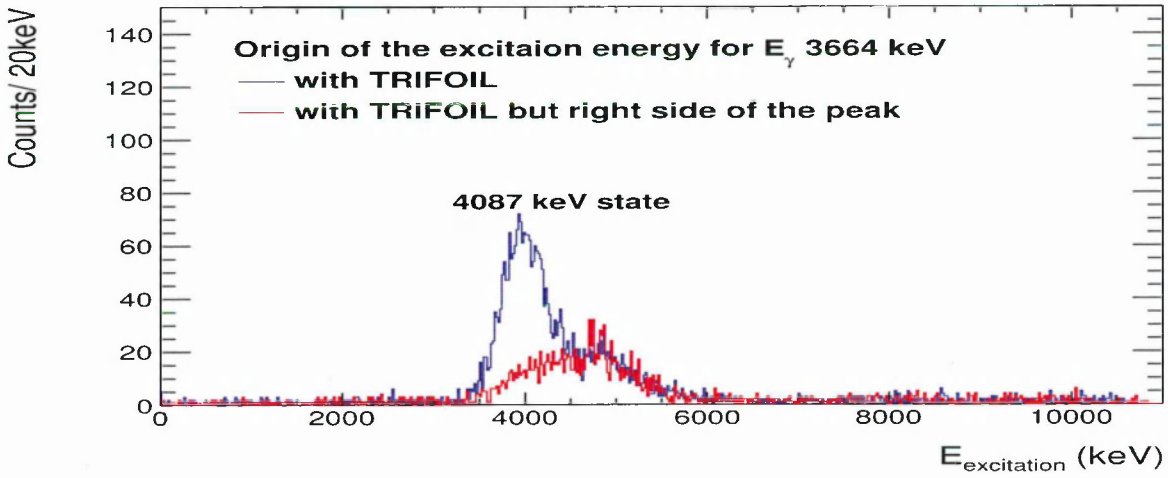

Figure 3.46: Excitation energy spectrum gated on a gamma ray at 3664 keV to see a state at 4087 keV ^{26}Na. For the background spectrum in red, the γ-ray limits, taken from the γ-ray energy spectrum, have the same width as in the 3664 keV γ-ray. And, this region corresponds to the right side of the γ-ray peak.

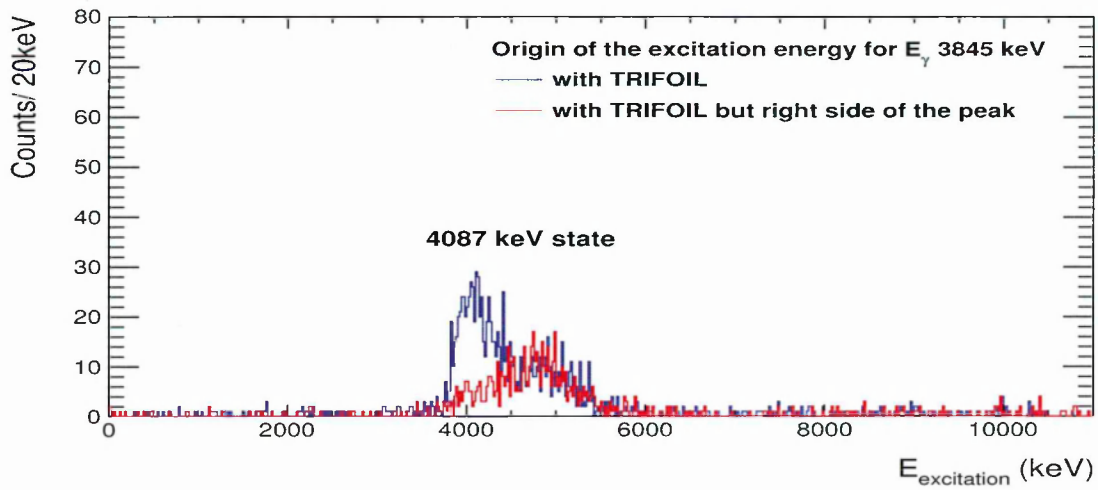

Figure 3.47: Excitation energy spectrum gated on a gamma ray at 3845 keV to see a state at 4.087 MeV ^{26}Na. For the background spectrum in red, the γ-ray limits, taken from the γ-ray energy spectrum, have the same width as in the 3845 keV γ-ray. And, this region corresponds to the right side of the γ-ray peak.

It's also noticed that the same excitation energy range between 3.5 and 4.5 MeV, as in figure 3.48, will provide a new γ-ray branch at 2275 keV to the postulated state at 4.087 MeV. It's because both the excitation energy range and the lower lying state at 1.805 MeV support this new cascade. The corresponding γ-ray spectrum can be seen in the figure 3.48.

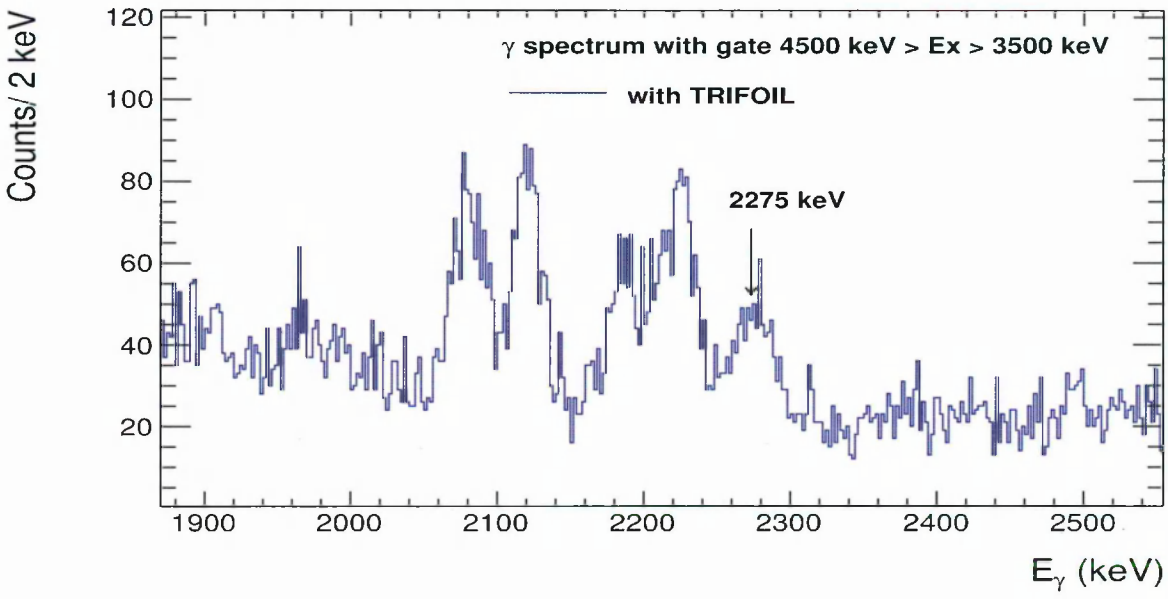

Figure 3.48: Individual gamma spectrum to check a gamma ray at 2275 keV decaying from a state at 4.087 MeV in ^{26}Na between excitation energy gate 3.5 MeV and 4.5 MeV.

For further investigation, the $\gamma - \gamma$ coincidence data might give an extra proof even if the statistics for $\gamma - \gamma$ coincidences get lower at high energies. However, 232 keV and 405 keV γ-rays from the lower lying states are seen in coincidence with 3664 keV and 3845 keV γ-rays to prove our claim about 3664 and 3845 keV γ-rays in the cascade from a new state at 4.087 MeV. Two $\gamma - \gamma$ coincidence spectra gated on separately 232 and 405 keV γ-rays are presented in the figure 3.49 and 3.50.

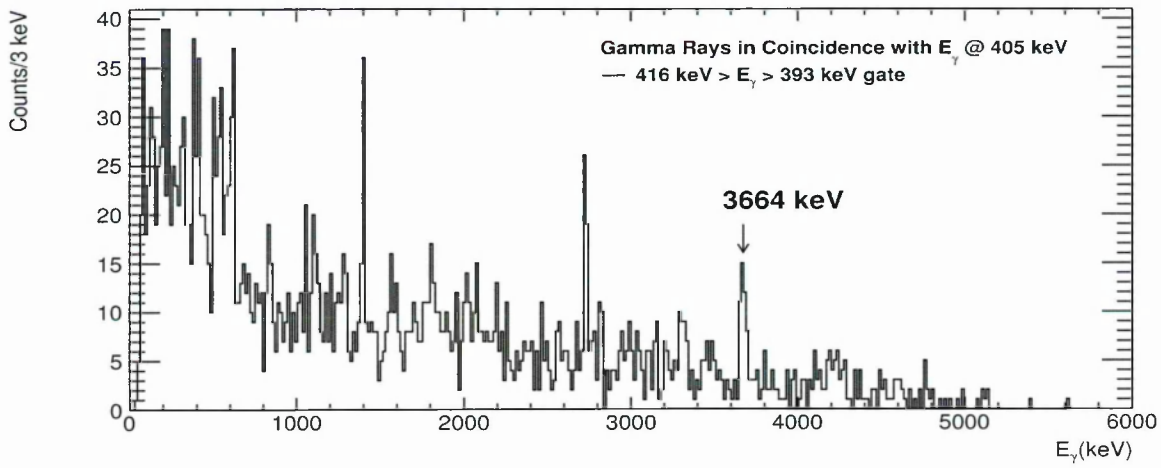

Figure 3.49: Coincidence gamma rays when gated on a 405 keV gamma ray in ^{26}Na

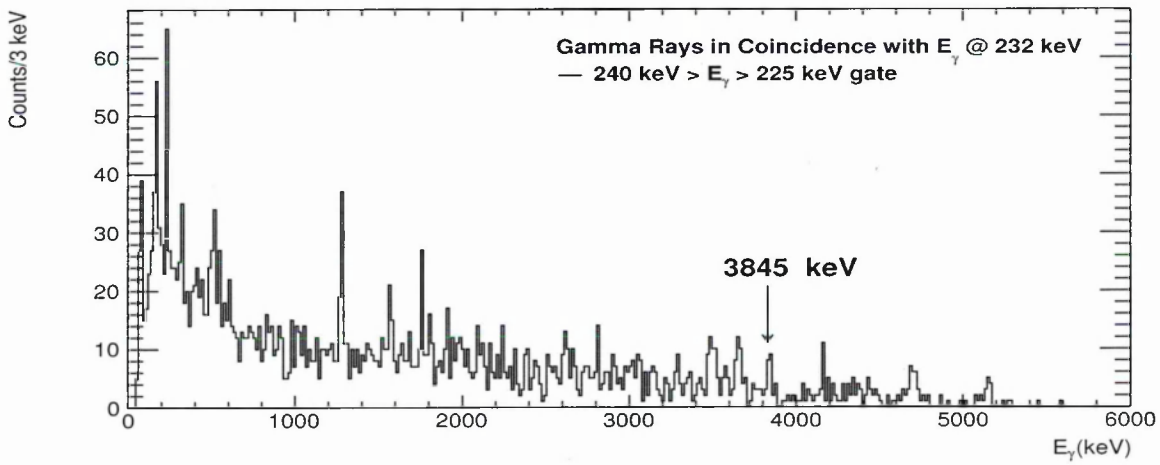

Figure 3.50: Coincidence gamma rays when gated on a 232 keV gamma ray in ^{26}Na

3.3.6 The Explanation of a New State at 4.800 MeV

Higher γ-ray energy ranges as in the figure 3.51 may have artificial count rise due to Compton edge of the higher lying states. For instance, some of the Compton edges for few

specific γ-rays are calculated as 4463 keV and 4557 keV from the higher energy γ-rays at at 4705 keV and 4799 keV. And, this makes difficult to see weak γ peaks. However, two strong γ-ray energies are obvious at 4705 and 4799 keV between the excitation energy 4.5 and 5.5 MeV in the figure 3.51. It can be noticed that they have more counts in the 4.5-5 MeV excitation energy limits.

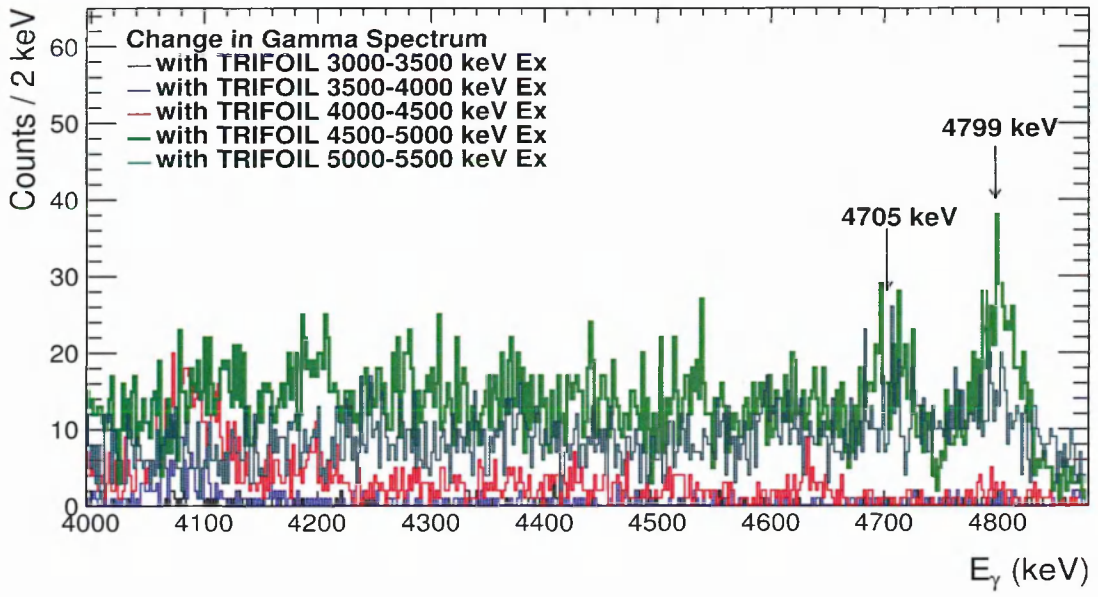

Figure 3.51: Gamma spectrum between 3 MeV and 5.5 MeV excitation energy to investigate a state at 4.800 MeV in ^{26}Na.

With even narrower excitation energy gate between 4.4 MeV and 5.4 MeV, the upper and lower panels in the figure 3.52 can still show the same γ-ray peaks.

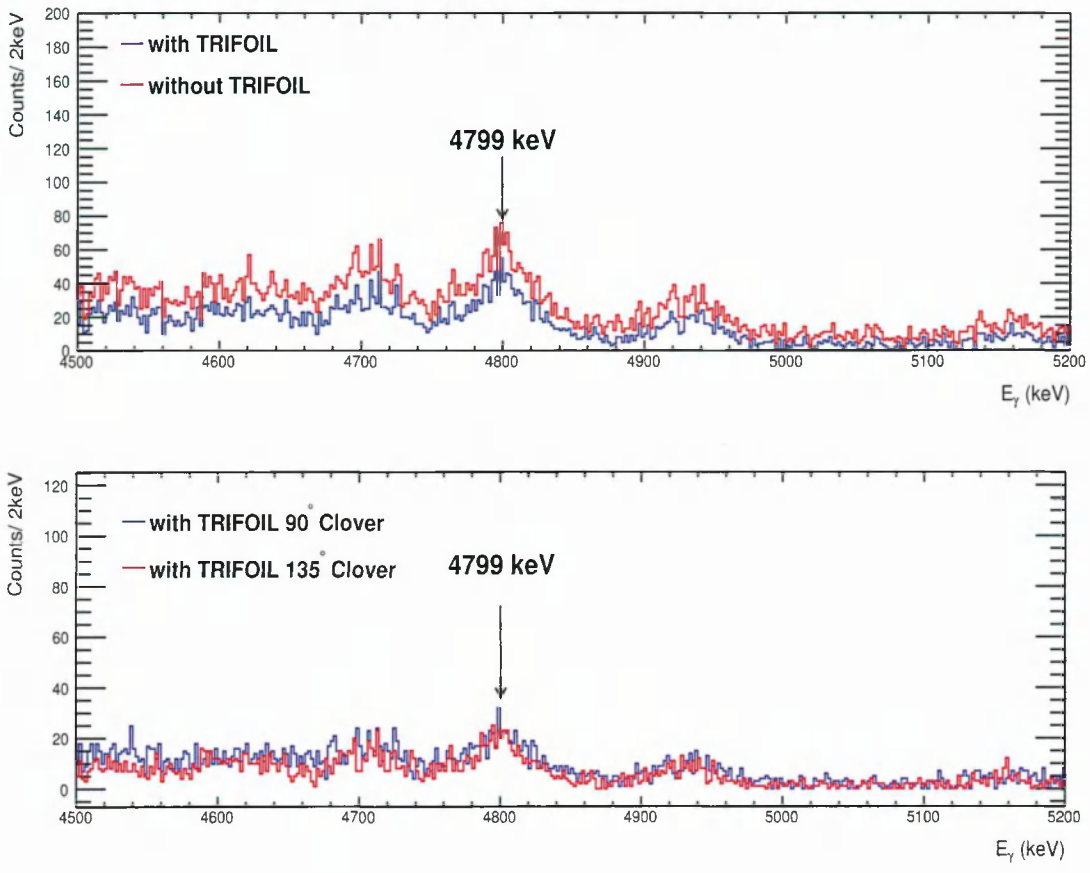

Figure 3.52: Gamma spectrum for narrow gate between 4.4 MeV and 5.4 MeV excitation energy to investigate a state at 4.800 MeV in ^{26}Na.

Once the γ-energy limits are identified in the γ-ray energy spectra, the excitation energy spectrum can be plotted by gating to the related γ energy at 4799 keV and its neighbouring region for background subtraction. This figure 3.53 enables us to make a quick decision about the excitation energy range where the γ-ray gate is originated. And, it definitely agrees with the excitation energy region around 4.8 MeV for 4799 keV γ-ray gate.

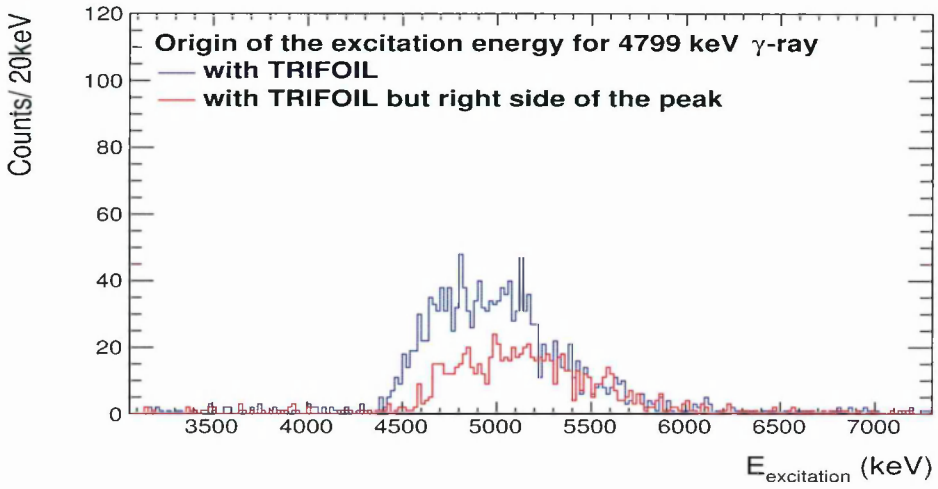

Figure 3.53: Excitation energy spectrum gated on a gamma ray at 4799 keV in ^{26}Na. For the background spectrum in red, the γ-ray limits, taken from the γ-ray energy spectrum, have the same width as in the 4799 keV γ-ray. And, this region corresponds to the right side of the γ-ray peak.

3.3.7 The Explanation of a New State at 4.597 and 4.932 MeV

As we go higher energies in γ-ray spectrum, there is this particular energy range between 4 and 4.6 MeV where the analysis gets very complicated due to high background and overlapping γ-ray peaks. One of the reasons is Compton tail of the higher energy *gamma*-rays are overlapping the real peaks. Figure 3.54 shows that the origin of the γ-rays in this energy region is mostly between 4.5 and 5 MeV. The region above 5 MeV also provides some contribution.

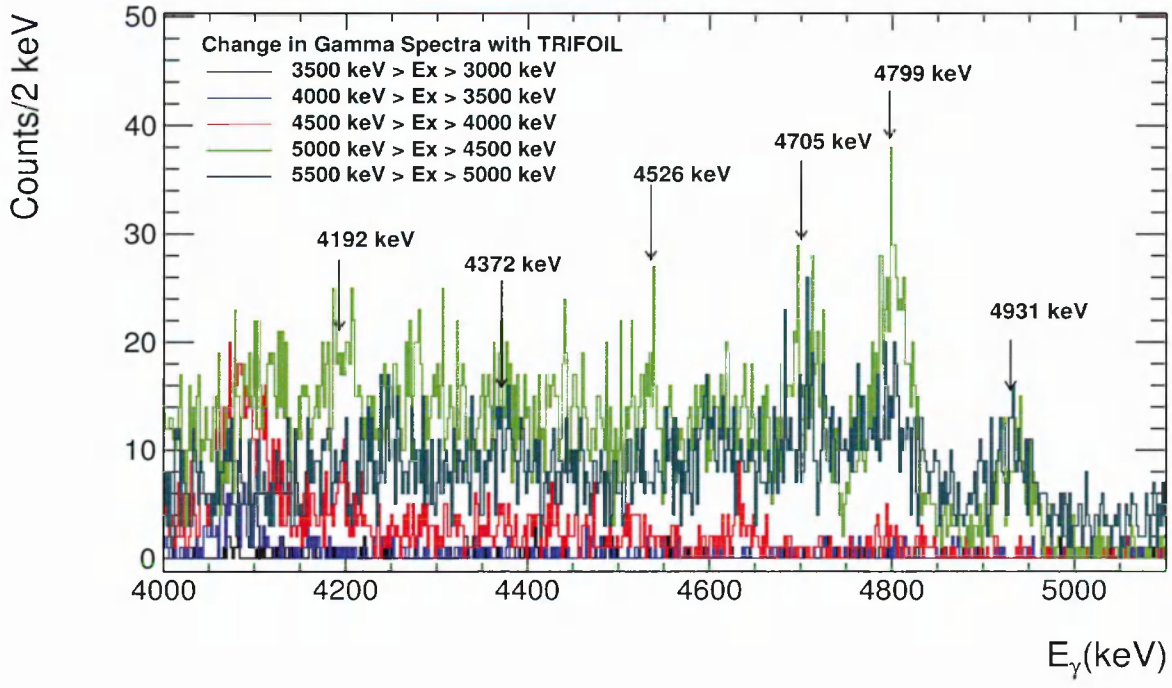

Figure 3.54: Gamma ray energy spectrum between 4000 and 5100 keV to identify γ-ray branches from 4932 keV state in ^{26}Na.

Figure 3.54 shows the region 4 MeV and 5 MeV with 2 keV binning due to the statistics. This indicates that the 4.5-5 MeV range of excitation energy is the source of several γ-rays. Peaks are still properly defined, so this gate is now carried to the figure 3.55 using 5 keV instead. A second order polynomial describes the background better in this region. Interestingly, almost other regions in the gamma ray spectrum have a background close to flat or a first order polynomial.

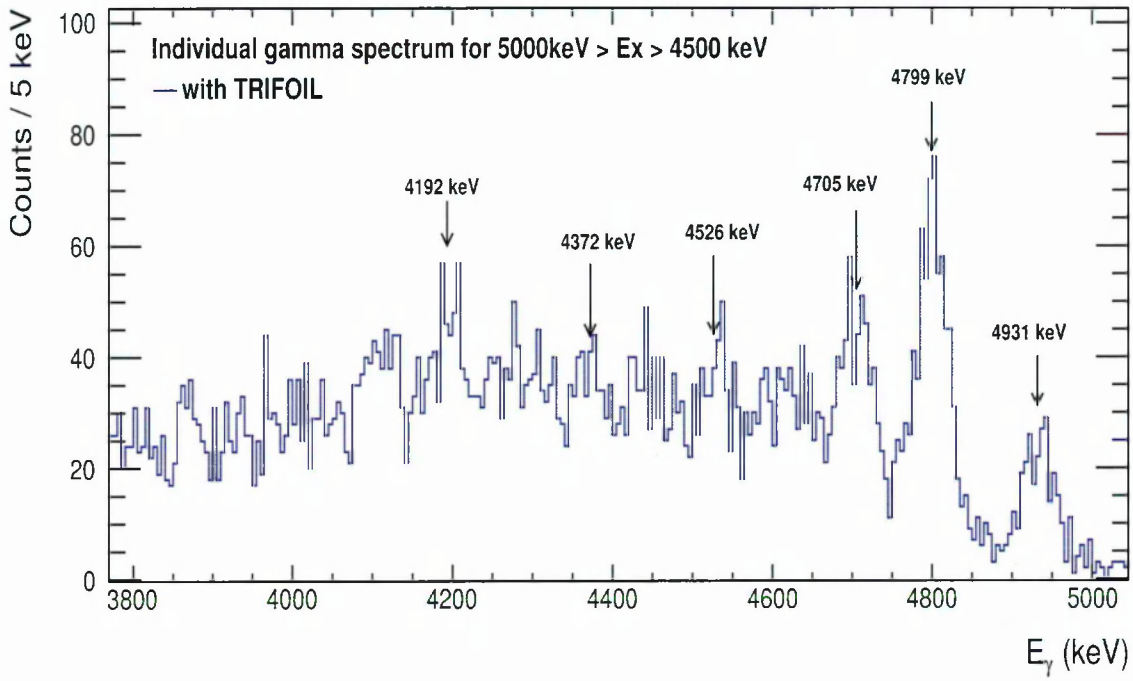

Figure 3.55: Individual gamma spectrum between 4.5 MeV and 5 MeV excitation energy range for a state at 4933 keV state in ^{26}Na.

It has been found that 4705 keV and 4931 keV γ-rays are the strong candidates of the γ branches decaying from a state at 4.932 MeV. On the other hand, other two γ-rays at 4192 keV and 4372 keV are in the γ branches of a state at 4.597 MeV. All these assumptions and further proofs are because of the ground state and the lower lying states at 232 keV and 405 keV. The γ-rays at 232 and 405 keV always supports a γ-ray cascade with higher γ-ray energies. Then, it becomes easier to add up two energies to reach the postulated higher energy excitation energies. If one plots excitation energy spectrum for a new state at 4932 keV by gating on the γ-ray energy at 4931 keV as seen before, the convincing result indicates that one of the claims above has already been proven by the figure 3.56.

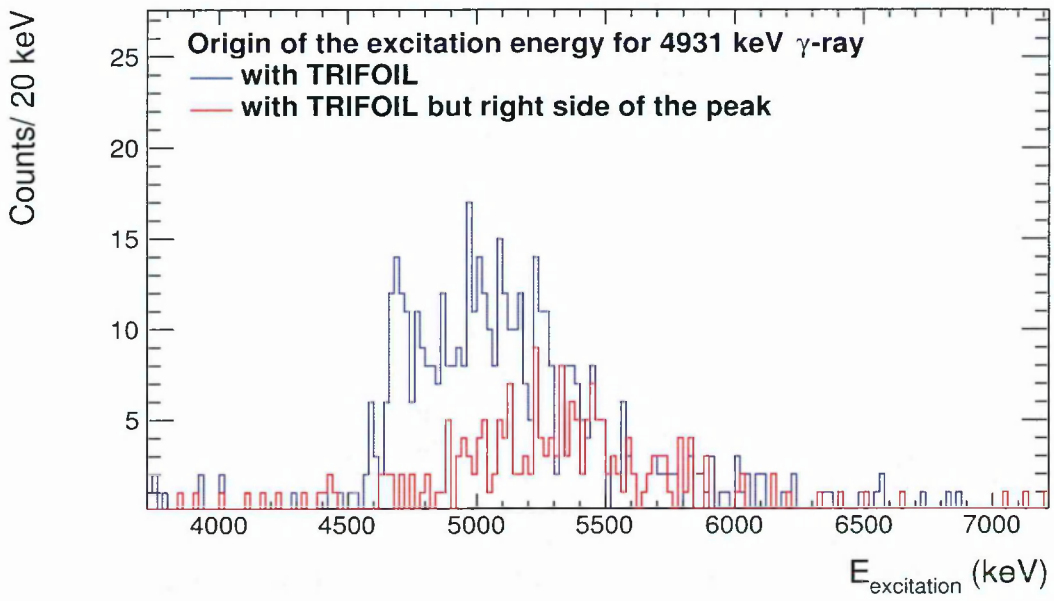

Figure 3.56: Excitation energy spectrum gated on a gamma ray at 4931 keV in ^{26}Na. For the background spectrum in red, the γ-ray limits, taken from the γ-ray energy spectrum, have the same Gaussian width as in the 4931 keV γ-ray. And, this region corresponds to the right side of the γ-ray peak.

3.3.8 The Explanation of a New State at 4.239 MeV

In the two figures 3.57 and 3.58, the γ-ray at 1104 keV will be investigated. Between the excitation energy range 1 MeV and 3 MeV, first figure has a strong 1275 keV γ-ray peak corresponding to the state at 1509 keV as displayed in the level scheme 1.7. This level scheme also shows another γ-branch at 1102 keV for the same state at 1509 keV. In contrast, the γ-ray spectrum in the first figure refers to the excitation energy range between 1.5 and 2 MeV without any indication of a γ-ray at 1104 keV. However, second figure is obviously showing the γ-ray at 1104 keV as it is decayed from higher excitation energy range between 4 and 5 MeV.

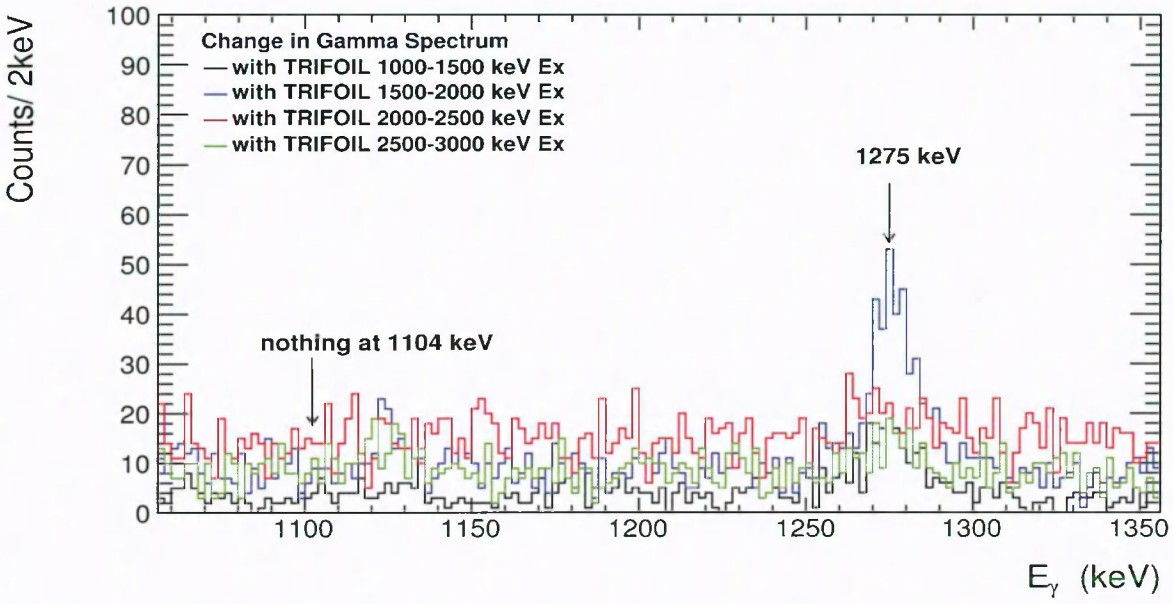

Figure 3.57: Gamma spectrum change between 1 MeV and 3 MeV excitation energy to investigate a state at 4239 keV via 1104 keV gamma ray in ^{26}Na.

Since we know for sure there is no state at 1104 keV as shown by figure 3.57, the only possibility is that the 1104 keV γ-ray comes from a higher lying state where the excitation energy range corresponds to 4-5 MeV in red and green as in figure 3.58. The only states known for sure in this range are the 3.135 and 3.511 MeV states. By making the assumption with these two known states, we should either have a new state at 4.239 MeV or at 4.615 MeV which decay via 1104 keV γ-ray. Then, the next thing is to check what the excitation energy spectrum gives when gated on a gamma ray at 1104 keV.

In figure 3.59, the visible excess between the excitation energy range 4.1 and 4.8 MeV implies more support for a state at 4.239 MeV than a state at 4.615 MeV.

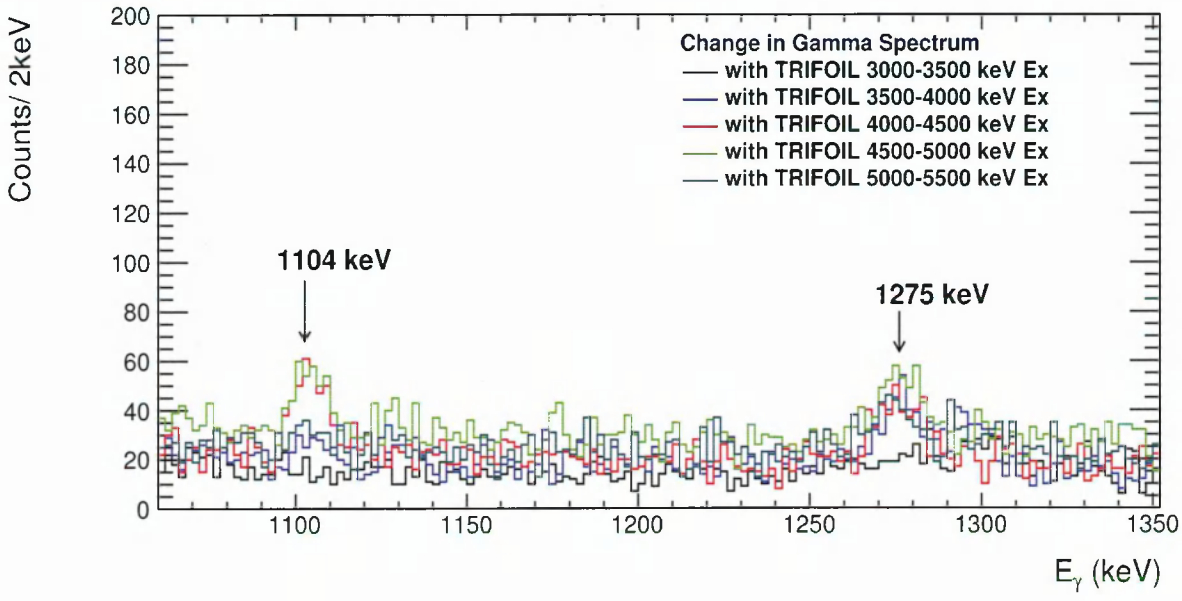

Figure 3.58: Gamma spectrum change between 3 MeV and 5.5 MeV excitation energy to investigate a state at 4239 keV via 1104 keV gamma ray in ^{26}Na.

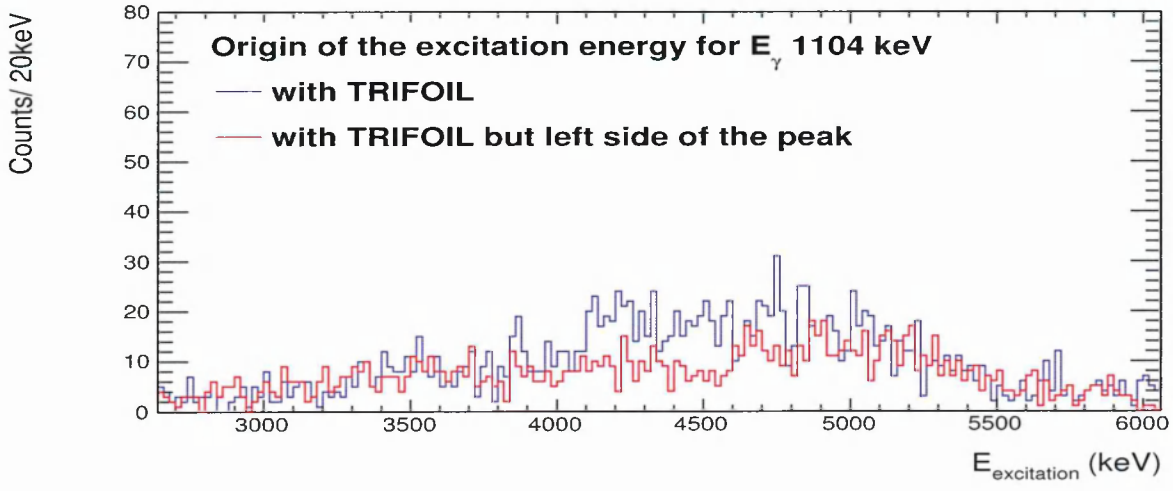

Figure 3.59: Excitation energy spectrum gated on a gamma ray at 1104 keV in ^{26}Na. For the background spectrum in red, the γ-ray limits, taken from the γ-ray energy spectrum, have the same Gaussian width as in the 1104 keV γ-ray. And, this region corresponds to the left side of the γ-ray peak.

3.3.9 The Explanation of a New State at 5.155 MeV

One of the highest γ energies that we have managed to detect is the γ-ray at 5154 keV. And, it is enough to look only the gamma spectra with excitation gates above this energy. For that reason, the figure 3.60 should be only checked for the excitation energy range above 5 MeV.

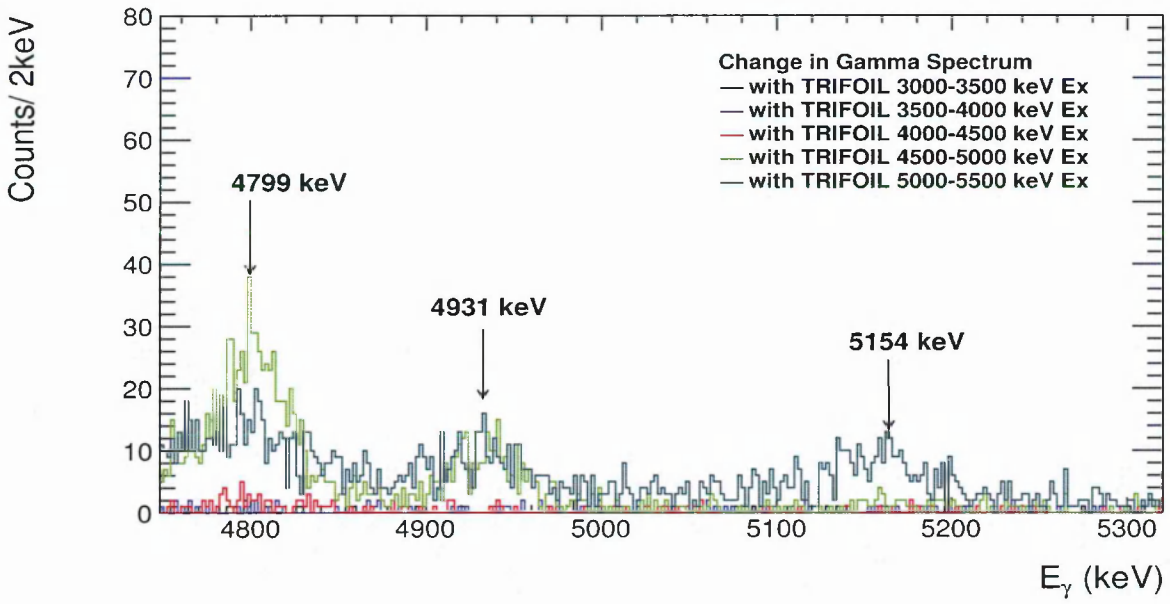

Figure 3.60: Gamma spectrum change between 3 MeV and 5.5 MeV excitation energy to investigate a state at 5163 keV in ^{26}Na.

As all the other new states above 5 MeV, this higher lying state at 5.155 MeV has also only one γ-ray branch which decays to the ground state. To decide the state energy, one can plot the excitation energy spectra gated on both the γ-ray at 5154 keV and its adjacent background to the right side of the peak as shown in the figure 3.61. This will bring the indication about where the state should be. From the subtraction of the excitation spectra in the same figure, one can narrow down the limits of the energy for

the populated state at 5.155 MeV.

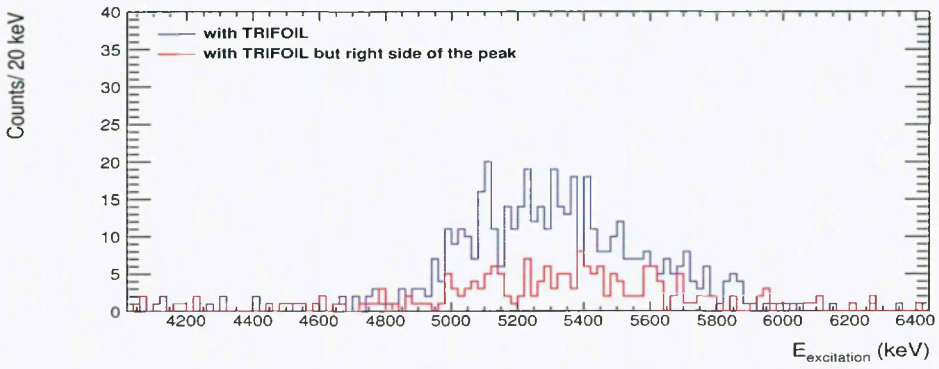

Figure 3.61: Excitation energy spectrum gated on a gamma ray at 5154 keV in ^{26}Na.

As one can notice, excitation energy spectra in general have poor resolution in comparison to good gamma resolution by HPGe detectors especially at higher energies. That's why we always use particle detector and gamma detectors together to confirm each others' claims. By gating only on an excitation energy cannot be enough due to close staying states next to each other, so we gate on a individual and exclusive gamma rays as a gate like in here.

3.3.10 The Explanation of a New State at 5.276 MeV

The main focus in this part of the analysis is the new γ-ray energy which seems to appear only in the excitation energy range between 5 MeV and 5.5 MeV. And, the figure 3.62 is a very good representative of showing the way how the γ-ray at 3511 keV changes for different excitation energy gates. The counts and intensity of the γ-ray of 3511 keV decreases slowly as the excitation energy increases. When the excitation energy gets to the energy limits above 5 MeV, it seems the peak splits into two as two different γ-rays. Because of the resolution of the γ detector at this energy, it's difficult to solve them as

completely two separate γ peaks.

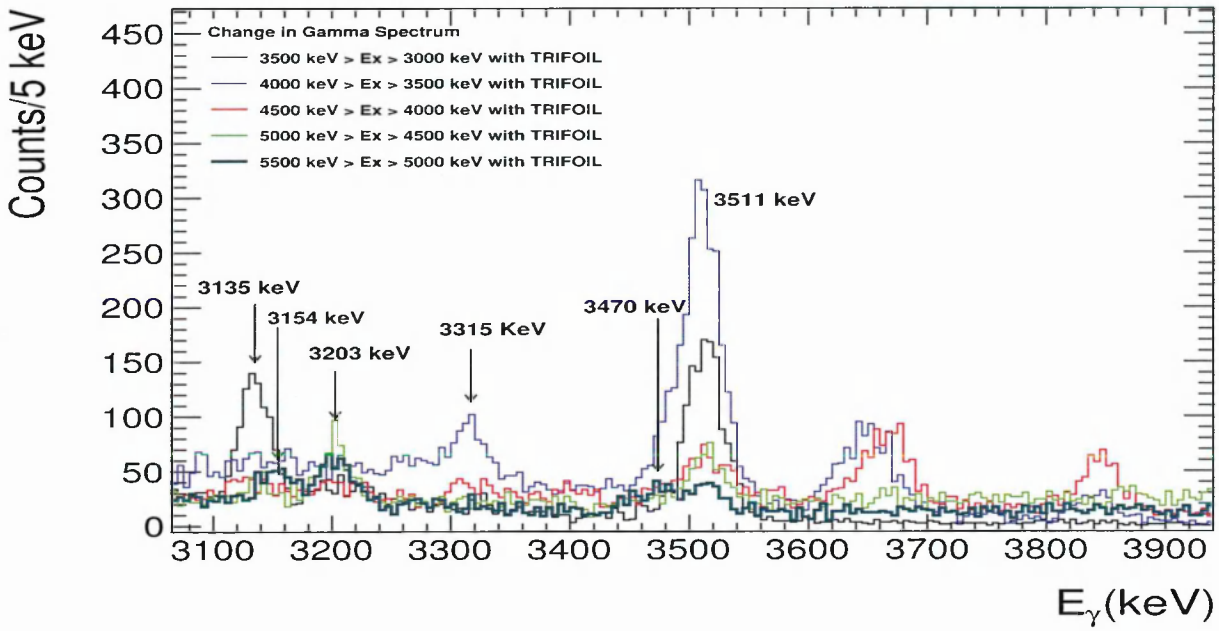

Figure 3.62: Gamma Spectrum Change for 3315 keV and 3470 keV gamma ray in ^{26}Na.

The separation of these individual peaks can be seen better in figure 3.63 because this version of the gamma spectrum displays much closer look on the γ-rays of interest. And, that will indicate that there might be indeed two peaks by falling into the similar γ energy range as in the adjacent γ-ray peaks at 3154 keV and 3203 keV for a comparison.

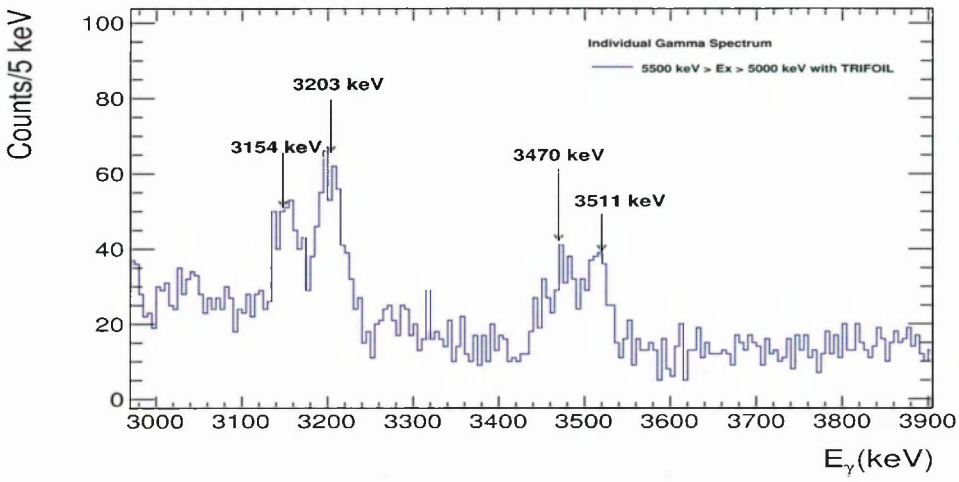

Figure 3.63: Individual Gamma Spectrum for 3315 keV and 3470 keV gamma ray in ^{26}Na.

Then, the next step is to confirm that there is another higher lying state which indeed emits this γ-ray at 3470 keV. The simple way to check this is to compare the excitation energy spectra gated on both the γ-ray energy limits of 3470 keV where there is possibly no contribution from the adjacent peak at 3511 keV. This is done by giving as narrow limit as we can because we can always apply a correction factor to retrieve the entire excitation energy spectrum corresponding to that γ-ray. The second excitation energy spectrum shown in the figure 3.64 as in black represents the background area on the left side the γ-peak at 3470 keV. If one does the subtraction of the two spectra, mostly the excitation energy limits after 4 MeV will remain only. In the end of trying all possible options to reach that excitation energy limits by combining lower lying states and the γ-ray at 3470 keV, it's concluded that 1805 keV γ energy is the best match to build a cascade up to the excitation level at 5276 keV. Namely, this new state decays only to 1805 keV state via 3470 keV γ-ray.

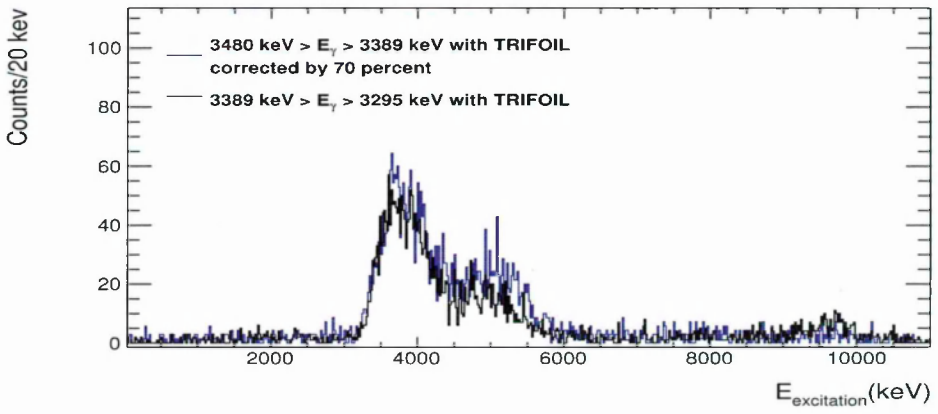

Figure 3.64: Excitation energy spectrum gated on a gamma ray at 3470 keV in ^{26}Na.

3.3.11 The Explanation of a New State at 5.384 MeV

The two highest γ-ray energies detected in our system are shown in the figure 3.65. The excitation energy between 5 MeV and 5.5 MeV is also the highest limits that we observe due to the highest proton detected in DSSSD detectors in the SHARC set up. Even though the detail analysis is carried out to find any γ-ray branch that can be in the cascade from the state of interest here as claimed at 5384 keV, it is found that there is only ground state decay for the highest state of 5384 keV via the γ-ray as seen in the gamma spectra below.

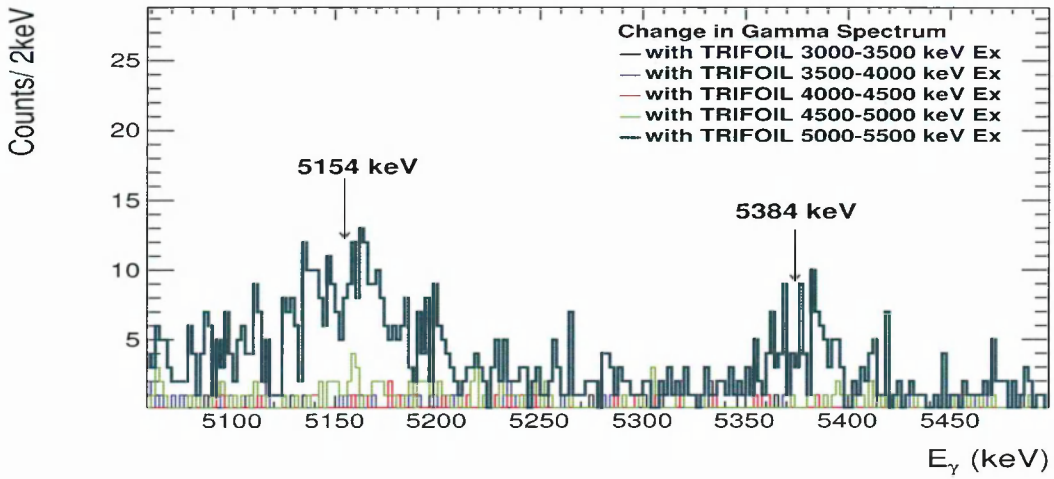

Figure 3.65: Gamma spectrum change between 3 MeV and 5.5 MeV excitation energy to investigate a state at 5384 keV in ^{26}Na.

After having the γ-ray energy limits from the gamma spectrum gated on excitation energy above 5 MeV, the excitation energy spectrum can be checked with the gate on a γ-ray of interest and the possible representative side of the same γ peak. The subtraction of the two spectra in the figure 3.66 will then show exact energy limits of the populated state at 5384 keV.

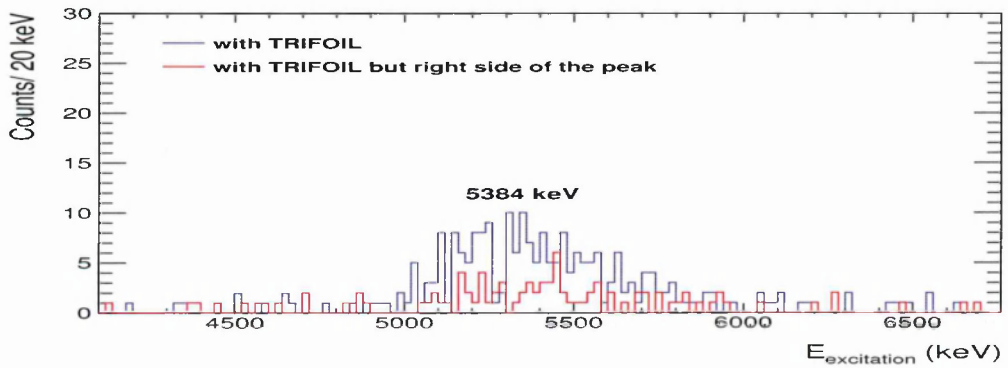

Figure 3.66: Excitation energy spectrum gated on 5384 keV gamma ray above 3 MeV excitation energy in ^{26}Na with TRIFOIL gate.

3.4 The Formalism of the Branching Ratio Calculations of the States in ^{26}Na

As a guide to the γ-ray analysis, the γ-ray peak width was first investigated as a function of energy. It is noted through the analysis that most of the work should be done separately for 90° and 135° TIGRESS clovers. The final result will then be deduced by combining the two results. The excitation energy gate is set as wide as possible, and then all the gamma peaks in 90° and 135° clovers are investigated for the full width half maximum (FWHM), the resolution of the γ-ray detectors. This enables us to set the σ parameter for individual γ-ray peaks in the spectrum during the fitting process. It gives precise measurement for Gaussian functions in both TIGRESS clover angles. Since all γ-rays are at different energies in different clovers, the energy dependence of σ value as shown in the figure 3.67 is varying. The sigma values are given by the ROOT program when Gaussian and first order polynomial background function are applied together to get the total counts under each γ-ray peak. The main purpose of the figure in 3.67 is to give an idea about the resolution of the detectors which is linked to the FWHM equal to $2.355\times\sigma$ value.

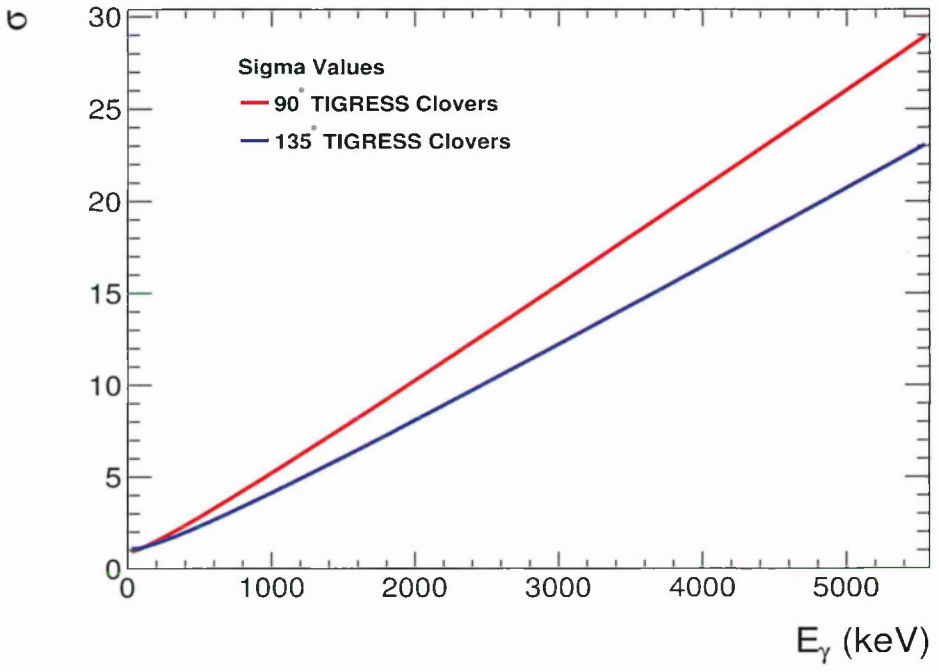

Figure 3.67: The sigma values in keV, where σ is equal to FWHM/ 2.35, are measured for γ-ray energy resolution in both 90° and 135° TIGRESS clovers.

Each clover at different angle with regard to the beam direction has its own characteristic behaviour, at 90° the peaks are expected to be broader due to the Doppler broadening. In addition to this fact, it is found that some γ-rays appear only in one clover due to its direction and energy. This makes us to investigate the gamma rays further since they may come from the stationary radiated surroundings. It may turn out that this gamma ray does not originate in the reaction of interest.

The function used for fitting the data in figure 3.67 is of the type of "$x + \sqrt{x} +$ *constant*". The charge pairs created in the semi conductor detectors depend on the deposited energy by the number of gamma rays detected. Thus, the standard deviation can be calculated by the square root of the counts by giving the sigma value as an important

parameter in the Gaussian function.

In the most basic case, the Gaussian function can be shown as:

$$f(x) = height \times \exp^{\frac{-(x-mean)^2}{2\times(sigma)^2}} \tag{3.1}$$

where height, mean, and sigma values refer to the parameters in Gaussian function. According to the formula above, the sigma parameter is also defined the shape of the Gaussian by helping to calculate the width of the peak.

Firstly, gamma spectra are plotted in both 90° and 135°. With the limits of the corresponding state energy, the integrals under the individual γ-ray peaks are found by fitting one Gaussian function and one first order polynomial background on to the data in the case of one isolated peak. Otherwise, two Gaussian functions and a first order polynomial as a background are used for fitting. In addition, to get the error in each integral (count), four values corresponding to the peak of interest are used respectively in the code for ROOT, data analysis framework: the limits of the width of the Gaussian function, all the parameters of the Gaussian function stored in an array, and the corresponding covariance matrix created by the error parameters of the same Gaussian function.

After calculating the branching ratio values for each branch separately for the 90° and 135° data, the weighted average formula in the equation 3.2 is used to calculate the final branching ratios.

$$W.A. = \frac{(\frac{x_1}{\sigma_1^2} + \frac{x_2}{\sigma_2^2})}{(\frac{1}{\sigma_1^2} + \frac{1}{\sigma_2^2})} \qquad \sigma = \sqrt{\frac{\sigma_1^2\sigma_2^2}{\sigma_1^2 + \sigma_2^2}} \tag{3.2}$$

The symbols in the equation 3.2 represent the weighted averaged final value (W.A.) and its error (σ). And, the values of x_1 and x_2 are the branching ratios for a particular γ-ray detected in different clover angles.

The values of branching ratios are derived from the ratio of the efficiency corrected integral value of a γ-ray peak to the overall integral of all the branches from the chosen state. Each integral under the γ-ray peaks represents the total counts detected for this peak. That is to say the branching ratio (BR) can be formulated in a general case as following.

$$N = x + y + ... \quad or \quad N = (\frac{n_x}{\epsilon_x}) + (\frac{n_y}{\epsilon_y}) + ... \tag{3.3}$$

where N is the total counts in all the detected γ-rays decaying from a specific state. And, $\frac{n_y}{\epsilon_y}$ represents the efficiency corrected counts for an individual γ-peak. Therefore, BR_i gives the branching ratio of an individual γ-ray, labelled as x, y, z, etc., emitted from a state.

$$BR_i = \frac{\frac{n_i}{\epsilon_i}}{N} \tag{3.4}$$

In the case of two branching ratios from a state, $f_1(x,y) = \frac{x}{x+y}$ and $f_2(x,y) = \frac{y}{x+y}$ represent the functions used to calculate the integral errors by using error propagation among uncorrelated values. In here, x, y, s_x, and s_y values represent the efficiency corrected counts of the γ-ray peaks and their standard deviations (errors). If one writes the standard deviation of a function in more general case,

$$s_f = \sqrt{(\frac{\partial f}{\partial x})^2 \times s_x + (\frac{\partial f}{\partial y})^2 \times s_y + (\frac{\partial f}{\partial z})^2 \times s_z + (\frac{\partial f}{\partial t})^2 \times s_t + ...} \tag{3.5}$$

After the necessary calculations have been made, the standard deviations, showing the errors, in the case of two γ-ray branches are :

$$s_{f_1} = \frac{1}{(x+y)^2}\sqrt{x^2 s_y^2 + y^2 s_x^2} \tag{3.6}$$

$$s_{f_2} = \frac{1}{(x+y)^2}\sqrt{x^2 s_y^2 + y^2 s_x^2} \tag{3.7}$$

This stresses that the errors in branching ratios must be equal when just two different γ-rays are emitted from a specific state.

For three branches, x, y, z, s_x, s_y, and s_z values represent the efficiency corrected integral values of the peaks and their standard deviations (errors). And also, $f_1(x,y,z) = \frac{x}{x+y+z}$, $f_2(x,y,z) = \frac{y}{x+y+z}$, and $f_3(x,y,z) = \frac{z}{x+y+z}$ represent the functions used to calculate the errors in branching ratios.

$$s_{f_1} = \frac{1}{(x+y+z)^2}\sqrt{(y+z)^2 s_x^2 + (s_y^2 + s_z^2)x^2} \tag{3.8}$$

$$s_{f_2} = \frac{1}{(x+y+z)^2}\sqrt{(x+z)^2 s_y^2 + (s_x^2 + s_z^2)y^2} \tag{3.9}$$

$$s_{f_3} = \frac{1}{(x+y+z)^2}\sqrt{(x+y)^2 s_z^2 + (s_x^2 + s_y^2)z^2} \tag{3.10}$$

And lastly, for four branches, x, y, z, t, s_x, s_y, s_z, and s_t values represent the efficiency corrected integral values of the peaks and their standard deviations (errors). In addition, $f_1(x,y,z,t) = \frac{x}{x+y+z+t}$, $f_2(x,y,z,t) = \frac{y}{x+y+z+t}$, $f_3(x,y,z,t) = \frac{z}{x+y+z+t}$, and $f_4(x,y,z,t) = \frac{t}{x+y+z+t}$ represent the functions used to calculate the errors in branching ratios. if $S = s_x^2 + s_y^2 + s_z^2 + s_t^2$ and $N = x+y+z+t$, The general formula can be written when i shows the γ-ray branch of interest and j refers to the efficiency corrected counts as given x, y, etc. as earlier in the equation 3.11.

$$s_{f_i} = \frac{1}{(N)^2}\sqrt{(N-j)^2 s_j^2 + j^2(S - s_j^2)} \tag{3.11}$$

3.4.1 Explanation of the Background and the γ-Ray Peak Correction Factors

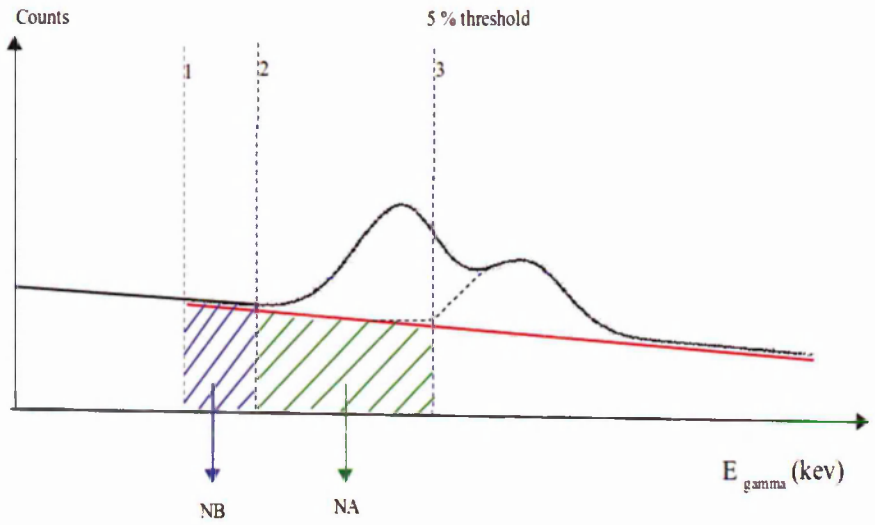

Figure 3.68: Background and Peak Correction Coefficient Explanation Diagram

The diagram drawn above reflects a fundamental idea and a method applied throughout the analysis. It's not always possible to get only one strong peak without any other contaminant peak nearby. Thus, a bit more common and complicated example here is chosen as seen in the figure 3.68. In this example, two Gaussian peaks have overlapping area due to their close mean values and sigma values. The width of each Gaussian is set up as $8 * \sigma$ to make sure that almost 100% of the peak is covered. Then, the 5% threshold rule is introduced to get the highest and the best ratio of the peak involved in the selection of the peak of interest process. In this method, starting from the left side of the first peak, the fit of the first Gaussian peak will scan bin by bin until the ratio of the integral of the second Gaussian peak to both Gaussian peaks reaches to 5% value. This is valid only the

peak of interest is the one on the left because the ratio will change to other side for the peak on the right. The program will note and print the x value where this 5% ratio starts which is marked with the dashed line number 3. By knowing the exact x limit, we can know the range from dashed line number 2 to 3. Then, the entire Gaussian range of the first peak on the left helps us to ask the program to calculate the ratio of the integrals of the area from the fit between the dashed lines 2 and 3 to the area under the fit of the full Gaussian range of this peak. This ratio will tell us the proportion of the contamination from the second peak. The figure 3.70 is one example of this case applied. The x axis values for dashed line 1 and 2 together with the percentage of the area where we only see the first peak are shown in the same figure, so the information can be easily read out from the plots. This ratio is called "peak correction factor (PCF)".

Now, we can introduce another coefficient to scale the background histogram which is taken by using a selected limits on the x axis shown as dashed line number 1 to 2. It's important to take into account the slope in the red polynomial background line. If the histogram for the blue marked area is multiplied by the scaling factor of $\frac{NA}{(NB*PCF)}$ which is called "background correction factor", (BCF), one would basically retrieve the representative histogram of the background just below the first peak for its entire range which spans $8 * \sigma$. In this occasion, it doesn't matter how wide or narrow the limits of the background histogram will be decided, so this gives the analyser flexibility. It is much more crucial when there are many peaks next to each other by restricting the choice of background limits for the background histogram. This complex concept will only be mentioned in here as a reference for the following examples of the γ-ray and the excitation energy spectra.

3.4.2 The Presentation of the γ-ray Branches for Particular States

The states at 0.232 MeV, 2.195 MeV, 2.225 MeV, 4.305 MeV ,and 4.932 MeV are chosen here to be presented for the explanation of the branching ratios of each individual γ-ray peaks. This energy range will also cover at least one example of the lower, medium, and higher energy γ-rays seen in the experiment.

One of the lower lying states at 0.232 MeV and its two γ-ray branches are shown in the figure 3.69. These two branches are decaying to 82 keV state and the ground state. The fitting actually gives slightly different numbers for the mean value and the total count detected for each single peak, this is noticeable in the figure 3.69. With regard to fitted first order polynomial as a background, it shows very smooth and flat nature here. This is because there is no neighbouring γ-rays within the similar γ-ray energy range to contribute to the counts of the γ-ray of interest, and both the Compton edge and the continuum of the higher γ-rays do not cause any issue in this region of γ-ray energies. As shown here in the first example, all analysis is carried out separately for different clovers, and then the final branching ratio is calculated by a weighted average of the two. as in the equation 3.2. The shape of the Gaussian functions suggest here that the branching ratios of same γ-ray, for instance at 150 keV, are similar in value in different clover angles.

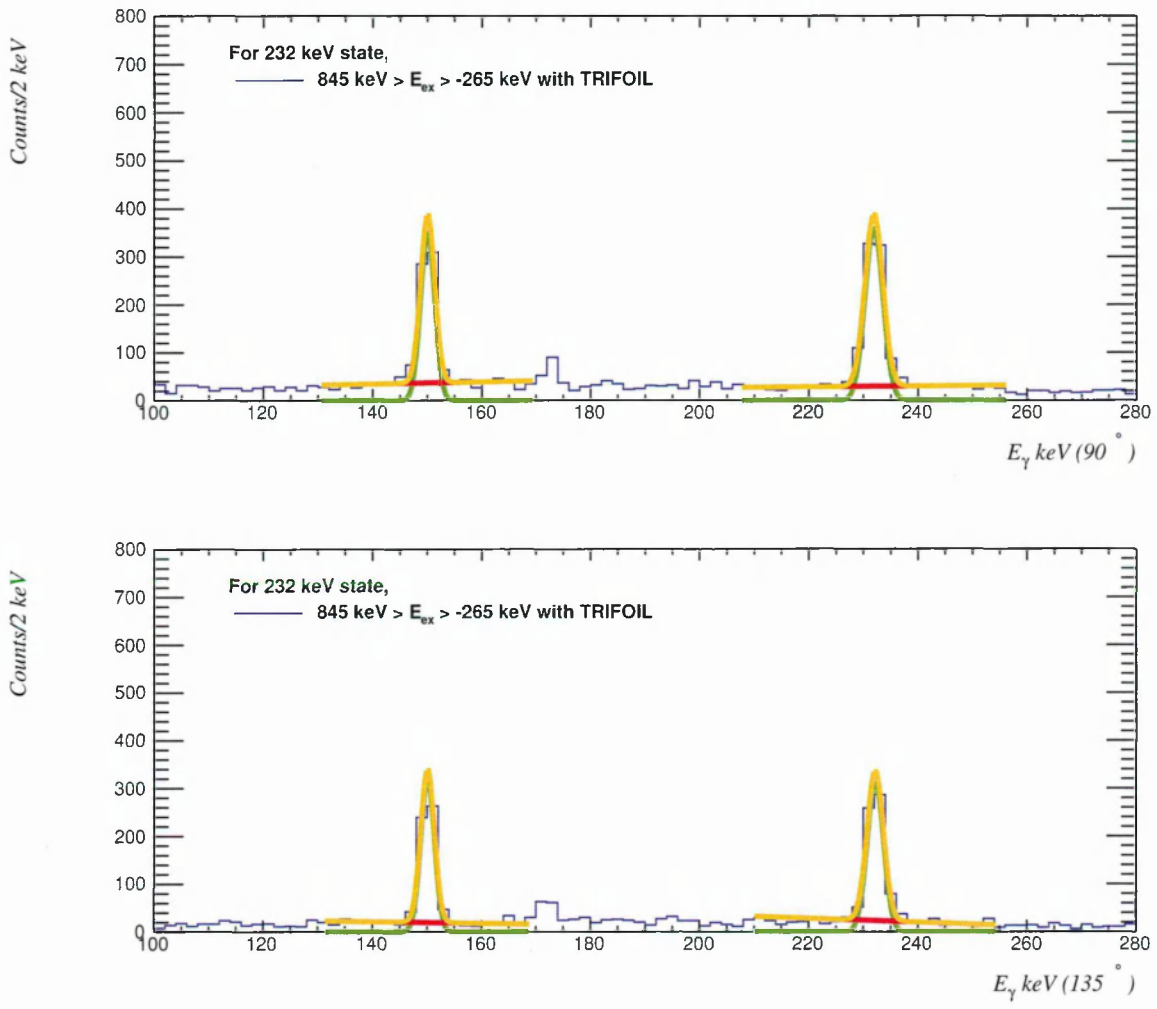

Figure 3.69: The γ-ray branches of the 232 keV state in ^{26}Na with TRIFOIL gate.

Now, if we move to the higher state at 2.195 MeV in the next example, overlapping γ-ray peaks can be seen. This causes a problem when finding the integral and the error under the γ-ray peaks which will eventually be used in the branching ratio calculations as explained in the section 3.4. This state at 2195 keV turned out to have two γ-ray branches going to the state at 0.232 MeV and the ground state. These γ-rays, emitted from the state 2.195 MeV, have adjacent γ-rays to the left of the γ-ray peak of interest. Therefore, the 5% threshold rule is applied here as the details are explained in the section

3.4.1. Thus, the 44.18 % and the 63.25 % of the 2195 keV γ-ray peaks in 90° and 135° clover angles has the counts coming from only the γ-ray of interest, not the adjacent γ-ray peak contribution.

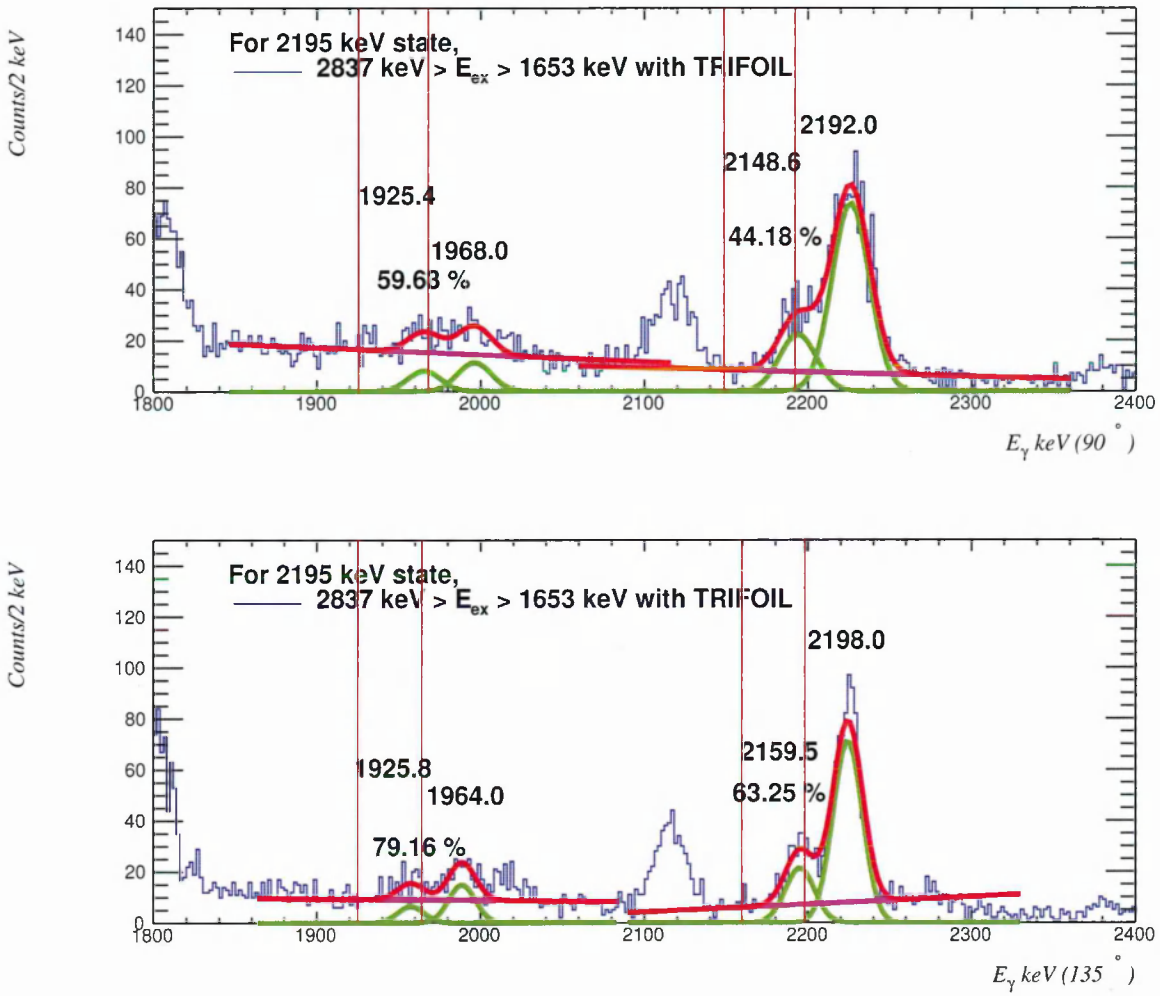

Figure 3.70: The branches of the 2195 keV state in ^{26}Na with TRIFOIL gate.

The same thing is seen for the lower γ-ray branch at 1962 keV for the state at 2.195 MeV. There is still neighbouring γ-ray contribution to the counts of the weak γ-ray peak at 1962 keV to be considered. This is possible by defining two separate Gaussian functions and a first order polynomial function as the fit function seen in the figure 3.70. In that way,

one can choose the Gaussian corresponding to the γ-ray peak of interest. The program is designed to give all the information; such as contamination ratio from adjacent peak, FWHM, etc., about this γ-ray peak for convenience by using the fit parameters.

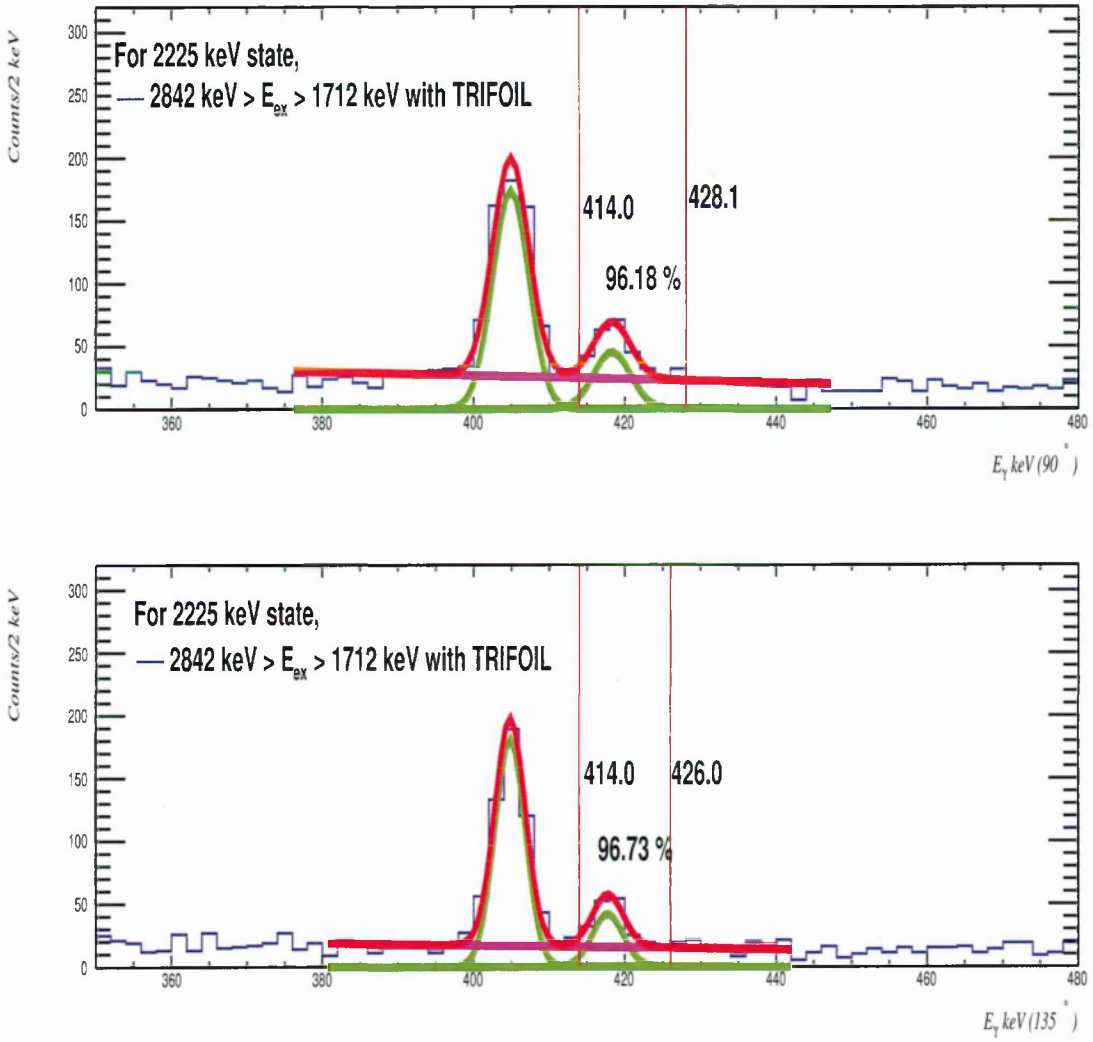

Figure 3.71: The lower branch of the 2225 keV state in ^{26}Na with TRIFOIL gate.

The state at 2.225 MeV (see fig.3.71 and 3.72) is one of the nice examples to show how important it is to use different sigma values as shown in the figure 3.67 for different γ-ray energies. The width of the Gaussian functions for the γ-rays at 418 keV and 2225

keV are noticeable different. On the other hand, it's important to use similar sigma values for fitting of the γ-rays at both 405 keV and 418 keV in the figure 3.71. Similarly, the γ-rays at 2185 keV and 2225 keV in the figure 3.72 have the same situation. However, it's possible to calculate the percentage of the contribution of each peak in the overlapping areas. This γ-ray limits for a particular γ-ray branch of a state will be deployed in the calculation of the proton and gamma-ray angular distributions. In addition to the lower γ-ray branch of the 2225 keV state, the higher branch also shows different peak limits and percentage in 90° and 135° clovers.

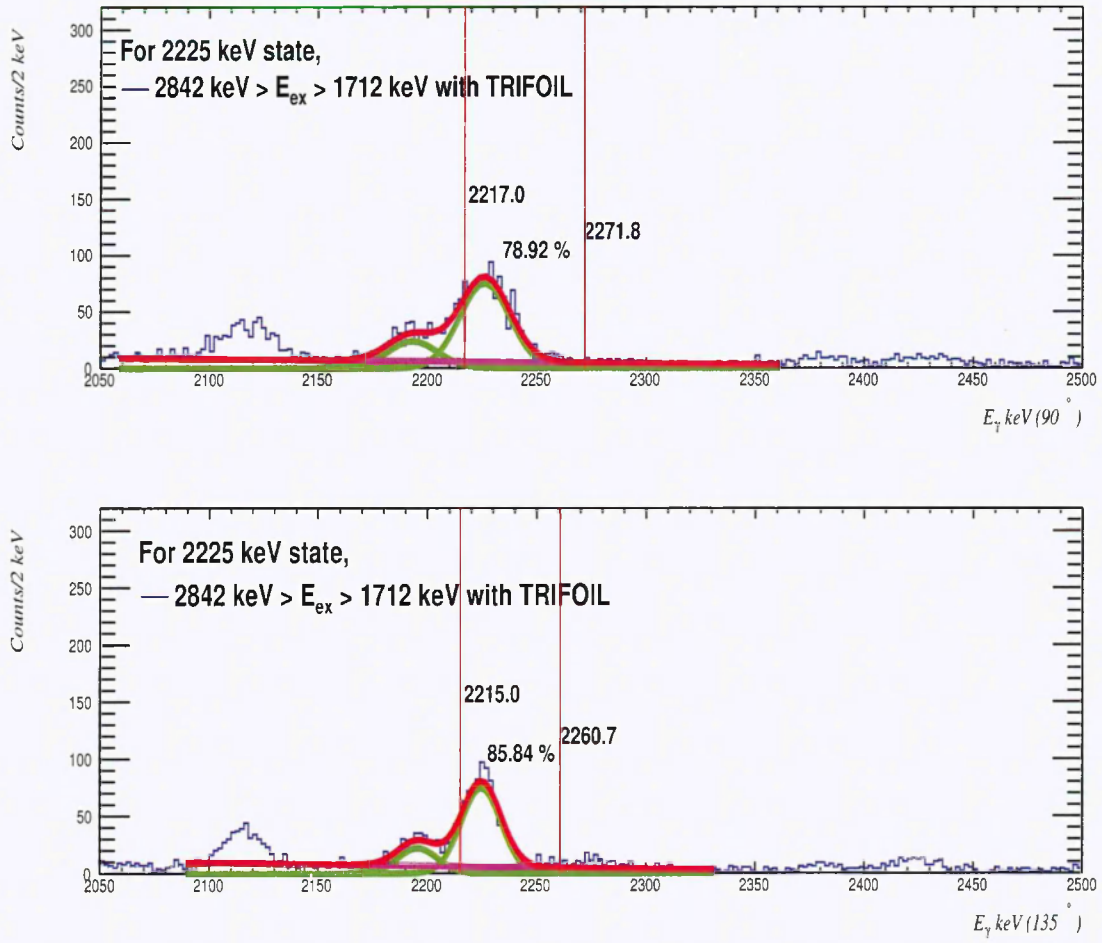

Figure 3.72: The higher branch of the 2225 keV state in ^{26}Na with TRIFOIL gate.

The next example is one of the higher lying states at 4.305 MeV. The energies of γ-rays that are emitted directly by this state are deduced to be 790, 2080, 2191 keV. The lower energy γ-ray branch is so clean as seen in the figure 3.73. However, the higher γ-ray branches have adjacent γ-rays from another states in the next figure 3.74. For this reason, four Gaussian functions and a first order polynomial function can be used to fit the peaks as in the figure 3.74.

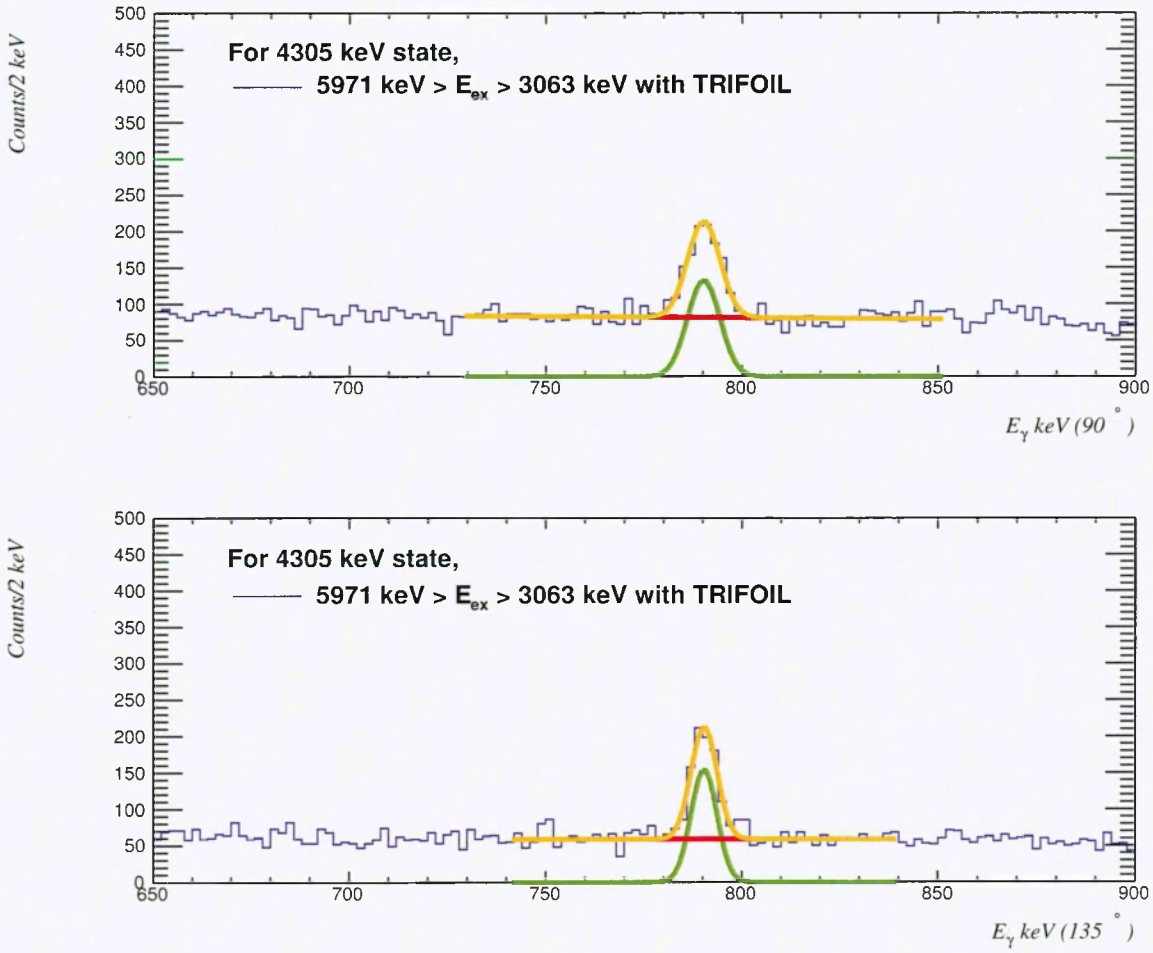

Figure 3.73: 4305 keV state branching in ^{26}Na with TRIFOIL gate.

It's found later on that the branching ratios for the state of 4305 keV are almost

identical for 90° and 135° clovers with approximately 30%, 40%, and 30% branching ratios for the 790 keV, 2080 keV, and 2191 keV γ-rays. This also proves that the peak at 2080 keV is consistently greater than at 2191 keV in both sets of clovers.

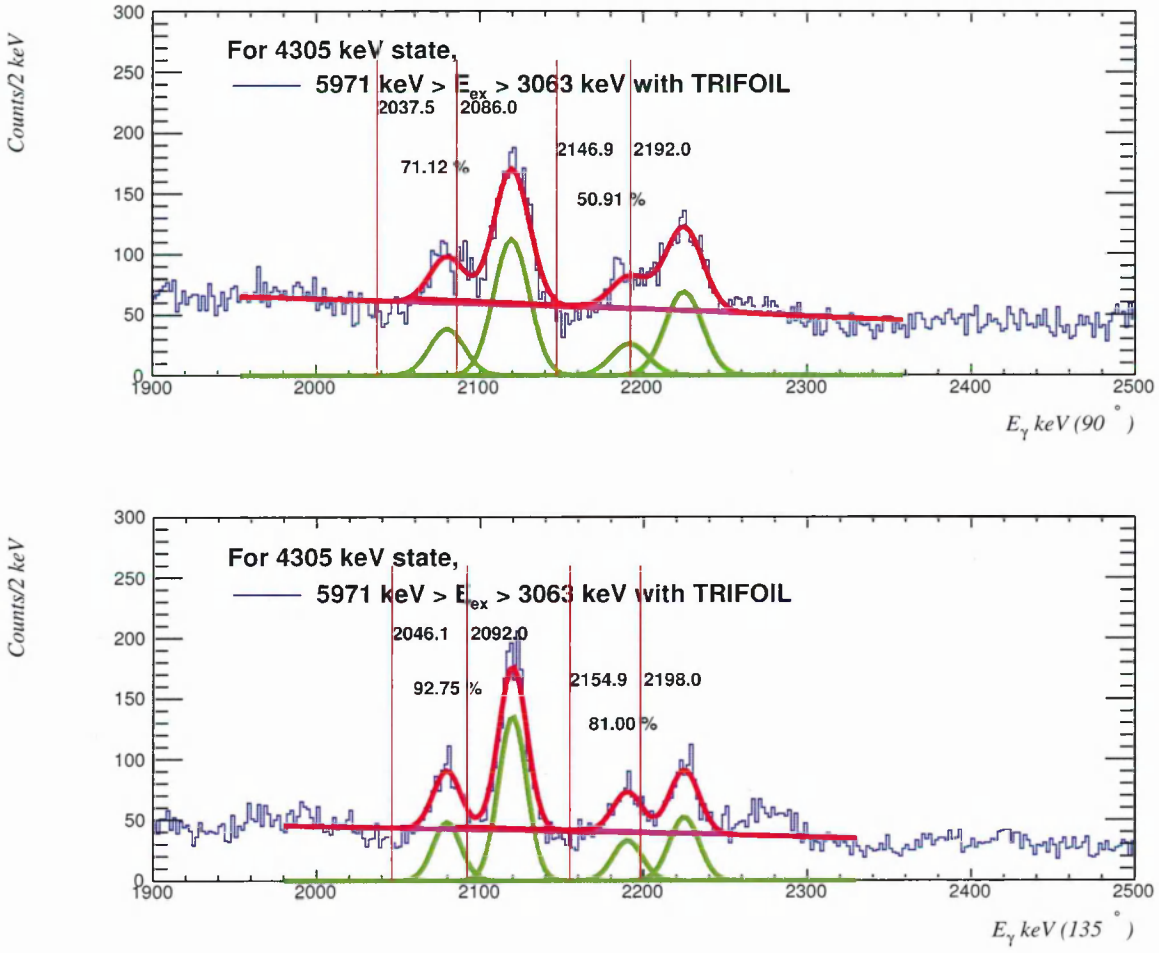

Figure 3.74: 4305 keV state branching in ^{26}Na with TRIFOIL gate.

Lastly, the 4.932 MeV state is picked for the complexity of the fitting since only the middle γ-ray at 4799 keV among the three in the fitting function will not be our interest. Depending on the 5% threshold rule, the γ-ray limits for the first and the last γ-rays in the figure 3.75 will be taken into an account. And, two γ-ray branches for this state, after

averaged from the results in 90° and 135°, at 4705 keV and 4931 keV will appear just after the region where the Compton edge and continuum of the higher energy γ-rays seem problematic in defining the individual γ-ray peaks below 4.6 MeV.

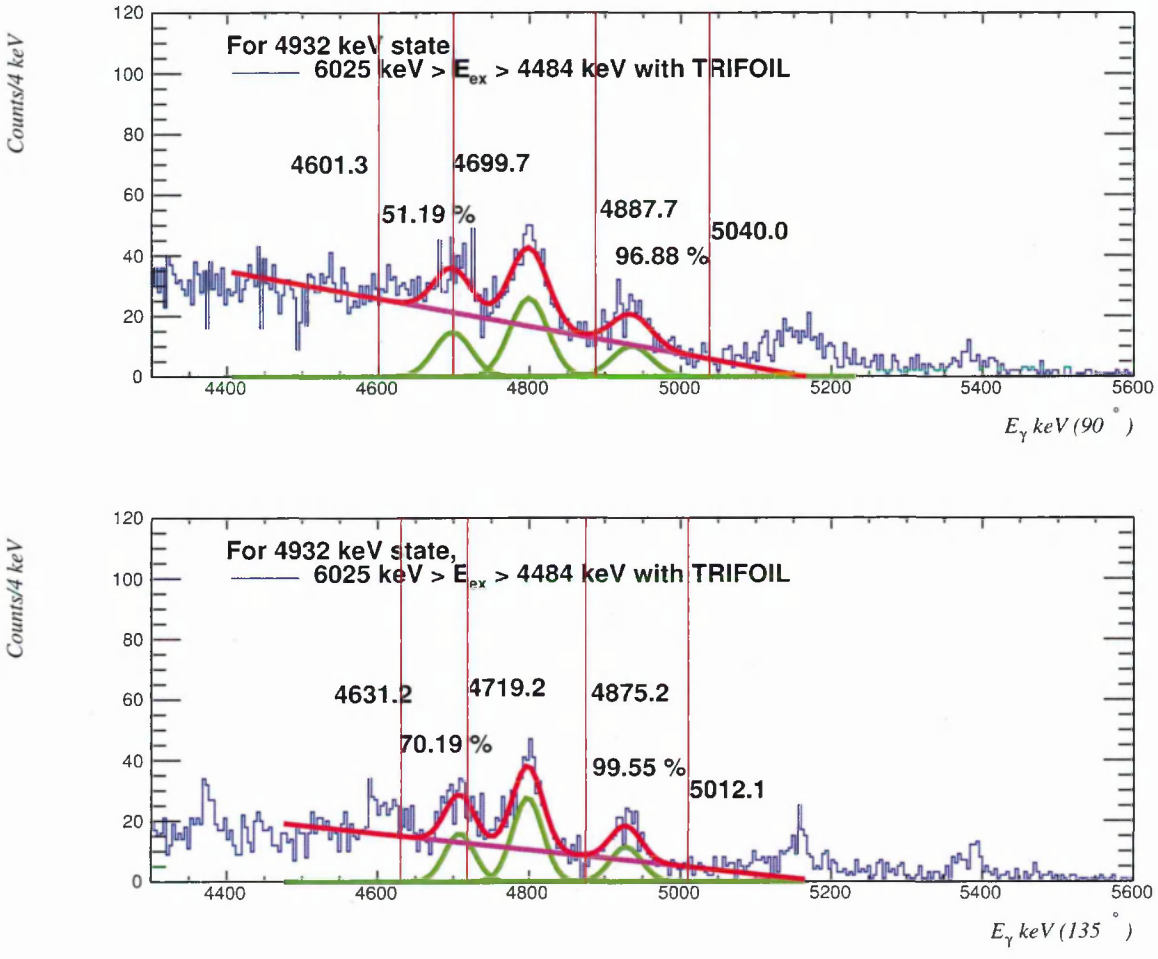

Figure 3.75: 4932 keV state branching in ^{26}Na with TRIFOIL gate.

For extra analysis, please refer to online appendix of this thesis [42].

3.4.3 Results of the Fitting Procedure in γ-ray Spectra and Final Level Scheme

By referring to the concept explained in the section 3.4.1, NA and NB are the total counts under the areas A and B in the figure 3.68. They were used to calculated so called "γ-ray peak correction factor" and "background correction factor". These coefficients enabled us to subtract the background efficiently as explained before. Last two columns of the table 3.4 are to indicate that the γ-ray spectrum that we applied fitting gives more counts for entire Gaussian of the corresponding γ-ray energy than the count extracted from the fit. That is indeed consistent with what we expected.

With regard to the table 3.5, it shows all the transitions for experimentally observed states. These gamma branches are calculated separately due to different behaviour of each peak in 90° and 135° clovers. Final results are shown in the last two columns including errors, which are calculated by the equation 3.2 from the branching ratios in 90° and 135° clovers.

Table 3.6 displays all the mean values of Gaussian functions from the fitting section 3.4.2 for different transitions. Each transition takes place between two states shown as E_1 and E_2. Final two columns are averaged results by the weight of the errors. These are the final γ-ray energies that appear on our final level scheme as presented in the figure 3.76.

In the table 3.6, the γ-ray energies decaying from the initial state of E_1 to final state E_2 are given separately for different clover angles. For those given gamma energies, the mean values of the Gaussian fit functions are noted with their error values separately. Those fits for different clovers are applied by the help of particular sigma values for each energy for distinctive TIGRESS clovers.

E_{ex} (keV)	E_γ (keV)	Clover Angle (degree)	γ-ray Efficiency	E_γ Peak Correction	NA	NB	E_γ Background Correction	Counts from fit	Counts from histogram
232	232	90	0.0278	1	187.563	189.000	0.992	926.05	987.000
		135	0.0278	1	135.272	153.000	0.884	721.074	758.000
405	405	90	0.0230	1	167.096	122.000	1.37	2238.15	2325.000
		135	0.0235	1	73.815	80.000	0.923	1823.551	1884.000
1507	1275	90	0.0138	1	244.415	270.000	0.905	445.334	518.000
		135	0.0146	1	134.778	131.000	1.029	324.428	361.000
1805	1805	90	0.0112	1	619.612	573.000	1.081	1239.263	1250.000
		135	0.0121	1	267.689	346.000	0.777	897.015	1015.000
2116	2116	90	0.0101	1	318.114	246.000	1.293	740.439	801.000
		135	0.0110	1	166.651	166.000	1.004	539.711	575.000
2195	2195	90	0.0098	0.44	173.377	223.000	1.76	1569.291	1650.000
		135	0.0107	0.63	126.213	256.000	0.78	1096.87	1208.000
2225	2225	90	0.0227	0.79	142.708	220.000	0.822	1624.894	1723.000
		135	0.0233	0.86	124.368	249.000	0.582	1245.437	1316.000
2843	2616	90	0.0086	1	747.407	945.000	0.791	981.539	1030.000
		135	0.0096	1	415.768	639.000	0.651	599.464	655.000
3135	3135	90	0.0075	1	1017.497	1091.000	0.933	1462.397	1481.000
		135	0.0084	1	484.129	563.000	0.86	901.485	981.000
3511	3511	90	0.0068	1	803.796	1515.000	0.531	2757.686	2883.000
		135	0.0078	1	381.292	558.000	0.683	2067.84	2227.000
4087	4087	90	0.0059	1	1097.595	1369.000	0.802	1331.66	1423.000
		135	0.0069	1	617.686	773.000	0.799	829.358	841.000
4239	1104	90	0.0149	1	1402.28	1399.000	1.002	1640.115	1625.000
		135	0.0157	1	752.223	850.000	0.885	975.337	1011.000
4305	790	90	0.0176	1	1331.369	1417.000	0.94	2013.859	2173.000
		135	0.0183	1	772.02	871.000	0.886	1408.574	1514.000
4597	4192	90	0.0057	0.93	1140.671	1147.000	0.994	1363.025	1451.000
		135	0.0068	0.96	676.378	539.000	1.255	764.873	829.000
4800	4800	90	0.0050	0.9	375.672	1303.000	0.319	1383.377	1456.000
		135	0.0060	0.95	218.457	724.000	0.316	820.253	873.000
4917	2796	90	0.0082	0.96	732.097	1109.000	0.689	1908.907	2071.000
		135	0.0091	0.99	385.44	626.000	0.625	1146.07	1286.000
4932	4931	90	0.0049	0.97	343.882	2391.000	0.148	731.2	754.000
		135	0.0059	1	220.517	1613.000	0.137	429.798	436.000
5009	3203	90	0.0073	0.82	565.141	924.000	0.742	1502.807	1581.000
		135	0.0083	0.92	353.022	524.000	0.736	918.185	976.000
5155	5154	90	0.0046	1	358.076	206.000	1.738	514.827	603.000
		135	0.0057	1	240.59	145.000	1.659	299.867	363.000
5276	3470	90	0.0068	0.33	323.071	851.000	1.143	1127.015	1134.000
		135	0.0078	0.48	208.792	447.000	0.964	702.251	753.000
5384	5384	90	0.0044	1	108.541	89.000	1.22	175.782	209.000
		135	0.0055	1	77.433	73.000	1.061	143.747	176.000

Table 3.4: Populated excited state energies of ^{26}Na, one γ-ray branch energy per state, γ-ray efficiencies, γ-ray and its background correction factors based on the explanations in section 3.4.1, and total counts under those selected γ-ray peaks after background correction are presented in here.

E_i (keV)	γ-Ray Branch Energies (keV)	E_f (keV)	BR at 90°	Error	BR at 135°	Error	Weighted Averaged BR	Error
232	150	82	0.4089	0.0038	0.4404	0.0042	0.4228	0.0028
	232	0	0.5911	0.0038	0.5596	0.0042	0.5772	0.0028
405	172	232	0.0350	0.0016	0.0316	0.0017	0.0335	0.0012
	323	82	0.1181	0.0026	0.1350	0.0027	0.1261	0.0019
	405	0	0.8469	0.0029	0.8334	0.0030	0.8405	0.0021
1507	1275	232	1.0000	0.0000	1.0000	0.0000	1.0000	0.0000
1805	1402	405	0.1008	0.0100	0.1383	0.0113	0.1174	0.0075
	1577	232	0.1475	0.0117	0.1227	0.0100	0.1332	0.0076
	1805	0	0.7516	0.0137	0.7390	0.0132	0.7451	0.0095
1992	1758	232	0.2219	0.0715	0.3356	0.0514	0.2968	0.0417
	1992	0	0.7781	0.0715	0.6644	0.0514	0.7032	0.0417
2116	2116	0	1.0000	0.0000	1.0000	0.0000	1.0000	0.0000
2195	1962	232	0.2303	0.0324	0.1987	0.0330	0.2148	0.0231
	2195	0	0.7697	0.0324	0.8013	0.0330	0.7852	0.0231
2225	418	1805	0.0521	0.0028	0.0547	0.0031	0.0533	0.0021
	2225	0	0.9479	0.0028	0.9453	0.0031	0.9467	0.0021
2423	2015	405	0.3856	0.0476	0.3934	0.0365	0.3905	0.0290
	2423	0	0.6144	0.0476	0.6066	0.0365	0.6095	0.0290
2843	2616	232	0.4240	0.0220	0.4188	0.0209	0.4213	0.0152
	2766	82	0.3188	0.0224	0.3656	0.0209	0.3438	0.0153
	2843	0	0.2572	0.0232	0.2156	0.0210	0.2343	0.0156
3135	2728	405	0.2994	0.0168	0.3908	0.0123	0.3588	0.0099
	3135	0	0.7006	0.0168	0.6092	0.0123	0.6412	0.0099
3511	3511	0	1.0000	0.0000	1.0000	0.0000	1.0000	0.0000
4087	2275	1805	0.0572	0.0117	0.1438	0.0114	0.1014	0.0082
	3664	405	0.4388	0.0238	0.3840	0.0214	0.4085	0.0159
	3845	232	0.2972	0.0215	0.2687	0.0185	0.2808	0.0140
	4087	0	0.2069	0.0225	0.2035	0.0194	0.2050	0.0147
4239	1104	3135	1.0000	0.0000	1.0000	0.0000	1.0000	0.0000
4305	790	3511	0.3076	0.0095	0.3048	0.0077	0.3059	0.0060
	2080	2225	0.3975	0.0140	0.3986	0.0113	0.3982	0.0088
	2191	2116	0.2949	0.0153	0.2966	0.0120	0.2960	0.0094
4597	4192	405	0.6101	0.0481	0.5707	0.0463	0.5896	0.0334
	4372	232	0.3899	0.0481	0.4293	0.0463	0.4104	0.0334
4800	4799	0	1.0000	0.0000	1.0000	0.0000	1.0000	0.0000
4917	612	4305	0.2989	0.0111	0.3747	0.0118	0.3343	0.0081
	1402	3511	0.0913	0.0115	0.0782	0.0105	0.0841	0.0077
	2796	2116	0.6098	0.0150	0.5471	0.0143	0.5770	0.0104
4932	4705	232	0.5700	0.0368	0.5612	0.0332	0.5652	0.0247
	4931	0	0.4300	0.0368	0.4388	0.0332	0.4348	0.0247
5009	3203	1805	1.0000	0.0000	1.0000	0.0000	1.0000	0.0000
5155	5154	0	1.0000	0.0000	1.0000	0.0000	1.0000	0.0000
5384	3470	1805	1.0000	0.0000	1.0000	0.0000	1.0000	0.0000
	5384	0	1.0000	0.0000	1.0000	0.0000	1.0000	0.0000

Table 3.5: Branching ratios of γ-ray branches for each depopulated states in ^{26}Na are calculated separately for TIGRESS clovers at 90° and 135°. The method of finding γ-ray branching ratios is explained in detail in section 3.4. Last two columns showing averaged value of branching ratio for the two clover angles and its error are our final branching ratios to declare in our level scheme 3.76.

E_i (keV)	γ-Ray Branch Energies (keV)	E_f (keV)	Mean at 90° keV	Error	Mean at 135° keV	Error	Weighted Average (keV)	Error
232	150	82	150.03	0.07	150.09	0.07	150.06	0.05
	232	0	231.91	0.07	232.21	0.07	232.06	0.05
405	172	232	172.72	0.21	171.87	0.23	172.35	0.15
	323	82	323.13	0.16	322.28	0.13	322.62	0.10
	405	0	405.19	0.07	404.90	0.05	405.02	0.04
1507	1275	232	1276.01	0.79	1275.50	0.56	1275.67	0.45
1805	1402	405	1402.74	1.53	1401.41	1.36	1402.00	1.02
	1577	232	1576.19	1.80	1577.94	1.26	1577.36	1.03
	1805	0	1806.70	0.57	1804.49	0.42	1805.26	0.34
1992	1758	232	1756.86	3.69	1757.77	1.55	1757.63	1.43
	1992	0	1996.87	2.08	1989.74	1.45	1992.07	1.19
2116	2116	0	2117.11	0.83	2115.56	0.61	2116.10	0.49
2195	1962	232	1965.55	3.19	1957.56	3.40	1961.81	2.33
	2195	0	2193.65	1.40	2194.99	0.92	2194.59	0.77
2225	418	1805	418.32	0.34	417.78	0.31	418.03	0.23
	2225	0	2226.17	0.52	2224.67	0.38	2225.19	0.31
2423	2015	405	2014.24	3.19	2015.63	1.82	2015.29	1.58
	2423	0	2431.36	2.41	2421.07	1.26	2423.28	1.12
2842	2616	232	2621.12	1.84	2611.83	1.54	2615.65	1.18
	2766	82	2768.56	4.27	2765.98	1.48	2766.26	1.40
	2843	0	2829.55	5.96	2846.35	3.11	2842.76	2.76
3135	2728	405	2743.97	4.11	2727.46	1.01	2728.41	0.98
	3135	0	3136.17	1.22	3134.54	0.85	3135.08	0.70
3511	3511	0	3512.37	0.51	3509.84	0.43	3510.88	0.33
4087	2275	1805	2265.47	4.36	2276.02	1.59	2274.78	1.49
	3664	405	3667.16	2.72	3662.55	2.29	3664.46	1.75
	3845	232	3850.27	2.08	3841.99	1.58	3845.02	1.26
	4087	0	4087.36	3.71	4086.44	2.27	4086.69	1.93
4239	1104	3135	1104.89	0.76	1103.56	0.64	1104.11	0.49
4305	790	3511	790.26	0.29	790.42	0.20	790.37	0.16
	2080	2225	2080.07	1.05	2079.74	0.69	2079.84	0.58
	2191	2116	2191.75	1.68	2190.24	0.97	2190.62	0.84
4597	4192	405	4198.14	4.12	4185.05	4.14	4191.62	2.92
	4372	232	4371.99	3.60	4371.99	3.60	4371.99	2.55
4800	4799	0	4799.33	1.97	4799.11	1.53	4799.19	1.21
4917	612	4305	611.61	0.17	612.31	0.15	612.01	0.11
	1402	3511	1402.42	1.40	1401.02	1.20	1401.62	0.91
	2796	2116	2796.87	0.87	2795.75	0.67	2796.16	0.53
4932	4705	232	4698.99	3.61	4708.89	2.71	4705.32	2.17
	4931	0	4935.48	3.04	4928.47	2.51	4931.30	1.94
5009	3203	1805	3203.39	1.71	3203.00	1.13	3203.12	0.95
5155	5154	0	5150.86	3.94	5156.87	3.22	5154.46	2.49
5384	3470	1805	3470.77	4.28	3469.54	6.16	3470.37	3.52
	5384	0	5381.43	5.41	5384.21	3.11	5383.52	2.70

Table 3.6: Mean values of each γ-ray branch of a particular state in ^{26}Na are given separately for both clovers at 90° and 135°. The last two columns show the weighted average values of mean values taken from different clover angles and and their errors. Then, these weighted average values are used to build level scheme 3.76.

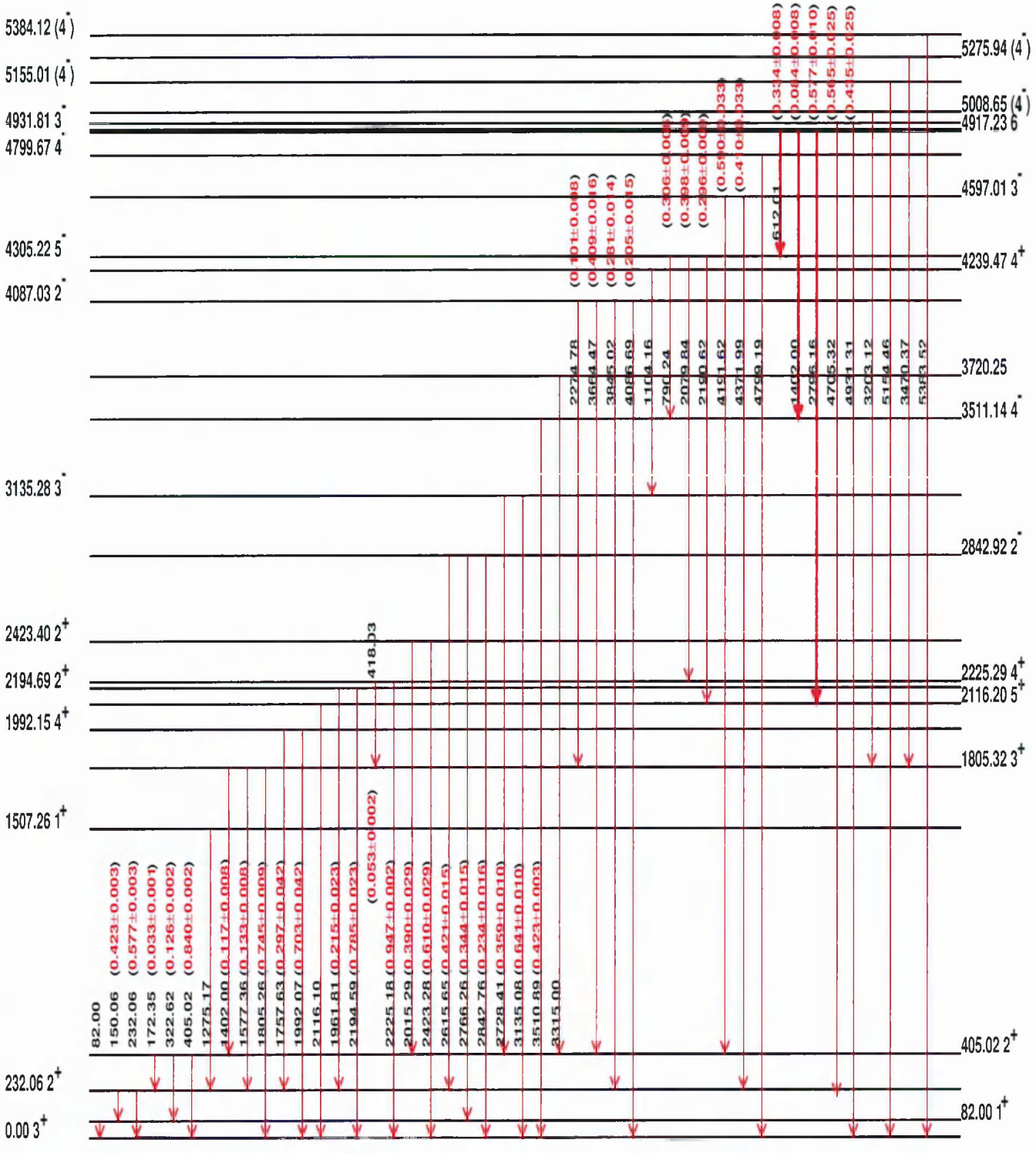

Figure 3.76: Final level scheme of ^{26}Na, showing spins and parities. The branching ratios with errors are shown in red. Due to proximity of the state 4.917 MeV and 4.932 MeV, first one is shown in thicker line with its corresponding γ-ray branches for differentiation.

3.5 Excitation Energy Spectra of the Excited States in ^{26}Na

The concept of peak and background correction factor was explained in the section 3.4.1 for gamma spectra, and this information will now be in use to plot the excitation energy spectra of the states. To be able to use these factors, so-called PCF and BCF, two excitation energy histograms should be plotted with the limits of chosen γ-ray peak and its background region. Then, those histograms should be corrected by the PCF and BCF as introduced before. These corrections will increase the data coverage in terms of the limits used to retrieve the excitation energy corresponding to entire γ-ray peak. In addition, background correction factor will enable us to retrieve the background excitation energy spectrum gated on corresponding background area under the γ-ray peak. Only after these corrections, one can make proper deduction of the two excitation energy spectra to get the corresponding excitation energy spectrum of the state. The subtraction may give sometimes negative values because not every part of the first histogram will have higher values than the background histogram has. The example of these will be seen in the following figures. Also, the excitation energy spectra shown in the following examples have been produced already by subtracting the background excitation spectra. Thus, there will be no need to fit polynomial function for the background subtraction. Keep in mind that all those assumptions about populated states in this thesis are restricted to the knowledge we manage to solve. Therefore, there might be still unresolved γ-rays and the states as a result due to the statistics that radioactive beam offers.

The limits of the γ-ray and excitation energies will be used together to get the angular distribution of both proton and γ-rays in the following sections It's also useful to prove the assumptions made about the populated states just looking at the corresponding peaks seen on these following plots. The γ-ray gates to plot these excitation energy

spectra are decided by checking all the γ-ray branches of the particular state which has been analysed in the section 3.4.2. Mostly, either the strongest or the easiest γ-ray branch in terms of accessibility of the γ-ray peak limits was in favour as a gate for excitation energy spectra.

The same state order used in the section 3.4.2 will be used here. Therefore, one of the lowest lying state at 232 keV is shown in the figure 3.77. For all the following figures in this section, the limits of the γ-ray peak and selected background are shown in blue and in red, respectively. The final result after the subtraction of the two spectra is shown in black with the green fit function. For all these excitation energy spectra, we do not need to use polynomial background function in addition to the Gaussian function. It's because there is almost no background subtraction in the final black spectrum.

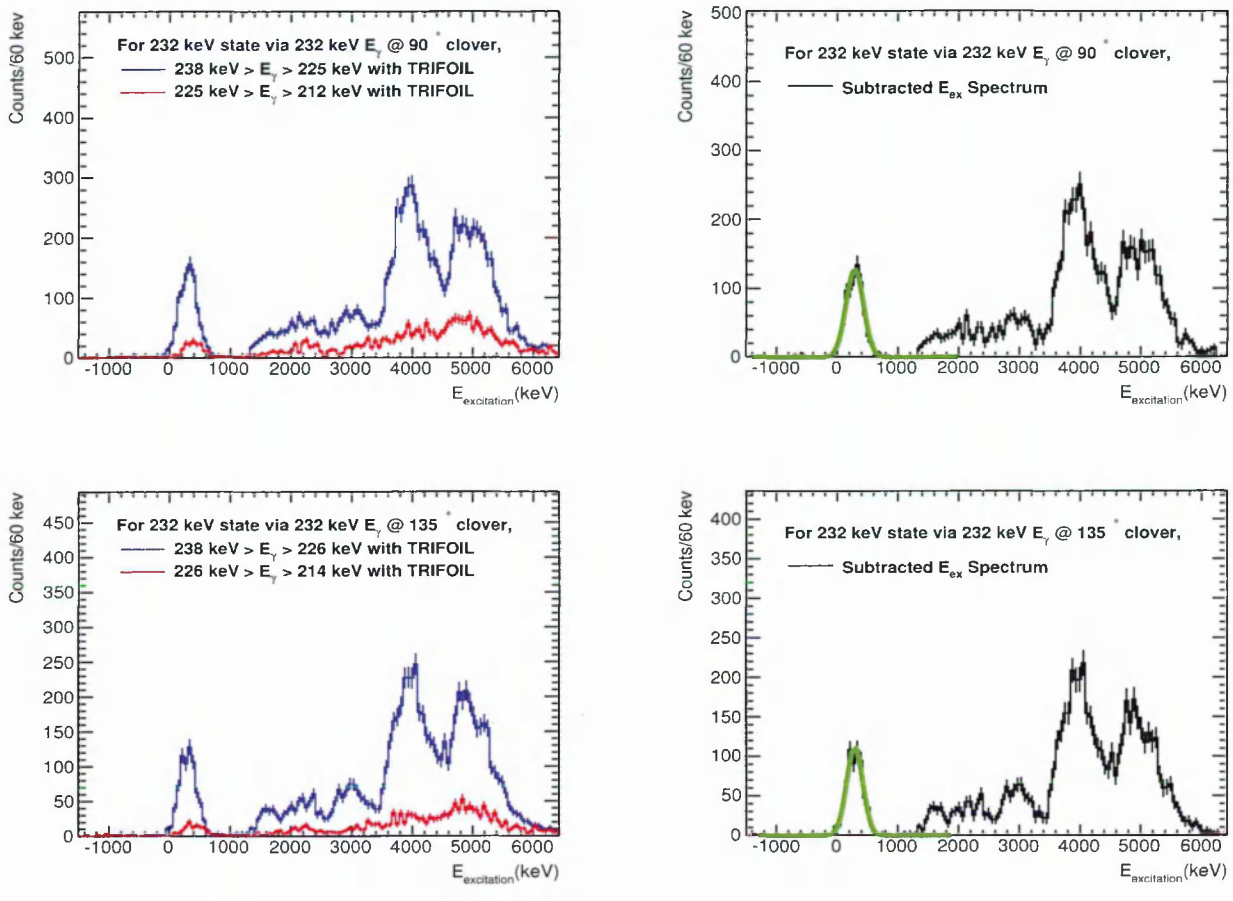

Figure 3.77: Excitation energy spectrum gated on 232 keV γ-ray

As this figure 3.77 nicely shows, almost all the other higher lying states eventually decay to this one of the lower lying states. This is another proof to the figure 3.9 where we can see the blob corresponding to 232 keV state stretches along the Y axis. As we have two TIGRESS clovers at 90° and 135°, the analysis throughout the thesis has been carried separately for both clovers as in the gamma spectra. The slight shifts in the gamma peak and its adjacent background region are noted and shown on the top of the plots as γ-ray gates. This also results in the slight shift on excitation energy limits. However, this might not be so obvious to observe by eye. The correction factors for the gamma peak and its

background are not shown here for clarity of the figures, but they are implemented in the code. Thus, the limits in the figures in this chapter reflects the γ-ray limits where the gated γ-ray peak has no contribution count from its neighbouring peak if it exists. Namely, if there is no adjacent γ-ray peak in the gamma spectra seen in the section 3.4.2, then the limits corresponds to entire width of the Gaussian for this γ-ray gate.

The next example is for the state at 2.195 MeV. And, one of the γ-ray gates to populate this state is the one at 2195 keV for ground state decay. These excitation energy spectra in the figure 3.78 shows different background subtraction for different Tigress clover angles. Even if all the γ-ray limits are taken separately from the γ-ray spectrum corresponding to different clover angles, there is discrepancy in the background spectra shown in red for 90° and 135° clovers. The difference between the two spectra in red and blue for 90° clover brings about negative counts in some parts of the spectrum, but it really doesn't affect the point we are making here about the state's excitation energy limits. The fit also shows in the black spectra that the peak in the excitation energy spectra supports the position of the state in energy in both plots in the figure 3.78.

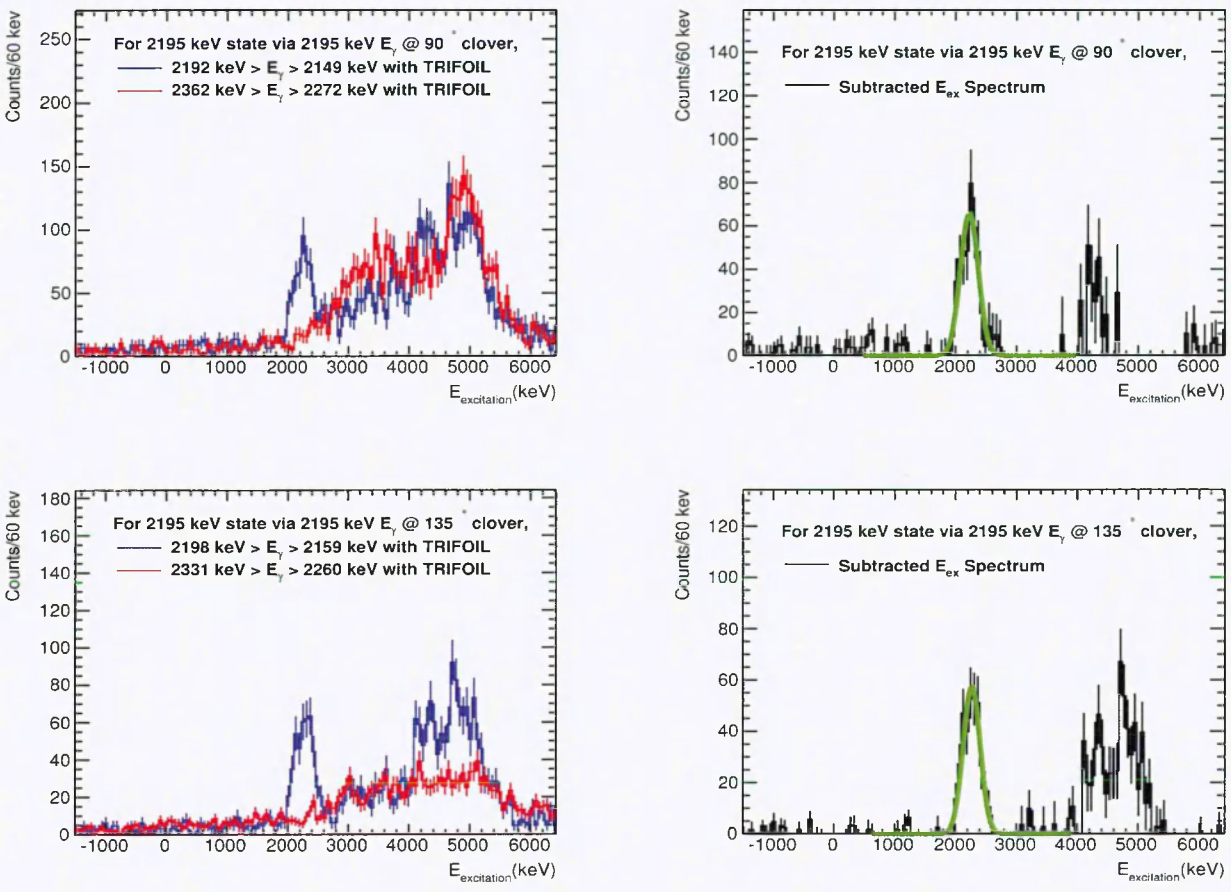

Figure 3.78: Excitation energy spectrum gated on 2195 keV γ-ray

The 2.195 MeV state is also one of the states where there is no feeding from any higher lying states. For this reason, it will be easier in terms of retrieving the angular distribution of proton and γ-ray as far as statistics and the strength of the state concerns. Even if the excitation energy spectra in figure 3.78 suggest feeding of the state between 4 MeV and 5 MeV, no other clue has been found about feeding with the current analysis results. Further investigations or new experiments may reveal this feeding in the future. Note that this state has possible two gamma branches via γ-rays at 1962 keV and 2195 keV shown in the figure 3.70. These gamma branches are weak ones in comparison to

their adjacent gamma peaks. Therefore, not too much information should be expected to extract from this state in terms of the proton and gamma-ray angular distribution analysis in the following chapter.

Another important state is 2.225 MeV state as shown in the figure 3.79. It's because it has a direct feeding from a state at 4.305 MeV and an indirect feeding from a state at 4.917 MeV via 612 keV γ-ray according to the level scheme 1.7. This is also proven in the excitation energy spectrum related to the 135° clover. With regard to the background spectrum shown in red for 90° clover for the 2.225 MeV state, it has the same characteristic as in the state of 2.195 MeV. However, the excitation energy peaks in both spectra is good enough to get the limits of the state in energy. Because of the wide excitation energy limits of the state that cover partly the higher lying feeding state's excitation energy limits as well, one should remove this contribution when dealing with the angular distributions of proton and γ-ray. Thus, this is one important thing to keep in mind about this state.

The fourth example here in the excitation energy section is the state at 4.305 MeV. This state feeds three lower lying states at 2.116 MeV, 2.225 MeV, and 3.511 MeV via γ-ray at the same time. However, only the highest state among the three will have feeding to its proton and γ-ray angular distributions due to the excitation energy limits set to the first two lower lying states at 2.116 MeV and 2.225 MeV.

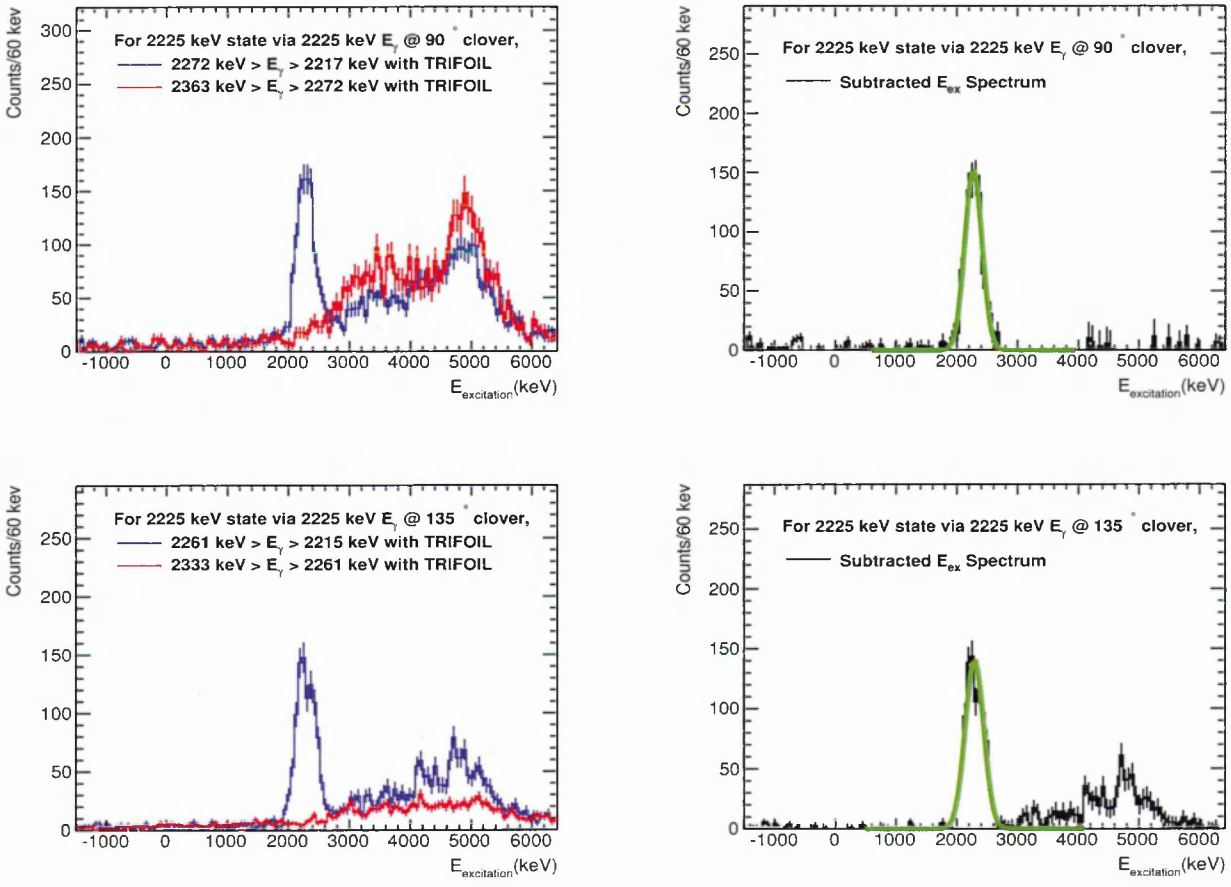

Figure 3.79: Excitation energy spectrum gated on 2225 keV γ-ray

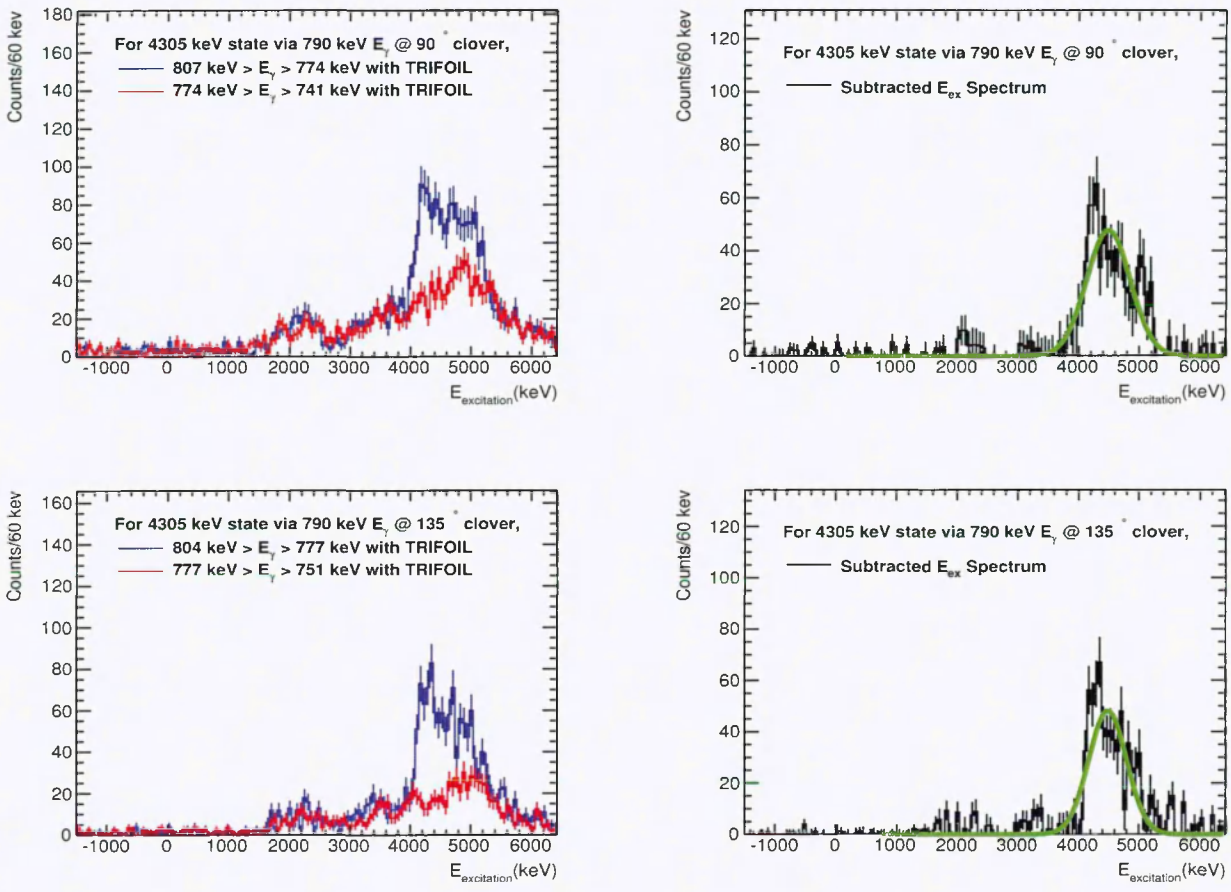

Figure 3.80: Excitation energy spectrum gated on 4305 keV γ-ray

This 4.305 MeV state is also the last and highest energetic state with a feeding from a higher lying state at 4.917 MeV whose angular distribution contribution should later be subtracted to get the directly populated proton angular distribution of the state at 4305 keV. The lowest energetic gamma ray at 790 keV has been chosen to get the angular distributions of the state. Gamma spectrum in the figure 3.74 highlights that other two gamma branches of this state at 2080 keV and 2191 keV have another adjacent gamma peaks nearby which makes it inconvenient to decide about background limits taken for these γ-ray peaks. Thus, right side of the peak at 790 keV is picked as the background

region as stated in figure 3.80.

The last example of this section is the state at 4.932 MeV which decays to the lower lying states via 4705 keV and 4931 keV γ-rays. Due to the recoil correction applied as described in the section 2.8 before, the state has slightly higher energy than the γ-ray decaying to the ground state. The highest γ-ray branch is chosen due to its position in the gamma spectrum to get the angular distribution of the state. This can be observed in its gamma spectrum in the figure 3.75. This example indicates no discrepancy between the two clover angles for the background spectrum shown in red. Therefore, the excitation energy spectra in the figure 3.81 is fairly clean with regard to fit and counts.

The states with only one γ-ray are at 82 keV, 1.507 MeV, 2.116 MeV, 3.511 MeV, 4.239 MeV and all the other states found above 5 MeV. It's noticed that half of the states above 5 MeV has ground state by emitting via very high energy γ-ray comparison to other low energies detected. All those states have automatically 100 % branching ratio for their branch, and they haven't been preferred to show γ-ray and excitation energy spectra here in the sections 3.4.2 and 3.5.

In conclusion of this section, one can reach the resolution of the SHARC array for excited states of ^{26}Na as in the figure 3.82. It's noticed that the difference between the TIGRESS clovers in 90° and 135° is too small at most of the excitation energies, but there are also slightly shift in terms of the mean values of the fits shown in black in all the figures of this section. The resolution seems deteriorating as the energy increases. This poor resolution is what makes us to deploy the high efficiency γ-ray array, TIGRESS to solve the states more precisely than one can do with particle detector, SHARC. For details of excitation energies, table 3.7 can be referred.

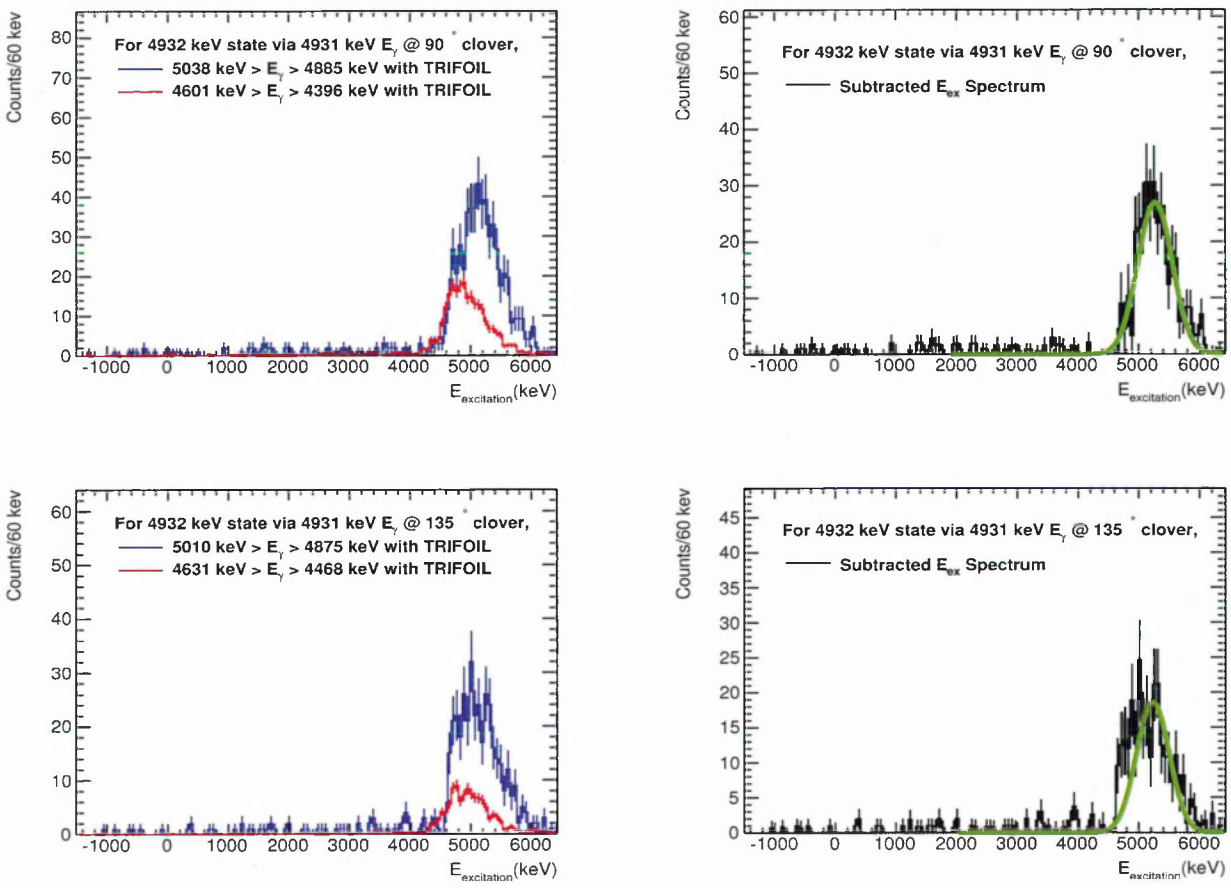

Figure 3.81: Excitation energy spectrum gated on 4932 keV γ-ray

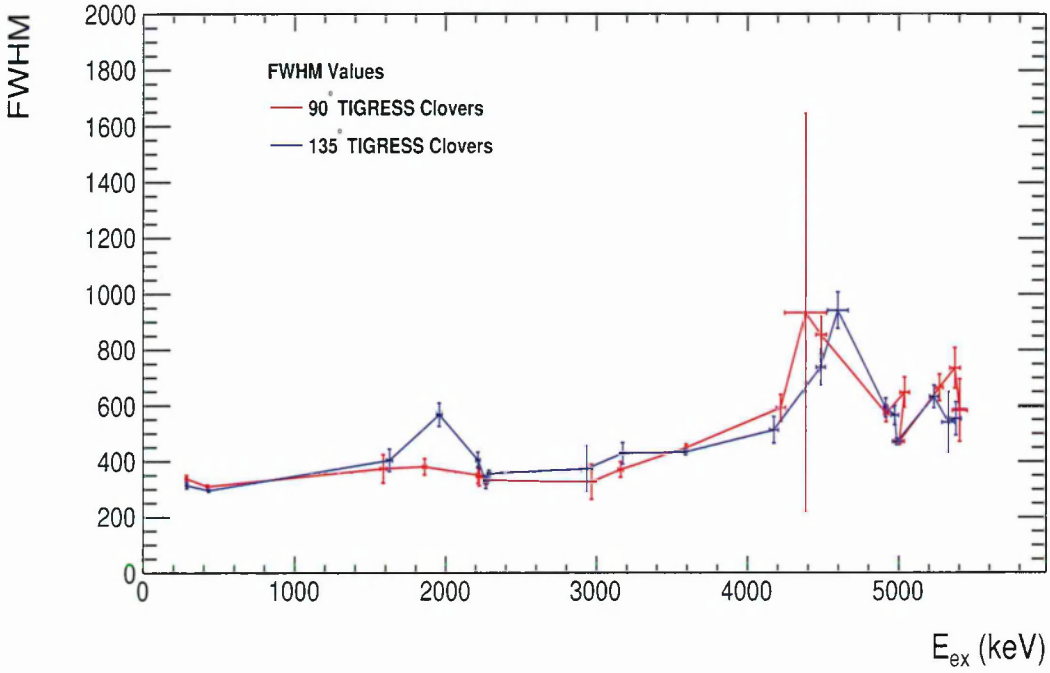

Figure 3.82: The FWHM of the excitation energies in ^{26}Na detected in the experiment $^{25}Na(d,p\gamma)^{26}Na$. The data around 2 MeV and 4.5 MeV that do not follow the trend arise from specific issues in fitting unresolved peaks but are included for completeness.

For extra analysis, please refer to online appendix of this thesis [42].

Case Number	Clover Angles	Mean with error	Sigma with error	FWHM
232	90	281.0 ± 6.8	145.3 ± 5.3	342
	135	288.2 ± 6.8	135.2 ± 5.2	319
405	90	425.8 ± 3.4	134.1 ± 2.6	316
	135	432.6 ± 3.3	125.7 ± 2.1	296
1507	90	1586.6 ± 21.0	155.2 ± 20.1	366
	135	1632.1 ± 19.4	174.2 ± 16.7	410
1805	90	1860.2 ± 13.8	166.8 ± 13.3	393
	135	1971.1 ± 18.2	250.5 ± 17.2	590
1992	90	2207.2 ± 83.9	274.2 ± 72.1	646
	135	2033.4 ± 35.4	156.4 ± 27.2	368
2116	90	2215.3 ± 12.1	145.1 ± 13.0	342
	135	2210.9 ± 13.9	186.8 ± 12.5	440
2195	90	2226.3 + 18.0	150.3 ± 15.9	354
	135	2265.6 ± 13.7	135.1 ± 9.2	318
2225	90	2273.7 ± 7.7	145.2 ± 7.0	342
	135	2289.0 ± 6.7	152.7 ± 4.9	360
2843	90	2986.4 ± 36.3	154.7 ± 29.4	364
	135	2924.8 ± 38.4	147.7 ± 39.5	348
3135	90	3157.3 ± 18.3	161.6 ± 12.7	381
	135	3169.7 ± 18.9	168.9 ± 14.8	398
3511	90	3594.9 ± 7.7	195.3 ± 5.6	460
	135	3590.1 ± 6.1	186.7 ± 4.5	440
4087	90	4215.7 ± 31.0	262.2 ± 21.5	617
	135	4185.7 ± 29.5	223.3 ± 20.0	526
4239	90	4383.8 ± 83.8	400.0 ± 265.0	942
	135	4589.9 ± 72.3	400.0 ± 16.8	942
4305	90	4488.7 ± 33.8	367.1 ± 26.6	865
	135	4487.0 ± 30.2	320.9 ± 26.4	756
4800	90	5037.2 ± 31.4	303.3 ± 25.3	714
	135	4980.7 ± 25.5	244.4 ± 14.6	576
4917	90	4917.3 ± 15.4	242.8 ± 12.7	572
	135	4913.1 ± 14.7	252.3 ± 14.4	594
4932	90	5283.2 ± 24.9	284.3 ± 19.7	670
	135	5220.1 ± 29.0	306.5 ± 19.6	722
5009	90	4998.7 ± 30.2	200.0 ± 4.8	471
	135	4981.0 ± 30.7	200.0 ± 4.5	471
5155	90	5373.6 ± 35.5	325.7 ± 33.5	767
	135	5371.1 ± 35.9	246.4 ± 26.1	580
5384	90	5409.4 ± 48.7	257.1 ± 44.6	605
	135	5329.0 ± 45.6	248.9 ± 48.8	586

Table 3.7: Fit results of Gaussian functions for excitation energy spectra in this section for separate TIGRESS clovers, shown in keV. Some of the figures showing excitation energy spectra are picked to demonstrate the fits applied onto a data. Excitation energies in the data are calculated by using mainly detected proton energies. Some values for full width at half maximum as extracted from the excitation energy spectra of this section can be seen in figure 3.82 as well.

3.6 The Position of the States in $E_{excitation}$ vs E_γ Plot

All the figures in this section are gated on a TRIFOIL, a clover angle, specific $E_{excitation}$ and E_γ limits where the state of interest can be populated as clean as possible. Therefore, the boxes shown in red in the following figures indicate the position of a state in terms of its gamma and excitation energy, and they are indeed slightly larger than displayed here due to the cleanest gates which have been chosen.

Two methods are applied to get the angular distribution of the background for the state of interest. And, the purpose of the following figures is to help the analyser to decide and judge which method should be used for the background subtraction of the angular distributions since one can see clearly if there is any contamination from the adjacent states or the contribution from the Compton part of the higher energetic γ-rays. Generally speaking, Compton edge and continuum of the higher energetic γ-rays may contribute to the counts of the peak at lower energies artificially. Then, this increases the count for the γ-ray decaying from this particular state. Therefore, to pick the best background representation of the state in the following figures, the first way is to keep the excitation energy limits of the state same by shifting the γ-ray limits preferentially to the left or right. That is to say that the representative red box for the position of the state in terms of $E_{excitation}$ and E_γ will be moved along the X axis to the left or right in the first example as shown in the figure 3.83. This only works well if there is no adjacent state right next to the γ-ray gate in interest. This can be easily check from the corresponding figures in the previous section 3.4.2. In the case of neighbouring γ-ray peak in the related gamma spectrum, the counts coming from the peak of interest will be deduced defined by the peak separation method applied as described in the section 3.4.1.

On the other hand, the second way is an alternative method to the first one where

the γ-ray limits used to populate the specific state will be kept the same by shifting the position of the state downwards along the Y axis in $E_{excitation}$ vs E_γ plots in the following examples. In that case, there will be no lower lying state peak for the same γ-ray gate. This can also be observed easily in the figures of the previous section 3.5.

One of the lowest lying state at 232 keV will be presented in both clovers with regard to its state position in the figure 3.83.

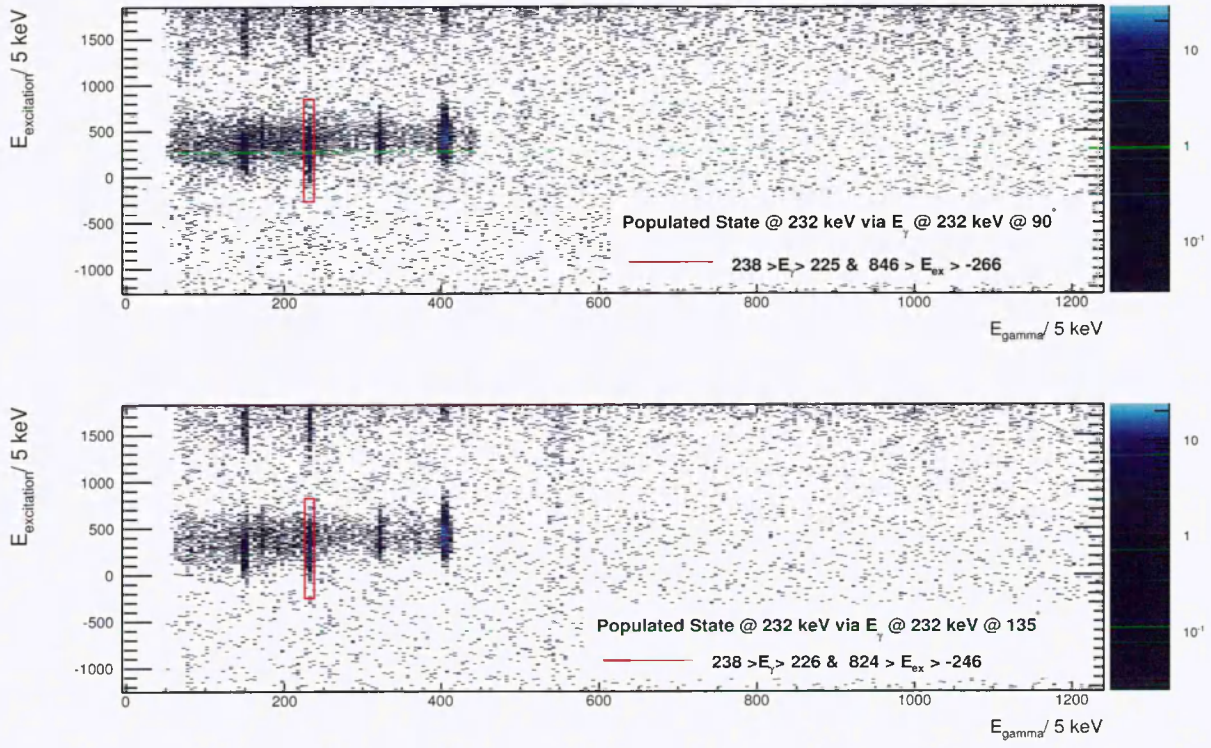

Figure 3.83: Position of the 232 keV state to g.s.

By using the information of excitation and gamma energy of the state from previous plots in 3.69 and 3.77 , we are now able to see the representative red box for the position of the state in the figure 3.83. This position displays only when the state is depopulated via 232 keV gamma ray for the purpose of getting the angular distributions of the state.

Generally speaking, the choice of gamma ray is due to the strength and the convenience of the gamma peak in the gamma spectrum among the other gamma branches of the state as one can decide from the spectra in the previous section 3.4.2. Otherwise, there is no limits as to which γ-ray branch should be chosen to populate the state.

As explained before, the choice of background side according to method 1 and 2 is important, so this figure 3.83, for instance, will be used to decide about the best method between the two. In that example, the Compton edge of the gamma ray at 405 keV coming from adjacent state at 405 keV lies at 248 keV, so the γ-ray of interest at 232 keV is staying just before the Compton edge of the higher energy γ-ray at 405 keV. That's the main reason why the figure 3.83 has more counts on both side of the marked red box. That is to say Compton continuum and edge of higher lying γ-rays contribute to the counts seen left and right side of the chosen area. The left side of the red box is chosen for background subtraction because we really want to remove this unwanted background from the angular distributions. Strictly speaking, the first method is employed for the state at 232 keV.

The next example is to decide the methodology for the state at 2.195 MeV with help of figure 3.84. To depopulate this state, the γ-ray at 2195 keV to ground state is chosen as far as the gamma ray strength concerns by looking at the plots in the figure 3.70. The second gamma branch at 1962 keV is so weak that it's not logical to choose this to get either the proton or gamma angular distributions of the state. Also, due to the proximity of the other adjacent states at 2116 keV and 2225 keV, it's better to use method two by keeping the gamma energy limits same but shifting the excitation energy limits to the lower region. Namely, taking the red box shown in the figure 3.84 downwards on the Y axis where the excitation energy is shown.

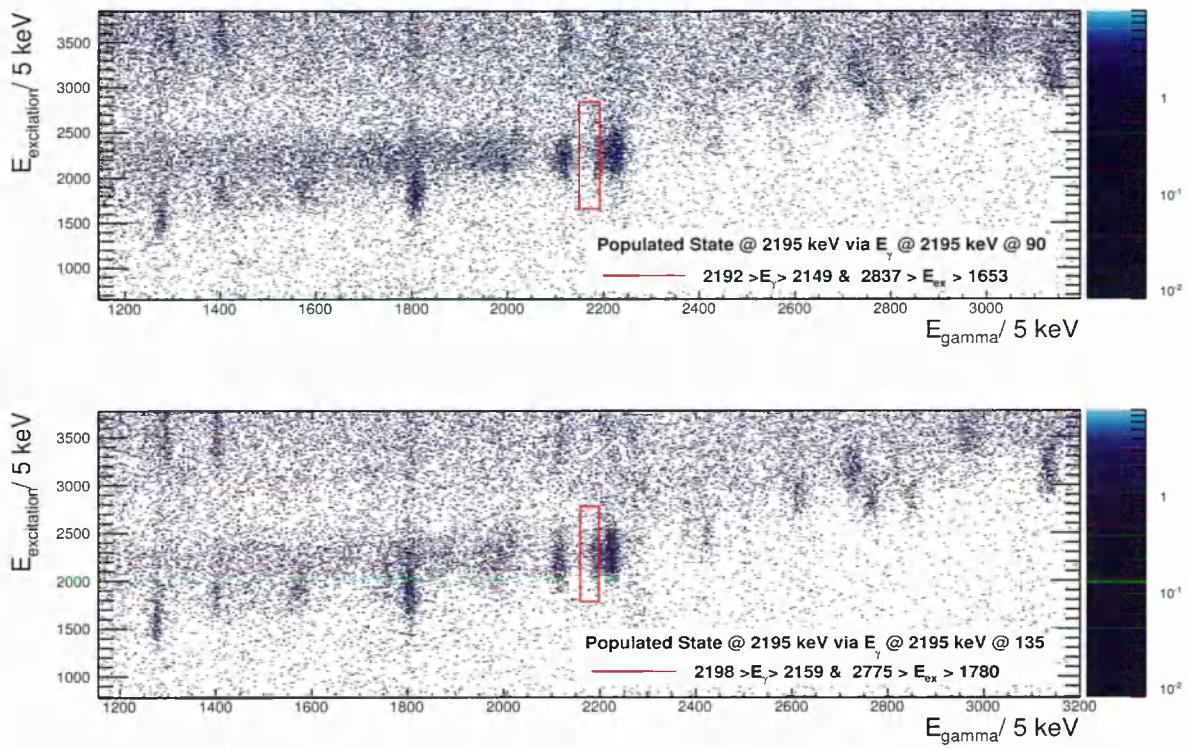

Figure 3.84: Position of the 2195 keV state to g.s.

Another state to investigate is 2.225 MeV by looking at both its γ-ray spectrum and excitation energy spectrum in the figures 3.72 and 3.79. Since the left side of the position of the state at 2225 keV is quite overwhelmed with other lower lying states, the right side of the red box in the figure 3.85 at this time is regarded as the background angular distribution deduction limits.

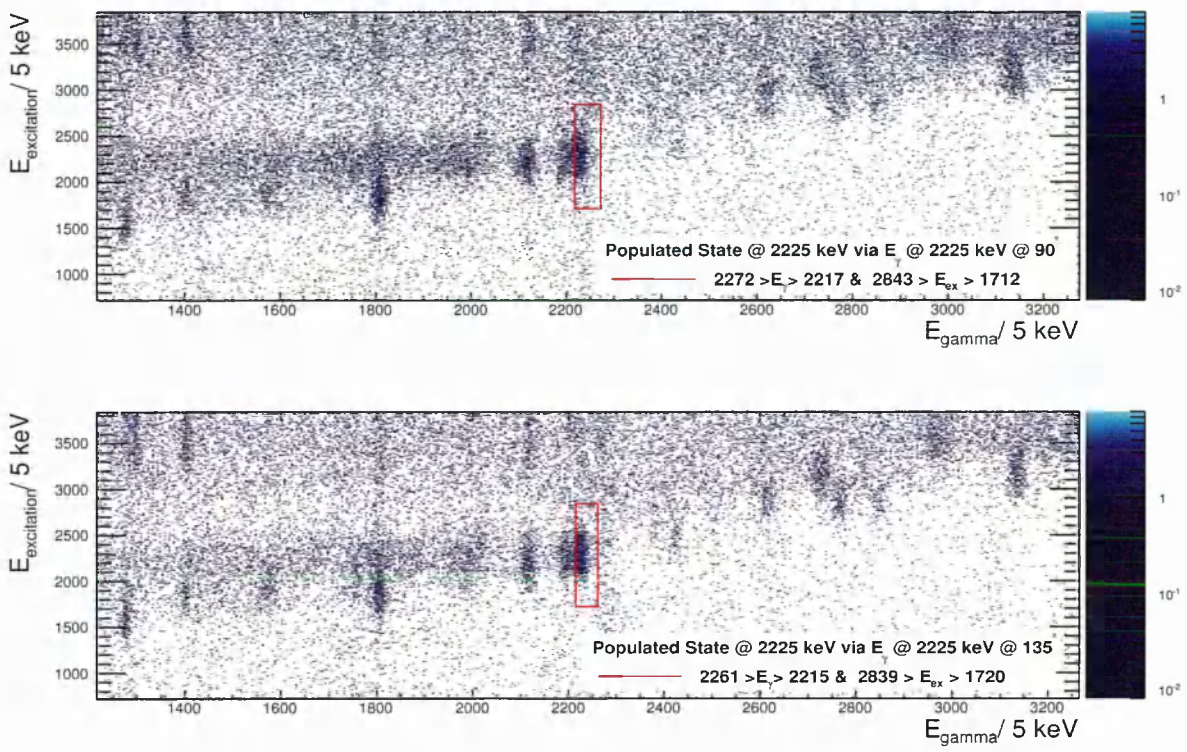

Figure 3.85: Position of the 2225 keV state to g.s.

In contrast to the previous state, the higher lying state at 4.305 MeV has no state blob as the dark blue counts indicate in the figure 3.86 on both side of the red box as a representation of the position for this state. However, this higher lying state at 4305 keV is staying in the area where all the Compton contribution of the higher lying states also affects the counts assigned for this state. This is a typical behaviour in any where of the $E_{excitation}$ vs E_γ plots, but it becomes more of an issue especially for higher gamma rays. Since they are populated with less statistics in comparison to lower lying states, the background subtraction for proton and γ-ray subtractions should be done carefully to be able to extract any information from the data. Therefore, the methods that one uses for the background subtraction become much more important for these high energy γ-ray

gated states. The excitation energy spectrum of the state in figure 3.80 gated on a γ-ray at 790 keV shows it's appropriate to use method one for the background subtraction when subtracting the angular distributions in the following sections.

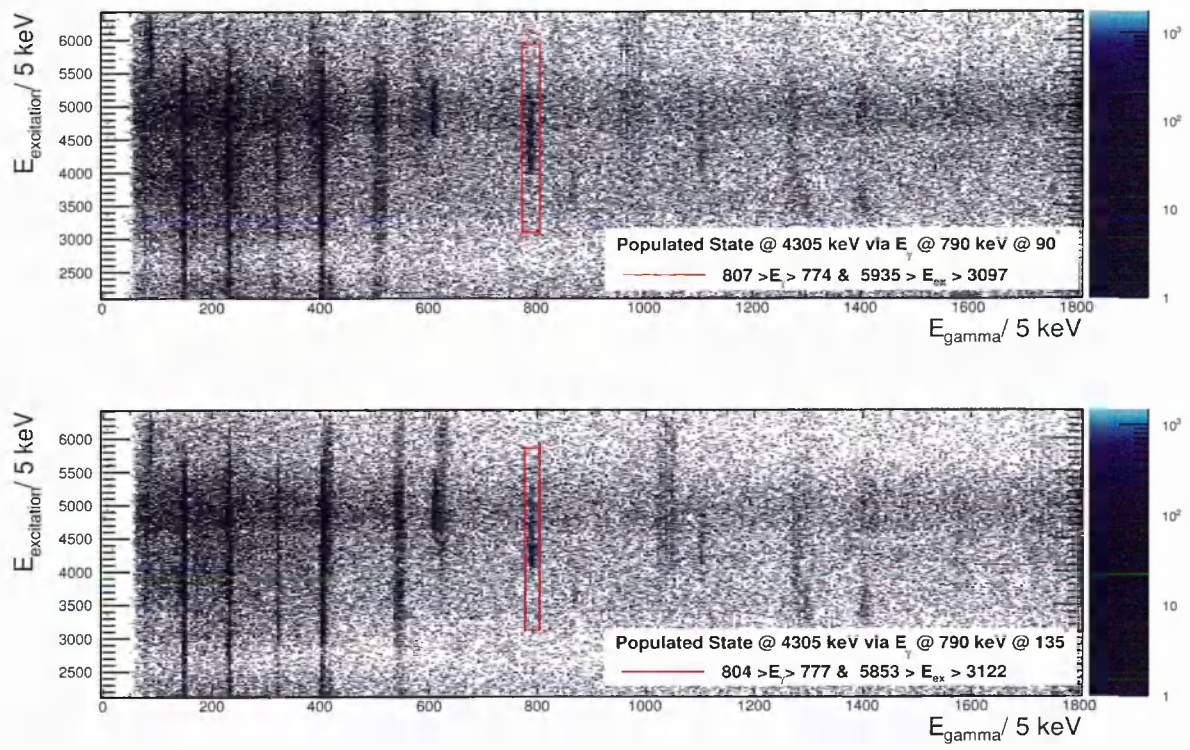

Figure 3.86: Position of the 4305 keV state to 3511 keV state via 790 keV gamma ray

Lastly, one of the weakly populated states at 4.932 MeV in terms of counts as seen in the figure 3.87 will be analysed in this part of the current work. Due to the weakness of the state, the method 2 is applied to get the background angular distribution of the state. Namely, lower side of the red box is used for the background subtraction of the angular distributions to keep the counts of the state at such a level that we can extract any information from the data. Another reason for this selection is the left side of the peak is dominated by the Compton edge of γ-ray, which is calculated as 4911 keV, of

the highest state at 5.383 MeV. With regard to the γ-ray gate chosen to populate this state, the gamma spectra in the figure 3.75 explains well why the weak gamma branch of the state at 4705 keV was not the gate, but instead the γ-ray at 4931 keV was selected to populate the state. That's is to say the strong γ-ray branch is most of the time the preferred one.

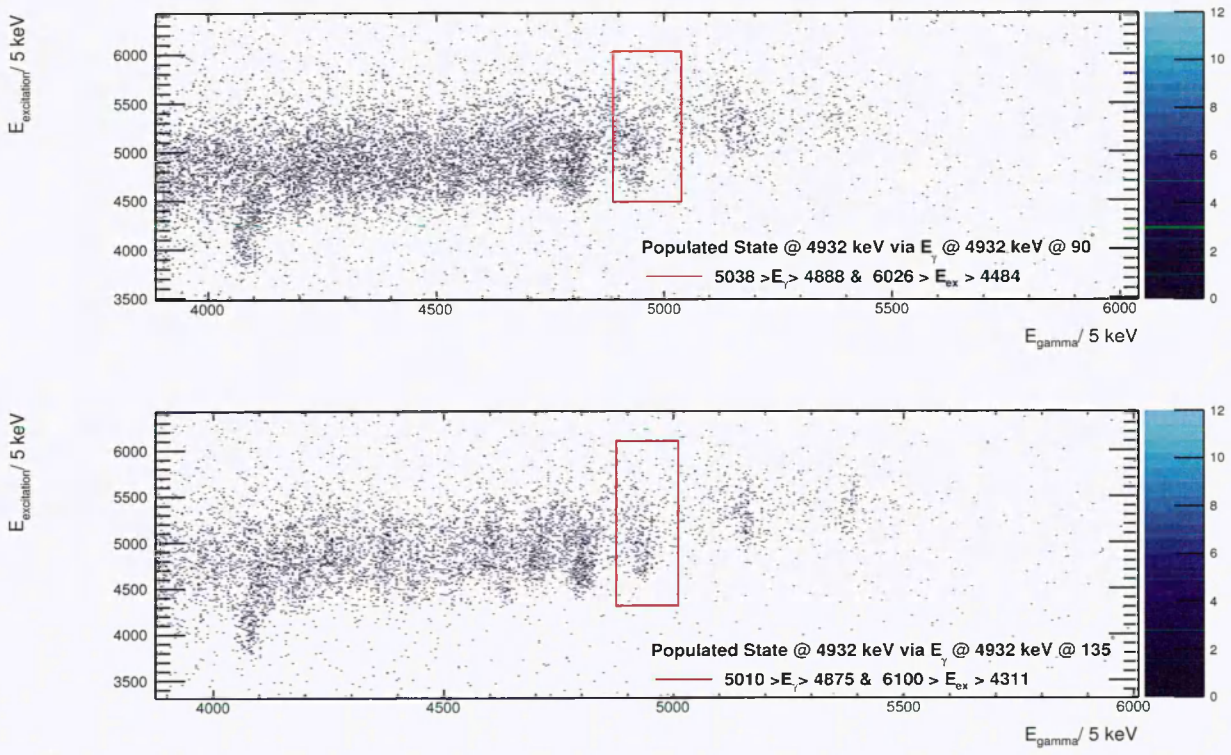

Figure 3.87: Position of the 4932 keV state to g.s.

For extra analysis, please refer to online appendix of this thesis [42].

3.7 The Analysis of Differential Cross Sections of Protons

The differential cross section of the proton in deuteron-induced transfer reaction in inverse kinematics has been extracted from the data by using ^{25}Na radioactive beam with 5

MeV/u energy on 0.5 mg/cm^2 CD_2 target via $^{25}Na(d,p\gamma)^{26}Na$ reaction. This extraction methodology will be explained in multiple steps as follows. At this stage, the formula 3.12 is grouped in that way because it reflects the best method used to get the differential cross section of the protons from the angular distribution of protons with regard to the polar angle, θ_p in laboratory frame.

$$\frac{d\sigma}{d\Omega} = N(\frac{1}{In_d\epsilon_{Si}})(\frac{1}{\epsilon_\gamma})(\frac{1}{d\Omega}) \tag{3.12}$$

In the equation 3.12, "N" represents the total detected counts for protons and the combination of all the parameters in $\epsilon_{Si} \times I \times n_d$ refers to the normalization factor. While the ϵ_γ shows the efficiency of the γ-ray detectors for a particular γ-ray, $d\Omega$ indicates the solid angle of the SHARC array which is calculated separately for the different parts of the SHARC array. The reason is because SHARC array has only four DSSSD in upstream, one fully instrumented DSSSD in downstream, and one annular CD detector in upstream. Therefore, this will affect the probability of detecting particles, especially proton, depending on the scattered angle in the corresponding directions. In terms of the parameters in the normalization factor, they represent respectively the number of incident beam particles, and the number of deuteron in 0.5 mg/cm^2 CD_2 (deuterated polyethylene) target, and the efficiency of the particle detectors.

The steps as shown respectively in the equation 3.12 will be applied to the data. In the end of the process, the unit conversion will be completed as mb/sr. In the first step, the proton angular distributions in 5° bins are produced by using four gates: a particular excitation and the γ-ray energy, TRIFOIL, and the clover angle for γ-ray detectors. However, the TRIFOIL option was flexible for a comparison reason. Thus, the proton differential cross sections are extracted without using TRIFOIL gate. Then, these proton

angular distribution histograms should be divided by the normalization factor (NF), the efficiency value of the γ-ray energy used in the gate, and lastly the solid angle histogram in 5° bins in laboratory frame as shown in the figure 2.20.

In the meanwhile, the normalisation factor is calculated from the scaling of the elastic scattering cross section theoretical lines on to the elastic scattering data. And, it was concluded that the theory given by Meurders [15] gave the best fit. This factor in value was $38000 \pm 1000\ mb^{-1}$. For detailed process of extracting the normalization factor from the data, one can refer to the thesis in the reference [1].

After all these divisions mentioned, the latest two histograms, produced separately for 90° and 135° clovers, will be checked in terms of reflecting the same differential cross section shape for a particular angular momentum transfer defined by the transfer reaction in $^{25}Na(d,p)^{26}Na$ for consistency. Then, the diagram in 3.88 and the formalism derived in the equations 3.13, 3.14, and 3.15 will be employed as it is described. In the final step of the analysis, two proton differential cross sections for different clover angles will be weighted averaged to get the final results.

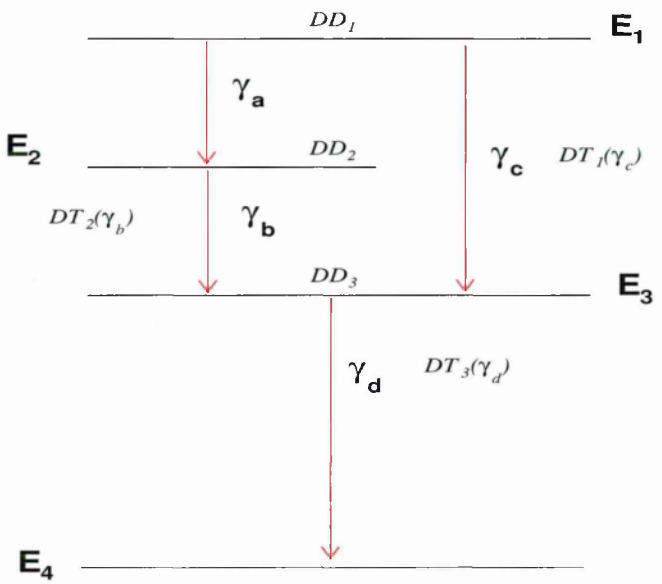

Figure 3.88: General diagram for the angular distribution formalism.

For some states in the proton differential cross section analysis, the higher lying states can contribute to the counts of the protons due to the wide excitation energy gate in the state of interest. The general formalism for the proton differential cross section calculation in different cases is written in the equations 3.13, 3.14, and 3.15. The meaning of the symbol $DT_i(\gamma_j)$ is the measured angular distribution gated on a γ_j of the state "i". Namely, this is what is produced after background angular distribution deduction explained in the first step. And, the meaning of the DD_i is the fully corrected angular distribution of the state "i". This is to say that this histogram is produced in the third step explained above after branching ratio correction. The symbols of ϵ_{γ_j} and $BR(\gamma_j)$ refers to the gamma efficiency and the branching ratio of the specific gamma ray to populate the state. Lastly, the symbol of NF is the normalization factor.

$$DT_1(\gamma_c) = DD_1 \times (NF) \times \epsilon(\gamma_c) \times d\Omega \times BR(\gamma_c) \tag{3.13}$$

$$DT_2(\gamma_b) = DD_2(NF)\epsilon(\gamma_b)d\Omega BR(\gamma_b) + DD_1(NF)\epsilon(\gamma_b)d\Omega BR(\gamma_b)BR(\gamma_a) \tag{3.14}$$

$$\begin{aligned} DT_3(\gamma_d) = {} & DD_3(NF)\epsilon(\gamma_d)d\Omega BR(\gamma_d)+ \\ & DD_2(NF)\epsilon(\gamma_d)d\Omega BR(\gamma_b)BR(\gamma_d)+ \\ & DD_1(NF)\epsilon(\gamma_d)d\Omega BR(\gamma_c)BR(\gamma_d) \end{aligned} \tag{3.15}$$

In conclusion, the values represented by the symbols of DD_i is the ones that one should find as an answer starting from the values of $DT_i(\gamma_j)$ which indeed represents the histograms that we produced in the first step of the analysis before making any division according to the equation 3.12.

To give an example of getting the theoretical proton differential cross sections from the experiment in this work, the populated states of ^{26}Na nucleus can be given as the best choice. The nucleus of ^{26}Na has 11 protons and 15 neutrons, so it's an odd-odd nucleus. Therefore, the valence proton and neutron can couple together to give wide range of spins in the final populated nucleus. The method used to get the states in ^{26}Na is (d,p) transfer reaction mechanism where one neutron is transferred into the neutron shell of the target nucleus, ^{25}Na. Since the ^{25}Na is initially odd-even nucleus in terms of its 11 protons and 14 neutrons, the characteristic of the nucleus is defined by the last un-paired proton in the $1d_{\frac{5}{2}}$ shell. And, the spin $\frac{5}{2}$ in here is called "target spin in incident channel" in TWOFNR [17] calculations. However, the additional transferred neutron will couple with this unpaired proton to create different spins in odd-odd ^{26}Na nucleus. After

the $1d_{\frac{5}{2}}$ closed neutron shell, there are 4 possible higher shells as the easiest options for the transferred neutron to enter according to the energies in the populated states of ^{26}Na. However, it's not expected to have enough energy to place this transferred neutron in to the higher shells than $1f_{\frac{7}{2}}$. Thus, we'll consider only $2s_{\frac{1}{2}}$, $1d_{\frac{3}{2}}$, $1f_{\frac{7}{2}}$, and $2p_{\frac{3}{2}}$ shells as options to transfer one neutron via (d,p) reaction. These shells are ordered respectively in terms of their energies from lower to the higher value. The coupling of un-paired proton in the $1d_{\frac{5}{2}}$ shell with the unpaired transferred neutron from one of these neutron shells can give us a range of final state spins that we can have. For instance, when one un-paired proton in $1d_{\frac{5}{2}}$ proton shell and one unpaired neutron in $2s_{\frac{1}{2}}$ neutron shell couple together, one can get the final spin in the range of $|\frac{5}{2} - \frac{1}{2}| \leqslant J_{final} \leqslant (\frac{5}{2} + \frac{1}{2})$. When the same procedure has been done for all four shell options as mentioned for a transferred neutron, the spin of 2 has been noticed to be the common spin option among the all. Thus, TWOFNR is run to get the differential cross sections of the scattered proton in the $^{25}Na(d,p)^{26}Na$ reaction by giving the final spin 2 as a parameter. Then, these theoretical lines for s, p, d, and f waves are used to find the best fit on to the proton differential cross sections extracted from the data. The Adiabatic Distorted Wave Approximation (ADWA) [43] reaction theory has been chosen to explain the data. By applying the Chi^2 rule for every data and theoretical points on the same proton angle (θ_p) in the following figures, the best scaling factors for each "l" transfer case has been found. Since the angle range from 90° to 180° has been known as the best angle range that explains the theory, minimization in ROOT by using the algorithm "Migrad" [44], has been applied to get the scaling factors of theoretical lines to the data points only in these angle ranges.

Note that all TWOFNR [17] results for proton differential cross sections are calculated for a final spin 2 since it suits any case of coupling between proton and possible

neutron shell as explained above. If the spectroscopic factors want to be compared with another spin in that particular state, the relationship of spin and differential cross section should be used as given in the equation 3.16.

$$SF_1 \times (2J_1 + 1) = SF_2 \times (2J_2 + 1) \tag{3.16}$$

where SF_1 refers to the spectroscopic factor for the spin 2 state, SF_2 indicates another spectroscopic factor to compare with the SF_1. Also, J_1 and J_2 show the final spins assigned to the populated states to get the spectroscopic factors SF_1 and SF_2, respectively.

One of the methods used to assign the spins in the populated states is to compare the current work with a nucleus which has the same number of neutrons but different numbers of protons, namely with the isotones. It's because the similar structure that they have in their proton and neutron shells may reflect the analogous selectivity in terms of populating the states in comparable energies. Therefore, $^{27}Al(d,p)^{28}Al$ reaction will be used as a reference. The level scheme of this isotone is given in the figure 3.89. In terms of the proton and neutron shells, the nucleus $^{28}Al_{15}$ has 13 proton numbers where the last 5 of them lies on the $1d_{5/2}$ shell; whereas, the last unpaired neutron among the other 14 neutrons can be in any shell above the shell in $1d_{5/2}$ depending on where the single neutron is transferred by the (d,p) transfer reaction. In comparison to $^{26}Na_{15}$ nucleus which was discussed before, $^{28}Al_{15}$ nucleus may have extra interactions due to the extra 2 protons in its $1d_{5/2}$ shell. At first glance, the lower lying states in both ^{28}Al and ^{26}Na tend to possess the spin 2^+ with $2s_{1/2}$ coupling in neutron shell. The states between 800 keV and 3 MeV seem to have d wave transfer. The only contrast is for the states above 3 MeV where p and f waves seem to be sharing the couplings with unpaired proton in the

shell model calculations of $^{26}Na_{15}$ nucleus while the $^{28}Al_{15}$ nucleus gives always f wave transfer experimentally.

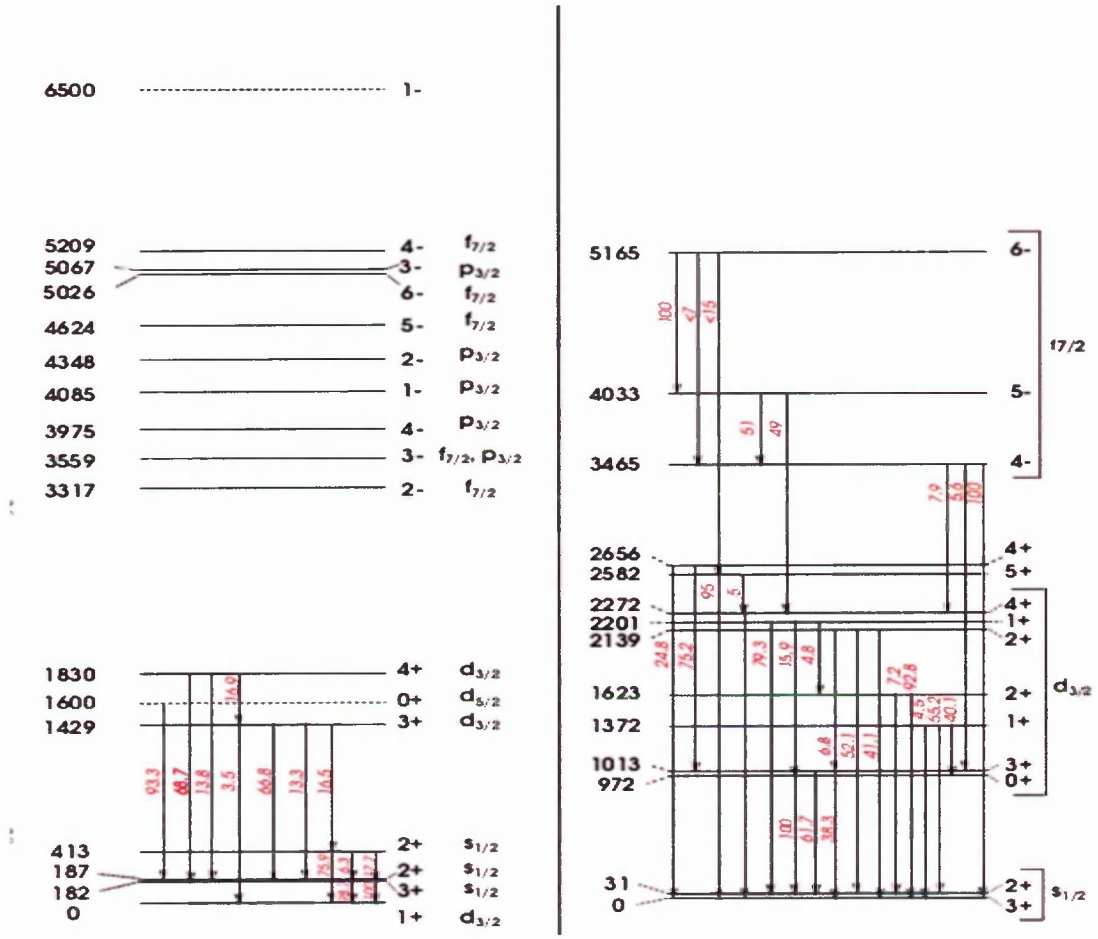

Figure 3.89: A comparison of the predicted states in $^{26}Na_{15}$ and the experimental states in $^{28}Al_{15}$ is shown here. The theoretical states were predicted by using USD and s-p-sd-pf interaction with a 0.7 MeV reduction in the gap between sd and pf shells. [1]

The first example in the figure 3.90 will be used as a reference to explain how the scaling factors are calculated. Generally speaking, the scaling factor is calculated by the chi-squared values found for all the proton angles with proton count in the data. Thus, each bin content is scanned corresponding to its bin centre in the histogram, shown in blue, with 5 degree binning. For each existing $\frac{d\sigma}{d\Omega}$ point in the data, the value for the

same bin centre from the theoretical line is read out to find each component of the sum in the formula of chi-squared in 3.17. Then, the smallest value for chi-squared is chosen to get the scaling factor. In the formula below, "OV" refers to observed value which is the bin content of the histogram per bin as shown in blue in the figure 3.90; whereas, "EV" indicates expected value from the theoretical line, produced by the TWOFNR [17] code, corresponding to the same bin centre multiplied by the scaling factor that we seek for. The reason for this multiplication is because the expected theoretical values should indeed overlap with data, so it represents the scaled data points from the theory. The function which returns to chi-squared value will be called 100 times until it finds the minimal value. The scaling factor will then be used to scale the theoretical lines, so they can go through the data points. Before starting to search for a minimal value for chi-squared, one should give the specific proton angle range to be scanned for minimization. The selection of angle range is important because it needs to reflect the selectivity of the (d,p) theory used to explain the data. In all cases, it is Adiabatic Distorted Wave Approximation (ADWA) [43] which fits on to the data points better for backward angles of 90 degree for scattered protons. Experimentally speaking, the theory has been tested as far as it matches with the data since the theory should represent the data. Therefore, one may try to fit other theories just to compare as well.

$$chi - squared = \sum_{i=1}^{n} \frac{(OV - EV) \times (OV - EV)}{(OE)^2} \tag{3.17}$$

To perform the log scale in our plots, the y axis range is set above zero in all the figures in this section to show $\frac{d\sigma}{d\Omega}$. However, the negative values for the data points are still in use in finding the scaling factor. They appear below the diagram due to log scale used. The upper limit of the error bars for all existing negative data points are saved in

a graph to plot as marked in red in the figures. Thus, whenever the red point appears in the histogram, it just displays where the upper limit of the error bar is for this specific data point. One will then notice that they are still in the plot in some sense.

The scaling factors are interpreted as the spectroscopic factor of the state in the end. Namely, it indicates what the percentage of the projection of the wave function in ^{25}Na on the wave function of the excited state in ^{26}Na.

With regard to the first figure 3.90, it's obvious to say that the best fit comes with the neutron transfer into $2s_{1/2}$ shell for 232 keV state. By knowing which "l" transfer has been succeeded in the experiment, we can then limit the range of possible spins that the populated state can have. For instance, the final spin range is given by $3 \geq J_{final} \geq 2$, and the final parity is assigned as positive due to the parity multiplication rule for $1d_{5/2}$ and $2s_{1/2}$ coupling. To make more interpretation about the 232 keV state, the figure 3.89 can be checked for the spin assignment of the state depending on the shell model results and the spin of the isotone nucleus for the same energy range. It can be noticed that all the predictions in the figure 3.89 assigns the lowest states as either 2^+ or 3^+ in this energy range.

The values for different wave transfer for neutron is presented in the table 3.8. The table shows that the analysis has been done for each plot in the figure 3.90. The errors in spectroscopic factors are respectively statistical due to fitting process and systematic error due to the error in normalization factor which was used to get the proton angular distributions as shown in the equation 3.12. The second error is calculated as the multiplication of the spectroscopic factor for a given state with the spin assigned and the error value 0.026 determined from the normalization factor. At this stage of the analysis, all final spins are set to two to find the scaling factor, the transformation of the spectroscopic factors for the true final spins will be done in the next section. According to the spectroscopic factors in

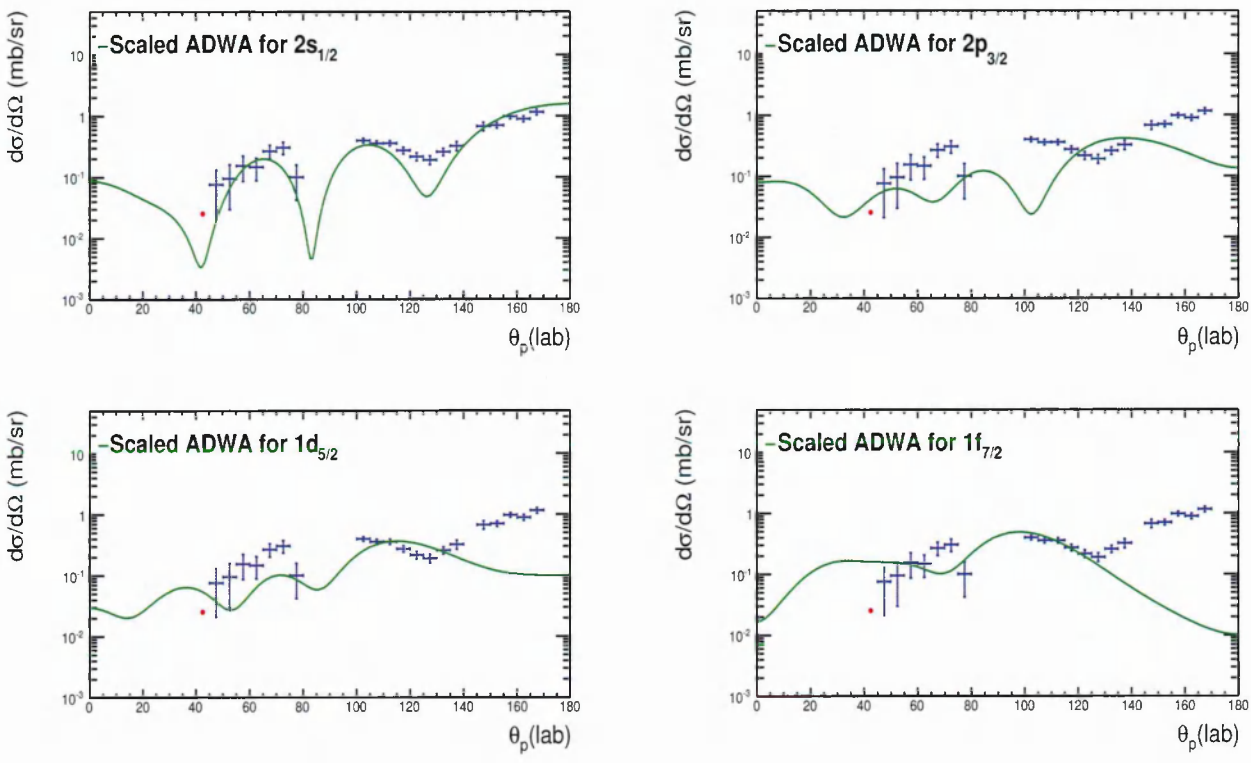

Figure 3.90: Differential cross sections of the protons to determine the "l" transfer in 232 keV state. In the text, the $2s_{1/2}$ transfer is selected as the best fit. The gates on γ-ray and its background energy for 90° clovers were $238keV > E_\gamma > 225keV$ and $225keV > E_\gamma > 212keV$, respectively. For 135° clovers, the gates on γ-ray and its background energy were $238keV > E_\gamma > 226keV$ and $226keV > E_\gamma > 214keV$, respectively. The gates on excitation energy and its background energy for 90° clovers were $845keV > E_{ex} > -266keV$ and $-266keV > E_{ex} > -1378keV$, respectively. For 135° clovers, the gates on excitation energy and its background energy were $824keV > E_{ex} > -246keV$ and $-246keV > E_{ex} > -1316keV$, respectively. The figure 3.69 for γ-ray energy spectra and the figure 3.77 for excitation energy spectra can be checked.

the table 3.8, the magnitude order from bigger to lower spectroscopic factor goes as for the waves $1f_{7/2}$, $1d_{5/2}$, $2s_{1/2}$ and $2p_{3/2}$, respectively. The selected value for s transfer is $0.1100 \pm 0.0036 \pm 0.0029$ with the errors as explained. Note that, it's not always possible to get the single particle state, so the combination of two possible wave contribution; such as $2s_{1/2}$ and $1d_{5/2}$ waves, occurs most likely for all the states. This part of the analysis will be explained here with figures in this work; however the results will be presented in table 4.1 in following section 4.1. The possible contribution of the $1d_{5/2}$ wave transfer, as shown in the theoretical line of the figure 3.90, should give the missing matching part for the data at 120° detected proton angle. This assumption is based on the combination of s and d wave theoretical lines, because both waves have their own characteristic shape especially after 100° proton angle. After the overlap of these lines, one may expect rather smooth dip at backward angle of 120°.

We can sum the two theoretical lines which give the same parity like s wave and d wave in this case. Then, the new theoretical line with the contribution of the two waves will reflect the structure of $(SF_1 * s_{wave}) + (SF_2 * d_{wave})$. Namely, we'll have two spectroscopic factors showing the individual weight of the two wave functions to get a particular spin and parity, which will be the same for both waves after coupling with proton shell in odd-odd nuclei ^{26}Na. In general, it's done by defining the expected value from the theoretical lines as the sum of two selected waves (for either s and d or p and f orbitals) to be used in the equation 3.17. Then, the ROOT will scan all the possible chi-squared values until it finds the lowest value. Two parameters (SF_1 and SF_2) will be implemented in the expected value, that is calculated per bin (as angle), in the form of $(SF_1 * s_{wave}) + (SF_2 * d_{wave})$. Therefore, one can indeed investigate the contributions of the two different couplings will give two different spectroscopic factors, SF_1 and SF_2, by

referring the weight of each individual component to constitute the final wave function of the excited state for the final agreed spin with this further analysis.

$$\Psi(2^+) = a \times \Psi(\nu 2s1/2 \times \pi 1d_{5/2}) + b \times \Psi(\nu 1d_{5/2} \times \pi 1d_{5/2}) + ... \quad (3.18)$$

In the equation 3.18, ν stands for neutron, and π represents proton where they couple as represented by the symbol $\times$ to get the final spin 2^+. This is the simplest case one can get without breaking any pair in the either neutron or proton shells. It's not explicitly shown in the equation 3.18 that one can couple proton and neutron in different ways. Therefore, by mixing the two theoretical lines for s wave and d wave, for instance, one can have a new theoretical line which is the representative of the mixture in s and d waves by the coefficients SF_1 and SF_2 as mentioned. This will then show the dominant wave contribution in the final wave function of the populated state as it appears in figure 3.91.

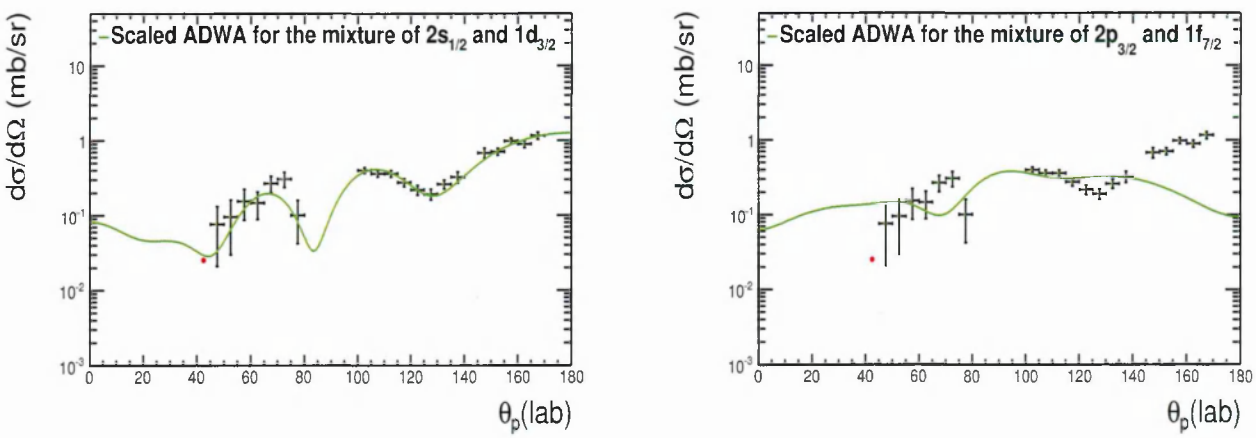

Figure 3.91: Differential cross sections of protons to determine the individual S.F. in mixed "l" transfer of the excited state at 232 keV. In the text, the $2s_{1/2}$ transfer is selected as the best fit, so this figure shows possible d wave contribution (see table 4.1).

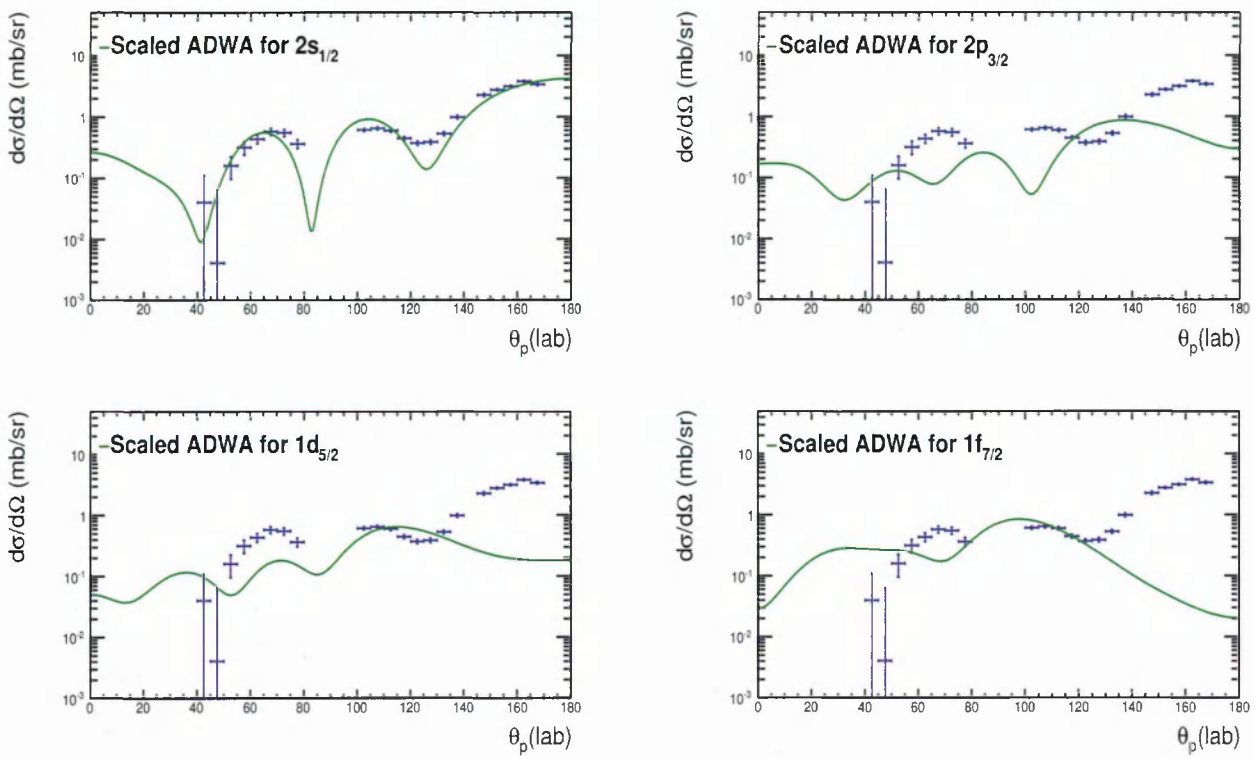

Figure 3.92: Differential cross sections of the protons to determine the "l" transfer in 405 keV state. In the text, the $2s_{1/2}$ transfer is selected as the best fit. The gates on γ-ray and its background energy for 90° clovers were $415keV > E_\gamma > 396keV$ and $395keV > E_\gamma > 376keV$, respectively. For 135° clovers, the gates on γ-ray and its background energy were $413keV > E_\gamma > 397keV$ and $396keV > E_\gamma > 380keV$, respectively. The gates on excitation energy and its background energy for 90° clovers were $938keV > E_{ex} > -85keV$ and $-85keV > E_{ex} > -1107keV$, respectively. For 135° clovers, the gates on excitation energy and its background energy were $910keV > E_{ex} > -46keV$ and $-46keV > E_{ex} > -1002keV$, respectively.

Another low lying state at 405 keV looks having similar angular momentum transfer in (d,p) reaction as in the 232 keV case. Especially the backward angles of 140° in the data as in the figure 3.92 explains the theoretical line, presented for s wave, better than other transferred neutron shells. In that case, the possible spin options can be in the range of $3 \geq J_{final} \geq 2$ due to same coupling in the odd-odd nuclei of ^{26}Na as in the 232 keV state. Then, of course the parity of the state will give the same answer as positive. The data points for detected protons between 40° and 70° match rather well as much as the angle range 140° and 180°. Also, the shape is maintained well in overall angles, this is the most important part for comparison with the theory. Final result for the spectroscopic factor of s wave transfer is given as $0.2956 \pm 0.0045 \pm 0.0077$ for spin 2 as listed with all the other wave transfers in the table 3.8. When a possible d wave contribution is taken into account, figure 3.93 gives smoother dip between 120° and 140° laboratory angles as seen in comparison to the figure 3.90. It's clear that even the combination of p and f waves fail in describing the data in various angles.

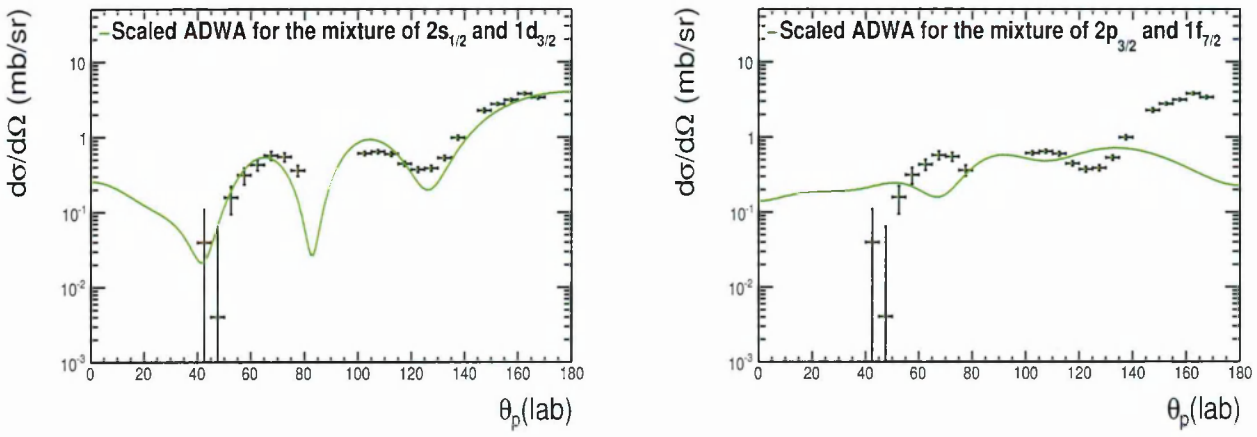

Figure 3.93: Differential cross sections of protons to determine the individual S.F. in mixed "l" transfer of the excited state at 405 keV. In the text, the $2s_{1/2}$ transfer is selected as the best fit, so this figure shows possible d wave contribution (see table 4.1).

The proton differential cross section for the state at 1.507 MeV gives the first d wave transfer in the current work. The spectroscopic factor of this state has not been extracted in previous work [1], so this will be presented in the table 3.8 for the first time. The only γ-ray branch at 1275 keV, used as a gate, of this state as seen on 3.21 enables us to get a good fit especially backwards of 100° where the ADWA works well for (d,p) reaction. After the "l" transfer is assigned to the $1d_{\frac{3}{2}}$ neutron shell, we can say that it's more likely to have spin range $4 \geq J_{final} \geq 1$ due to coupling with $1d_{\frac{5}{2}}$ proton shell in ^{26}Na. Then, the parity of the final state is calculated by the parity multiplication formula in $\pi_{final} = \pi_{dwave} \times \pi_{dwave}$ as positive again. The spectroscopic value of the state is calculated as $0.2349 \pm 0.0138 \pm 0.0061$ from the scaling in d wave in figure 3.94 by using the final spin 2 in TWOFNR code [17] for convenience.

Note that this state has no feeding from higher lying states, so it's rather easier to extract the differential cross section of the protons by using the term DD_1 in the formula

3.13 as explained before. However, it was more complicated to extract the data using the term DD_2 in the formula 3.14 for the state at 232 keV where we have feeding from the state 405 keV.

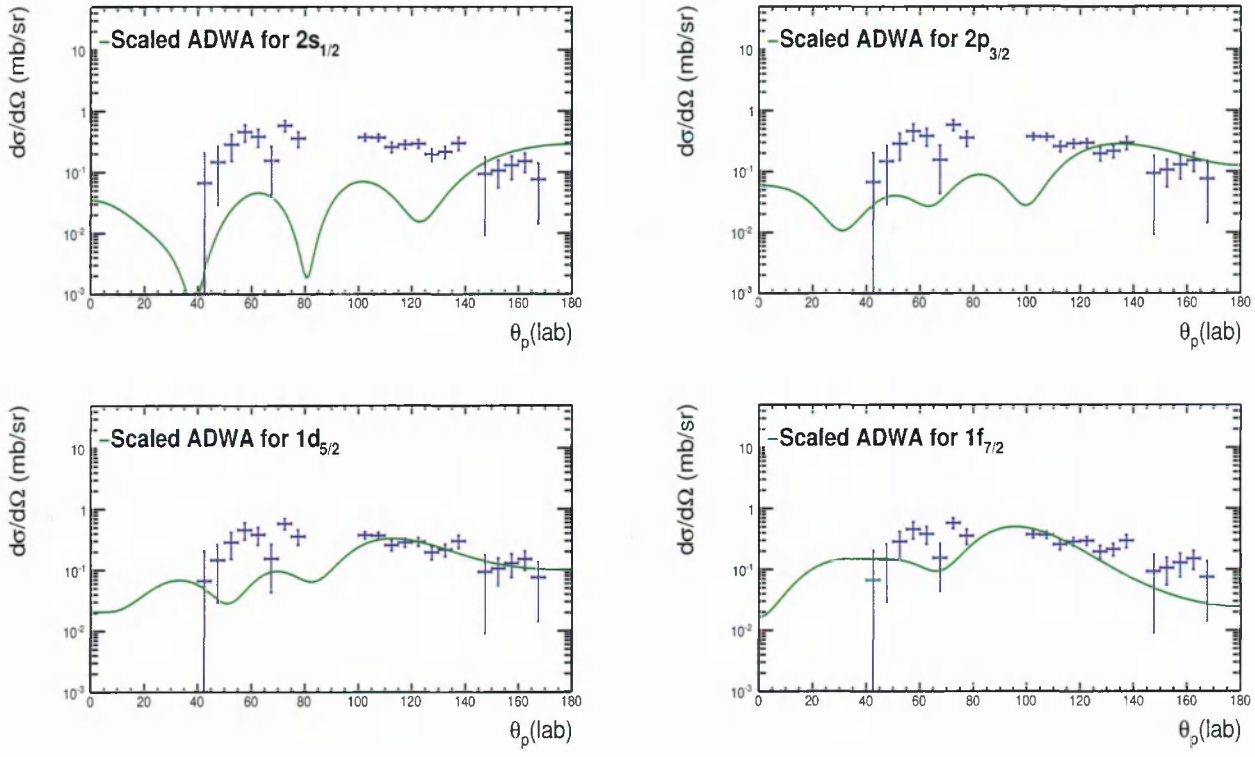

Figure 3.94: Differential cross sections of the protons to determine the "l" transfer in 1507 keV state. In the text, the $1d_{3/2}$ transfer is selected as the best fit. The gates on γ-ray and its background energy for 90° clovers were $1302keV > E_\gamma > 1250keV$ and $1250keV > E_\gamma > 1198keV$, respectively. For 135° clovers, the gates on γ-ray and its background energy were $1296keV > E_\gamma > 1255keV$ and $1255keV > E_\gamma > 1213keV$, respectively. The gates on excitation energy and its background energy for 90° clovers were $2123keV > E_{ex} > 1033keV$ and $1033keV > E_{ex} > -58keV$, respectively. For 135° clovers, the gates on excitation energy and its background energy were $2254keV > E_{ex} > 986keV$ and $986keV > E_{ex} > -282keV$, respectively.

At this stage, we can only say the contribution of d wave is quite strong in comparison

to s wave from the values in the table 3.8. However, figure 3.95 does not show this interpretation explicitly due to the good f wave matching in the figure 3.94. What we see in the figure 3.95 is purely this effect. Table 4.1 will show individual spectroscopic factor contributions for corrected spin assignment in section 4.1, we'll see again d wave gives the dominant weight in the mixing.

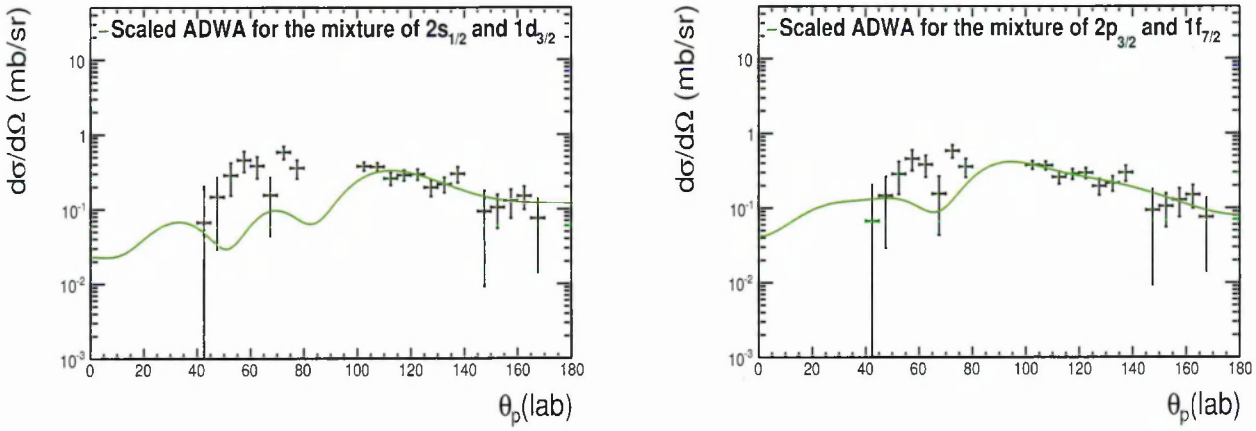

Figure 3.95: Differential cross sections of protons to determine the individual S.F. in mixed "l" transfer of the excited state at 1.507 MeV. In the text, the $1d_{3/2}$ transfer is selected as the best fit, so this figure shows possible s wave contribution (see table 4.1).

The next state to analyse for defining the "l" transfer is 1.805 MeV state as seen in figure 3.96. Due to wide excitation energy limits that result in being fed by the higher lying state at 2.225 MeV, one should subtract the additional angular distribution that results from the angular distribution of the state at 2.225 MeV as formulated with DD_2 term in the formula of 3.14. Thus, the necessary subtraction will be handled by this formula. It's found that the data points in previous work [1] lies about at the same level after 90°; however, they are slightly higher below 90° proton angle. Also, the scaling in the previous work [1] has been done manually by shifting the theoretical line by eye.

It turns out the different way of analysing the data can affect the spectroscopic factor results (see figure 4.5). In the current work, everything is done by using codes in $C++$ and ROOT rather than using traditional methods. Previously, the spectroscopic factor for the final spin 3^+ is noted as 0.216 without error bars. On the other hand, it's found as $0.4430 \pm 0.0206 \pm 0.0115$ with statistical and systematic errors for the final spin 3 in this work for a comparison at this stage of the analysis. The spectroscopic factors seen in the table 3.8 is not adjusted by the final assigned spin by using the equation 3.16 in this section because the spin assignments will be done in section 4.1.

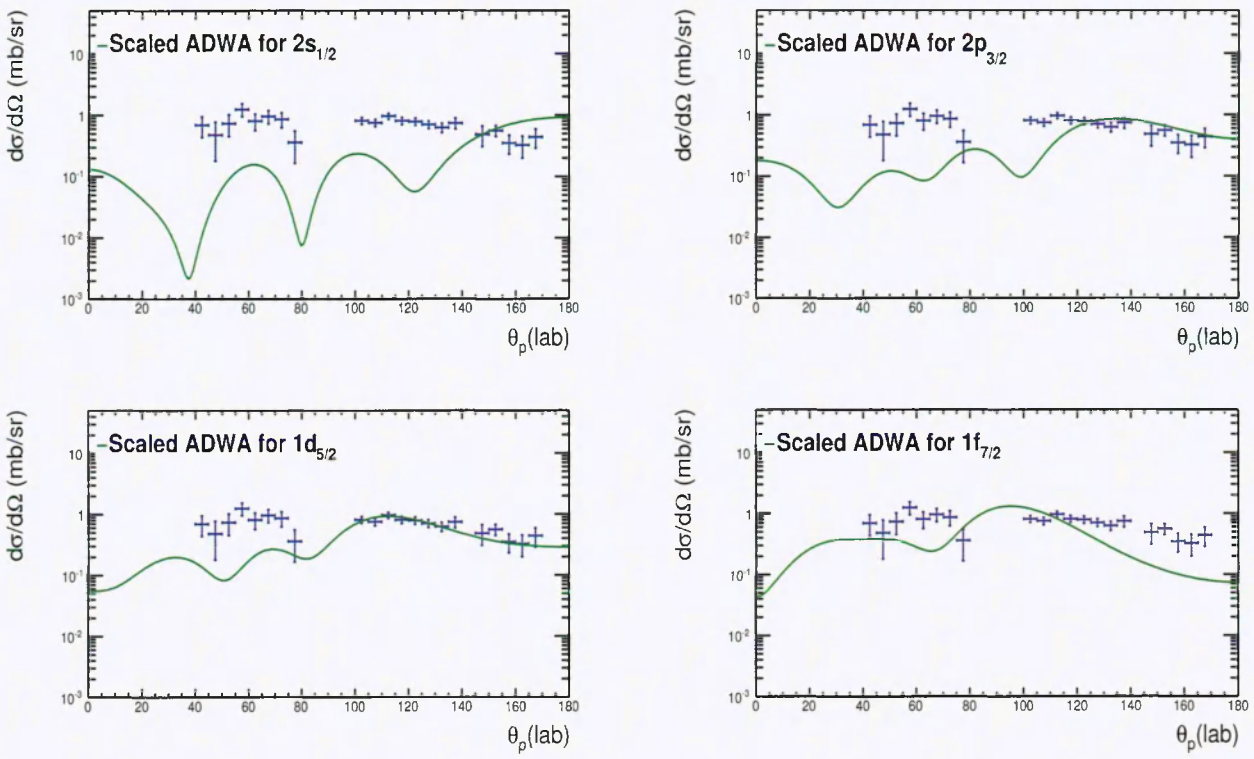

Figure 3.96: Differential cross sections of the proton to determine the "l" transfer of the excited state at 1805 keV. In the text, the $1d_{3/2}$ transfer is selected as the best fit. The gates on γ-ray and its background energy for 90° clovers were $1844keV > E_\gamma > 1769keV$ and $1919keV > E_\gamma > 1844keV$, respectively. For 135° clovers, the gates on γ-ray and its background energy were $1834keV > E_\gamma > 1775keV$ and $1893keV > E_\gamma > 1834keV$, respectively. The gates on excitation energy and its background energy for 90° clovers were $2843keV > E_{ex} > 1260keV$ and $1260keV > E_{ex} > 74keV$, respectively. For 135° clovers, the gates on excitation energy and its background energy were $2517keV > E_{ex} > 1270keV$ and $1270keV > E_{ex} > 23keV$, respectively.

Normally, the possible spin range for this state is $4 \geq J_{final} \geq 1$ due to the coupling, but the analogical isotone nucleus of $^{28}Al_{15}$ and the shell model give some interpretation of the final spin based on the excitation energy of interest as seen in the figure 3.89. It seems they both provide different suggestions for the similar excitation energy range.

After deciding which "l" transfer occurred in the figure 3.96, we can calculate single wave contributions in the total wave function of ^{26}Na by the help of figure 3.97 where we consider mixing of given orbitals in the figure. The scaling is based on backwards angles of 90° since ADWA theory gives better results for the (d,p) reaction. It's also clear again that the figure 3.97 itself is not enough to decide about the type of wave in terms of s, p, d, and f orbitals due to their proximity in these two mixtures (either s-d or p-f).

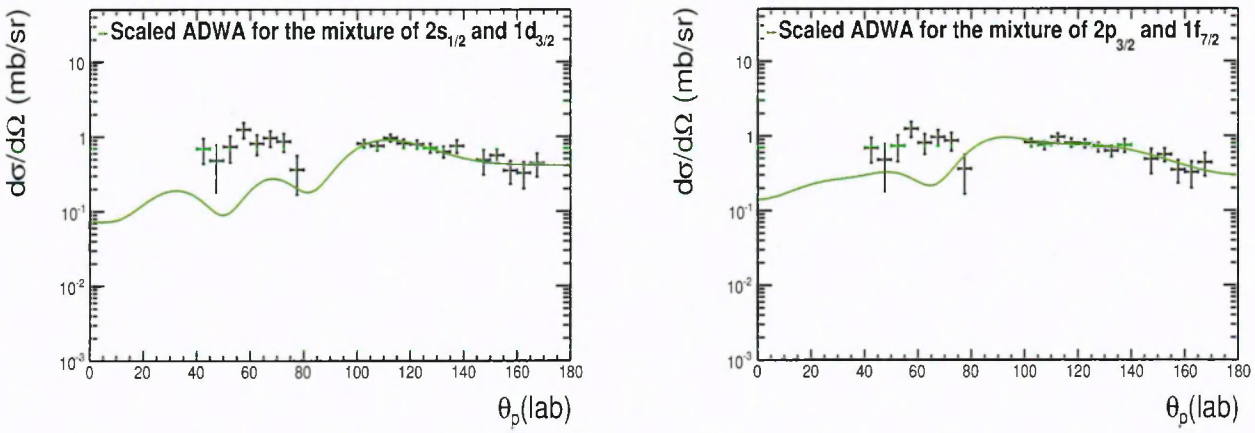

Figure 3.97: Differential cross sections of protons to determine the individual S.F. in mixed "l" transfer of the excited state at 1.805 MeV. In the text, the $1d_{3/2}$ transfer is selected as the best fit, so this figure shows possible s wave contribution (see table 4.1).

The only exception for neutron to transfer into the d orbital is the 2.116 MeV state. The theoretical differential cross section analysis is carried out for $1d_{5/2}$ neutron shell instead of $1d_{3/2}$ with the final spin 2 in TWOFNR code [17]. The reason will be explained when the spin assignments are done in the following chapter.

With regard to extract the proton differential cross section from the data, the 2.116 MeV state is one of the simplest cases. This is because it does not have feeding from the higher lying state in the excitation energy range given to populate this state. Thus,

one can simply use the DD_1 term in the formula 3.13 to retrieve the corresponding $\frac{d\sigma}{d\Omega}$ from the data with the help of normalization factor, γ-ray efficiency, solid angle of the SHARC array, and lastly the branching ratio of the γ-ray gate used to populate the state. Apart from the strong statistical fluctuations in the result of the previous work [1], the data points were roughly aligned between 0.1 mb/sr and 1 mb/sr for the $1d_{3/2}$ neutron shell transfer. The differences in the data points for different proton angles might result from slightly different either the γ-ray efficiency or the calculated solid angle values for the SHARC array between the previous[1] and current work. After the detailed comparison, it's concluded that both the efficiency and the solid angle should not affect the results so much since they are different at negligible levels from each other.

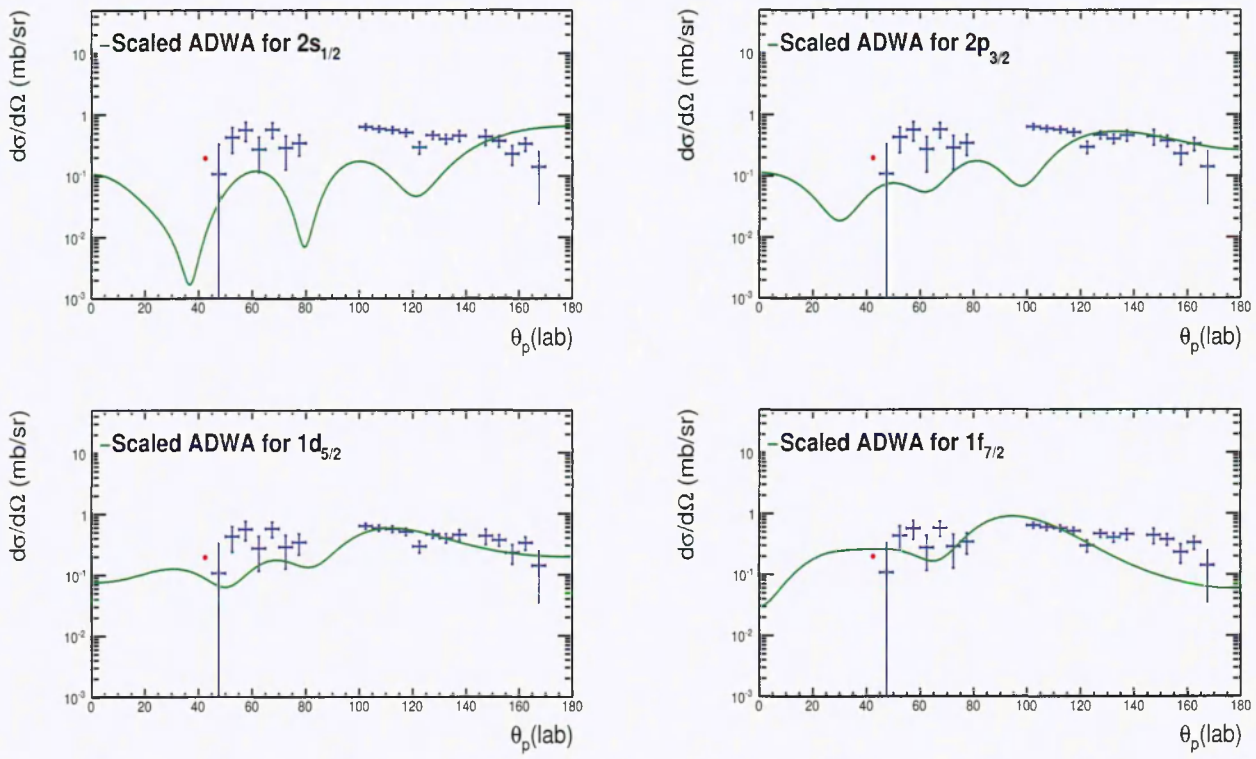

Figure 3.98: Differential cross sections of the proton to determine the "l" transfer of the excited state at 2116 keV. In the text, the $1d_{5/2}$ transfer is selected as the best fit. The gates on γ-ray and its background energy for 90° clovers were $2160keV > E_\gamma > 2074keV$ and $2084keV > E_\gamma > 2034keV$, respectively. For 135° clovers, the gates on γ-ray and its background energy were $2150keV > E_\gamma > 2081keV$ and $2084keV > E_\gamma > 2034keV$, respectively. The gates on excitation energy and its background energy for 90° clovers were $2690keV > E_{ex} > 1721keV$ and $1721keV > E_{ex} > 751keV$, respectively. For 135° clovers, the gates on excitation energy and its background energy were $2726keV > E_{ex} > 1635keV$ and $1635keV > E_{ex} > 545keV$, respectively.

In figure 3.98, the only negative data point around 42 degree is marked with red marker on its upper limit. Thus, it can be noticed the error bar of this data point is still on the theoretical line. The matching of data points and theoretical line for the final spin 2 and neutron transferred in to the $1d_{5/2}$ shell is found better in comparison to the $1d_{\frac{3}{2}}$

shell and the others. This state was previously assigned to 4^+ spin due to the coupling of the proton in the $1d_{5/2}$ shell and the neutron in the $1d_{3/2}$ shell in the work [1]. The table 3.8 will indicate the updated spectroscopic factors for the final spin 2 at this stage to get the initial idea about individual strengths of spectroscopic factors for different neutron orbital transfer. For mixing of the same parity waves, figure 3.99 can be viewed.

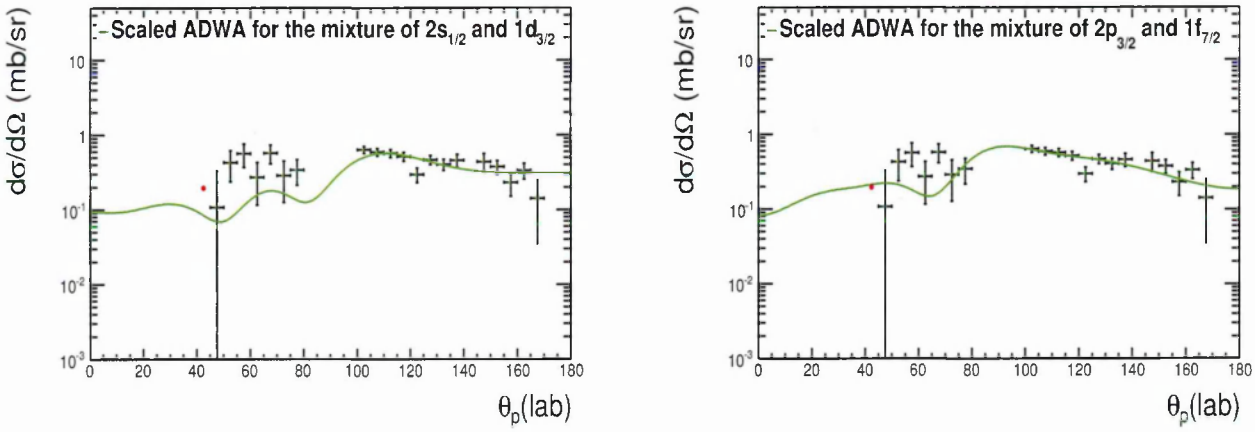

Figure 3.99: Differential cross sections of protons to determine the individual S.F. in mixed "l" transfer of the excited state at 2.116 MeV. In the text, the $1d_{5/2}$ transfer is selected as the best fit, so this figure shows possible s wave contribution (see table 4.1).

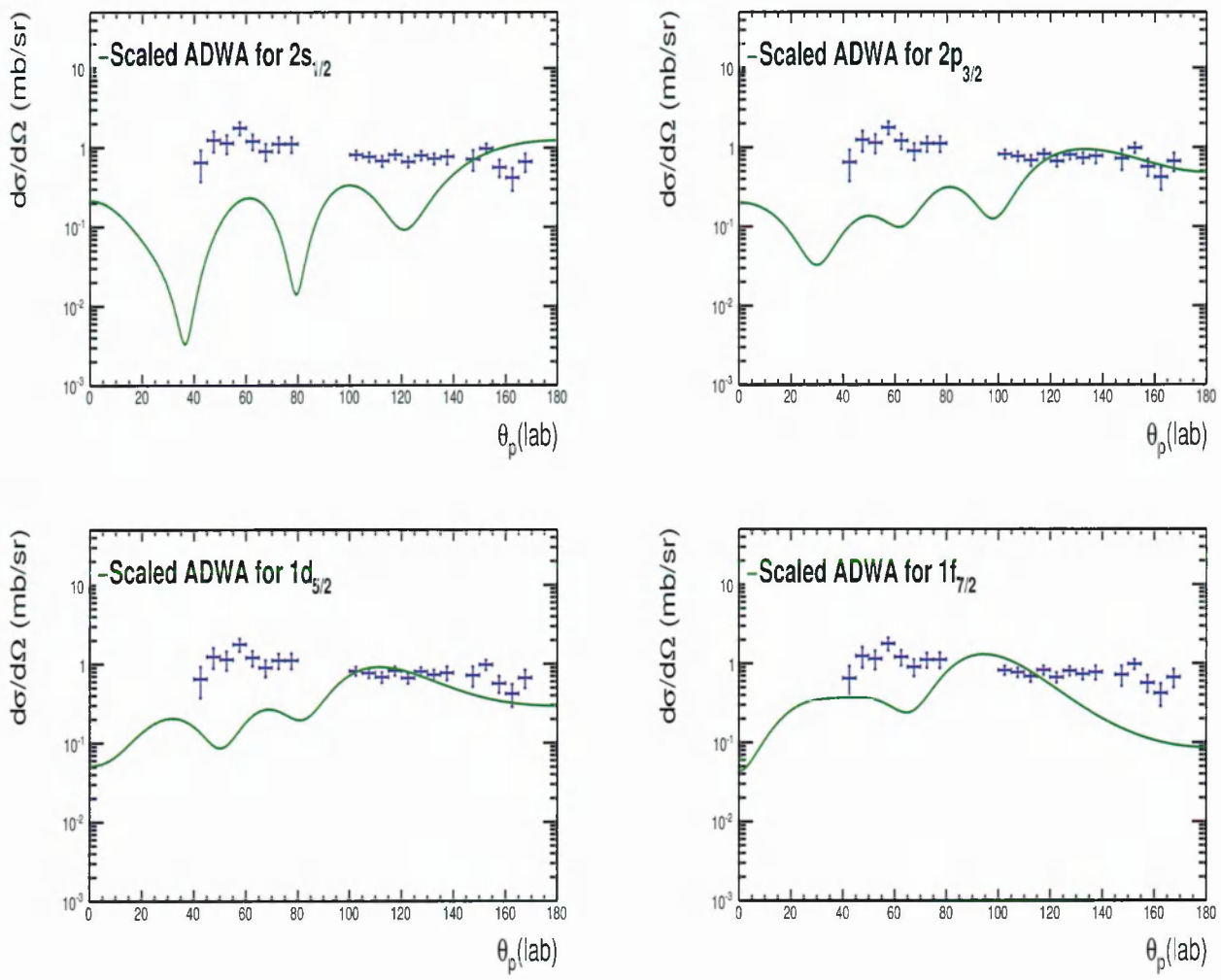

Figure 3.100: Differential cross sections of proton to determine the "l" transfer of the excited state at 2195 keV. In the text, the $1d_{3/2}$ transfer is selected as the best fit. The gates on γ-ray and its background energy for 90° clovers were $2192keV > E_\gamma > 2149keV$ and $2362keV > E_\gamma > 2272keV$, respectively. For 135° clovers, the gates on γ-ray and its background energy were $2198keV > E_\gamma > 2159keV$ and $2331keV > E_\gamma > 2260keV$, respectively. The gates on excitation energy and its background energy for 90° clovers were $2837keV > E_{ex} > 1653keV$ and $1653keV > E_{ex} > 469keV$, respectively. For 135° clovers, the gates on excitation energy and its background energy were $2775keV > E_{ex} > 1780keV$ and $1780keV > E_{ex} > 785keV$, respectively.

For the first time in this work, the 2.195 MeV state is analysed for its spectroscopic factor by extracting the differential cross section of the protons from the data as seen in figure 3.100. This state is similar to the 2.116 MeV state in terms of having no feeding from higher lying states due to the excitation energy gate chosen. Therefore, the figure 3.88 and the equation 3.13 should be referred to know how to extract the data for different cases. The γ-ray branches at 1962 keV and 2195 keV are shown in 3.70 for this state, and the strongest γ-ray branch at 2195 keV has been chosen as a gate to populate this state to extract the proton differential cross sections. Generally speaking, all the γ-ray figures in the section 3.4.2 helps a lot for identifying the best choice of γ-ray gate in this section.

The "l" transfer of the neutron shows two similar plots for p and d wave transfer. The d wave indicates better match with the data at 100° and the backward angles more than the competitive p wave transfer. Another supportive information can be seen in the figure 3.89 where $d_{\frac{3}{2}}$ wave is dominant among others in the range of $3MeV > E_{excitation} > 500keV$ in both level schemes. Therefore, this helps us to assign the "l" value as d wave by quoting the spectroscopic factor in the table 3.8 for final spin 2 and the neutron transferred in to the $d_{\frac{3}{2}}$ shell. Figure 3.101 shows pretty much the same look for the two mixing in angles backward of 90°, but the peak points for backward angles are at 100° and 90° respectively in these two mixture plots.

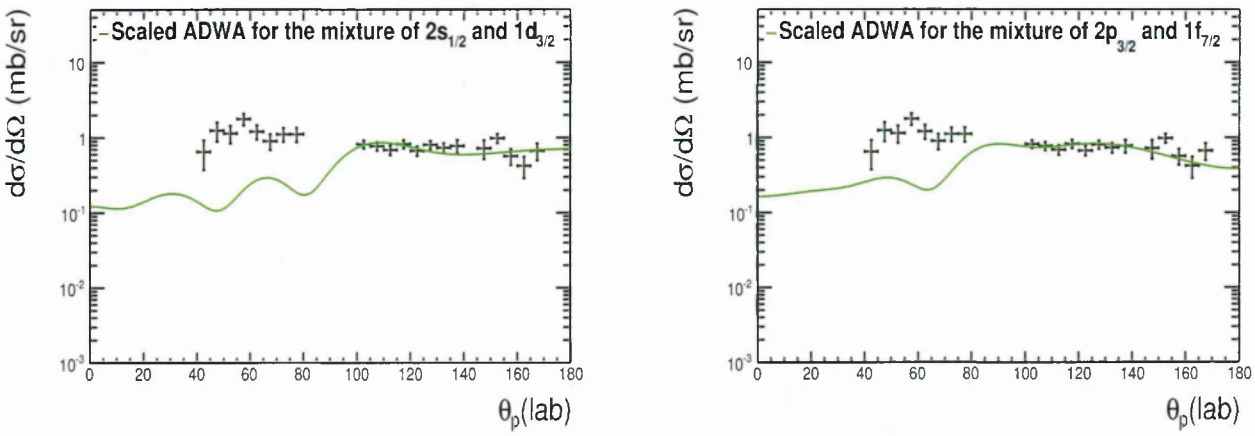

Figure 3.101: Differential cross sections of protons to determine the individual S.F. in mixed "l" transfer of the excited state at 2.195 MeV. In the text, the $1d_{3/2}$ transfer is selected as the best fit, so this figure shows possible s wave contribution (see table 4.1).

The next analysed state at 2.225 MeV normally has feeding from higher lying state at 4.305 MeV, but the excitation energy gate used to extract the spectroscopic factor information avoids any feeding contribution for proton angular distribution of the state. Therefore, this is also a state to be analysed by using the term DD_1 in the formula 3.13. A nice match between 90° and 140° proton angle by reflecting the shape of the theoretical line for d wave transfer leaves no doubt about the the shell where the neutron is transferred as shown in figure 3.102. Both the shell model results for $^{26}Na_{15}$ and the results from isotone nucleus $^{28}Al_{15}$ supports this state to have d wave transfer as seen 3.89. It's found that the data points are slightly higher forward of 90° proton angle than those found in the previous work [1]. However, it turns out this does not affect the spectroscopic factor and "l" transfer found as the table 3.8 can be checked. Once, the spectroscopic factor in the table 3.8 is adapted for the final spin 4^+ as in the figure 1.7, the comparable spectroscopic factor can be calculated as $0.4534 \pm 0.0125 \pm 0.0118$ for the 2.225 MeV state in comparison

to the value 0.432 as given by Wilson [1].

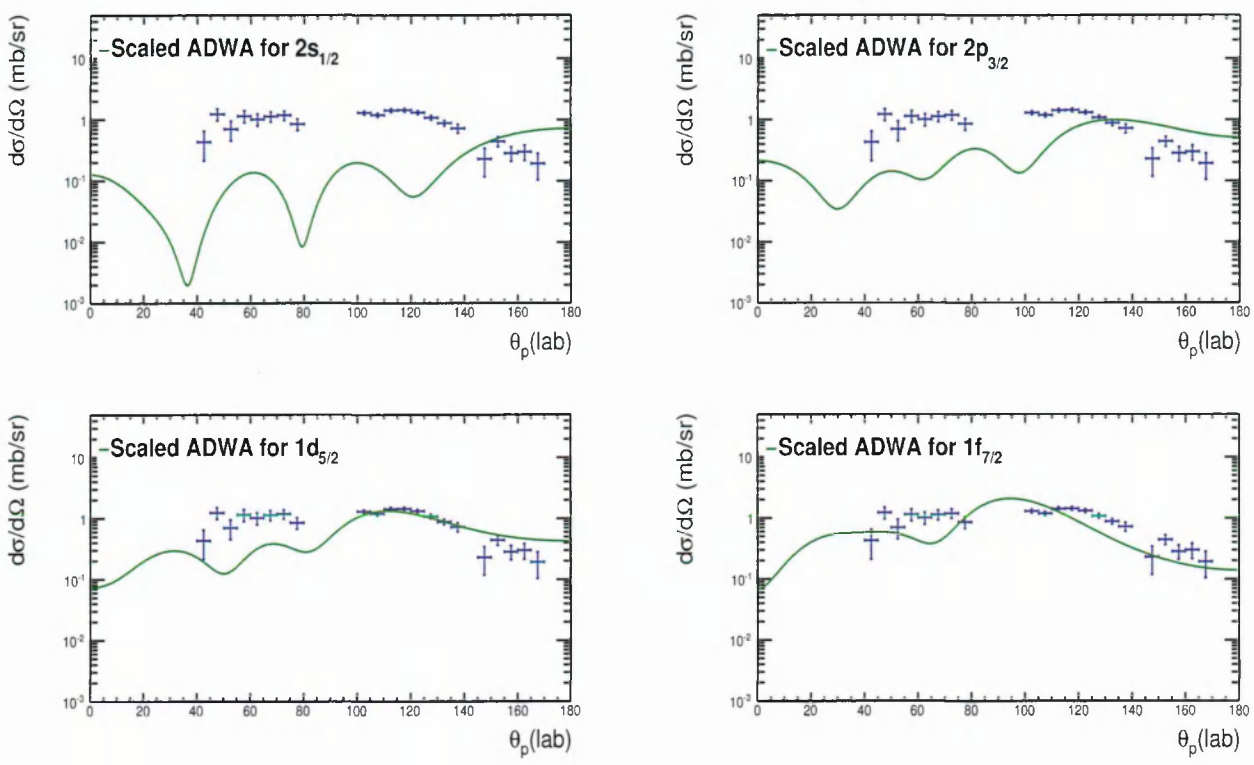

Figure 3.102: Differential cross sections of proton to determine the "l" transfer of the excited state at 2225 keV. In the text, the $1d_{3/2}$ transfer is selected as the best fit. The gates on γ-ray and its background energy for 90° clovers were $2272keV > E_\gamma > 2217keV$ and $2363keV > E_\gamma > 2272keV$, respectively. For 135° clovers, the gates on γ-ray and its background energy were $2261keV > E_\gamma > 2215keV$ and $2333keV > E_\gamma > 2261keV$, respectively. The gates on excitation energy and its background energy for 90° clovers were $2843keV > E_{ex} > 1712keV$ and $1712keV > E_{ex} > 582keV$, respectively. For 135° clovers, the gates on excitation energy and its background energy were $2839keV > E_{ex} > 1720keV$ and $1720keV > E_{ex} > 560keV$, respectively.

Knowing the scaling has been done for data points in the proton angle range 90° – 180°, s-d wave mixture in figure 3.103 shows slightly better fit for 120° proton angle. Despite that, the real purpose of these figures showing the mixture of different orbitals

is to get specific weights for a specific orbital transfer, not for an identification of this particular orbital where the neutron is transferred. Thus, figures like 3.103 are mostly for a demonstration.

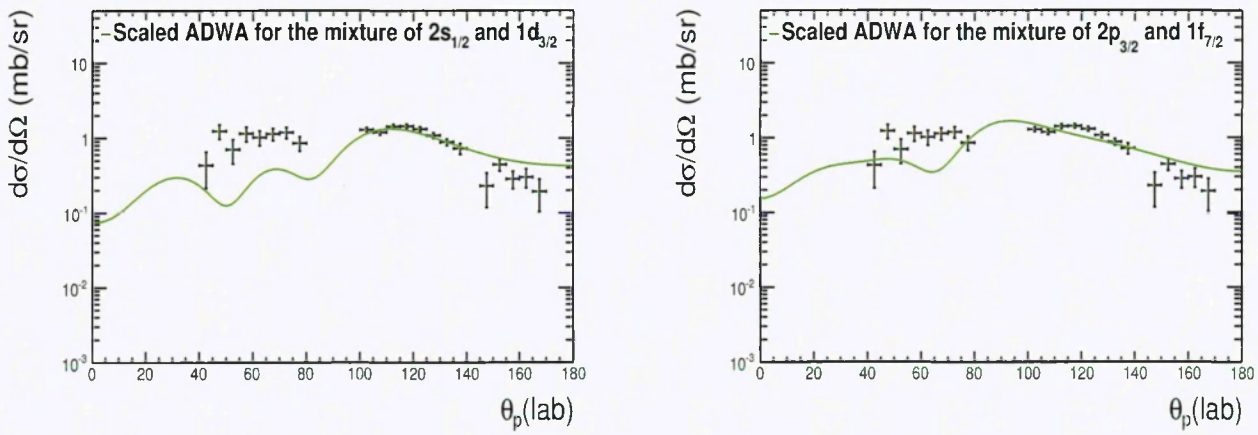

Figure 3.103: Differential cross sections of protons to determine the individual S.F. in mixed "l" transfer of the excited state at 2.225 MeV. In the text, the $1d_{3/2}$ transfer is selected as the best fit, so this figure shows possible s wave contribution (see table 4.1).

The state at 2.843 MeV in figure 3.104 is one of the state which has not been analysed to extract the spectroscopic factor before. It is assigned to p wave transfer, but this assignment is not really a conclusive one at this stage. Further analysis considering the parity of nearby states and the character of decays in terms of transition types is necessary. Final spin assignment of the state will be discussed in following section 4.1 in detail. The possible spin range that this state can have for p wave selection is $4 \geq J_{final} \geq 1$. Again, the values for spectroscopic factors for different wave transfer are listed in the table 3.8 for the final spin 2 before assigning the agreed spin later.

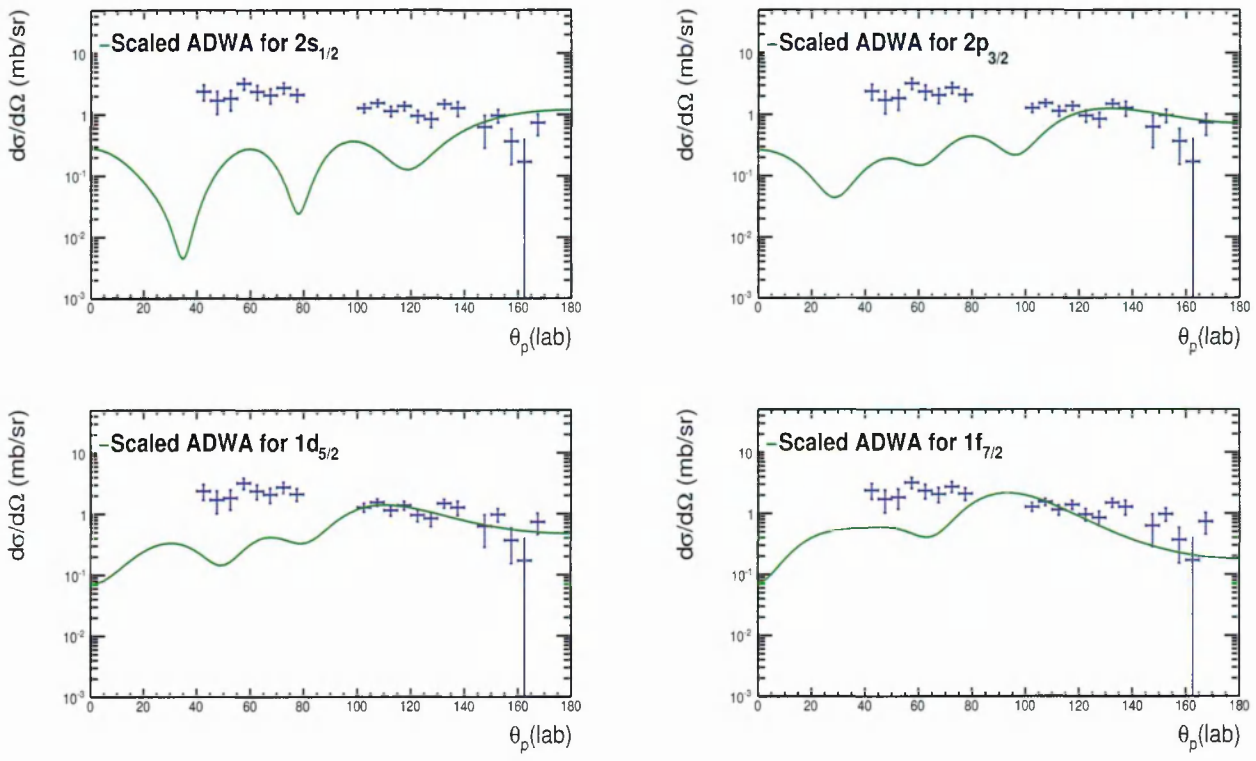

Figure 3.104: Differential cross sections of proton to determine the "l" transfer of the excited state at 2843 keV. In the text, the $2p_{3/2}$ transfer is selected as the best fit. The gates on γ-ray and its background energy for 90° clovers were $2675keV > E_\gamma > 2567keV$ and $2560keV > E_\gamma > 2445keV$, respectively. For 135° clovers, the gates on γ-ray and its background energy were $2654keV > E_\gamma > 2569keV$ and $2560keV > E_\gamma > 2445keV$, respectively. The gates on excitation energy and its background energy for 90° clovers were $3852keV > E_{ex} > 2252keV$ and $2242keV > E_{ex} > 642keV$, respectively. For 135° clovers, the gates on excitation energy and its background energy were $3817keV > E_{ex} > 2217keV$ and $2209keV > E_{ex} > 609keV$, respectively.

In the figure 3.89, there is almost 1.7 MeV gap between 1830 keV and 3317 keV. Thus, there is no spin assignment for a similar state energy. On the other hand, 2.656 MeV state is assigned to 4^+ state in the isotone nucleus of $^{28}Al_{15}$ as seen in the same figure. Thus, there is no additional and supportive information that we can bring about.

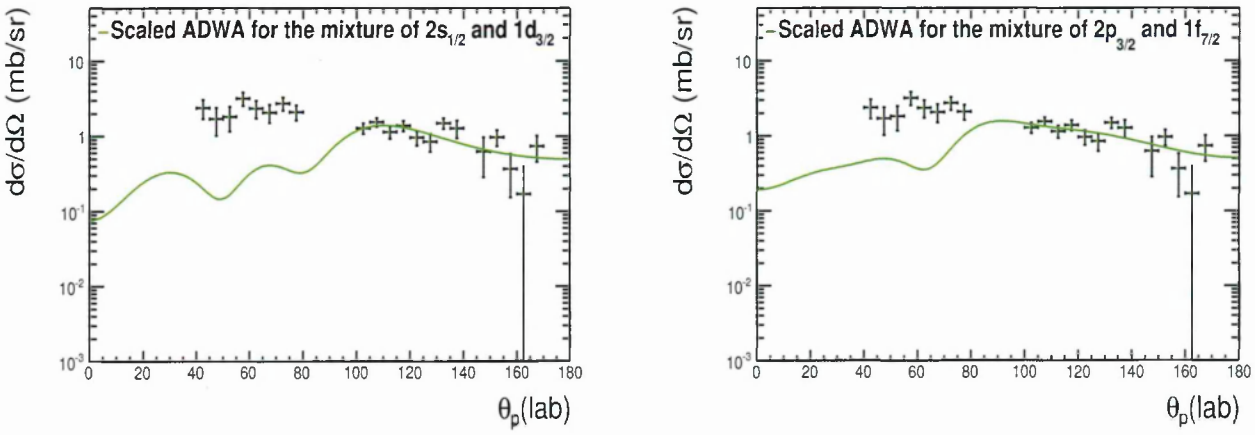

Figure 3.105: Differential cross sections of protons to determine the individual S.F. in mixed "l" transfer of the excited state at 2.843 MeV. In the text, the $2p_{3/2}$ transfer is selected as the best fit, so this figure shows possible f wave contribution (see table 4.1).

When the $2p_{3/2}$ shell is assumed to be the choice, it's observed that data points forward of 90° seem to stay closer to the mixed theoretical lines of the "p-f" combination in the lower panel of figure 3.105. Other than that, both "p-f" and "s-d" mixture are shown and scaled by using only backward of 90° part of the data and theoretical points.

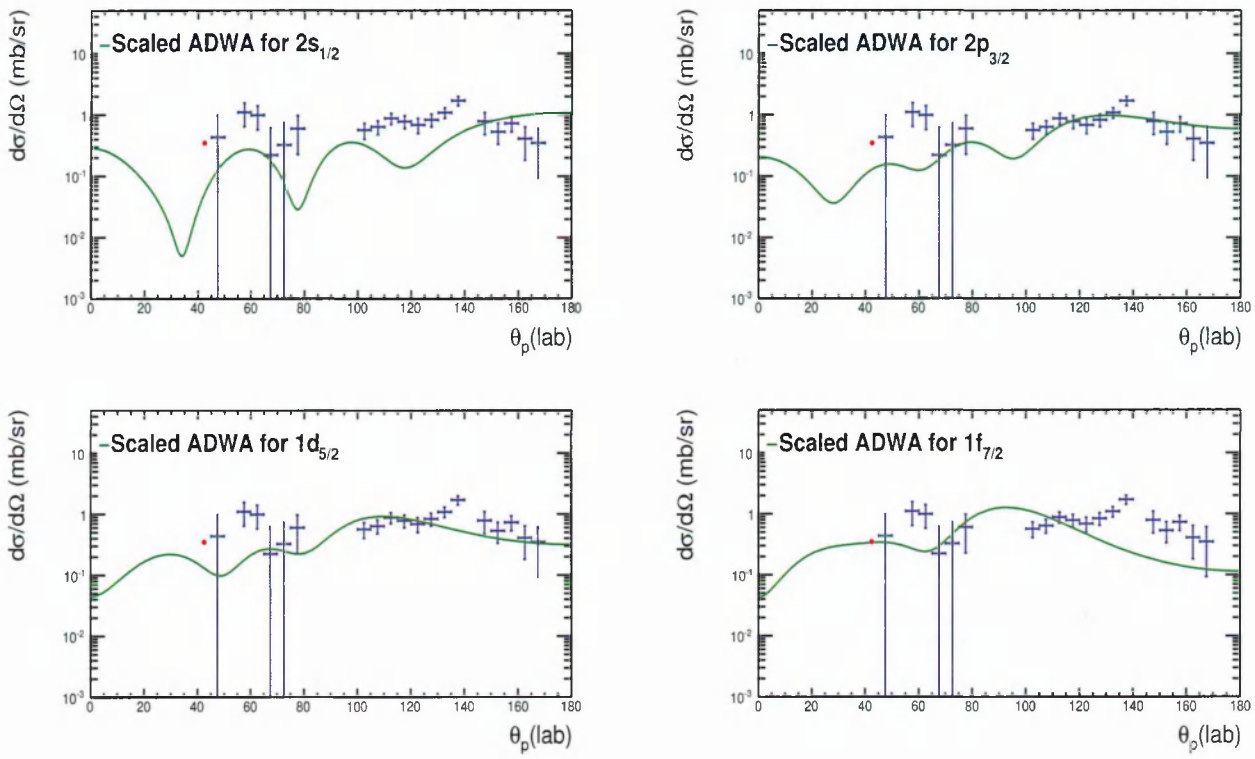

Figure 3.106: Differential cross sections of proton to determine the "l" transfer of the excited state at 3135 keV. In the text, the $2p_{3/2}$ transfer is selected as the best fit. The gates on γ-ray and its background energy for 90° clovers were $3200keV > E_\gamma > 3073keV$ and $3327keV > E_\gamma > 3200keV$, respectively. For 135° clovers, the gates on γ-ray and its background energy were $3186keV > E_\gamma > 3083keV$ and $3288keV > E_\gamma > 3186keV$, respectively. The gates on excitation energy and its background energy for 90° clovers were $3805keV > E_{ex} > 2522keV$ and $2522keV > E_{ex} > 1240keV$, respectively. For 135° clovers, the gates on excitation energy and its background energy were $3887keV > E_{ex} > 2459keV$ and $2459keV > E_{ex} > 1032keV$, respectively.

The 3.135 MeV state is previously thought as a state with no γ-ray feeding from higher lying states, but the further analysis discovered one misplaced γ-ray at 1104 keV in comparison to the level scheme 1.7. This γ-ray indeed decays from the new higher lying state at 4.239 MeV to the 3.135 MeV state. Therefore, the DD_2 term in the second

formula 3.14 is deployed to extract the proton differential cross section. The spectroscopic factor is found similar comparison to the previously extracted value as shown in the table 3.8. The red point shows the upper limit of the error bar of the negative data point, so it's obvious that even this negative data point is on the theoretical line within the error bar for the assigned angular momentum according to $2p_{3/2}$ shell in neutron transfer. Although p and d waves look similar to each other at first glance, the p wave gives better fit for the angle range close to 140° proton angle. All the other spectroscopic factors for different "l" transfer can be found in the table 3.8 as well. The mixture of the same parity waves can be presented in figure 3.107. Even the mixture of favoured orbital covers the data points better than "s-d" orbital mixture, especially between 100° and 135°.

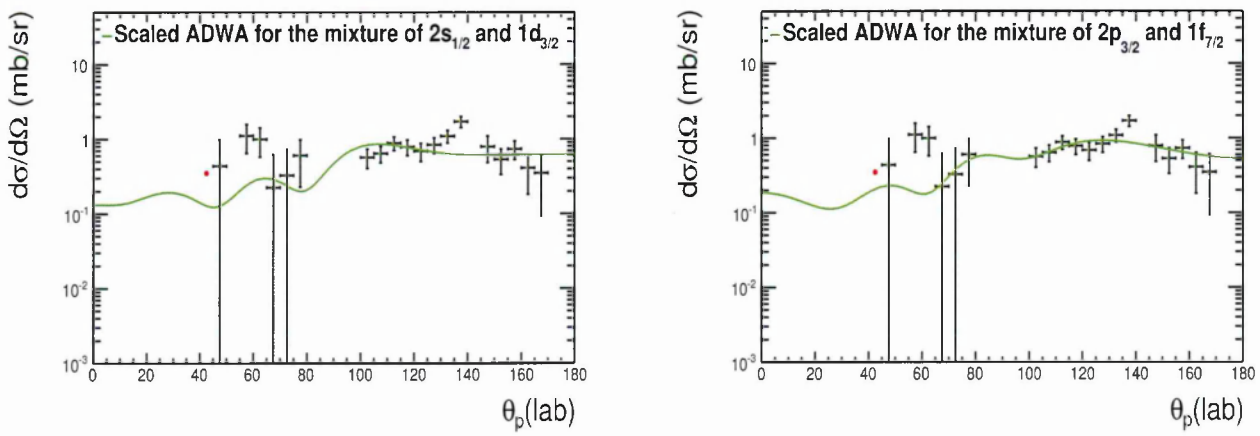

Figure 3.107: Differential cross sections of protons to determine the individual S.F. in mixed "l" transfer of the excited state at 3.135 MeV. In the text, the $2p_{3/2}$ transfer is selected as the best fit, so this figure shows possible f wave contribution (see table 4.1).

The 3.511 MeV has been the most complicated state in terms of extracting the proton differential cross section due to existing two feeding states in the excitation energy gate given. This is because the excitation energy limits of 3.511 MeV is wide enough to

cover partly both the excitation energy limits of 4.305 MeV and 4.917 MeV states. The dominant "l" transfer assigned to this neutron transfer is $2p_{\frac{3}{2}}$ as its better fit is seen in figure 3.108.

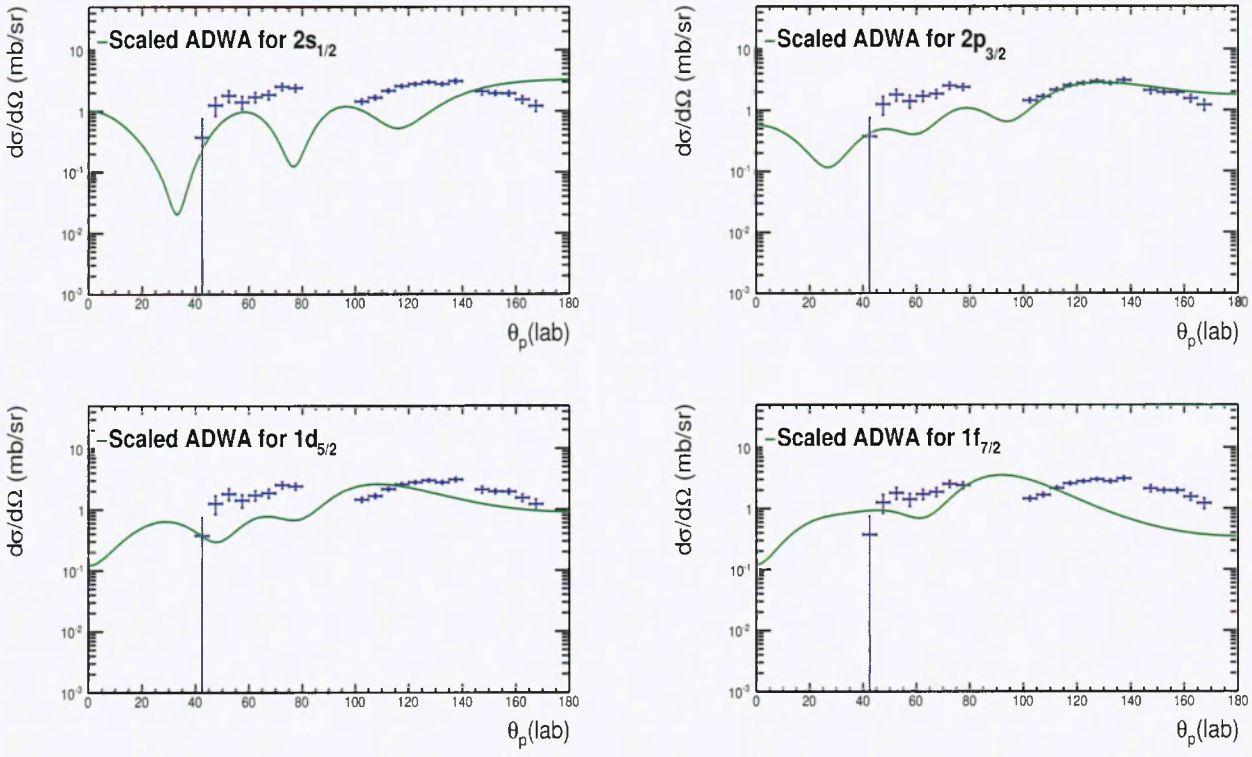

Figure 3.108: Differential cross sections of proton to determine the "l" transfer of the excited state at 3511 keV. In the text, the $2p_{3/2}$ transfer is selected as the best fit. The gates on γ-ray and its background energy for 90° clovers were $3584keV > E_\gamma > 3441keV$ and $3441keV > E_\gamma > 3297keV$, respectively. For 135° clovers, the gates on γ-ray and its background energy were $3567keV > E_\gamma > 3453keV$ and $3453keV > E_\gamma > 3338keV$, respectively. The gates on excitation energy and its background energy for 90° clovers were $4307keV > E_{ex} > 2853keV$ and $2853keV > E_{ex} > 1400keV$, respectively. For 135° clovers, the gates on excitation energy and its background energy were $4307keV > E_{ex} > 2863keV$ and $2863keV > E_{ex} > 1419keV$, respectively.

As an example, the isotone nucleus of $^{28}Al_{15}$ in the figure 3.89 assigned the spin and

parity as 4^- as in the previous work [1] for similar excitation energy. However, the shell model predicts the contribution of p and f wave for the energy at 3.559 MeV as seen in the same figure. Most of the case, it is less likely to get "pure" shell model state, so one should consider the mixing of two different "l" transfer here as well as shown in figure 3.109.

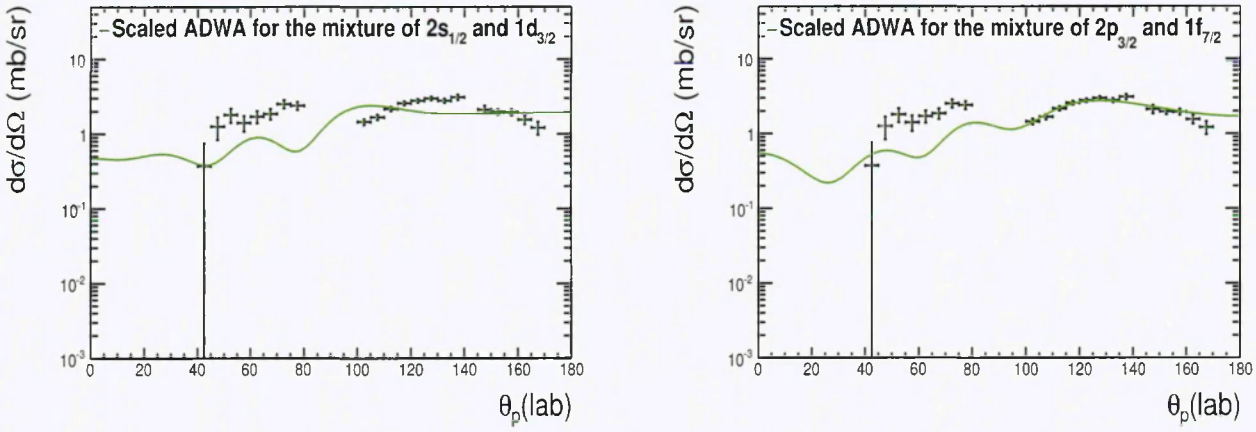

Figure 3.109: Differential cross sections of protons to determine the individual S.F. in mixed "l" transfer of the excited state at 3.511 MeV. In the text, the $2p_{3/2}$ transfer is selected as the best fit, so this figure shows possible f wave contribution (see table 4.1).

Finally, to get the final proton differential cross sections for this state at 3.511 MeV, the term DD_3 in the formula 3.15 is used to eliminate the contribution of DD_2 and DD_1 coming from the states at 4.305 MeV and 4.917 MeV, respectively. However, the table 3.8 refers to the spectroscopic factors extracted individually for different waves, so the mixing of the two waves is not taken into account in this table.

The 4087 keV state is one of the new states that is analysed only in this work in terms of spectroscopic factor extraction from the data as shown in the figure 3.110. As the proton angle range backward of 90° is used as a reference for scaling, the $2p_{3/2}$ shell

is chosen as the best fit for our transferred neutron. In that case, the possible final spins will be in the range of 1 to 4. In terms of parity, the state will have the negative parity due to the coupling of positive parity due to the proton orbital (d) and negative parity due to the neutron orbital (p). While the shell model prediction in the figure 3.89 says it is close to p wave transfer for this range of energy, the analogous nucleus $^{28}Al_{15}$ indicates f wave transfer for every state above 3.4 MeV. This is another reason we need to check mixing in spectroscopic factors to help us for our spin interpretation as well. Figure 3.111 represents possible mixtures in terms of transferred neutron shells.

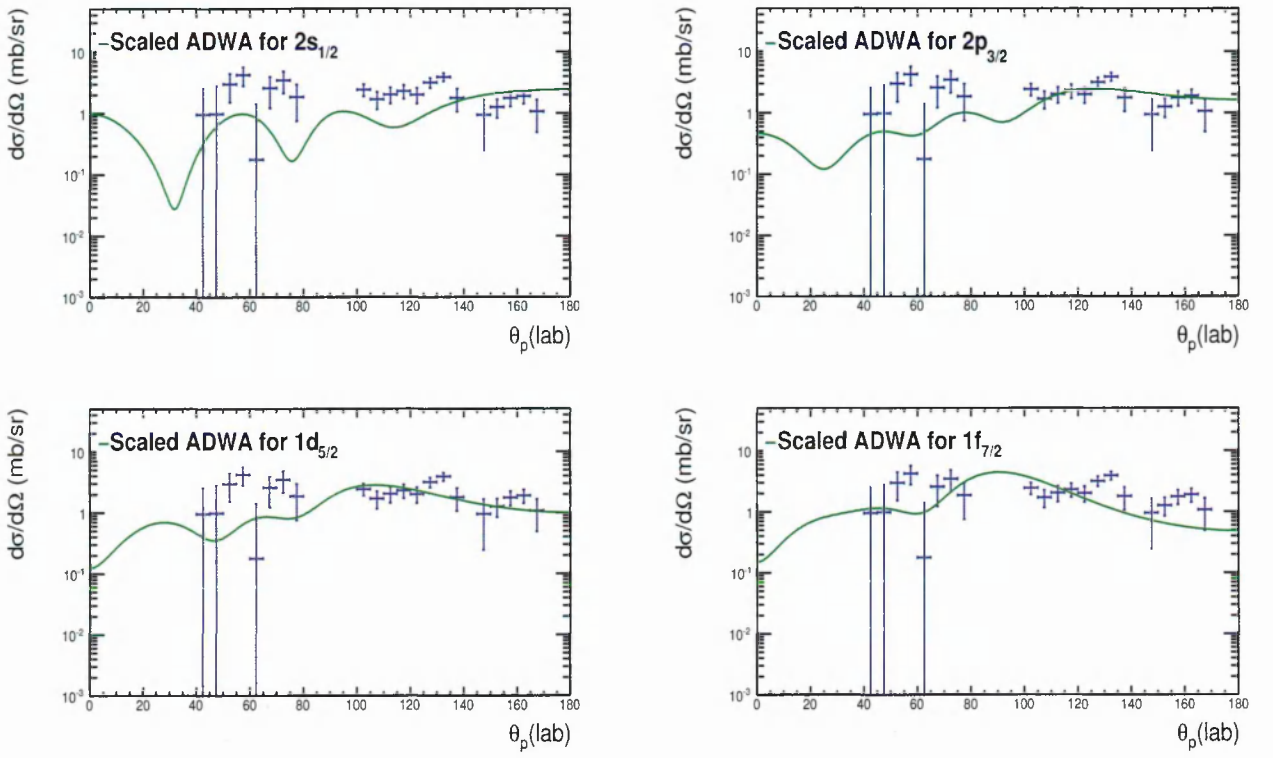

Figure 3.110: Differential cross sections of proton to determine the "l" transfer of the excited state at 4087 keV. In the text, the $2p_{3/2}$ transfer is selected as the best fit. The gates on γ-ray and its background energy for 90° clovers were $4172keV > E_\gamma > 4002keV$ and $4342keV > E_\gamma > 4172keV$, respectively. For 135° clovers, the gates on γ-ray and its background energy were $4154keV > E_\gamma > 4019keV$ and $4289keV > E_\gamma > 4154keV$, respectively. The gates on excitation energy and its background energy for 90° clovers were $5324keV > E_{ex} > 3317keV$ and $3117keV > E_{ex} > 911keV$, respectively. For 135° clovers, the gates on excitation energy and its background energy were $5030keV > E_{ex} > 3315keV$ and $4289keV > E_{ex} > 4154keV$, respectively.

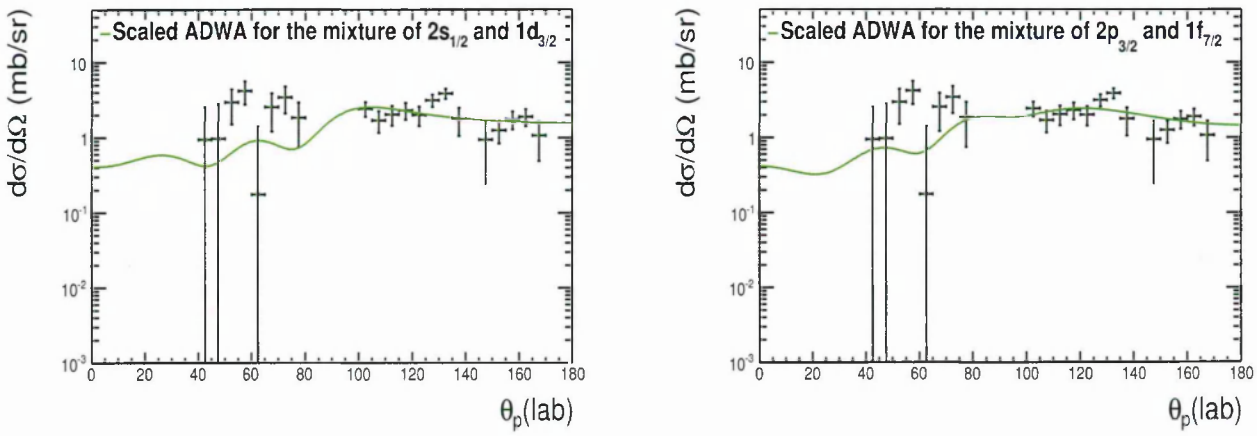

Figure 3.111: Differential cross sections of protons to determine the individual S.F. in mixed "l" transfer of the excited state at 4.087 MeV. In the text, the $2p_{3/2}$ transfer is selected as the best fit, so this figure shows possible f wave contribution (see table 4.1).

Another higher lying new state at 4.239 MeV for the ^{26}Na nucleus is analysed as shown in figure 3.112. Without having any feeding from the γ-rays of higher lying states, the same proton differential cross section extraction method as explained for similar states is also applied here. The similarity between d and f wave is quite strong for this particular state, so this really makes difficult to choose the appropriate "l" transfer for the neutron. It's obvious that further investigation is needed to assign a spin and parity for the state, but mostly the parity will be the dominant factor for assigning the spin whose range is defined by the selection of the wave type of transferred neutron orbital in this stage of the analysis. Namely, if one assigns an orbital quantum number of 2 for this state, then the final spin can be in the range between 1 and 4 instead of 1 and 6 in the case of f wave transfer. Therefore, the possibility of having spin 6 may also play role in the distinction. Even though a conclusive answer for this state will be given in following section 4.1, the transferred orbital angular momentum for the neutron will be assigned as $1d_{3/2}$ here.

Figure 3.113 shows slightly misleading indication since the mixing of "p-f" orbitals looks also encouraging. More convincing discussion to assign the final spin will be introduced in following section 4.1 depending on how possible spin assignments will fit into a level scheme 3.76 in a way this specific state decays with regard to its neighbours.

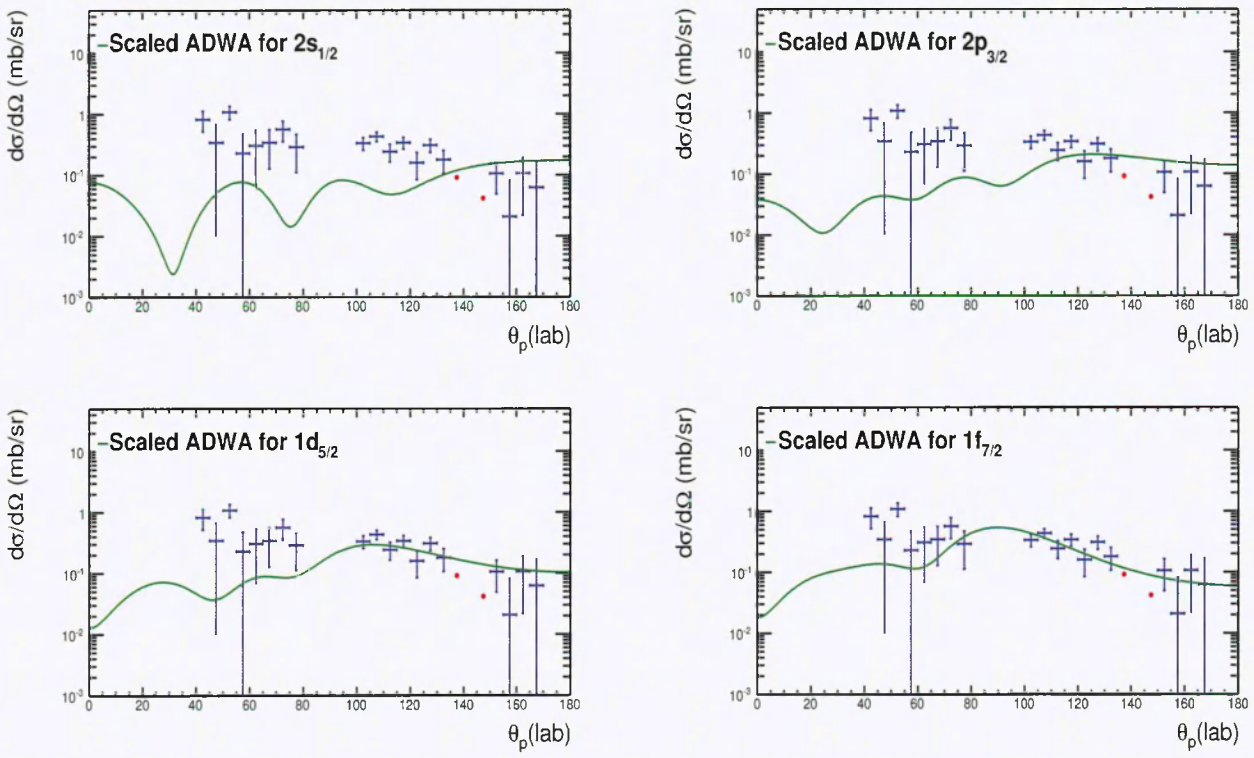

Figure 3.112: Differential cross sections of proton to determine the "l" transfer of the excited state at 4239 keV. In the text, the $1d_{3/2}$ transfer is selected as the best fit. The gates on γ-ray and its background energy for 90° clovers were $1128keV > E_\gamma > 1082keV$ and $1173keV > E_\gamma > 1128keV$, respectively. For 135° clovers, the gates on γ-ray and its background energy were $1122keV > E_\gamma > 1085keV$ and $1158keV > E_\gamma > 1122keV$, respectively. The gates on excitation energy and its background energy for 90° clovers were $5340keV > E_{ex} > 3245keV$ and $3245keV > E_{ex} > 1150keV$, respectively. For 135° clovers, the gates on excitation energy and its background energy were $6174keV > E_{ex} > 2974keV$ and $2974keV > E_{ex} > -226keV$, respectively.

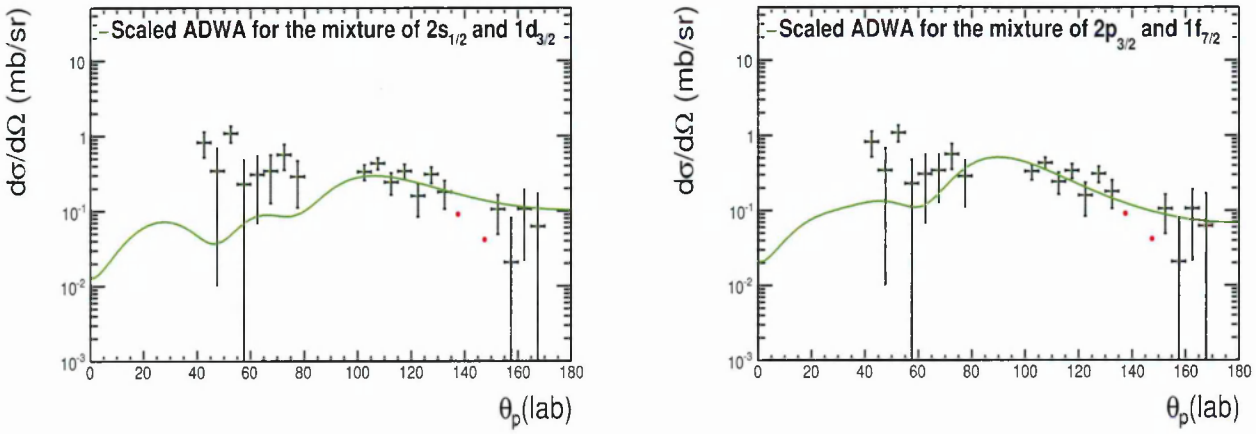

Figure 3.113: Differential cross sections of protons to determine the individual S.F. in mixed "l" transfer of the excited state at 4.239 MeV. In the text, the $1d_{3/2}$ transfer is selected as the best fit, so this figure shows possible s wave contribution (see table 4.1).

Previously identified 4.305 MeV state was not analysed before for its spectroscopic factor, so it is another new finding in the current work. For this state, the γ-ray feeding from 4.917 MeV state should be considered to extract the proton angular distributions as for the 3.135 MeV state. This is the first state the predictions started to give always the f wave transfer as the best estimate. It's hard to say any conclusive result for this state because there are two wave transfers, d and f, look very identical to each other. Therefore, the parity of this state may play a selective role again when all the γ-ray decay possibilities are considered to the lower lying states in the level scheme 3.76.

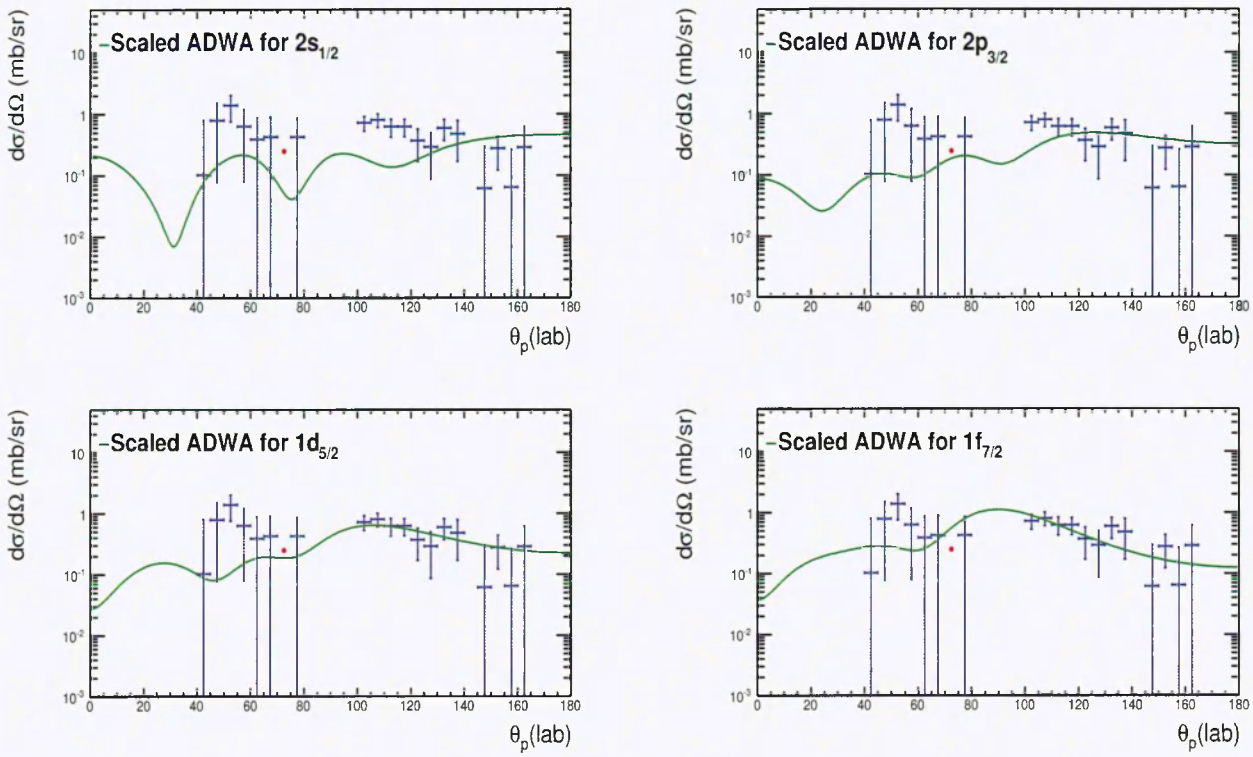

Figure 3.114: Differential cross sections of proton to determine the "l" transfer of the excited state at 4305 keV. In the text, the $1f_{7/2}$ transfer is selected as the best fit. The gates on γ-ray and its background energy for 90° clovers were $807keV > E_\gamma > 774keV$ and $774keV > E_\gamma > 741keV$, respectively. For 135° clovers, the gates on γ-ray and its background energy were $804keV > E_\gamma > 777keV$ and $777keV > E_\gamma > 751keV$, respectively. The gates on excitation energy and its background energy for 90° clovers were $5935keV > E_{ex} > 3097keV$ and $3097keV > E_{ex} > 258keV$, respectively. For 135° clovers, the gates on excitation energy and its background energy were $5164keV > E_{ex} > 3564keV$ and $3122keV > E_{ex} > 391keV$, respectively.

Figure 3.115 as all the following figures for states above 4.3 MeV will not help us to assign any indisputable transferred neutron orbital assignment. The reason might be due to low statistics for higher lying states which stay along the proton detection threshold energy level. To see this effect, kinematic plot in the figure 3.1 can be checked as an

example. Kinematic plot investigation has been done for different states as well to check consistency, and this will be mention briefly in result section with another example as well.

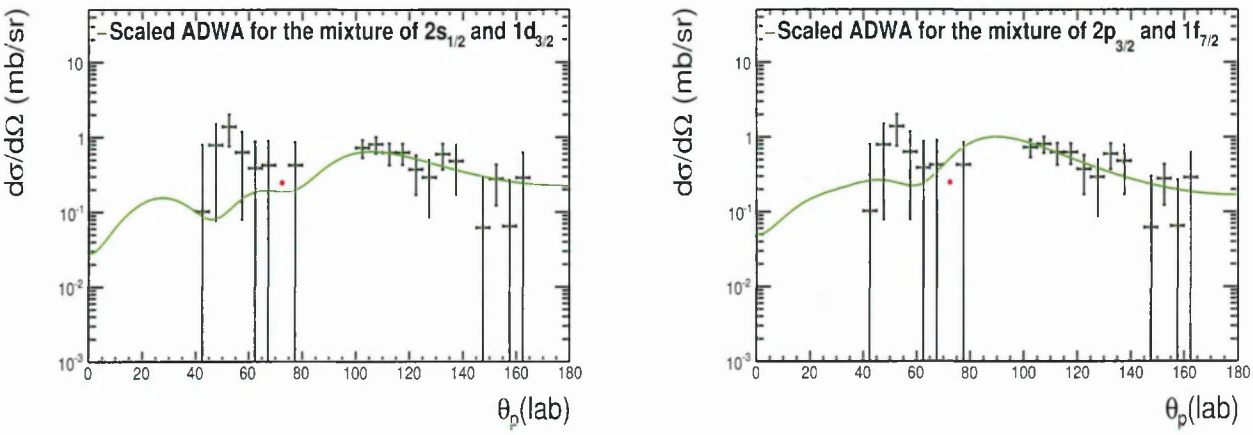

Figure 3.115: Differential cross sections of protons to determine the individual S.F. in mixed "l" transfer of the excited state at 4.305 MeV. In the text, the $1f_{7/2}$ transfer is selected as the best fit, so this figure shows possible p wave contribution (see table 4.1).

One of the new higher lying states at 4.597 MeV is shown for its proton differential cross section analysis in the figure 3.116. It's assigned to f wave transfer as the data match is better in backward angles, but overall shape of the cross section is also retained well. With the f transfer of neutron, the possible final spins assignments vary from 1 to 6. For all the states above 4.3 MeV, the orbital momentum transfer is decided as 3 due to the f wave selection of the shell where the neutron is transferred. In addition, one may notice the negative data points are observable in the following figures for the states 4.932 MeV, 5.009 MeV, 5.155 MeV, 5.276 MeV, and the last populated state 5.384 MeV since the upper limit of the error bar for these data points are selected and marked in red. However, the states at 4.8 MeV and 4.917 MeV do not have any negative data points at all. This is also due to the subtraction done for these higher lying states with low statistics. Following

figures show fitting results of the other states analysed in this work as tables 3.8 and 4.1 can be referred for their spectroscopic factors for a given spin and coupling.

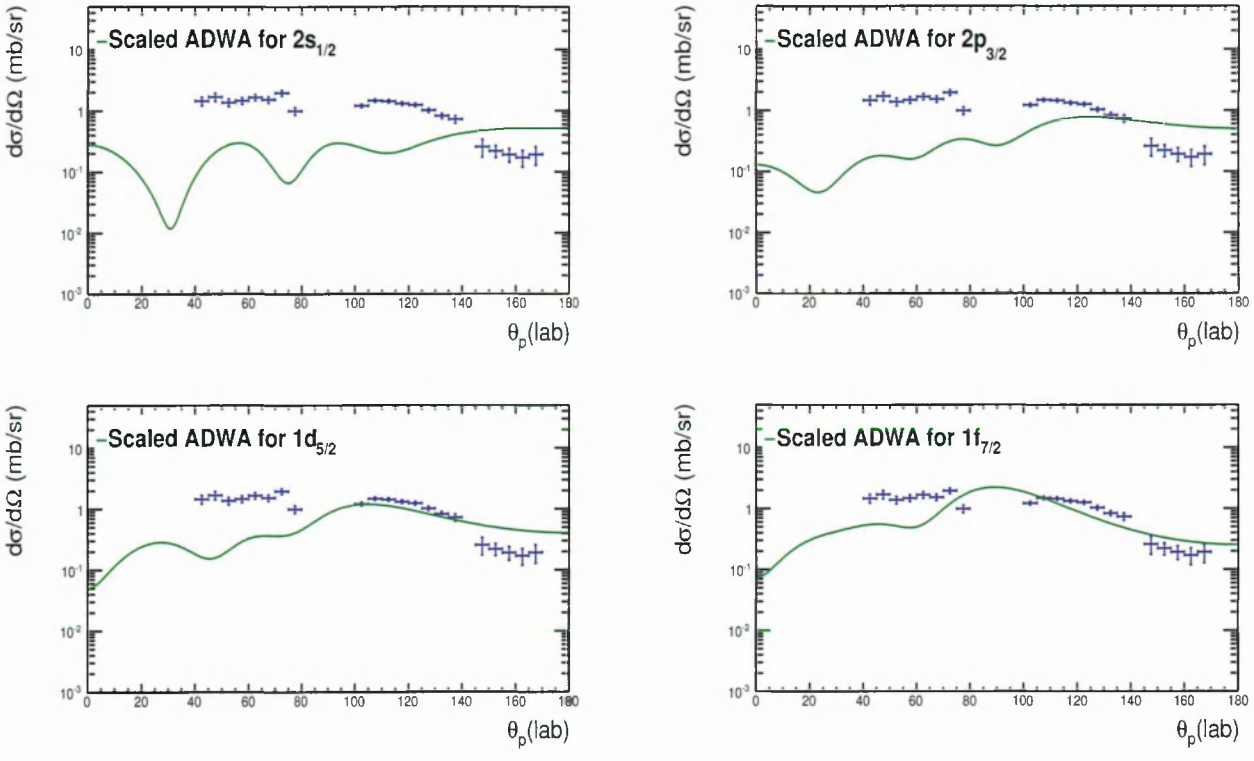

Figure 3.116: Differential cross sections of proton to determine the "l" transfer of the excited state at 4597 keV. In the text, the $1f_{7/2}$ transfer is selected as the best fit. The gates on γ-ray and its background energy for 90° clovers were $4284keV > E_\gamma > 4164keV$ and $4019keV > E_\gamma > 3845keV$, respectively. For 135° clovers, the gates on γ-ray and its background energy were $4250keV > E_\gamma > 4151keV$ and $4030keV > E_\gamma > 3891keV$, respectively. The gate on excitation energy for 90° clovers was $5840keV > E_{ex} > 4294keV$. For 135° clovers, the gate on excitation energy was $5530keV > E_{ex} > 4470keV$.

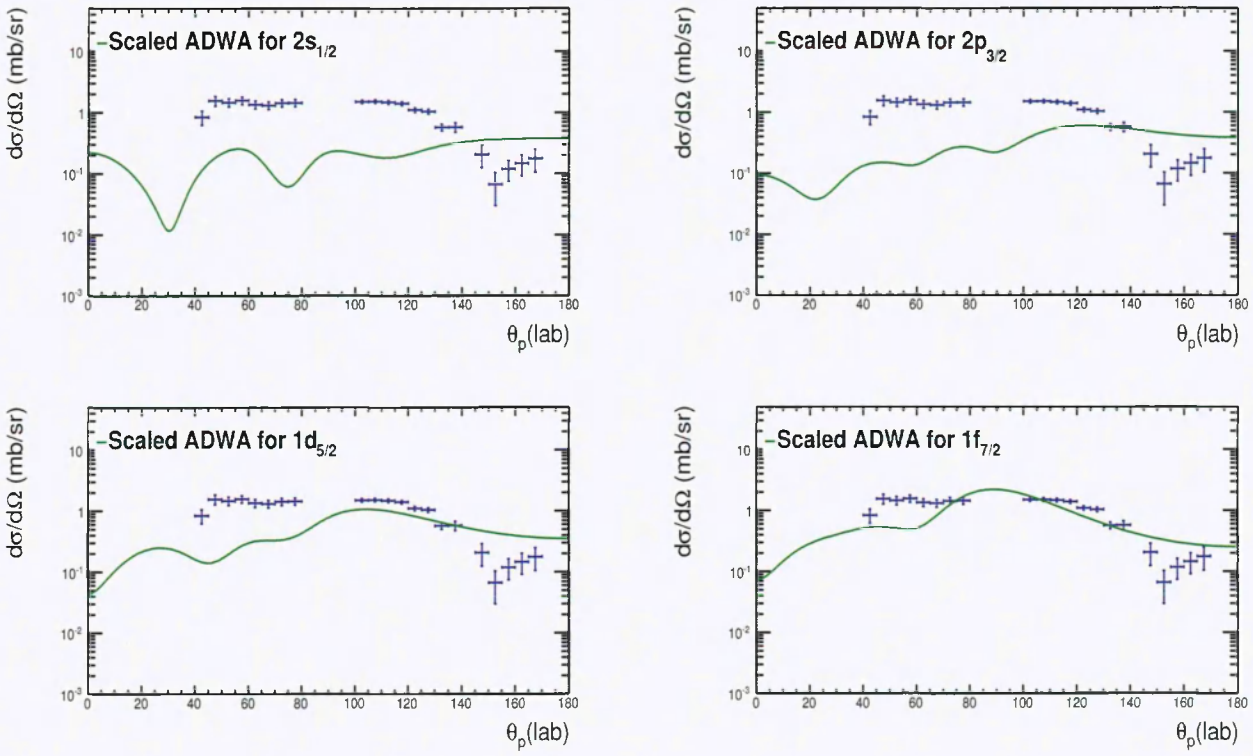

Figure 3.117: Differential cross sections of proton to determine the "l" transfer of the excited state at 4800 keV. In the text, the $1f_{7/2}$ transfer is selected as the best fit. The gates on γ-ray and its background energy for 90° clovers were $4855keV > E_\gamma > 4765keV$ and $4570keV > E_\gamma > 4402keV$, respectively. For 135° clovers, the gates on γ-ray and its background energy were $4855keV > E_\gamma > 4765keV$ and $4570keV > E_\gamma > 4402keV$, respectively. The gates on excitation energy and its background energy for 90° clovers were $5824keV > E_{ex} > 4424keV$ and $4224keV > E_{ex} > 2625keV$, respectively. For 135° clovers, the gates on excitation energy and its background energy were $5969keV > E_{ex} > 3975keV$ and $3975keV > E_{ex} > 1981keV$, respectively.

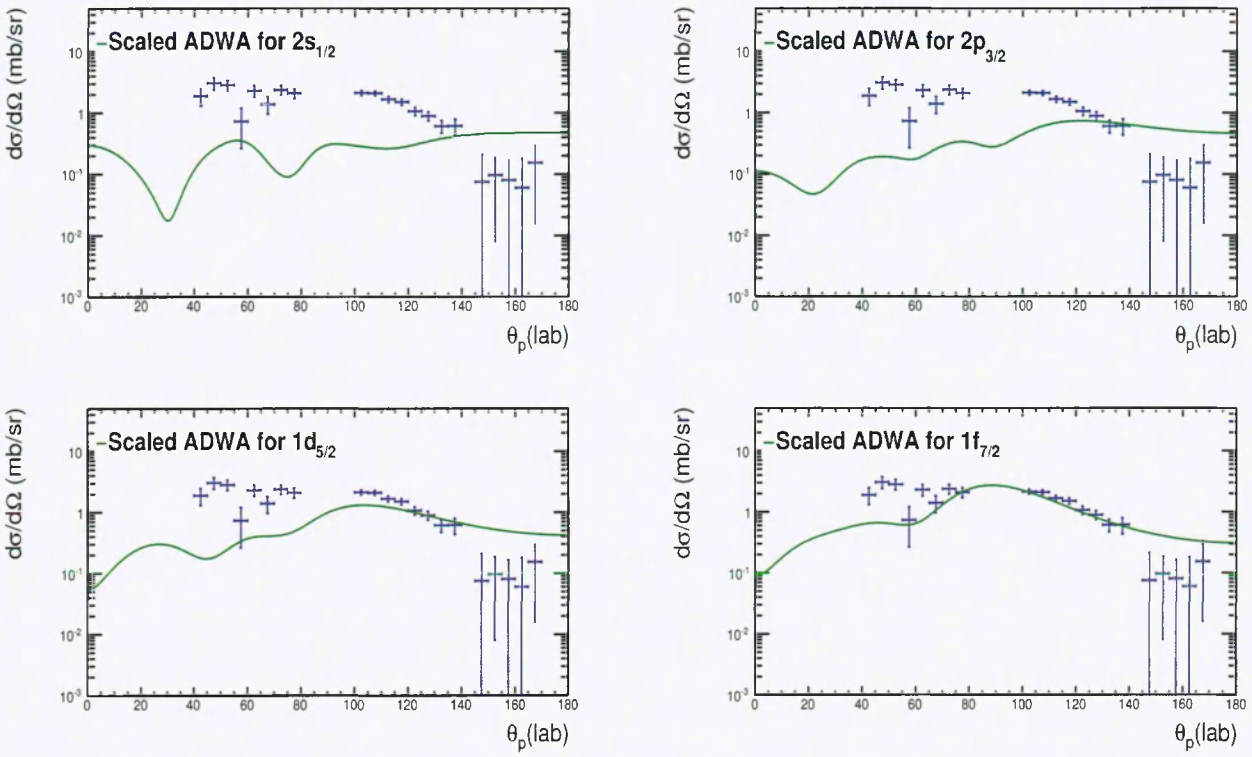

Figure 3.118: Differential cross sections of proton to determine the "l" transfer of the excited state at 4917 keV. In the text, the $1f_{7/2}$ transfer is selected as the best fit. The gates on γ-ray and its background energy for 90° clovers were $1431keV > E_\gamma > 1374keV$ and $1374keV > E_\gamma > 1316keV$, respectively. For 135° clovers, the gates on γ-ray and its background energy were $1424keV > E_\gamma > 1378keV$ and $1378keV > E_\gamma > 1333keV$, respectively. The gates on excitation energy and its background energy for 90° clovers were $5732keV > E_{ex} > 4068keV$ and $4068keV > E_{ex} > 2404keV$, respectively. For 135° clovers, the gates on excitation energy and its background energy were $5805keV > E_{ex} > 4018keV$ and $4018keV > E_{ex} > 2231keV$, respectively.

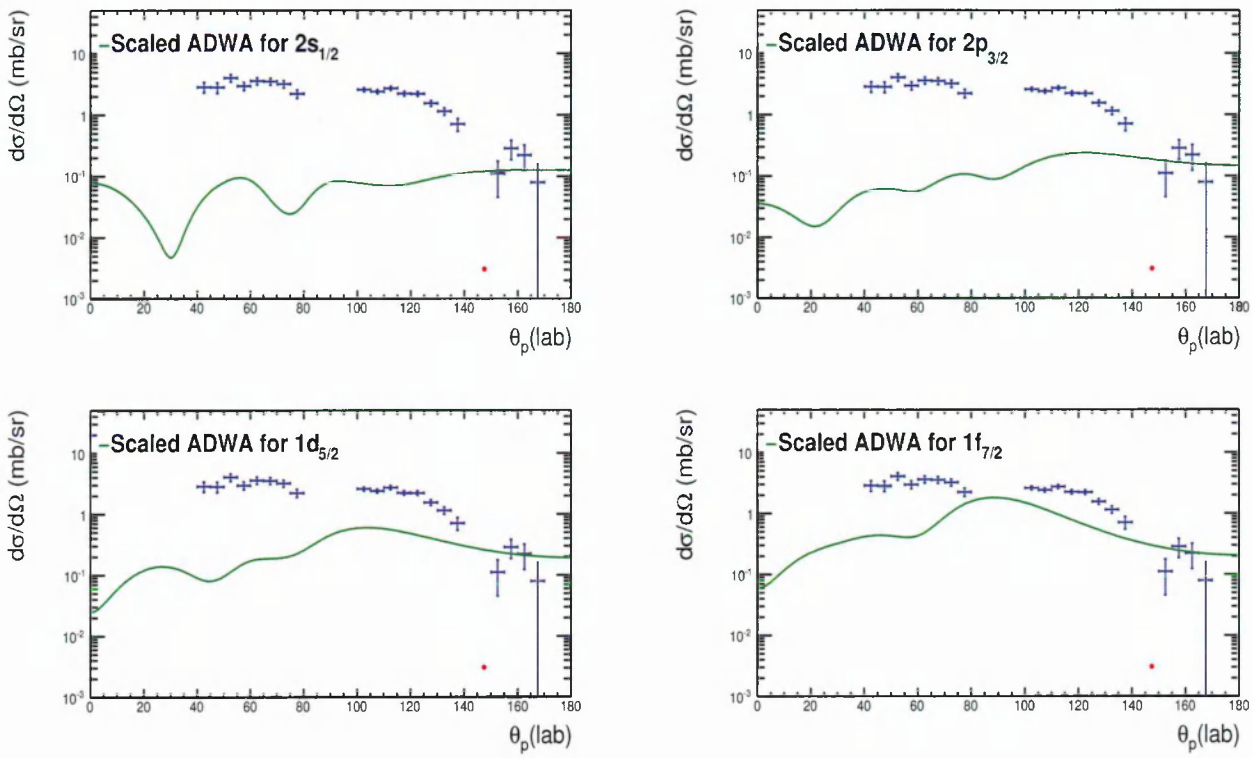

Figure 3.119: Differential cross sections of proton to determine the "l" transfer of the excited state at 4932 keV. In the text, the $1f_{7/2}$ transfer is selected as the best fit. The gates on γ-ray and its background energy for 90° clovers were $5038keV > E_\gamma > 4885keV$ and $4601keV > E_\gamma > 4396keV$, respectively. For 135° clovers, the gates on γ-ray and its background energy were $5010keV > E_\gamma > 4875keV$ and $4631keV > E_\gamma > 4468keV$, respectively. The gates on excitation energy and its background energy for 90° clovers were $6026keV > E_{ex} > 4484keV$ and $4484keV > E_{ex} > 2943keV$, respectively. For 135° clovers, the gates on excitation energy and its background energy were $6100keV > E_{ex} > 4311keV$ and $4311keV > E_{ex} > 2523keV$, respectively.

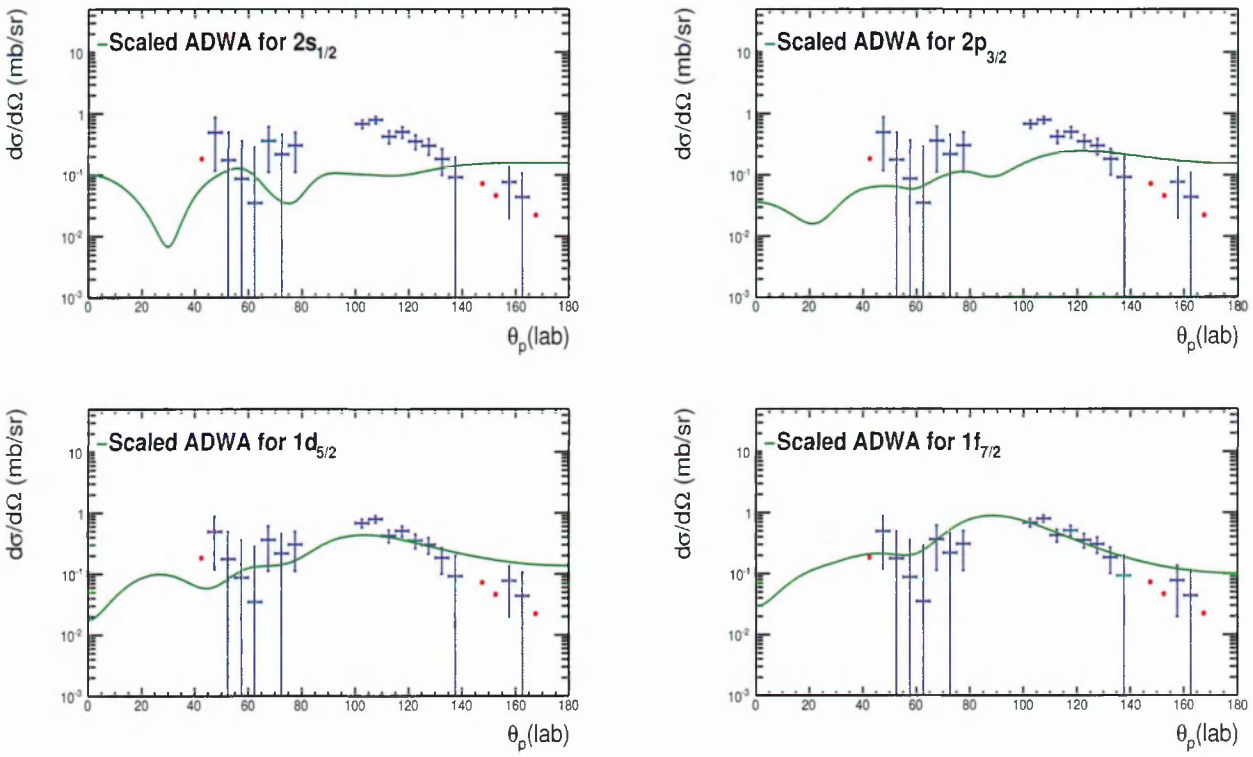

Figure 3.120: Differential cross sections of proton to determine the "l" transfer of the excited state at 5009 keV. In the text, the $1f_{7/2}$ transfer is selected as the best fit. The gates on γ-ray and its background energy for 90° clovers were $3269keV > E_\gamma > 3188keV$ and $3401keV > E_\gamma > 3269keV$, respectively. For 135° clovers, the gates on γ-ray and its background energy were $3255keV > E_\gamma > 3185keV$ and $3360keV > E_\gamma > 3255keV$, respectively. The gates on excitation energy and its background energy for 90° clovers were $5801keV > E_{ex} > 4201keV$ and $2607keV > E_{ex} > 1007keV$, respectively. For 135° clovers, the gates on excitation energy and its background energy were $5792keV > E_{ex} > 4192keV$ and $2171keV > E_{ex} > 1111keV$, respectively.

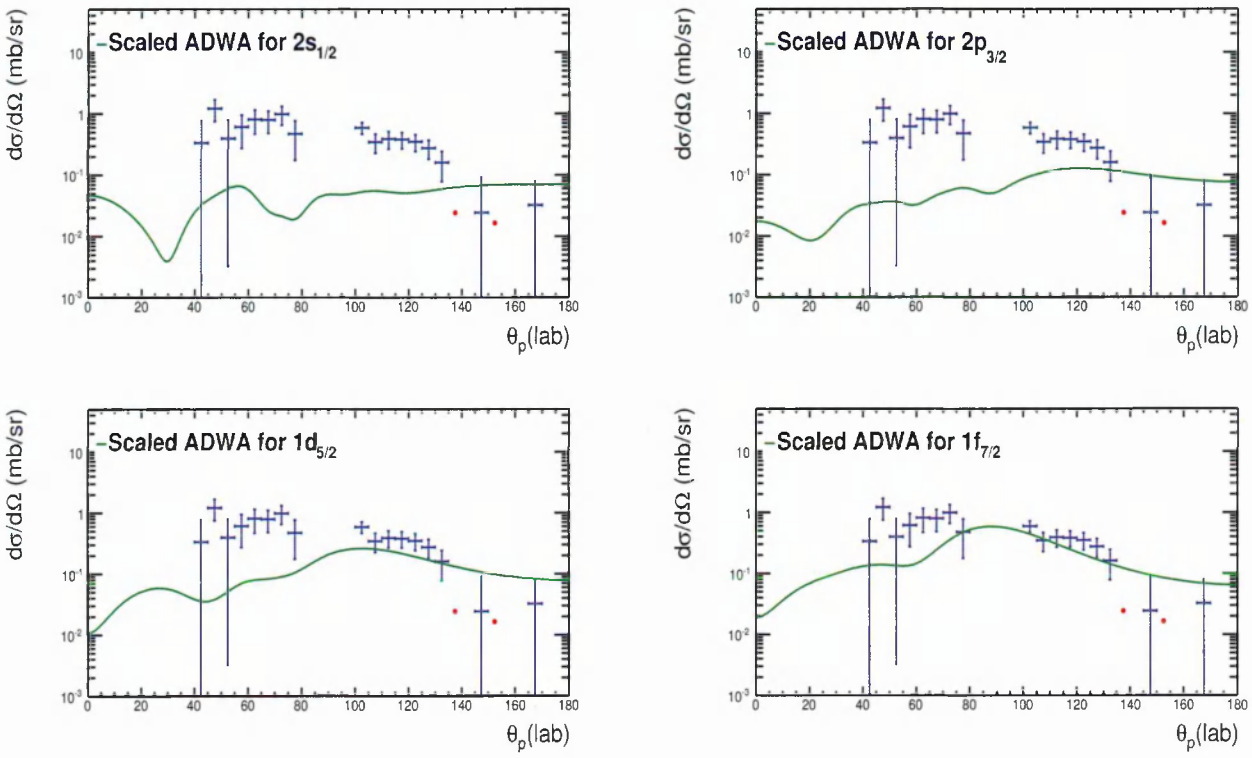

Figure 3.121: Differential cross sections of proton to determine the "l" transfer of the excited state at 5155 keV. In the text, the $1f_{7/2}$ transfer is selected as the best fit. The gates on γ-ray and its background energy for 90° clovers were $5260keV > E_\gamma > 5049keV$ and $5080keV > E_\gamma > 4994keV$, respectively. For 135° clovers, the gates on γ-ray and its background energy were $5263keV > E_\gamma > 5072keV$ and $5080keV > E_\gamma > 4994keV$, respectively. The gates on excitation energy and its background energy for 90° clovers were $6772keV > E_{ex} > 3987keV$ and $3987keV > E_{ex} > 1202keV$, respectively. For 135° clovers, the gates on excitation energy and its background energy were $6479keV > E_{ex} > 4287keV$ and $4287keV > E_{ex} > 2095keV$, respectively.

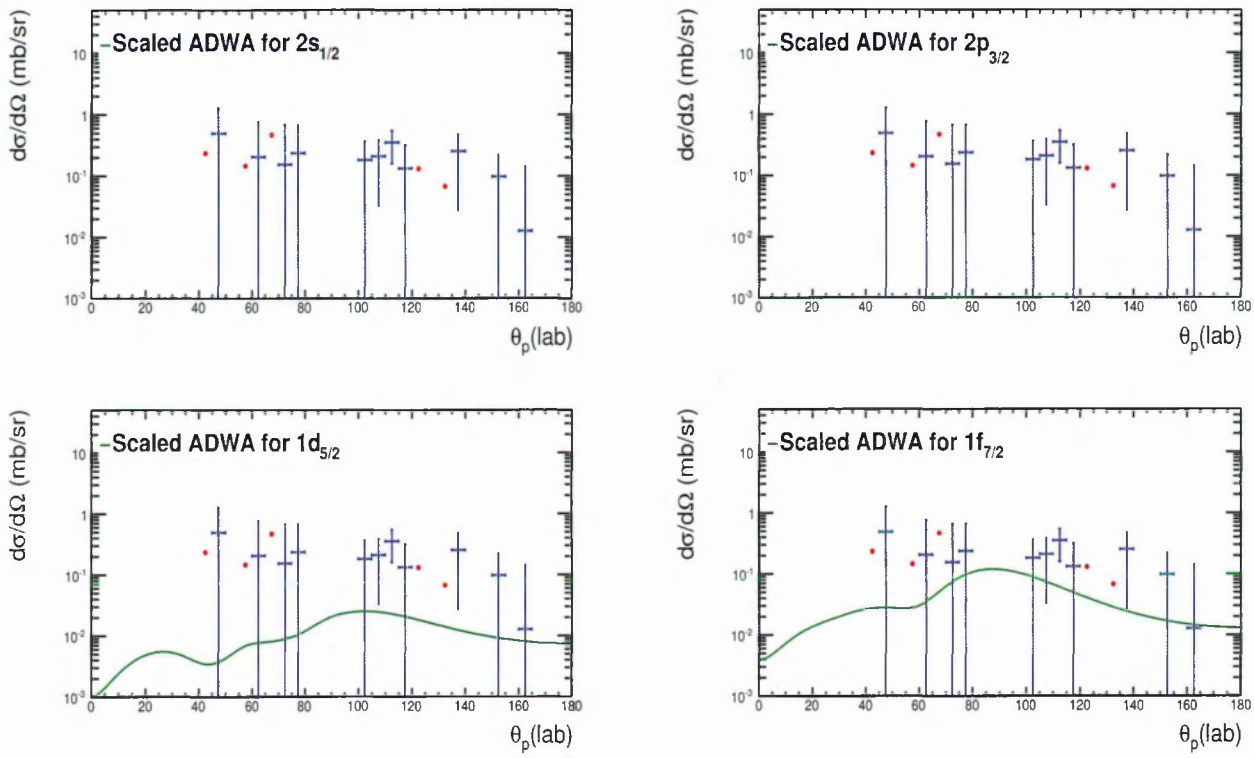

Figure 3.122: Differential cross sections of proton to determine the "l" transfer of the excited state at 5276 keV. In the text, the $1f_{7/2}$ transfer is selected as the best fit. The gates on γ-ray and its background energy for 90° clovers were $3463keV > E_\gamma > 3399keV$ and $3399keV > E_\gamma > 3256keV$, respectively. For 135° clovers, the gates on γ-ray and its background energy were $3469keV > E_\gamma > 3413keV$ and $3413keV > E_\gamma > 3299keV$, respectively. The gates on excitation energy and its background energy for 90° clovers were $6146keV > E_{ex} > 4408keV$ and $4408keV > E_{ex} > 2670keV$, respectively. For 135° clovers, the gates on excitation energy and its background energy were $6778keV > E_{ex} > 3578keV$ and $3578keV > E_{ex} > 377keV$, respectively.

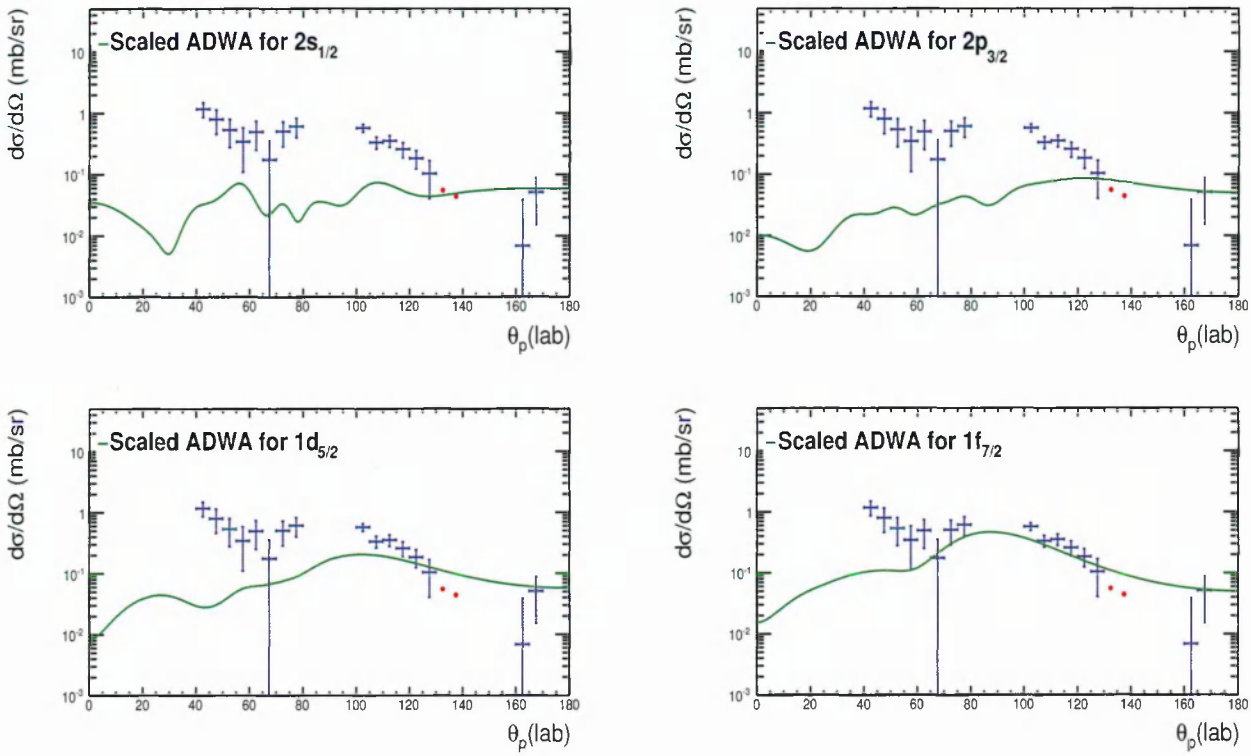

Figure 3.123: Differential cross sections of proton to determine the "l" transfer of the excited state at 5384 keV. In the text, the $1f_{7/2}$ transfer is selected as the best fit. The gates on γ-ray and its background energy for 90° clovers were $5494keV > E_\gamma > 5269keV$ and $5330keV > E_\gamma > 5242keV$, respectively. For 135° clovers, the gates on γ-ray and its background energy were $5474keV > E_\gamma > 5295keV$ and $5330keV > E_\gamma > 5242keV$, respectively. The gates on excitation energy and its background energy for 90° clovers were $6181keV > E_{ex} > 4606keV$ and $4606keV > E_{ex} > 3032keV$, respectively. For 135° clovers, the gates on excitation energy and its background energy were $6205keV > E_{ex} > 4471keV$ and $4571keV > E_{ex} > 2738keV$, respectively.

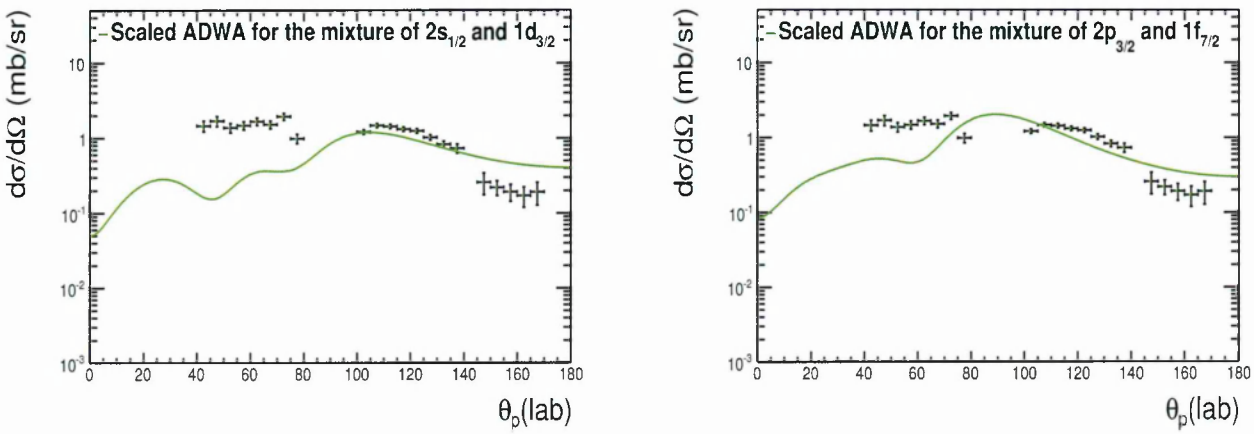

Figure 3.124: Differential cross sections of protons to determine the individual S.F. in mixed "l" transfer of the excited state at 4.597 MeV. In the text, the $1f_{7/2}$ transfer is selected as the best fit, so this figure shows possible p wave contribution (see table 4.1).

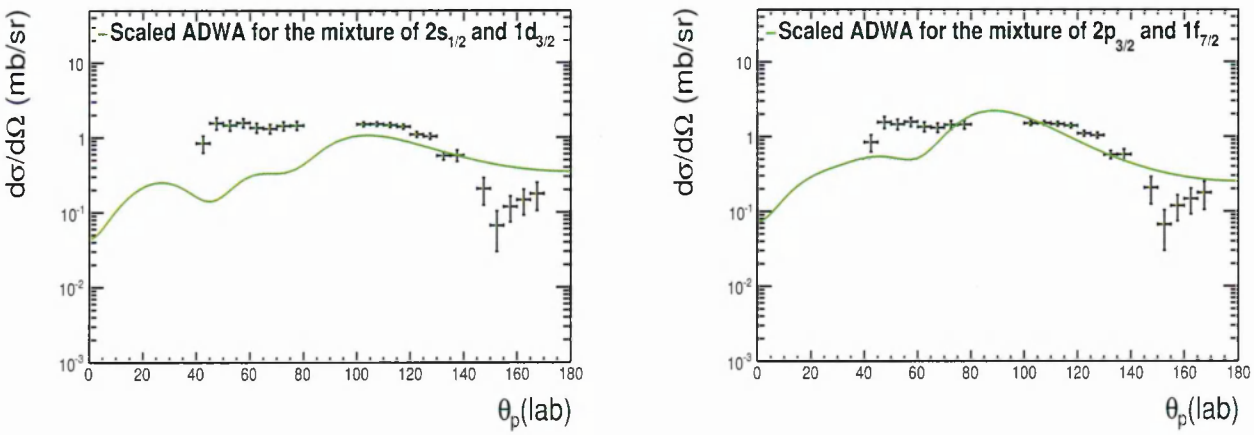

Figure 3.125: Differential cross sections of protons to determine the individual S.F. in mixed "l" transfer of the excited state at 4.800 MeV. In the text, the $1f_{7/2}$ transfer is selected as the best fit, so this figure shows possible p wave contribution (see table 4.1).

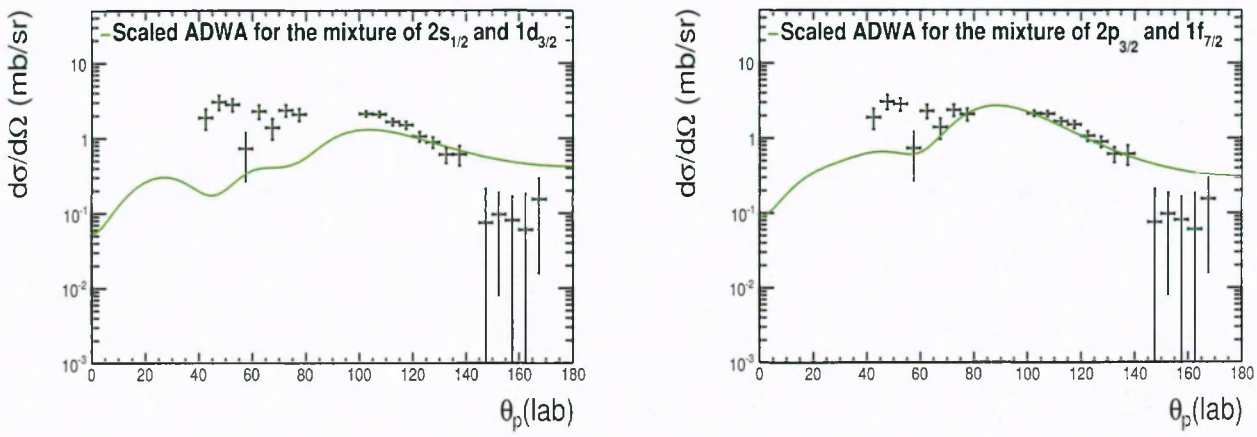

Figure 3.126: Differential cross sections of protons to determine the individual S.F. in mixed "l" transfer of the excited state at 4917 MeV. In the text, the $1f_{7/2}$ transfer is selected as the best fit, so this figure shows possible p wave contribution (see table 4.1).

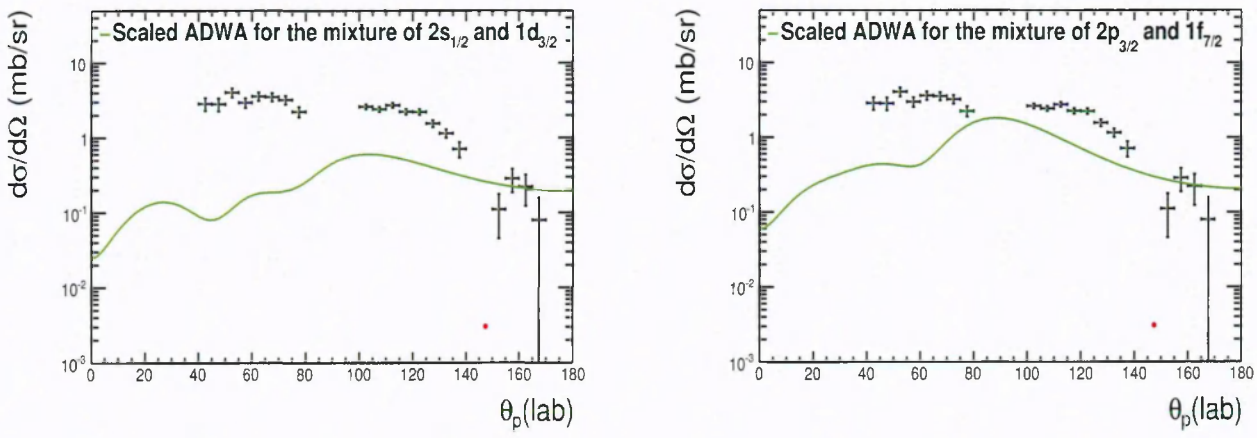

Figure 3.127: Differential cross sections of protons to determine the individual S.F. in mixed "l" transfer of the excited state at 4.932 MeV. In the text, the $1f_{7/2}$ transfer is selected as the best fit, so this figure shows possible p wave contribution (see table 4.1).

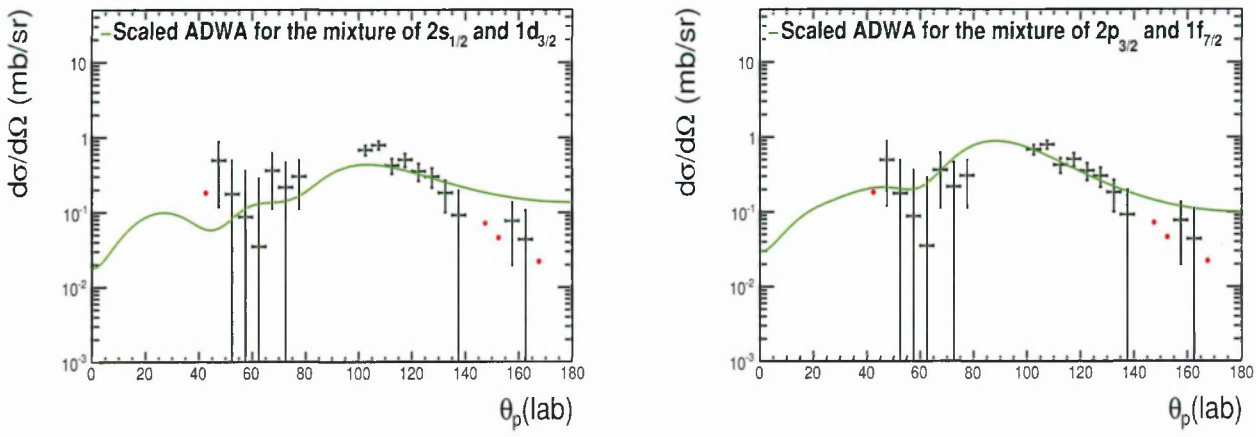

Figure 3.128: Differential cross sections of protons to determine the individual S.F. in mixed "l" transfer of the excited state at 5.009 MeV. In the text, the $1f_{7/2}$ transfer is selected as the best fit, so this figure shows possible p wave contribution (see table 4.1).

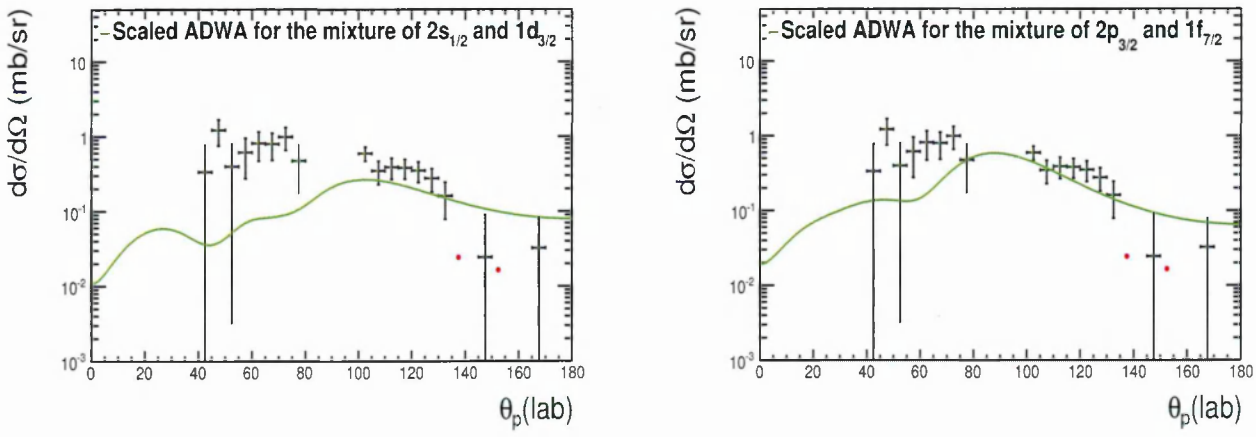

Figure 3.129: Differential cross sections of protons to determine the individual S.F. in mixed "l" transfer of the excited state at 5.155 MeV. In the text, the $1f_{7/2}$ transfer is selected as the best fit, so this figure shows possible p wave contribution (see table 4.1).

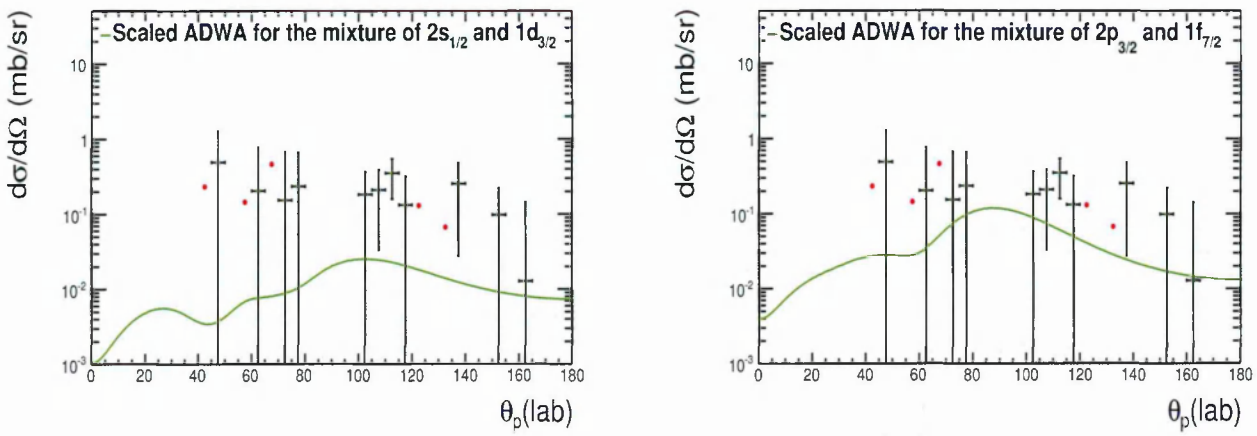

Figure 3.130: Differential cross sections of protons to determine the individual S.F. in mixed "l" transfer of the excited state at 5.276 MeV. In the text, the $1f_{7/2}$ transfer is selected as the best fit, so this figure shows possible p wave contribution (see table 4.1).

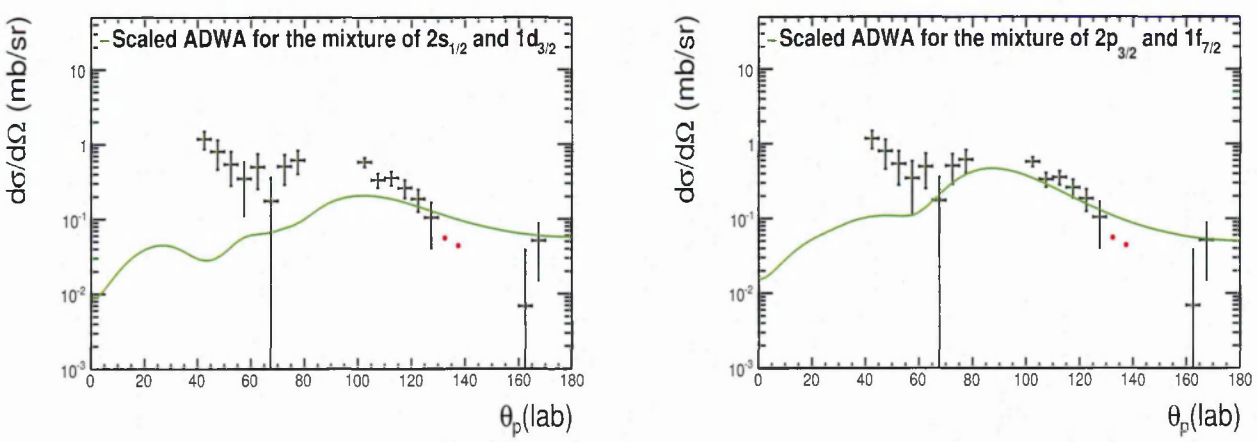

Figure 3.131: Differential cross sections of protons to determine the individual S.F. in mixed "l" transfer of the excited state at 5.384 MeV. In the text, the $1f_{7/2}$ transfer is selected as the best fit, so this figure shows possible p wave contribution (see table 4.1).

For the full detail of the analysis results for the section 3.7, the results are presented in the table 3.8. Only the spectroscopic factors extracted from the data in the previous

work [1] are shown in the last column. It's noticed in the personal discussions through the analysis that the wrong theoretical line was used for the scaling of the 3.511 MeV state in the work [1] as it's obvious in the figure 4.5. The spectroscopic factor found for the same spin, 4^-, shows half amount of the previous result in the same figure where the comparison is done schematically. It's been confirmed that they give indeed the similar results after the discussion. Another important point is the spectroscopic factor extracted for the 3.135 MeV state before in the work [1] is now also updated, as all the others, with the extra differential cross section subtraction made due to the new higher lying state at 4.239 MeV via the γ-ray 1104 keV.

In conclusion, not only the previous results are updated and revised, but also all the new states are analysed to get a unique interpretation which then enable us to investigates the structure of the ^{26}Na nucleus with the help of new level scheme 3.76, branching ratios, and spectroscopic factors extracted from the data.

Table 3.9 summarizes all the state energies that have been analysed in this section to get the proton angular distributions, a specific γ-ray that was used to depopulate for each state, and their corresponding background energy limits. In addition to this information, the γ-ray peak correction factors (PCF) and their background correction factors (BCF) in the table 3.4 with their explanation in the section 3.4.1 were used together to get proton angular distributions as the first example differential cross section of proton distributions in the figure 3.90 showed. The correction factors for the excitation energies and their backgrounds are used as 1 since the excitation energy spectra have no peak or background correction factor as in the γ-ray spectra.

Current Work						Previous Work [1]		
E_{ex}	SF(l=0)	SF(l=1)	SF(l=2)	SF(l=3)	Coupling	Coupling[1]	J^{π}[1]	S.F.[1]
232	0.110 ± 0.004 ± 0.003	0.064 ± 0.003 ± 0.002	0.324 ± 0.013 ± 0.008	0.556 ± 0.024 ± 0.014	$2s_{1/2}$	$s_{1/2}$	2^+	0.1333
405	0.296 ± 0.005 ± 0.008	0.132 ± 0.003 ± 0.003	0.556 ± 0.013 ± 0.015	0.936 ± 0.024 ± 0.024	$2s_{1/2}$	$s_{1/2}$	2^+	0.3125
1507*	0.021 ± 0.002 ± 0.001	0.041 ± 0.003 ± 0.001	0.235 ± 0.014 ± 0.006	0.476 ± 0.029 ± 0.012	$1d_{3/2}$			
1805	0.071 ± 0.006 ± 0.002	0.125 ± 0.007 ± 0.003	0.620 ± 0.029 ± 0.016	1.187 ± 0.062 ± 0.031	$1d_{3/2}$	$d_{3/2}$	3^+	0.216
2116	0.053 ± 0.004 ± 0.001	0.077 ± 0.004 ± 0.002	0.309 ± 0.014 ± 0.008	0.779 ± 0.038 ± 0.020	$1d_{5/2}$	$d_{3/2}$	4^+	0.216
2195*	0.102 ± 0.007 ± 0.003	0.138 ± 0.007 ± 0.004	0.570 ± 0.026 ± 0.015	1.111 ± 0.058 ± 0.029	$1d_{3/2}$			
2225	0.060 ± 0.004 ± 0.002	0.146 ± 0.005 ± 0.004	0.816 ± 0.023 ± 0.021	1.763 ± 0.052 ± 0.046	$1d_{3/2}$	$d_{3/2}$	4^+	0.432
2843*	0.114 ± 0.012 ± 0.003	0.186 ± 0.013 ± 0.005	0.765 ± 0.047 ± 0.020	1.654 ± 0.109 ± 0.043	$2p_{3/2}$		2^-	
3135	0.114 ± 0.012 ± 0.003	0.149 ± 0.011 ± 0.004	0.471 ± 0.037 ± 0.012	0.913 ± 0.085 ± 0.024	$2p_{3/2}$	$p_{3/2}$	3^-	0.0983
3511	0.403 ± 0.012 ± 0.011	0.445 ± 0.010 ± 0.012	1.233 ± 0.029 ± 0.032	2.369 ± 0.066 ± 0.062	$2p_{3/2}$	$p_{3/2}$	4^-	0.54
4087*	0.418 ± 0.039 ± 0.011	0.419 ± 0.032 ± 0.011	1.198 ± 0.093 ± 0.031	2.648 ± 0.232 ± 0.069	$2p_{3/2}$			
4239*	0.034 ± 0.006 ± 0.001	0.037 ± 0.004 ± 0.001	0.121 ± 0.012 ± 0.003	0.311 ± 0.031 ± 0.008	$1d_{3/2}$			
4305*	0.095 ± 0.019 ± 0.003	0.087 ± 0.013 ± 0.002	0.258 ± 0.033 ± 0.007	0.636 ± 0.080 ± 0.017	$1f_{7/2}$		(5^-)	
4597*	0.142 ± 0.006 ± 0.004	0.147 ± 0.005 ± 0.004	0.454 ± 0.012 ± 0.012	1.180 ± 0.031 ± 0.031	$1f_{7/2}$			
4800*	0.129 ± 0.007 ± 0.003	0.122 ± 0.005 ± 0.003	0.389 ± 0.012 ± 0.010	1.117 ± 0.033 ± 0.029	$1f_{7/2}$			
4917*	0.192 ± 0.017 ± 0.005	0.157 ± 0.010 ± 0.004	0.469 ± 0.023 ± 0.012	1.338 ± 0.060 ± 0.035	$1f_{7/2}$		(6^-)	
4932*	0.051 ± 0.008 ± 0.001	0.050 ± 0.005 ± 0.001	0.214 ± 0.014 ± 0.006	0.886 ± 0.044 ± 0.023	$1f_{7/2}$			
5009*	0.073 ± 0.011 ± 0.002	0.054 ± 0.006 ± 0.001	0.152 ± 0.013 ± 0.004	0.426 ± 0.034 ± 0.011	$1f_{7/2}$		$(3^-, 4^-)$	
5155*	0.041 ± 0.014 ± 0.001	0.030 ± 0.007 ± 0.001	0.090 ± 0.014 ± 0.002	0.270 ± 0.037 ± 0.007	$1f_{7/2}$			
5276*	0.000 ± 0.019 ± 0.000	0.000 ± 0.012 ± 0.000	0.009 ± 0.024 ± 0.000	0.054 ± 0.0591± 0.001	$1f_{7/2}$			
5384*	0.054 ± 0.013 ± 0.001	0.023 ± 0.005 ± 0.001	0.068 ± 0.009 ± 0.002	0.206 ± 0.023 ± 0.005	$1f_{7/2}$			

Table 3.8: All these spectroscopic factors for different "l" transfer are tabulated by the assumption of final state spin to be 2. This assumption has been made by the fact that proton and neutron coupling will always give spin 2 in the possible spin range that ^{26}Na state can have. Then, the necessary conversion of a spectroscopic factor for a concluded correct spin in the following section 4.1 will be based on the formula 3.16. This was purely for the convenience of the calculations. In addition to all these updated values of previous work by Wilson [1], values corresponding to states marked with an asterisk (*) are presented in the current work for the first time.

E_{ex} (keV)	E_γ $(keV)(gate)$	Clover Angle (degree)	E_γ *limits* (keV)	E_γ B_{limits} (keV)	E_{ex} *limits* (keV)	E_{ex} B_{limits} (keV)
232	232	90	$238 > E_\gamma > 225$	$225 > E_\gamma > 212$	$845 > E_{ex} > -266$	$-266 > E_{ex} > -1378$
		135	$238 > E_\gamma > 226$	$226 > E_\gamma > 214$	$824 > E_{ex} > -246$	$-246 > E_{ex} > -1316$
405	405	90	$415 > E_\gamma > 396$	$395 > E_\gamma > 376$	$938 > E_{ex} > -85$	$-85 > E_{ex} > -1107$
		135	$413 > E_\gamma > 397$	$396 > E_\gamma > 380$	$910 > E_{ex} > -46$	$-46 > E_{ex} > -1002$
1507	1275	90	$1302 > E_\gamma > 1250$	$1250 > E_\gamma > 1198$	$2123 > E_{ex} > 1033$	$1033 > E_{ex} > -58$
		135	$1296 > E_\gamma > 1255$	$1255 > E_\gamma > 1213$	$2254 > E_{ex} > 986$	$986 > E_{ex} > -282$
1805	1805	90	$1844 > E_\gamma > 1769$	$1919 > E_\gamma > 1844$	$2843 > E_{ex} > 1260$	$1260 > E_{ex} > 74$
		135	$1834 > E_\gamma > 1775$	$1893 > E_\gamma > 1834$	$2517 > E_{ex} > 1270$	$1270 > E_{ex} > 23$
2116	2116	90	$2160 > E_\gamma > 2074$	$2084 > E_\gamma > 2034$	$2690 > E_{ex} > 1721$	$1721 > E_{ex} > 751$
		135	$2150 > E_\gamma > 2081$	$2084 > E_\gamma > 2034$	$2726 > E_{ex} > 1635$	$1635 > E_{ex} > 545$
2195	2195	90	$2192 > E_\gamma > 2149$	$2362 > E_\gamma > 2272$	$2837 > E_{ex} > 1653$	$1653 > E_{ex} > 469$
		135	$2198 > E_\gamma > 2159$	$2331 > E_\gamma > 2260$	$2775 > E_{ex} > 1780$	$1780 > E_{ex} > 785$
2225	2225	90	$2272 > E_\gamma > 2217$	$2363 > E_\gamma > 2272$	$2843 > E_{ex} > 1712$	$1712 > E_{ex} > 582$
		135	$2261 > E_\gamma > 2215$	$2333 > E_\gamma > 2261$	$2839 > E_{ex} > 1720$	$1720 > E_{ex} > 560$
2843	2616	90	$2675 > E_\gamma > 2567$	$2560 > E_\gamma > 2445$	$3852 > E_{ex} > 2252$	$2242 > E_{ex} > 642$
		135	$2654 > E_\gamma > 2569$	$2560 > E_\gamma > 2445$	$3817 > E_{ex} > 2217$	$2209 > E_{ex} > 609$
3135	3135	90	$3200 > E_\gamma > 3073$	$3327 > E_\gamma > 3200$	$3805 > E_{ex} > 2522$	$2522 > E_{ex} > 1240$
		135	$3186 > E_\gamma > 3083$	$3288 > E_\gamma > 3186$	$3887 > E_{ex} > 2459$	$2459 > E_{ex} > 1032$
3511	3511	90	$3584 > E_\gamma > 3441$	$3441 > E_\gamma > 3297$	$4307 > E_{ex} > 2853$	$2853 > E_{ex} > 1400$
		135	$3567 > E_\gamma > 3453$	$3453 > E_\gamma > 3338$	$4307 > E_{ex} > 2863$	$2863 > E_{ex} > 1419$
4087	4087	90	$4172 > E_\gamma > 4002$	$4342 > E_\gamma > 4172$	$5324 > E_{ex} > 3317$	$3317 > E_{ex} > 911$
		135	$4154 > E_\gamma > 4019$	$4289 > E_\gamma > 4154$	$5030 > E_{ex} > 3315$	$4239 > E_{ex} > 4154$
4239	1104	90	$1128 > E_\gamma > 1082$	$1173 > E_\gamma > 1128$	$5340 > E_{ex} > 3245$	$3245 > E_{ex} > 1150$
		135	$1122 > E_\gamma > 1085$	$1158 > E_\gamma > 1122$	$6174 > E_{ex} > 2974$	$2974 > E_{ex} > -226$
4305	790	90	$807 > E_\gamma > 774$	$774 > E_\gamma > 741$	$5935 > E_{ex} > 3097$	$3097 > E_{ex} > 258$
		135	$804 > E_\gamma > 777$	$777 > E_\gamma > 751$	$5164 > E_{ex} > 3564$	$3122 > E_{ex} > 391$
4597	4192	90	$4284 > E_\gamma > 4164$	$4019 > E_\gamma > 3845$	$5840 > E_{ex} > 4294$	
		135	$4250 > E_\gamma > 4151$	$4030 > E_\gamma > 3891$	$5530 > E_{ex} > 4470$	
4800	4800	90	$4855 > E_\gamma > 4765$	$4570 > E_\gamma > 4402$	$5824 > E_{ex} > 4424$	$4224 > E_{ex} > 2625$
		135	$4855 > E_\gamma > 4765$	$4570 > E_\gamma > 4402$	$5969 > E_{ex} > 3975$	$3975 > E_{ex} > 1981$
4917	2796	90	$1431 > E_\gamma > 1374$	$1374 > E_\gamma > 1316$	$5732 > E_{ex} > 4068$	$4068 > E_{ex} > 2404$
		135	$1424 > E_\gamma > 1378$	$1378 > E_\gamma > 1333$	$5805 > E_{ex} > 4018$	$4018 > E_{ex} > 2231$
4932	4931	90	$5038 > E_\gamma > 4885$	$4601 > E_\gamma > 4396$	$6026 > E_{ex} > 4484$	$4484 > E_{ex} > 2943$
		135	$5010 > E_\gamma > 4875$	$4631 > E_\gamma > 4468$	$6100 > E_{ex} > 4311$	$4311 > E_{ex} > 2523$
5009	3203	90	$3269 > E_\gamma > 3188$	$3401 > E_\gamma > 3269$	$5801 > E_{ex} > 4201$	$2607 > E_{ex} > 1007$
		135	$3255 > E_\gamma > 3185$	$3360 > E_\gamma > 3255$	$5792 > E_{ex} > 4192$	$2171 > E_{ex} > 1111$
5155	5154	90	$5260 > E_\gamma > 5049$	$5080 > E_\gamma > 4994$	$6772 > E_{ex} > 3987$	$3987 > E_{ex} > 1202$
		135	$5263 > E_\gamma > 5072$	$5080 > E_\gamma > 4994$	$6479 > E_{ex} > 4287$	$4287 > E_{ex} > 2095$
5276	3470	90	$3463 > E_\gamma > 3399$	$3399 > E_\gamma > 3256$	$6146 > E_{ex} > 4408$	$4408 > E_{ex} > 2670$
		135	$3469 > E_\gamma > 3413$	$3413 > E_\gamma > 3299$	$6778 > E_{ex} > 3578$	$3578 > E_{ex} > 377$
5384	5384	90	$5494 > E_\gamma > 5269$	$5330 > E_\gamma > 5242$	$6181 > E_{ex} > 4606$	$4606 > E_{ex} > 3032$
		135	$5474 > E_\gamma > 5295$	$5330 > E_\gamma > 5242$	$6205 > E_{ex} > 4471$	$4571 > E_{ex} > 2738$

Table 3.9: This table shows the limits of γ-rays and excitation energies together with their corresponding background energy limits (B_{limits}) for separate TIGRESS clovers to depopulate states in ^{26}Na. Second column shows which γ-ray was chosen to depopulate a particular state. This information was used to get proton angular distributions.

3.8 Gamma-Ray Angular Distribution Analysis

3.8.1 Gamma-Ray Angular Distributions Measured as a Function of Angle θ_γ Relative to the Beam Direction

The analysis of the gamma-ray angular distributions are focused on nine different transitions that are expected to be the most interesting ones in terms of their shapes. The process of extracting the gamma distributions from the data and theory has 5 major steps. In the first step, the raw histograms for a particular given excitation energy and gamma energy limits are produced corresponding to both the transition of interest and its background. In this first process, the same excitation and gamma energy limits are used as in the proton differential cross section. By using the background subtraction, the final histograms are reached at this step. Segment angles without TRIFOIL gate is chosen as an interest of the analysis. Core angles are also checked previously to compare with the counts in the segments of the TIGRESS clovers. Note that, the gamma distribution analysis has also been done separately for 90° and 135° TIGRESS clovers. Final results are combined in the end. In the second step, the same formalism as in the 3.13, 3.14, and 3.15 is used to get the final distributions with the help of the branching ratios. In the later step, the theoretical results for gamma rays are checked for the comparison with the data. The angular distribution value in theory is stated with the symbol "$W_{\theta_p}(\theta_\gamma)$". This basically says just looking at its expression that the gamma counts as a function of gamma angles will change for a specific proton angle in the frame of interest. That's why the particle gamma correlation plays a role for the type of experiments as in $^{25}Na(d,p\gamma)^{26}Na$ reaction. What one can search for is whether or not the proton distributions are distorted by the selection of a particular gamma angle detection, or vice versa. This may help the exper-

imental physicists how to place their particle and gamma detectors in their experimental set-up if any effect is proven. Especially, it's very difficult job to look for consistency between data and theory under the conditions that we had in the experiment with the radioactive beam. Comparison to stable beam experiments, the gamma counts are fairly low, so the main focus indeed in entire thesis has been mainly extracting any information about spins of the populated states by using proton angular distributions, instead. For every single θ_p angle, it is expected to see different gamma-ray angular distribution line in the range of θ_γ from 0° to 180° in the laboratory frame. However, the proton angular distribution will restrict the possible theoretical lines that one can get from "$W_{\theta_p}(\theta_\gamma)$" values. The reason for that is SHARC detector will not be able to detect a proton for every event and a transition at every angle due to the number of detectors placed in the set-up. Overall proton distribution plots in the previous sections will tell us the range of proton angles that the "$W_{\theta_p}(\theta_\gamma)$" value can be selected to sum to give the total gamma counts weighted by the proton data for a detected θ_p. This sum will reflect the entire gamma counts detected during the experiment for a particular transition at a particular θ_p angle. Finally, this one theoretical line, which is the representative of the total counts for all the detected protons at certain angles of θ_p in SHARC, will be ready to be scaled on the top of the gamma distribution data for a comparison.

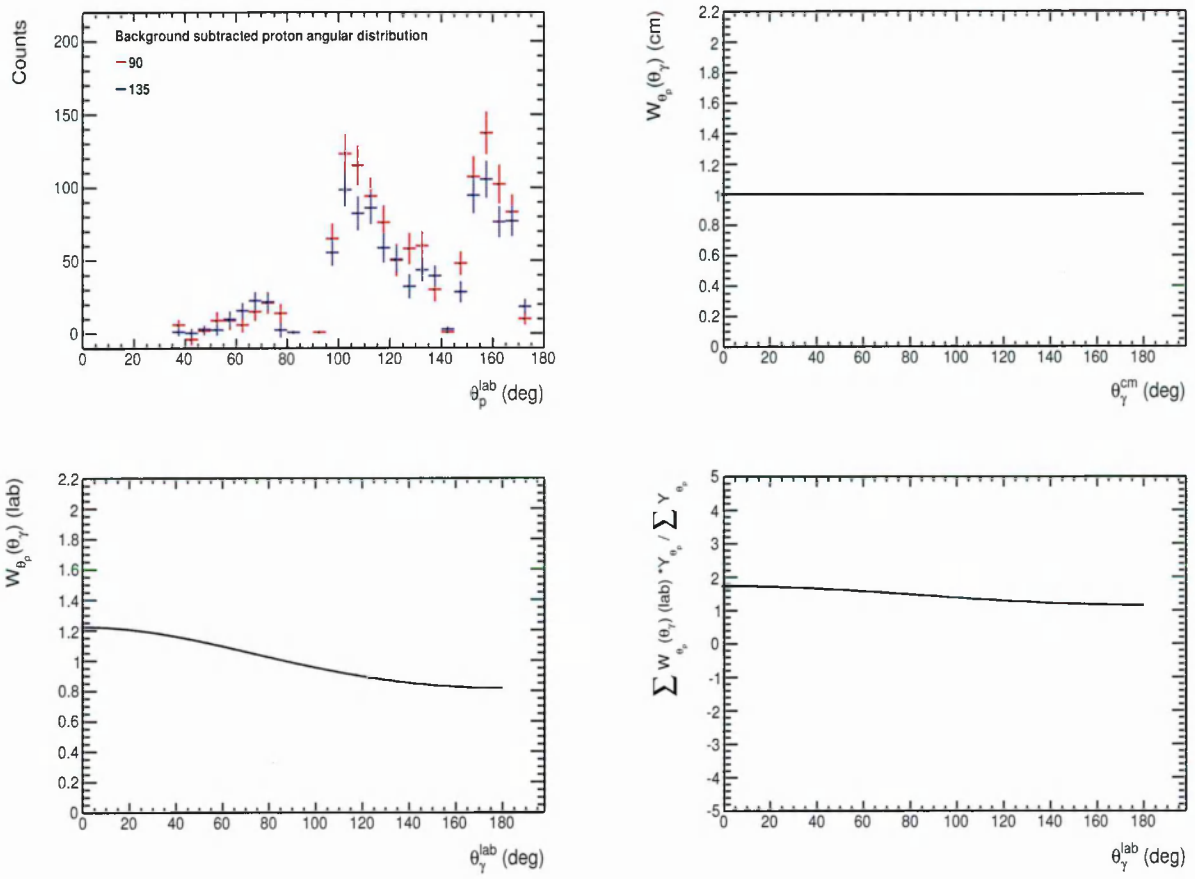

Figure 3.132: The final step of getting the gamma distribution theoretical line weighted by the proton distribution data for the state at 232 keV.

The figure 3.132 is for the M1 transition of the E_γ at 232 keV from the 2^+ state at 232 keV to the 3^+ the ground state. In the first plot, the proton differential cross sections from data is shown to be used for weighting the gamma-ray angular distribution by the help of the equation in 3.19. Since the particular states at 232 keV and 405 keV have $2s_{1/2}$ transfer, the weight of the sub-states will be distributed equally. This has very strong effect on the shape of the gamma distribution because the formula in 2.28 indicates that $B_2(J_1)$ coefficient will be equal to zero by making the a_2 coefficient zero as well. This will give the value of 1 for normalized gamma-ray angular distribution in 2.24. That will

explain the a_K coefficient plots in 3.133 and the gamma-ray angular distribution, shown as the second plot on the top, in centre of mass frame in the figure 3.132.

$$W_{final}(\theta_\gamma) = \frac{\sum_{\theta_p} Y_{\theta_p} W_{\theta_p}(\theta_\gamma)}{\sum_{\theta_p} Y_{\theta_p}} \tag{3.19}$$

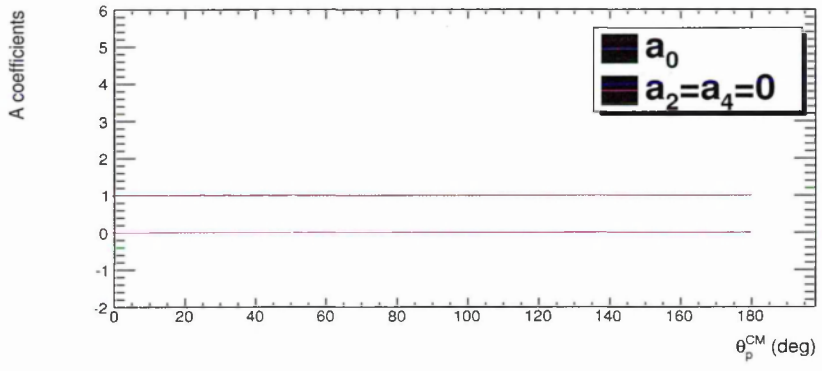

Figure 3.133: a_K coefficient as a function of scattered proton angle θ_p for the M1 transition from 2^+ 232 keV state to the 3^+ ground state.

The third plot showing the $W_{\theta_p}(\theta_\gamma)$ in laboratory frame in the figure 3.132 is changed its shape due to the headlight effect and the frame transformation in gamma-ray angular distribution as explained in the previous sections and in the equation 2.42. These two angular distribution plots both in the centre of mass frame and in the lab frame in the figure 3.132 show indeed 181 different theoretical lines which are identical at the same magnitude overlapping on top of one another. Thus, this is not a good example to show how the scattered proton angular distribution and the weight of the sub-states related to those angles affect the gamma-ray angular distribution lines. Also, the shape of the theoretical gamma-ray angular distribution line keeps its form for all proton angles in the detector coverage in θ_p before and after weighting by the proton angular distribution data

points as proved in the last plot of the figure 3.132 for this type of isotropic transition of the s wave transfer in $^{25}Na(d,p\gamma)^{26}Na$ reaction. Scaled gamma distribution line ,which is taken from the last step of the figure 3.132, is overlapped on to a gamma distribution data showing both segment angles in 90° and 135° clovers as seen in figure 3.134.

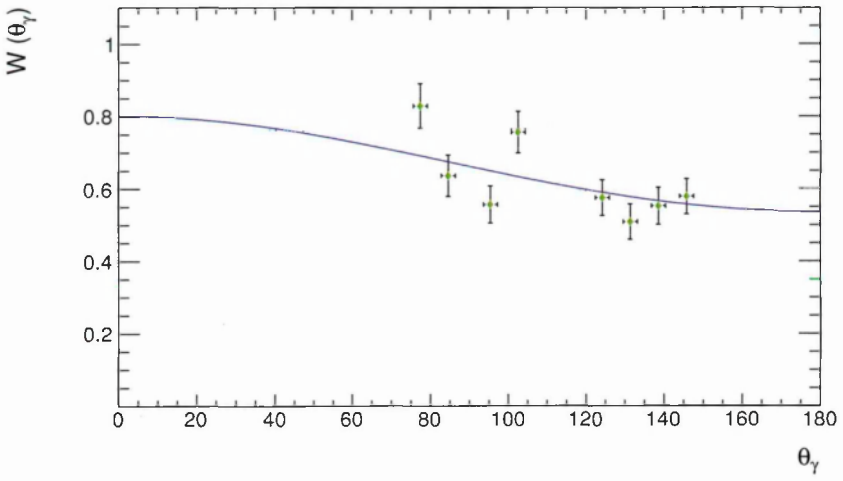

Figure 3.134: Gamma-ray angular distribution as a function of θ_γ in laboratory frame is overlapped with the theoretical line as mentioned in the last step of the figure 3.132 for the M1 transition from 2^+ 232 keV state to the 3^+ ground state.

Figures 3.135 and 3.136 reflect the change on a_K coefficients and the gamma-ray angular distributions due to the sub-state population of the 6^- state at 4.917 MeV for different θ_p angles. Since the populated state spin is quite high, K_{max} value will go up to 8 by giving different K values starting from 0 in even integer steps. Different shape of the a_K coefficient will result mainly from drastically changing sub-state weights of the state in the $B_K(J_1)$ calculations.

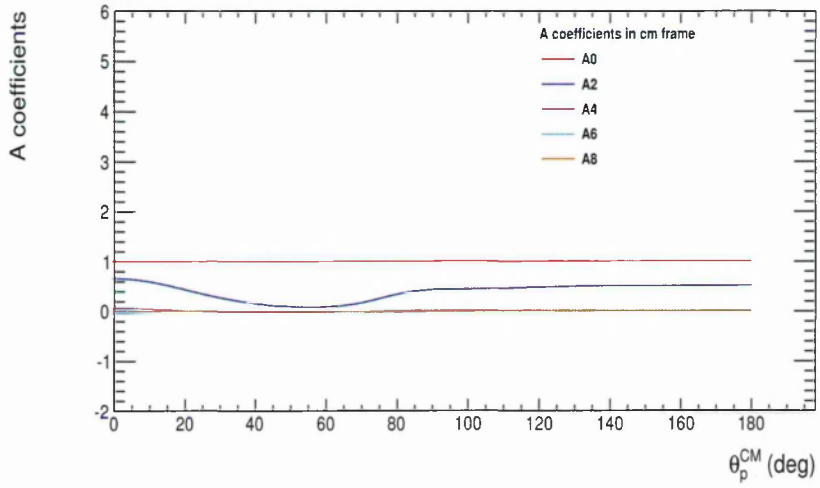

Figure 3.135: The change in the a_K coefficients as a function of scattered proton angle θ_p for the M1 transition from 6^- 4.917 MeV state to the 5^- 4.305 MeV state.

In comparison to s wave transfer, where the weight of the sub-states are evenly distributed for individual sub-states of any populated spin, the gamma-ray angular distribution lines in the figure 3.136 show separation from each other for chosen backward angles in SHARC corresponding to the upstream part. However, it's noticed that when those selected theoretical lines for the proton angles with count in SHARC are summed up by the weight of the proton data to consider the particle-γ correlation effect as in the equation 3.19, the final gamma distribution line in the last plot on the right bottom in the figure 3.137 shows minor change in shape in comparison to the same plot in the figure 3.132 especially around 90° for θ_γ in lab frame. It looks as if the drop in counts are expected more at this 90° gamma angle.

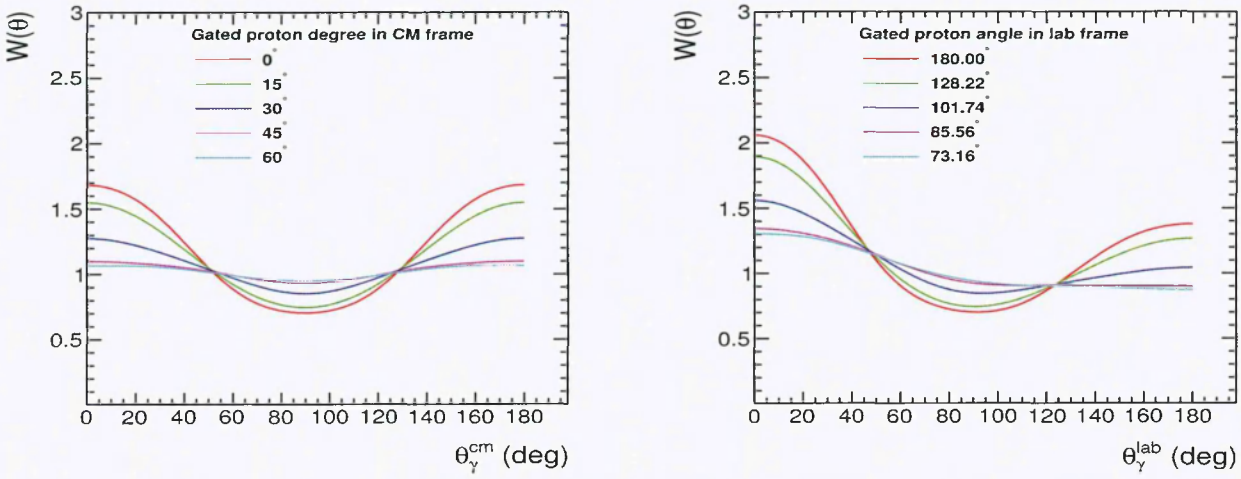

Figure 3.136: Gamma-ray angular distributions on both frames for certain scattered proton angles as a function of θ_γ angle for the M1 transition from 6^- 4917 keV state to the 5^- 4305 keV state.

As explained before, summing up the theoretical lines of $W_{\theta_p}(\theta_\gamma)$ in lab frame in the figure 3.137 by using the proton angular distribution data as a weight is an effective method to take different detected proton angle effect in gamma detection.

We should notice that different gamma distribution theoretical lines in the figure 3.137 for different proton angles have more variety in terms of up and downs in its characteristic shape. Summation of these theoretical lines are shown in figure 3.138 after scaling on gamma distribution data points by using chi-squared rule. Despite the fact that the segment angle distribution data from TIGRESS could have been fitted better by using particular proton angle, fitting procedure is applied for all proton angles with a hit in SHARC array. This shows the theoretical line does not follow the data after scaling.

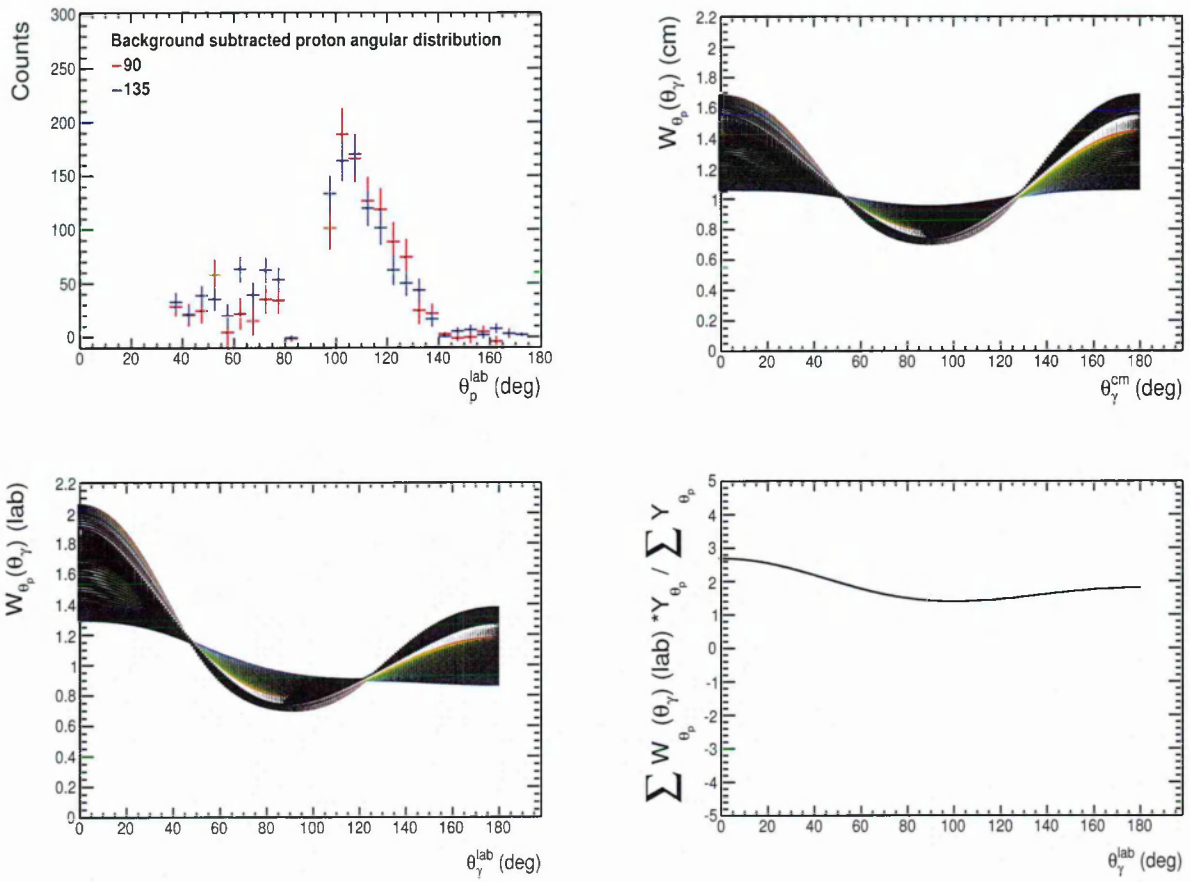

Figure 3.137: The final step of getting the gamma distribution theoretical line weighted by the proton distribution data for the state at 4917 keV.

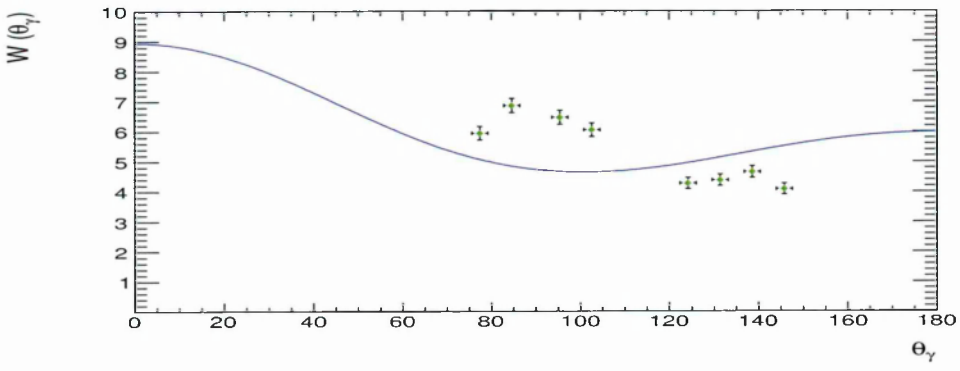

Figure 3.138: Gamma-ray angular distribution as a function of θ_γ in laboratory frame is overlapped with the theoretical line as mentioned in the last step of the figure 3.137 for the M1 transition from 6^- 4917 keV state to the 5^- 4305 keV state.

$E_{ex}(1)(keV)$	$E_{ex}(2)(keV)$	$E_\gamma(keV)$	J_i^π	J_f^π	δ_R	Transition type
232	g.s.	232	2^+	3^+	0	**M1**, E2, M3
405	g.s.	405	2^+	3^+	0	**M1**, E2, M3
1805	g.s.	1805	3^+	3^+	10^6	M1, **E2**, M3
2225	g.s.	2225	4^+	3^+	10^6	M1, **E2**, M3
2843	232	2616	2^-	2^+	0	**E1**, M2, E3
3511	g.s.	3511	4^-	3^+	0	**E1**, M2, E3
4087	g.s.	4087	2^-	3^+	0	**E1**, M2, E3
4917	4305	612	6^-	5^-	0	**M1**, E2, M3
4932	g.s.	4932	3^-	3^+	0	**E1**, M2, E3

Table 3.10: These values are used to get γ-ray angular distributions in figure 3.139. For method of deciding transition type, see section 2.5. Necessary formulas were given in section 2.5.3 for γ-ray angular distributions.

Table 3.10 shows the transitions that has been analysed for their γ-ray angular distributions. To find these γ-ray distributions as shown in figure 3.139, there are some elementary information to be used as an input to get the theoretical lines for γ-ray distri-

butions. These are mass number of depopulated state ^{26}Na initial and final spins where the transition took place, the dominant transition type, and a mixing ratio to clarify this transition type in the equation 2.26. Some of the method was given in section 2.5. Mixing ratio for $R_K(J_1J_2)$ coefficient is chosen to be either 0 or 10^6 as in the table. When zero mixing ratio makes the first transition type dominant, a value of 10^6 assigns the second transition type as the strongest.

Note that the weight of the sub-states for a chosen depopulated state comes from TWOFNR [17] results. These values help to define $B_K(J_1)$ and a_K coefficients to find γ-ray angular distributions as explained in section 2.5.3. While the lowest multipolarity is defined by the difference between initial and final spins as $|J_i - J_f|$ where the transition occurs, the dominant γ-ray multipolarity is defined by the strengths of the transition types.

In general, the angular distributions in figure 3.139 show reasonable agreement with the theory in about half of the cases studied, and in particular for the two cases expected to be isotropic in the centre of mass. The agreement suggests that there does not appear to be any problem with the gamma-ray data themselves. In the other half of the cases, the gamma-ray yield near 90 degrees is high compared to the theoretical expectation. It is difficult to identify any consistent factor that is related to this effect. It does not appear to be obviously related to the multipolarity inferred for the transition, or the excitation energy or the parity of the decaying state. Thus, a more detailed study will need to await the future work.

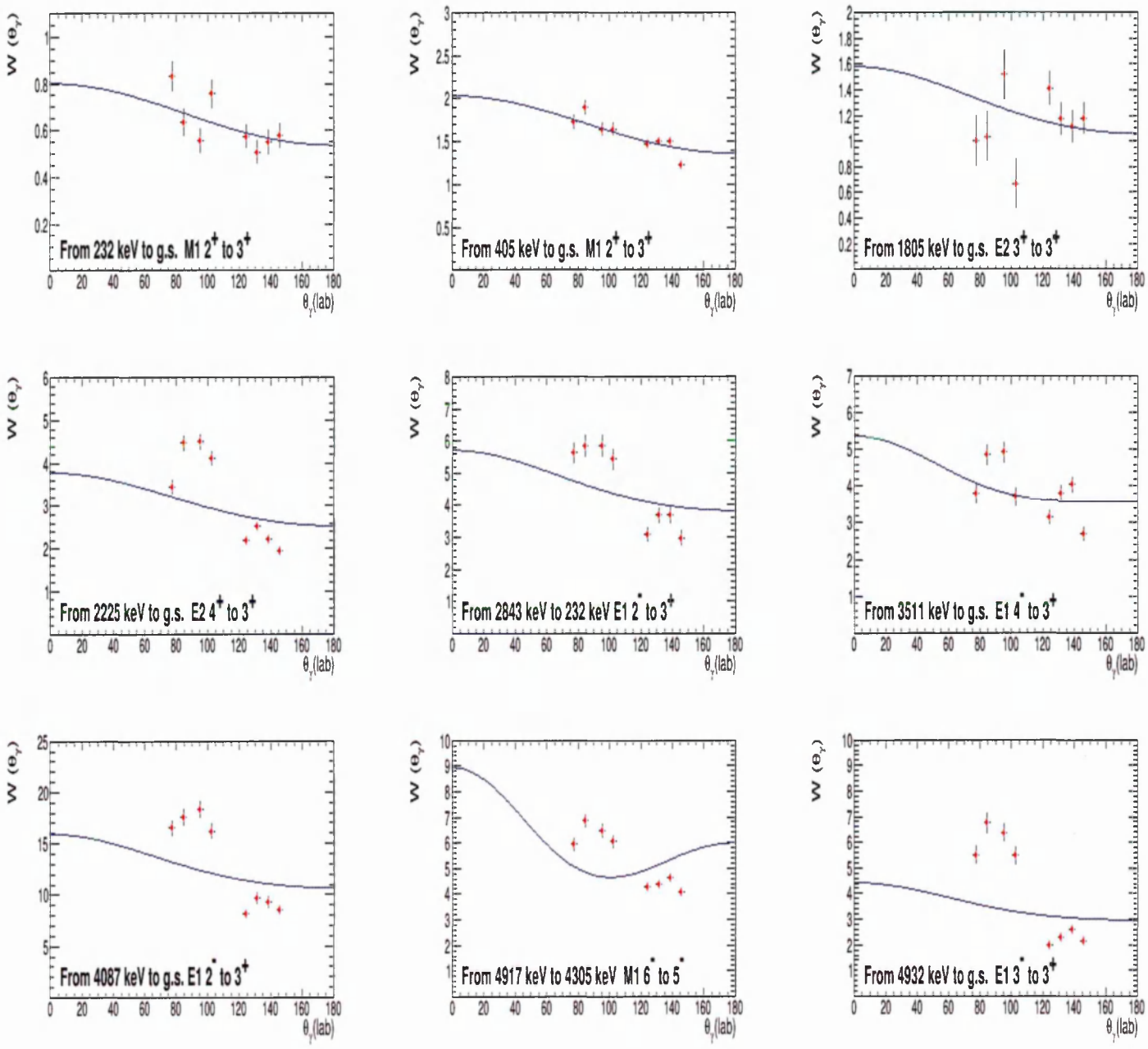

Figure 3.139: Angular distributions for gamma-rays emitted in coincidence with individual states in ^{26}Na in laboratory frame. Corrections have been applied for gamma-ray efficiency, background subtraction and feeding. The theoretical curves and gamma-ray multipolarity assignments are discussed in the text. The transition takes place between the states given here.

3.8.2 Gamma-Ray Angular Distributions Measured as a Function of Polar Angle ϕ_γ Around the SHARC Detector

For the populated states at 405 keV and 3.511 MeV in ^{26}Na, it has been possible to make a detailed study of the distribution in azimuthal angle of the decay gamma-rays. This is of interest for a number of reasons: it may be that it can yield additional information in future experiments, concerning spins of the states involved, and also it is something that needs to be known from an experimental perspective, if the experimental set-up for detecting particles is not axially symmetric around the beam direction. All of the gamma-ray correlation theory that has been used in the present work has included the assumption of cylindrical symmetry in the particle detection. This is why the gamma-ray angular distributions, as predicted, are functions of the angle theta only, and contain only even-order Legendre polynomials [32]. If the cylindrical symmetry of the particle detection is removed, then the cylindrical symmetry of the gamma-ray distribution may also be removed.

In the present experiment, approximate cylindrical symmetry is achieved for the particle detection backward of 90 degree in the laboratory. Forward of 90 degrees, there is only one fully instrumented DSSSD detector on the right side of the downstream box towards beam direction. The possible effects of departures from symmetry have been investigated by analysing data from the individual sides of the upstream and downstream boxes in SHARC array. In this analysis, minor effects on overall normalisation due to missing strips in SHARC have not been taken into account (which affects the comparison between the different sides of the upstream box), and the different yields for upstream and downstream due to the proton differential cross section have not been taken into account. Also, for these cases, the background contribution is very low and hence there is

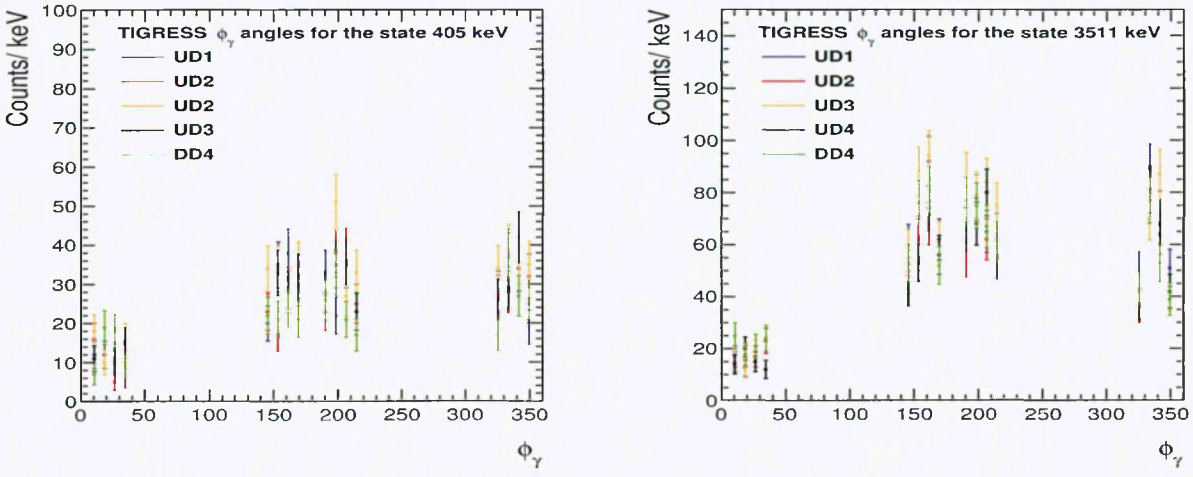

Figure 3.140: Gamma-ray angular distribution in azimuthal angle ϕ_γ for two states in ^{26}Na, measured using the clover detectors centred at 90 degrees and gated on various different detectors in the SHARC box.

no background subtraction and the gating is simply on gamma-ray energy and excitation energy, using the same gates as for the proton differential cross sections. There is no correction for gamma-ray efficiency.

Evidently, one of the clover detectors has a lower efficiency than the others. Note that this will have no effect on any of the analysis discussed previously, which has only depended on the overall efficiency for gamma-ray detection of either the complete clover array at 90 degrees or the complete clover array at 135 degrees. In addition, it is apparent that there is no strong dependence, and indeed no observable dependence, of the gamma-ray yield on the polar angle in the present experiment. Whilst this means unfortunately that there is no extra information about ^{26}Na that can be learned from this type of analysis, it also means that the polar angle distribution of gamma rays cannot have had any influence on the analysis, which had been assumed to be the case. The assumption had been based upon the approximate cylindrical symmetry of the proton detection system,

for the proton data backward of 90 degrees in the laboratory, but had been extended to apply implicitly to the proton data forward of 90 degrees.

It is worth commenting further on the proton data forward of 90 degrees at this point. For proton differential cross sections, especially when comparing with the best-fit theoretical cross sections, it appears that the data points forward of 90 degrees are consistently high. In the preceding analysis, this has not caused a problem because the considerations of goodness of fit and the normalisations to the data did not use the forward angle points. The backward angle points were considered to be more reliable theoretically, and therefore the forward angle points were not used. Inspection, however, suggests that they may be consistently high. It may be relevant that these are the data points for which the proton detection is not at all cylindrically symmetric. Due to equipment limitations, only one side of the downstream box could be instrumented. If there were a correlation between azimuthal angles of the detected proton and the emitted γ-rays, then this could make the assumed γ-ray efficiency invalid. For example, there is only the detector to the right of the beam that was fully instrumented in the downstream SHARC array. If the physics were such that the protons in this detector corresponded to gamma-rays that were preferentially emitted to the left or right of the beam, then the efficiency for gamma-ray detection would have been under-estimated since the clover detectors are indeed situated to the sides of the SHARC array and there is no coverage directly above and below SHARC. In this hypothetical case, with the gamma-array efficiency being underestimated, the data points in the proton differential cross section would come out to be too high. However, the evidence from the data, as shown in figure 3.140, is that no such effect appears to exist in the data, because there is no observable phi-dependence in the gamma-ray angular distributions.

Chapter 4

Results

4.1 Summary of the Identification of the States in ^{26}Na

The assignments for the lowest four states in ^{26}Na are already known from previous work. Beta decay has given the ground state spin to be 3^+ and the low-lying quadruplet of 3^+, 1^+,2^+ and 2^+ has been identified via (t, ^3He) charge exchange reactions. This is summarised in the $^{14}C(^{14}C,pn)^{26}Na$ paper by Lee [45]. The two 2^+ states were populated in the present work and are indicated by circled assignments in figure 4.1. The description of what is plotted in figure 4.1 will be given below.

The second 1^+ state at 1.507 MeV has been identified in the beta decay of ^{26}Ne [46] and also possibly seen in ($^{14}C,pn$) [45]. This was also populated in the present work and its assignment is also circled in figure 4.1. Note that the ground state (3^+) and the isomeric first excited (1^+) state could not be isolated in the present work, for the purposes of extracting a proton angular distribution. Apart from these lowest lying five levels, none of the levels observed in the present work has previously been observed, except in the preliminary analysis of the present (d,p) data by Wilson [1]. The neutron

transfer reaction (d,p) evidently has a greater and different selectivity than the previously employed ($^{14}C, pn$) and (t, ^{3}He) reactions. The states highlighted by the transfer should be the best suited to comparisons with shell model calculations, due to their significant single-particle structure.

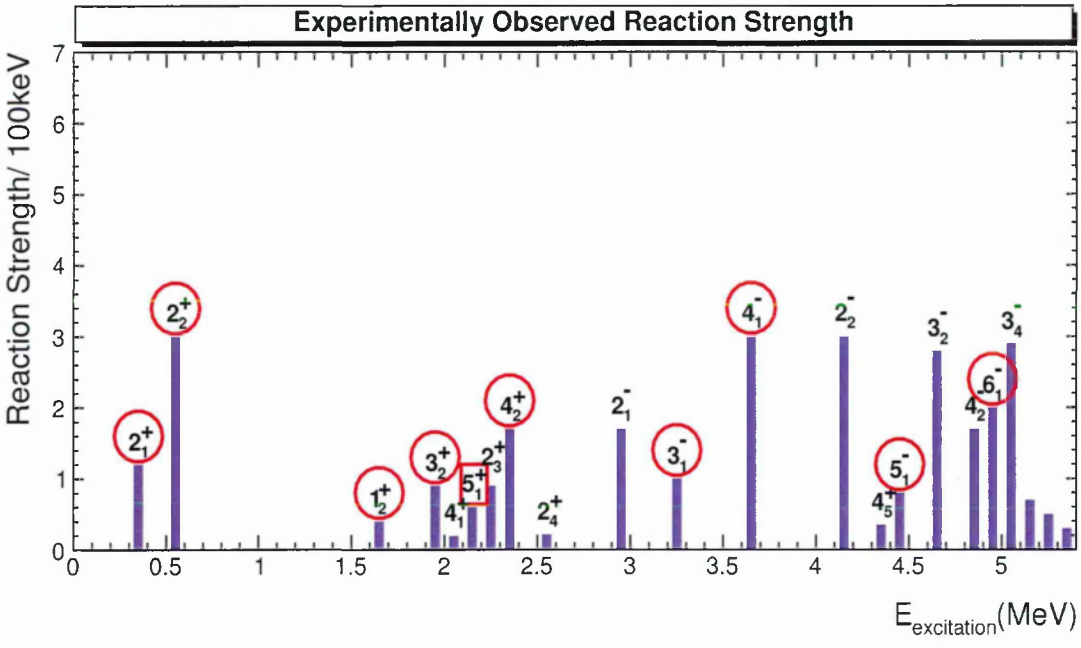

Figure 4.1: For each state observed in the experiment, the maximum magnitude of the experimental proton differential cross section (mb/sr) in the angular range from 90° to 180° in the laboratory frame is shown. Figures in section 3.7 can be checked to see data points in (mb/sr).

A number of states above the second 1^+ have been identified from an initial analysis of the $^{25}Na(d,p)^{26}Na$ reaction by Wilson [1]. These states are indicated by circled assignments in figure 4.1. In this figure, each state is plotted at the experimentally observed excitation energy and the ordinate is a number proportional to the maximum value of the differential cross section for (d,p) as measured in the present work. The assignments that are not circled will be justified in the discussion that follows.

The assignment of levels here is based upon considerations of (a) the observed γ-ray decay branching ratios, (b) the observed population strength in the (d,p) reaction, (c) the predicted excitation energies from shell model calculations, (d) the predicted reaction strengths, (e) the observed angular momentum transfer in the (d,p) reaction, and (f) analogies with the experimentally observed γ-decay properties of the isotone ^{28}Al. The predicted reaction strengths for states are calculated from the shell model spectroscopic factors (SF) and the spin of the states as shown in the tables 2.3 and 2.4, and a weighting factor (kinematical factor) that measures the relative magnitudes of the differential cross sections for a spectroscopic factor of 1 as calculated with the ADWA reaction theory for the different partial waves, for transfer into the $s_{1/2}$, $d_{3/2,\ 5/2}$, $f_{7/2}$ and $p_{1/2,\ 3/2}$ orbitals as appropriate. The weightings for the different angular momentum transfers 0, 1, 2 and 3 are found from these calculations to be 10, 7, 2, and 1.25 respectively. Thus, it is possible to obtain approximate predicted reaction strengths from theoretical spectroscopic factors.

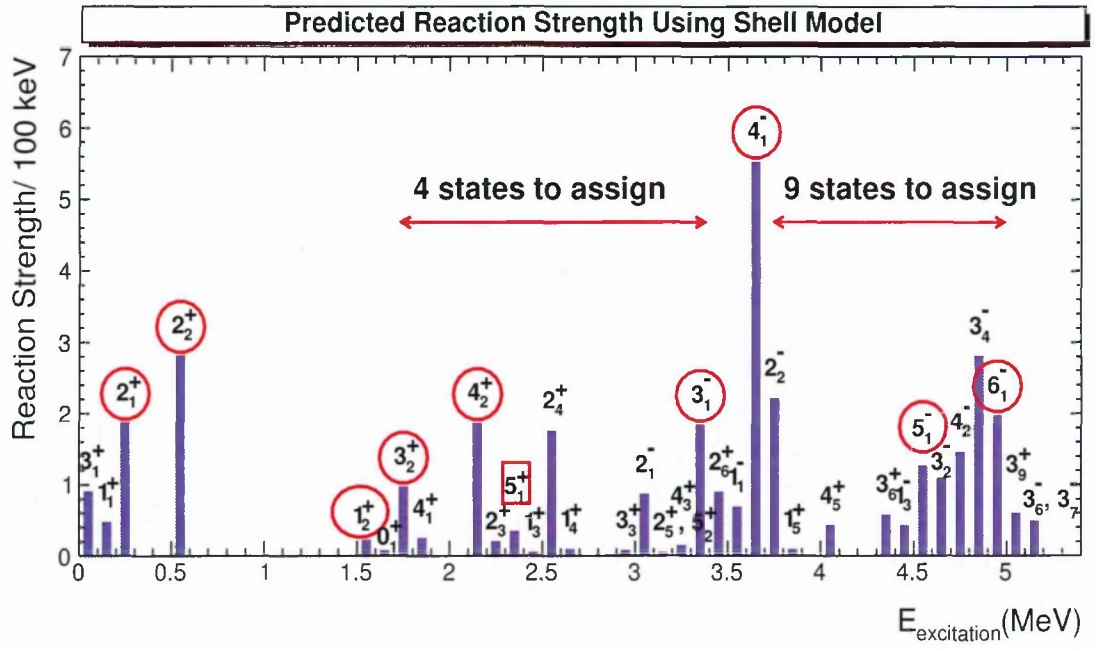

Figure 4.2: Predicted reaction strengths for all states up to an excitation energy of 5.2 MeV in ^{26}Na according to shell model calculations and the calculation discussed in the text. The normalisation factor is chosen as 5 to assist comparison with the figure 4.1. Circled states were identified experimentally in previous work [1], and the experimental candidate for the state in the box is reassigned from a former 4^+ assignment, in the present work. The energy ranges that encompass the 13 newly observed states in the present work are indicated.

Strong similarities may be observed between the predicted and observed strength distributions. This can be a good guide to the identification of states, but it cannot be a primary guide because of the possible inaccuracies in the shell model calculations (which this experiment seeks eventually to reduce) and the approximate translation of shell model spectroscopic factors into reaction strength.

Up to an energy of 2 MeV, the states that are expected to be populated appear to have been observed. The state at 1.507 MeV identified as the second 1^+ state is close to the energies previously reported in beta decay [46] and fusion-evaporation studies [45].

It has a characteristic gamma-decay that selects one final state only, the lowest 2^+ level. The differential cross section indicates an "l=2" transfer, and is in strong contrast to the predominantly "l=0" transfer seen for the first and second 2^+ states. This is all consistent with the 1^+ identification.

The state at 1.805 MeV identified as the second 3^+ state decays to the 2^+ and 3^+ members of the ground state quartet, but not to the 1^+ member and not to the 1.507 MeV state. This suggests that the gamma-ray multipolarity would need to be greater, to connect to a 1^+ state, which in turn suggest a possible assignment of spin 3. The shell model predictions in figure 4.2, which include all predicted states, strongly support an association with the second 3^+ state. This state also features in the gamma-decay branches of several higher lying states, which will serve to support its identification in the following discussion.

Several states of intermediate strength experimentally are found above the 3^+ and two of them have particularly distinctive features in relation to gamma-decay. The state at 2.116 MeV is populated by the decay of states that will be deduced below to have spins of 5^- and 6^- respectively, and decays itself only to the 3^+ ground state and not to any spin 2 or 1 states. This suggest a spin close to 5 or 6 and certainly above 3. It is a natural candidate for the first 5^+ state expected in this region, since this is the only predicted state that would stand out from any of its neighbours (by virtue of the higher spin) and hence be selected so specifically in the gamma-decays. The differential cross section is also most accurately reproduced by "l=2" , which is consistent. The state will be populated via to transfer to the neutron $d_{5/2}$ orbital, noting that a neutron pair will be excited from $d_{5/2}$ to a higher orbital for some fraction of the time in the ground state of ^{25}Na.

Another strong state in this group near 2 MeV is that observed at 2.225 MeV which

was previously identified as being the second 4^+ state [1]. This state gamma-decays only to the 3^+ ground state and the higher lying 3^+ state at 1.807 MeV. It is populated in the decay of a higher lying level that will be identified as a 5^- state. The proton differential cross section indicates "l=2" for the transfer and a relatively large spectroscopic factor. This is all consistent with the predicted properties of a 4^+ state, and the excitation energy and large spectroscopic factor suggest that the level corresponds to the second 4^+ state in ^{26}Na, from a comparison with the shell model predictions.

One of the strongest states of all, in the experimental spectrum, is the state at 3.511 MeV. It has a single gamma-ray decay branch, which leads to the 3^+ ground state. This immediately suggests a spin greater than 3. This level is also populated in the gamma-decay of two other levels. The fact that those higher levels decay exclusively via cascades means that they have relatively high spin and the 3.511 has an intermediate spin. This is a natural candidate for the state predicted to be the strongest of all in (d,p) which is the lowest 4^- state. The higher lying states are then obvious candidates for the 5- and 6- states that are expected to be populated and which will be likely to decay via the 4^- state. The isotone ^{28}Al has states identified [47] as the lowest 5^- and 6^- states which are each seen to decay via a cascade through the 4^- state which is also populated strongly in (d,p). Finally, the proton differential cross section clearly indicates a predominant "l=1" transfer and hence negative parity. The 3.511 MeV is therefore identified as the first 4^- state in ^{26}Na.

The higher lying levels at 4.305 and 4.917 MeV have gamma-decays that include a branch to the 4^- state and the analogy with the decays of the 5^- and 6^- states in ^{28}Al helps to identify them. The level at 4.305 MeV decays to the levels identified above as the second 4^+ and the first 5^+ states, in addition to the 4^- state at 3.511 MeV. The level

at 4.917 MeV decays to first 5^+ and the 4^-, and also to the level at 4.305 MeV, but not to the 4^+ level. This indicates that the level at 4.917 MeV has a higher spin than that at 4.239 MeV, which in turn has a spin of at least 5. The upper level is unlikely to have a spin higher than 6, given the decay to the 4^-. The proton differential cross sections, and in particular the strong dip towards 180 degrees (which corresponds to zero degrees in the centre of mass frame) is strongly reminiscent of the differential cross sections for the 5^- and 6^- states observed in the isotone ^{28}Al, as populated by (d,p) [47]. This would help to support an "l=3" assignment, but it may also be that the data for the angles closest to 180 degrees are subject to an energy threshold in the detector as they correspond to the lowest energy protons and they are very close to the minimum detectable energy. In any case, the present differential cross section data by themselves would not strictly rule out "l=2". These cross sections had not been extracted at all, before the present work. Ultimately, the strongest evidence for the assignments comes from the observed gamma-decay cascades, and the natural identification is to assign spins of 5^- and 6^- to the 4.305 MeV level and the 4.917 MeV level respectively. The decay of the 6^- to the state at 2.116 MeV is the key evidence in favour of the 5^+ assignment to that level, also.

There is one state not yet discussed, amongst those identified with circles in figure 4.1. This is the state at 3.135 MeV, previously identified as the first 3^- state, and the present data also support that assignment. The gamma-decay populates 3^+ and 2^+ members of the ground state quartet, but not the 1^+ member. This suggests a spin of at least 3 and indeed unlikely to be more than 3. The differential cross section for this state is reported in the present work for the first time. Transfers of "l=0" and "l=1" by themselves are ruled out by the observed shapes of these cross section plots, but it is unfortunately not possible to distinguish between an "l=2" distribution and a mixture of

"l=1" and "l=3" contributions. The shell model predicts only one candidate with spin 3 or higher that is likely to be strongly populated in this region of excitation energies, namely the first 3^- state. Furthermore, this level is clearly unique in some important way, as it is exclusively selected as the unique gamma-decay pathway for the level at 4.239 MeV which will be discussed below. It is the negative parity that gives this uniqueness amongst its near neighbours. The data therefore strongly supports the association of the 3.135 MeV level as corresponding to the lowest 3^- state in ^{26}Na.

Having addressed the levels previously identified, and having established that the present data are in very good agreement with the previously suggested spin assignments (with a revision for the 5^+, which was previously suggested to have a 4^+ assignment), it is appropriate to consider the 13 previously unassigned levels observed in the present work. These include four levels that were previously reported but not identified [1] and a further 9 levels reported here for the first time. The observation of these additional levels has been made possible by the development of improved methods of data analysis for the data that were previously analysed in a preliminary fashion [1].

The first four levels that are considered are the four levels lying in the lower region of excitation energy indicated in figure 4.2, below the 4^- state. This is a region dominated by positive parity states, according to the shell model predictions. The state at 1.992 MeV has not previously been reported and the other three (at energies of 2.194, 2.423 and 2.843 MeV) have no previous assignments. The strongest predicted and unassigned states in this region (see figure 4.1) are the 2^+ and 2^-. The 1.992 and 2.194 MeV levels gamma-decay in preference to the 3^+ ground state, with some decay also to the lowest 2^+ state. The 2.423 MeV level decays to 3^+ and 2^+ in somewhat more equal measure, and it is the second 2^+ state that is selected.

The 2.843 MeV level decays to the 3^+, 1^+ and lowest 2^+ states fairly equally and is the only one of these states to include a 1^+ state in its gamma-decay. None of these states are observed to be populated in the gamma-decay of any higher lying states in the present work. The 2.843 MeV level is distinguished in this group by decaying to all three spins 1^+, 2^+ and 3^+ which suggest a possible spin of 2 for this state. The strongest of the predicated states are indeed a 2^+ at 2.452 MeV and a 2^- at 2.940 MeV. Mainly on the basis of excitation energy, the 2^- option is favoured. The proton differential cross section is of modest assistance. Compared to single "l" transfers, it would be best fit by "l=2", but the implied spectroscopic factor for 2^+ would be rather high at 0.76. The fit for a mixture of "l=1 and 3" distributions is as good as the fit for a combination of "l=0 and 2", and the spectroscopic factor deduced for the state if it is 2^- is 0.10 for the dominant p-wave contribution (and a high but very poorly defined spectroscopic factor for the "l=3" component which is intrinsically a much smaller contribution due to the poorer kinematic matching). The gamma-decay to all three spins 1^+, 2^+ and 3^+ is behaviour that matches the second 2^- state in the isotone ^{28}Al, although the first 2^- in ^{28}Al has no 2^+ branch. In summary, guided mostly by the facts that this is one of the strongest of the four previously unidentified states, and the closeness to the predicted excitation energy for the 2^- state, the 2.843 MeV level is most naturally interpreted as the lowest 2^- state in ^{26}Na. As shown below, this leads to natural interpretations for the remaining three levels in this energy range.

The 1.992 MeV level has no observed decay to a spin 1 state, but rather it decays to levels with 2^+ and 3^+ assignments only. This distinguished it from the remaining two unidentified states. The strongest unassigned state in the energy region has spin 2^+, followed then by the first 4^+ state. Based on the observed uniqueness of its gamma-

decay pattern, the 1.992 MeV level is best matched to the lowest 4^+ level. This is indeed expected to come lower in energy than any candidate 2^+ level, so the 2.194 and 2.423 MeV levels are better 2^+ candidates. The 1.992 MeV level was not populated sufficiently strongly for the proton differential cross section to be extracted reliably. Based on the relative strength of the ground state gamma-ray transition compared to the nearby 1.805 MeV state, the strength of the state in (d,p) can be estimated under the assumption that the transfer is "l=2" as for the 1.805 MeV state, but there is no independent measure of the transferred angular momentum "l" for this state. Assuming "l=2" as above, and an assignment as the lowest 4^+ state, the spectroscopic factor is deduced to be essentially equal to the shell model prediction. This success then matches the similar success for the shell model in reproducing the spectroscopic factor for the second 4^+ state which occurs at 2.225 MeV according to the present interpretation. The shell model appears to provide a rather good description of the various 4^+ states in ^{26}Na, including the lowest 4^+ which is identified with the 1.992 MeV level.

The two states at 2.194 and 2.423 MeV have only a single clear candidate as their theoretical partner, as may be seen by comparing Figures 1 and 2, taking note of the above arguments. This is the fourth 2^+ state. These two states have very similar gamma-decay schemes, each favouring the 3^+ ground state and also decaying to one of the two 2^+ states in the ground state quartet, which is certainly consistent with a 2^+ assignment. In fact, the fourth strongest theoretical state in this energy region (out of those with no previous identification) also has a 2^+ assignment, namely the third 2^+ state. Most likely, these two observed states should be assigned as the third and fourth 2^+ states, respectively. The observed excitation energies agree well with the shell model predictions, but the partitioning of spectroscopic strength in the transfer reaction is not well reproduced, with

the observations being more or less opposite to the predictions for these two quite closely spaced 2^+ levels. The shell model appears to be less successful at describing the 2^+ levels than any of the other spins, amongst the positive parity states below 3 or 4 MeV (at least). The 2^+ assignments for the 2.194 and 2.423 MeV levels complete the identifications of the four previously unidentified levels below the 4- state in ^{26}Na.

Above the 4^- state, there are just four levels predicted to be strongly populated according to the shell model, in addition to the 5^- and 6^- previously discussed. In order of increasing excitation energy, these are the second 2^- state and then two 3^- states that straddle the second 4^- state and come close to the 6^- state in energy. Of the nine newly observed levels in this region, it is also the case that just four are populated particularly strongly. Three of them are close to the 6^-, and all are above the 5^-, whilst the fourth is at 4.087 MeV which is more than 500 keV lower than the rest and is below the 5^- level.

The 4.087 MeV level, based on its excitation energy and large cross section is an obvious candidate for the second 2- state. The proton differential cross section, if fitted with a single "l"-transfer, is marginally better fit with "l=1" than "l=2", but the distinction is inconclusive. The 2- is predicted to have a predominantly "l=1" transfer. The gamma-decays of the 4.087 MeV level are to the 3^+ ground state, to the two 2^+ states in the ground state quartet and to the second 3^+ state at 1.805 MeV. It is the only state seen to have four decay branches in the present work. There is no branch to the 1^+ state. Concerning the second 3^+ decay, the other three levels that are observed to decay to that state are the 4^+ state at 2.225 MeV (which also decays to the 3^+ ground state) and two of the four levels above 5 MeV (which decay uniquely to the second 3^+ state). The gamma-decay branching tentatively suggest a spin of 3 or possibly 2, based on the lack of branches to 1^+ or 4^+ states. There is however no other viable candidate for the predicted strong 2^-

level. Therefore the 4.087 MeV level is inferred to be identified with the second 2^- state in ^{26}Na.

The 4.8 MeV level is more characteristic in its gamma-decay than the levels at 4.239 MeV and 4.597 MeV and is considered next. It has a single gamma-decay branch, to the 3^+ ground state. This suggests a spin of more than 3. The only candidate of such a spin provided by the shell model predictions is the second 4- state which is predicted to lie within 70 keV of the observed energy. The proton angular distribution is not well described either by "l=1" or "l=3" but a combination of them gives a fit that is no worse than either "l=2" or a combination of "l=0" and "l=2". The proton distribution is therefore inconclusive. However, the unique gamma-decay signature gives confidence that the 4.8 MeV level must correspond to the second 4- state in ^{26}Na.

The 4.932 MeV level is observed to gamma-decay to the 2^+ and 3^+ members of the ground state quartet, and not to the 1^+ member or to any other states such as the 4^+ states at 1.992 and 2.225 MeV. This suggests a possible spin of 3. This is also one of the most strongly populated states in the reaction as in the figure 4.1 and it can be seen that the strongest of the predicted states in this region of energy is the fourth 3^- state in the figure 4.2. The proton cross section is again inconclusive. Based on both its reaction strength and the observed gamma-decay pattern, the 4.932 MeV level is identified with the fourth 3^- state in ^{26}Na.

The 4.597 MeV level has gamma-decay branches to the two 2^+ states in the ground state quartet but not the 1^+ or 3^+ members. This suggests a spin of 2 or within a unit of 2. The proton cross section again provides difficulties in interpretation. It is quite clear from the shell model predictions in the figure 4.2 that this state must have negative parity, and by elimination it would be the second 3^- state, which is consistent with the

gamma-decay. It appears that the shell model is successful in predicting a concentration of strength to 3^- states near 4.7 MeV but is unable to correctly predict the splitting of strength between the individual closely spaced 3^- levels. This is similar to the behaviour noted previously for the 2^+ levels near 2.3 MeV.

At this point in the discussion, it has been noted for several levels above 4.5 MeV that the proton differential cross sections show a drop towards 180 degrees that is not reproduced by the reaction calculations, and particularly for the 3^- and 4^- states that should have significant reaction strength via the well-matched "l=1" contribution (the 6^- state can only be populated via "l=3", which has a characteristic dip towards 180 degrees in any case). It is worth a careful consideration of the detection thresholds, because these backward laboratory angles for these high-lying excited states correspond to the lowest energy protons seen in the experiment. Upon close inspection, it has been deduced that the energy threshold is indeed likely to reduce the observed cross section for angles greater than 130 degrees and excitation energies greater than 4.5 MeV. An example is shown in figure 4.3, which shows the proton energies for the case of the 4.8 MeV state. The overall normalisations of the theoretical reaction cross sections to the data are however driven by the points with better statistics and smaller error bars at angles between 100 and 130 degrees, and hence the spectroscopic factors deduced from those fits are not unduly biased by the effects of the energy threshold on the differential cross section.

The 4.239 MeV level is the only level below 5 MeV that has not so far been discussed. This level gamma-decays in a remarkable fashion, completely distinct from any other state in the experiment. It has a single decay branch, which is to the lowest 3^- state at 3.135 MeV. The fact that its decay is so different to any of its neighbours indicates a uniqueness that is best explained if it is of a different parity. The two candidate states are the fifth

4^+ and the sixth 3^+. The lack of a decay branch to the lowest 2^- level at 2.843 MeV favours the 4^+ assignment. According to the proton cross sections, there is little to choose between the "l=2" and "l=3" fits. Based on the evidence from the gamma-decay scheme, this level is identified with the fifth 4^+ state in ^{26}Na.

The four levels observed above 5 MeV have very distinctive gamma-decay patterns, but this in not sufficient to identify the states in ^{26}Na to which they correspond. The levels at 5.009 and 5.276 MeV decay via a single branch to the second 3^+ state at 1.805 MeV. The levels at 5.155 MeV and 5.384 McV also decay via a single branch to a 3^+ state, but in this case it is the ground state of ^{26}Na. The theoretical candidates in the figure 4.2 are the ninth 3^+ state and the sixth and seventh 3^- states. Decays to 3^+ states would be reasonable in either of these cases. The available information is not sufficient to make individual assignments for these highest lying levels observed in ^{26}Na.

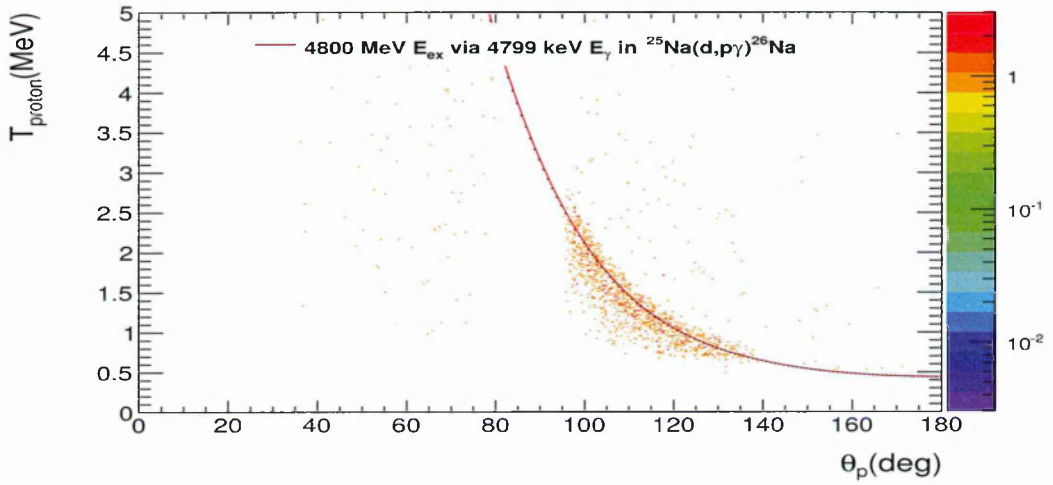

Figure 4.3: Measured kinetic energy of the scattered proton (after correction for the thickness effects) as a function of the laboratory angle in the region of the upstream box and CD detector. The yield for angles greater than 140° is almost completely suppressed by the virtue of the threshold energy for detection which is approximately equal to 0.6 MeV. This figure corresponds to the data selected for the 4^- state at 4.8 MeV in ^{26}Na; in general the effect is important for excitation energies above 4.5 MeV as can be noticed in SF plots previously.

Table 4.1 shows a summary of the assignments discussed above. The observed gamma-decay branches, which were critical in helping to decide the identifications, are given in order of intensity according to spin.The spectroscopic factors extracted by scaling the ADWA differential cross sections are shown.

Ultimately, in comparing the shell model predictions with the observed levels, and particularly in using this comparison to arrive at spin assignments, it is important to note that the shell model sets a very strict limit on the number of states of each spin that can realistically be expected. That is, every experimentally proposed state should definitely have a feasible theoretical counterpart. Similarly, but slightly less certainly, every theoretical state that is clearly predicted to be strong in the transfer reaction should ideally

have an experimental counterpart. These principles have been applied in the preceding discussion.

Whereas the cross sections were compared earlier with calculations employing a single "l"-value, the final fitting has been performed using orbital angular momentum combinations of either 0 and 2 or 1 and 3. The different shapes of the cross sections for different "l"-values mean that the scaling values (spectroscopic factors) for single dominant "l" values are not significantly affected by using the combination, but on the other hand the new fits can quantify the two contributions when both partial waves contribute to the cross section. According to the shell model, this is the case for a number of the states. There is generally very good agreement indeed between theory and experiment for both the excitation energies and the spectroscopic factors. The large suppression of magnitude for "l=3" transfers relative to "l=1" can lead, in this combined fitting, to an overestimate of the spectroscopic factors for "l=3" in the cases where "l=3" does not dominate the shape of the cross section, i.e. where there are comparable "l=1" and "l=3" spectroscopic factors.

					Experimental SF				Shell Model SF				Shell Model (USDA/WBP-M)	Shell Model
E_{ex}	J_i^π	Count	Coupling	J_f^π	SF(l=0)	SF(1)	SF(2)	SF(3)	$s_{1/2}$	$p_{3/2}$	$d_{5.3/2}$	$f_{7/2}$	Energy (MeV)	Shift(keV)
232 *	2^+	1	$2s_{1/2}$	$3^+, 1^+$	0.08		0.16		0.15		0.19		0.148	-84
405 *	2^+	2	$2s_{1/2}$	$3^+, 1^+, 2^+$	0.28		0.07		0.27		0.06		0.416	11
1507*	1^+	2	$1d_{3/2}$	2^+	0.00		0.39		0.00		0.19		1.409	-98
1805*	3^+	2	$1d_{3/2}$	$3^+, 2^+$	0.01		0.42		0.00		0.35		1.676	-129
1992**	4^+	1		$3^+, 2^+$	0.00		0.07		0.00		0.07		1.758	-234
2116*	5^+	1	$1d_{5/2}$	3^+	0.01		0.16		0.00		0.08		2.24	124
2195**	2^+	3	$1d_{3/2}$	$3^+, 2^+$	0.04		0.49		0.01		0.06		2.142	-52
2225*	4^+	2	$1d_{3/2}$	3^+	0.00		0.45		0.00		0.52		2.048	-177
2423**	2^+	4		$3^+, 2^+$	0.00		0.14		0.13		0.23		2.452	29
2843**	2^-	1	$2p_{3/2}$	$2^+, 1^+, 3^+$		0.1		1.10		0.05		0.20	2.94	93
3135*	3^-	1	$2p_{3/2}$	$3^+, 2^+$		0.09		0.19		0.15		0.13	3.23	93
3511*	4^-	1	$2p_{3/2}$	3^+		0.23		0.20		0.44		0.00	3.51	2
4087**	2^-	2	$2p_{3/2}$	$2^+, 3^+$		0.34		0.78		0.31		0.03	3.69	-397
4239**	4^+	5	$1d_{3/2}$	3^-	0.00		0.12		0.00		0.12		3.975	-264
4305*	5^-	1	$1f_{7/2}$	$4^+, 4^-$		0.01		0.25		0.00		0.46	4.40	96
4597**	3^-	2	$1f_{7/2}$	2^+		0.02		0.76		0.10		0.10	4.46	-135
4800**	4^-	2	$1f_{7/2}$	3^+		0.0		0.62		0.05		0.37	4.73	-68
4917*	6^-	1	$1f_{7/2}$	$4^+, 4^-, 5^-$		0.00		0.51		0.00		0.61	4.88	-36
4932**	3^-	4	$1f_{7/2}$	$2^+, 3^+$		0.00		0.63		0.28		0.05	4.77	-157
5009**	?		$1f_{7/2}$	3^+		0.00		0.24						
5155**	?		$1f_{7/2}$	3^+		0.00		0.15						
5276**	?		$1f_{7/2}$	3^+		0.00		0.29						
5384**	?		$1f_{7/2}$	3^+		0.00		0.14						

Table 4.1: Summary of the identification for the populated states in ^{26}Na via (d,p) reaction. The states marked with * were assigned in previous work [1]; however, all the states in the table have their updated versions with the new analysis in the present work in addition to the reassigned 5^+ spin to the state at 2116 keV instead of previously assigned 4^+. The states marked with ** are measured for the first time in the present work. Spins shown with question mark indicate indecisive spin assignments, and the spins are assumed as 4^- for given spectroscopic factors of the last four states.

The shell model calculations included in table 4.1 use the USD-A interaction in the sd shell [26] for the positive parity states and the WBP-M interaction in the spsdpf space [25] for the negative parity states. (Note that the excitation energies in the WBP-M are measured relative to the predicted ground state of 1^+ in that calculation, whereas the USD-A correctly predicts a 3^+ ground state and positive parity excitation energies are measured relative to this state). The excitation energies are given remarkably well, within the typical shell model accuracy of 150 keV, with few exceptions. Most notably, the first 4^+state and especially the second 2^- state, which ought to be predicted rather well, exceed this acceptable level of discrepancy. As discussed above, the relative strengths of the two prominent 2^+ states near 2.2 MeV are incorrect, reflecting a mistake in the prediction of the mixing of different configurations in the 2^+ states. A similar situation arises with the two relatively closely spaced 3^- levels at 4.6 and 4.9 MeV. The agreement in all other cases is sufficiently good that it would be appropriate to make a detailed study to compare the observed gamma-ray branching ratios with shell model predictions. Such a calculation is however beyond the scope of the present work.

In addition to the calculations performed in this work, the spectroscopic factors given by the shell model calculations presented in the previous work [1] are shown schematically in the figure 4.4 for a comparison with the experimental results for the corrected final spins in the current work. Their values for spin 2 are given in the table 3.8. The results showing the spectroscopic factors are matching with the shell model especially for the lower lying states. However, the shell model seems to have higher values from the experimental spectroscopic factors after 5 MeV. Overall picture stays still promising for the shell model in explaining the spectroscopic factors extracted experimentally from the proton angular distributions.

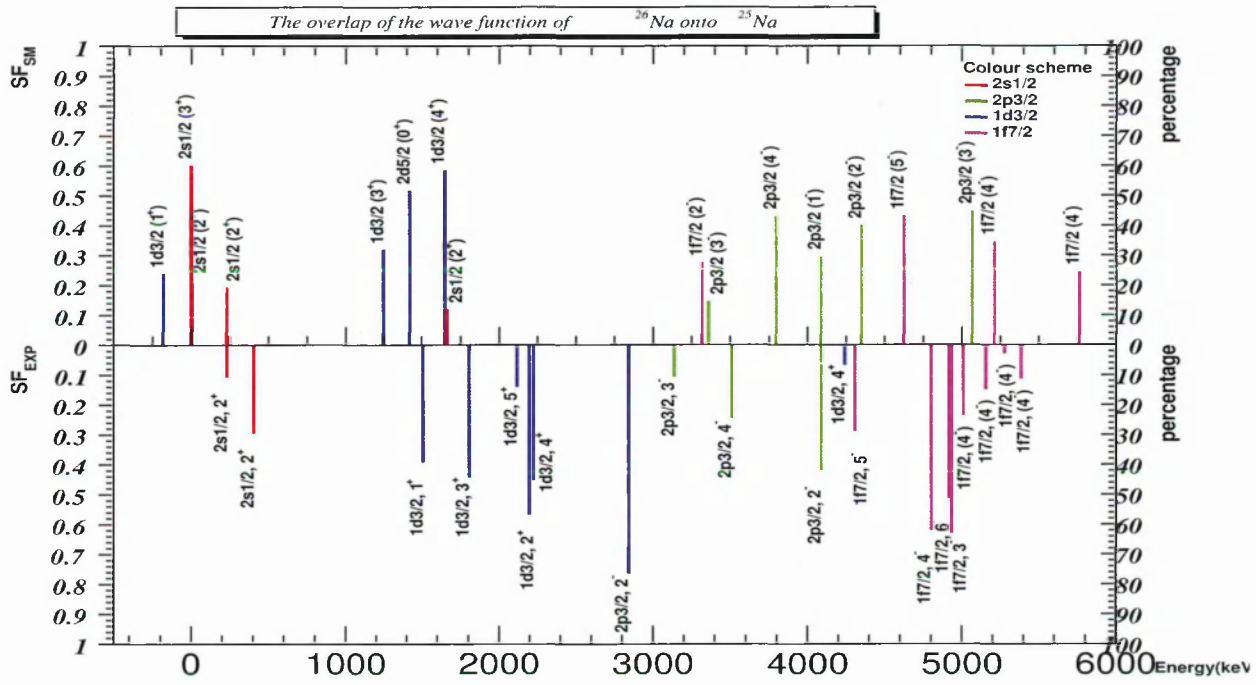

Figure 4.4: Spectroscopic factors from the shell model predictions are presented in the upper panel in consideration of USD interactions for the first 8 state energies and spdf-1$\hbar\omega$ interactions for the rest. These calculations were performed by Ed Simpson and G.L.Wilson in the previous work [1] (page 174) for the same data of $^{25}Na(dp\gamma)^{26}Na$.

Lastly, a comparison of the current work and the previous work by Wilson [1] is presented in figure 4.5. While there are only 7 states analysed for their spectroscopic factor in the previous work [1], their updated values in addition to 14 new values for other states in ^{26}Na are studied in the current work for the first time. The matching values for common states show strong agreement with the current work.

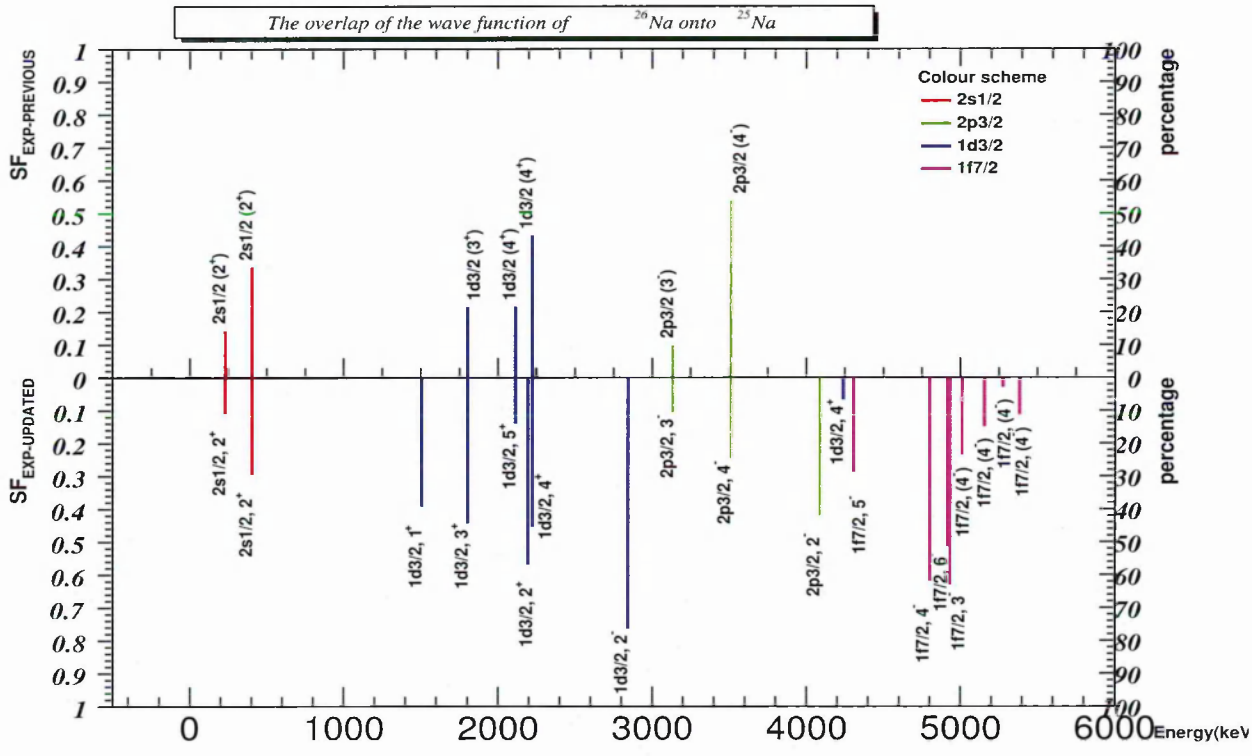

Figure 4.5: A comparison of the experimental spectroscopic factors of the excited states in ^{26}Na in the previous work by Wilson [1] and current work.

Chapter 5

Conclusion

5.1 Conclusion

In this thesis, the radioactive beam (RIB) ^{25}Na at 5 MeV/u with up to 3×10^7 particle/s on a $0.5 mg/cm^2$ deuterated polyethylene (CD_2) target has been used via the highly selective $(d, p\gamma)$ transfer reaction in inverse kinematics. The SHARC (the Silicon Highly-segmented Array for Reactions and Coulex) and TIGRESS (The TRIUMF-ISAC Gamma-Ray Escape-Suppressed Spectrometer) arrays were used.

The motivation of this work was to combine the information extracted from the particle and the γ detection in $^{25}Na(d, p\gamma)^{26}Na$ reaction and then compare the experimental results with the theoretical results coming from states in the shell model predictions. Because of the mass and shell structure of ^{26}Na excited states in terms of proton and neutron levels, the detailed study of the magic number 20 becomes possible with this experiment. The odd number of protons in the projectile of ^{25}Na enables different angular momentum couplings when one neutron transfer reaction takes place to populate odd-odd ^{26}Na nucleus. It's this interaction between the proton and neutron that makes the change in

the usual properties of the nucleus in ^{26}Na as one adds neutron to create a new isotope. To study with radioactive beam provides great opportunities for a better understanding of nuclei and nuclear reactions far from stability. The reduced γ-ray intensity due to the beam intensity (more than 100 times less than a typical stable beam) results in challenges for applying different methods of analysis effectively to the data. The normally powerful method of using $\gamma - \gamma$ coincidences has been shown to be very limited in applicability, especially for the higher energy γ-rays. That is why the high purity germanium (HPGe) and silicon array have each been developed , to be as efficient as possible in terms of solid angle, so as to deal with the low intensity of the beam and γ-rays in comparison to those experiments done by stable nuclei.

The present work has succeeded in identifying 10 new states in ^{26}Na as well as confirming the properties of previously discovered ones in [1]. Some differences were observed for a few states, most notably a state at 2.116 MeV, formerly assigned as 4^+, was identified as the first 5^+ state. The branching ratios corresponding to γ-ray decays of 24 different states have been measured to affirm the excitation energy of the individual states. A technique for gating on a particular γ-ray energy and a clover angle, to position the states in the two dimensional plot shown in the figure 3.9 for checking the γ-ray and excitation energy gates to be used to extract the proton and γ-ray angular distributions was developed and refined. This allowed us to compare the experimental and theoretical proton cross sections to find the spectroscopic factors of the states which have a different orbital angular momentum transfer, to make use of the analogies with ^{28}Al nucleus as indicated in the figure 3.89, and lastly to compare the excited state energies with those predicted in the shell model.

As the particle detection part of the set-up, the SHARC array enabled us to calcu-

late both the normalization factor as explained in sections 1.4 and 3.7 and the excitation energies of ^{26}Na as implemented in the sort code of the data. In consideration of the kinematics of the experiment, it's found essential to have $1500\mu m$ thick PAD detectors in the downstream for the full particle detection in the case of penetrating through the first layer of $140\mu m$ thick DSSSD in the downstream. However, the $1000\mu m$ thick upstream DSSSD detectors have been enough to stop the scattered particles, especially protons, in the backward angles. The elastic scattering part of the experiment took place in the downstream part, where the deuteron from elastic scattering with ^{25}Na were recorded. Fits to these data using an optical model analysis gave a normalization factor that resulted in absolute cross sections. The uncertainty in the normalization meant that the data had systematic errors folded in to the results given. Then, this error is added into the spectroscopic factors extracted from scaling the theoretical proton differential cross sections to the data points , in addition to the statistical errors which are determined by using ROOT [44].

Another important part of the analysis with SHARC array was determining the solid angle of the SHARC array as explained in the section 2.7. The results of the solid angle are presented in the histograms in both centre of mass and laboratory frames in the figure 2.20. The discussion in the section 4.1. where the spin assignments are done, also referred to the coverage of the SHARC array to explain the difference between the proton differential cross section data points in forward and backward angles. The essentially complete ϕ angle coverage of the SHARC array enabled us to study γ-ray distributions by using the information in the article by Rose & Brink [32] for cylindrically symmetric particle detection. Therefore, the only angular dependence is in terms of the θ zenith angle of the scattered protons and the γ-rays. This makes the entire γ-ray distribution

analysis so that it is based on the angles with regard to the beam direction, and not on the polar angle.

The resolution of the SHARC detector is also investigated as indicated in the figure 3.82, and it's concluded that the high efficiency HPGe detectors were necessary. As a test, when gated on 135° clovers the FWHM values of excitation energy peaks were found as 315 keV, 434 keV, and 553 keV for the populated states 232 keV, 3.511 MeV, and 5.384 MeV; however, with the gate on 90° TIGRESS clovers they were seen as 338 keV, 449 keV, and 583 keV for the same state energies. This agreement confirms that the different clover angles didn't distort the excitation energy of the states too much. However, this poor resolution in the SHARC array data gives no chance to separate those states with close proximity without the help of the γ-rays. As an example, the states at 232 keV and 405 keV or the states at 2195 keV and 2225 keV would not have been resolved. As discussed below, the γ-ray detection gives an order of magnitude improvement in the resolution for excitation energy.

Despite the disadvantages of the SHARC array, the elastic scattering normalization could not have been done without it. The particle identification that we have for punch through particles in the SHARC array was useful in the analysis. In this particular experiment, we could not get the transferred angular momentum very easily, because for many states it was possible to have two different angular momenta contribution. For instance, a weak p wave contribution could be as strong as an f wave contribution for a larger spectroscopic factor. If the projectile was spin zero, then the transferred angular momentum would be unique and the differential cross section would again be useful to give us the transferred angular momentum. In any case, the particle data also gave us the magnitudes of the spectroscopic factors, which would be more or less impossible without the particle

data, because too many assumptions about the validity of the reaction theory (ADWA) would be necessary. Therefore, the SHARC array is recommended for the same type of experiments in the future.

With regard to γ-ray detection overall, the highly segmented TIGRESS array with 32 segments and 4 cores per clover provided excellent energy resolution. The sigma values of each Gaussian peak corresponding to individual γ-ray energies detected in the experiment separately for both clover angles are presented in the figure 3.67 to give an idea of the resolution of the HPGe detectors in the experiment. For instance, the FWHM can be retrieved from the same figure as 3.83 keV, 42.67 keV, and 66.08 keV for the γ-rays at 232 keV, 3511 keV, and 5384 keV in 90° clovers. On the other hand, in the 135° clovers, the FWHM values varies as 3.49 keV, 33.84 keV, and 52.70 keV for the same γ-rays. This shows a steadily increasing resolution as the detected γ-ray energy rises. Also, the resolution at 90° is $10-25\%$ poorer than the resolution measured at 135°, for these reaction γ-rays. This arises due to Doppler broadening, which is given with respect to angle by the derivative of the equation for Doppler shift ($E'_\gamma = E_\gamma\gamma(1-\beta\cos\theta_\gamma)$), and is approximately proportional to $E_\gamma\gamma\beta\sin\theta_\gamma$ and hence reaches a maximum at 90°.

This information comes from the fits of the experimental data points for individual γ-rays as presented in the same figure 3.67. The important thing to notice here is the resolution does not differ too much for different clover angles as much as they alter for the excitation energies.

The need to have the TIGRESS array in addition to the SHARC array was crucial in the particle-γ correlation work. The $\gamma-\gamma$ coincidence data was also deployed efficiently for the low energy region, but it became no use for the higher energies due to the intensity limitations. If one does the similar correlation experiment with the stable beam, the

coincidence data will help more, for sure, to identify the states via the cascade decay of γ-rays for the states of interest. With regard to efficiency of the TIGRESS detectors, the relative efficiency values are achieved by the help of γ-rays coming from stationary sources , rescaled to two data points giving the absolute efficiencies for the γ-ray energies at 846 keV and 1238 keV as obtained from the ^{56}Co coincidence data. Since every calculation is done separately for the results of 90° and 135° clovers, the absolute efficiency curves are also presented separately in figure 2.15. The absolute efficiency values for each individual γ-ray energy is then read separately in the code when extracting the differential cross section of the protons to get the final spectroscopic factors (SF). The main formula used for SF is given in equation 3.12. As one can notice, the efficiency is one of the parameters to be implemented in the codes written to get the angular distributions of protons and γ-rays. For the angular distributions of γ-rays analysis, only the 8 different segment angles corresponding to both 90° and 135° clovers have been used, in the analysis. An analysis that ignored the segmentation information and employed just the 4 core angles and spanned the same clover angles was used to checked the consistency of the data points in the γ-ray angular distributions at the early stage. Eventually, the core angles were redundant in the analysis.

One of the most crucial parts of the set-up in terms of identifying the γ-rays and then the populated states was the scintillator detector, TRIFOIL. Prior to this experiment, no information was known about the TRIFOIL in terms of how efficiently we can use and how much benefit it can provide us. However, it was found to be very useful for making decisions about γ-rays and the excitation energies due to the reduction of the background that it brings in the qualitative analysis of a γ-ray spectra. That's because of the unique property of the zero degree detector, TRIFOIL, which enables the beam particles and the

similarly light particles to get through but stops and rejects the heavy compound nucleus products with the help of aluminium foil placed in front of it. It was used as a gate to identify any γ-rays decaying mainly from the transfer reaction products of interest and to distinguish them from other reactions which can contaminate the γ-ray spectrum too much. In terms of the final spectroscopic factor results and the γ-ray angular distributions TRIFOIL was not used in the quantitative analysis because the efficiency of the detector might be affected by radiation damage during the experiment.

For the coding perspective of the analysis, everything was done in C++ and ROOT which is an object oriented framework for large scale data analysis. And, it is found that they were extremely effective tools for analysing the data. The data acquisition often triggered an electric noise, and the sort code has been developed to select only the events of interest when the SHARC trigger is fired by a real event instead of going through all the data that are of no interest. This gave a big saving in the time elapsed for the data sorting.

Lastly, the new findings in the $^{25}Na(d,p\gamma)^{26}Na$ experiment will hopefully give some new insights about the shell gap for the magic number 20 as far as the coupling of valence neutron and the proton number of ^{26}Na concerns since the thing that is causing this change primarily is the change in the number of protons and neutrons.

The changes will be primarily in the orbitals where these protons can interact strongly with the neutrons. By using one neutron transfer as in the current experiment, we can probe the neutron orbitals that we are filling mainly up to $1f_{7/2}$ and $2p_{3/2}$ shell. The requirement of a strong spatial overlap of the wave function, $< \psi_1 | \psi_2 >$, of a valence proton with the wave function of a valence neutron tends to require the same, or similar principal quantum number n and a similar angular momentum quantum number "l" for a

particularly strong interaction. For example, the $d_{5/2}$ interaction with $d_{3/2}$ is very strong for the state at 2.195 MeV and 2.225 MeV in ^{26}Na, as all the coupling details are stated in the table 4.1. And, this is indeed what the experimental results are aimed to reflect in comparison with the current shell model predictions (performed by Prof.Wilton Catford and Dr. Adrien Matta) as discussed in the shell model chapter. The final results are found mostly matching with the predictions of the shell model except for a few cases , for instance, first 2^-, first 4^-, second 3^- states as indicated experimentally and theoretically in terms of their reaction strengths in the figure 4.1 and 4.2, respectively. The small discrepancies that have been observed can hopefully help to refine the interaction used in the calculations and lead to improved shell model calculations for these light neutron rich nucleus.

Bibliography

[1] G. Wilson, 2012. Investigating the Evolution of the Nuclear Magic Numbers via Single-Neutron Transfer Populating ^{26}Na. PhD Thesis, University of Surrey.

[2] W. N.Catford, Lecture Notes for The Euroschool on Exotic Beams, Vol. IV (2014). Available at http://personal.ph.surrey.ac.uk/ phs1wc/transfer/catford-euroschool-transfer.pdf, 2014.

[3] F. Nunes, N. Upadhyay, *et al.*, Reaction theory for studying rare isotopes, 2012 J. Phys.: Conf. Ser. 403 012029 , 2012.

[4] I. Thompson and F. Nunes, Nuclear Reactions for Astrophysics, Cambridge University Press, Cambridge 2009.

[5] R.C.Johnson and P.J.R.Soper, Phys. Rev. C 1, 976 (1970).

[6] O. Sorlin and M.-G. Porquet, Phys. Src. T152 (2013).

[7] T. Otsuka *et al.*, Phys. Rev. Lett. 87, (2001).

[8] M. G. Mayer, Phys. Rev. **75**, 1969 (1949).

[9] O. Haxel, J. H. D. Jensen, and H. E. Suess, Phys. Rev. **75**, 1766 (1949).

[10] Otsuka, T. (2013). Exotic nuclei and nuclear forces. Physica Scripta, 2013(T152), p.014007.

[11] Lise.nscl.msu.edu, (2014). LISE++ : Exotic Beam Production. [online] Available at: http://lise.nscl.msu.edu/documentation.html .

[12] Lise.nscl.msu.edu,(2014).PACE4.[online] Available at: http://lise.nscl.msu.edu/pace4.html .

[13] Oecd-nea.org, (2014). DWUCK-4/5, Scattering Cross-Sections of Spin 0 and 1/2 and 1 Particles by DWBA. [online] Available at: http://www.oecd-nea.org/tools/abstract/detail/nesc9872/ .

[14] Fresco.org.uk, (2014). Fresco. [online] Available at: http://www.fresco.org.uk/ .

[15] F. Meurders and G. D. Korte, Nuclear Physics A 249, 205 (1975).

[16] R. Varner, W. Thompson, T. McAbee, E. Ludwig, and T. Clegg, Physics Reports **201**, 57 (1991).

[17] J. A. Tostevin, University of Surrey version of the code TWOFNR (of M. Toyama, M. Igarashi and N. Kishida) and code FRONT (private communication).

[18] J. Lee, M. Tsang, and W. Lync, Phys. Rev. Lett. 95 , **222501**, (2005).

[19] K. S. Krane, Introductory Nuclear Physics (1987).

[20] B. L. Cohen, *Concepts of Nuclear Physics*, 16 ed. (McGraw-Hill, ADDRESS, 1999).

[21] N. K. Glendenning, *Direct Nuclear Reactions* (World Scientific Publishing, ADDRESS, 2004).

[22] G.R.Satchler, *Introduction to Nuclear Reactions* (PUBLISHER, ADDRESS, 1980).

[23] B.A.Brown and B. Wildenthal, Ann. Rev.Nucl.Part.Sci. 38 (1988).

[24] W. N. Catford *et al.*, Phys. Rev. Lett. 104 (2010).

[25] S. M. Brown *et al.*, Phys. Rev. C85 (2012).

[26] B.A.Brown and W.A.Richter, Phys.Rev. C74 (2006).

[27] E.K.Warburton and B.A.Brown, Phys. Rev. C46 (1992).

[28] B.A.Brown, A.Etchegoyen, and W.D.M.Rae, Computer code OXBASH, 1994.

[29] Zettili, N. (2009). Quantum mechanics. 2nd ed. Chichester: Wiley.

[30] P. Endt, Atomic Data and Nuclear Data Tables **55**, 171 (1993).

[31] Lecture Notes – Physics 564 Nuclear Physics , Professor Calvin W. Johnson, San Diego State University.

[32] H.J.Rose and D.M.Brink, Reviews of Modern Physics **39**, 306 (1967).

[33] Dudley H. Williams, Methods of Experimental Physics, Part A, Vol. 13, 1976.

[34] R.D.Gill, Gamma Ray Angular Correlations, UKAEA, Culham Laboratory, 1975.

[35] Root.cern.ch, (2014). RooFit — ROOT. [online] Available at: http://root.cern.ch/drupal/content/roofit .

[36] NNDC data tables, http://www.nndc.bnl.gov/chart/ 29 January 2013.

[37] Radware.phy.ornl.gov, (2014). Notes on the use of gf3 (html). [online] Available at: http://radware.phy.ornl.gov/gf3/gf3.html .

[38] Cplusplus.com, (2014). cplusplus.com - The C++ Resources Network. [online] Available at: http://www.cplusplus.com.

[39] http://www.micronsemiconductor.co.uk/pdf/cat.pdf.

[40] Srim.org, (2014). James Ziegler - SRIM & TRIM. [online] Available at: http://www.srim.org .

[41] R.B.Firestone, Nuclear Data Sheets **110, 1691**, (2009).

[42] I. C. Celik, 2014. http://personal.ph.surrey.ac.uk/ phs1wc/report/Celik-PhD-Thesis-Online-Appendix-2014.pdf . PhD Thesis Online Appendix, University of Surrey.

[43] R.C.Johnson and P.J.R.Soper, Phys. Src. T152 (2013).

[44] Root.cern.ch, (2014). Numerical Minimization — ROOT. [online] Available at: http://root.cern.ch/drupal/content/numerical-minimization.

[45] S. Lee *et al.*, Phys. Rev. C 73, (2006).

[46] S. Franchoo, L.Gaudefroy, O. Sorlin, *et al.*, Phys. Rev. C 70 (2004).

[47] R.M.Freeman, F.Haas, A.R.Achari, and R.Modjtahed-Zadeh, Phys. Rev. C 11, (1975).